



NTNU – Trondheim
Norwegian University of
Science and Technology

Geological and Mineralogical Investigation of The Western Part of The Nussir Copper Deposit

With focus on the geological relationship
between the Upper- and the Lower
mineralized horizons

Kjersti Moen

Geology

Submission date: June 2014

Supervisor: Kurt Aasly, IGB

Co-supervisor: Audun Sletten, Nussir ASA
Rune Berg Larsen, IGB

Norwegian University of Science and Technology
Department of Geology and Mineral Resources Engineering

Abstract

In this study, two mineralized horizons in the Nussir copper deposit were compared. The horizons were found by diamond drilling conducted by Nussir ASA in the western part of Nussir West in Kvalsund Municipality, Finnmark County. The Nussir copper deposit is hosted by sedimentary and volcanic rock of Precambrian- Palaeoproterozoic age (2.5-1.6 Ga) that was deposited in an intracratonic half graben. It is classified as sediment-hosted stratabound copper deposit where bornite, chalcocite and chalcopyrite occurs as disseminated grains in a dolomitic rock with mineralization along veins.

Geological mapping, re-logging of diamond drill cores, thin section analysis, micro probe analysis of thin sections, statistical analysis of chemical data and a correlation of geophysical measurements in drill holes was performed.

Geological mapping indicated a conformation between the sedimentary Units in the Saltvatn Group. Drill core logging indicated a thicker and dolomite-rich Upper mineralized horizon and a more slate-rich dolomite in the Lower mineralized horizon. Because of the increasing contents of slate in the Lower mineralized horizon, it seem to pinch out towards west. The most western drill hole seemed to cut through the Upper mineralized horizon. This is in contradiction to the pre-classification of this horizon, which had classified it as being part of the Lower horizon. This observation comes from re-logging and study of polarized thin sections, which showed similarities with the Upper horizon. Microprobe analysis indicate a higher concentration of copper in bornite in the Upper mineralized horizon, and a higher concentration of silver in bornite and chalcocite in the Lower mineralized horizon. Multivariate analysis indicate great similarity between the Upper- and Lower mineralized horizon, and a lateral similarity along the mineralized horizon from east to west. Previous trace element analysis have been performed by use of different methods. In particular, one set of methods were utilized for the samples analysed in 2008 and before, and another set for the samples from 2008 and later. Geophysical measurements using induced polarization (IP) in the mineralized horizons indicated highest response from chalcocite, and natural gamma radiation indicated a higher content of feldspar in the Upper mineralized horizon.

Earlier studies have been speculated if the origin of the two mineralized horizons, whether it is (a) of sedimentary origin, or (b) caused by a tectonic repetition in form of duplex structures of one mineralized horizon. Previous studies have not been able to answer this, but stated that there is absence of geological structures that could support a theory of a tectonic repetition. The results from this work support a tectonic repetition of the occurrence of the two mineralized horizon with epigenetic mineralization, but the lack of observed duplex structures lead to the conclusion that there is need for further investigation to be able to uncover the real origin of Nussir copper deposition.

Sammendrag

To mineraliserte horisonter i Nussir kobberforekomst i Kvalsund kommune, Finnmark fylke ble sammenlignet. De to horisontene ble påvist ved diamantboring. Kobber forekomsten ligger i en dolomitt med omliggende skifer-holdig sandsteinslag i sedimentære og vulkanske bergarter av Prekambrisk-Palaeosoisk alder (2.5-1.6 Ga), som ble avsatt i en intra-kratonisk halv graben. Forekomsten er klassifisert som sediment-hosted stratabound copper deposit (SSC), der bornite, chalcocite og chalcopyrite hovedsaklig forekommer som disseminerte korn i en dolomitt med mineralisering langs årer.

Det er gjennomført geologisk kartlegging, re-logging av diamant borekjerner, analyser av tynn slip, mikrosonde analyser av tynn slip, statistiske analyser av analyse-data og korrelasjon av geofysiske målinger i borehull.

Geologisk kartlegging indikerte en konformitet mellom de sedimentære sekvensene i Saltvatn Gruppen. Undersøkelser av borekjerner viste et tykkere og mere dolomitt-rikt øvre mineralisert horisont og et skifer-rikt dolomitt lag i den nedre mineraliserte horisonten. På grunn av et økende skifer-innholdet i den nedre mineraliserte horisonten, synes den å kile ut mot vest. Det vestligste borehullet syntes å tilhøre en øvre mineraliserte horisonten, som tidligere er klassifisert å tilhøre den nedre mineraliserte horisonten. Mikrosonde analyser indikerte en høyere konsentrasjon av kobber i den øvre mineraliserte horisonten, og et høyere innhold av sølv i bornite og chalcopyrite i den nedre mineraliserte horisonten. Multivariate analyser indikerte likhet mellom den øvre- og nedre mineraliserte horisonten, og ga indikasjoner på en lateral likhet langs den mineraliserte horisonten fra øst til vest. Tidligere analyser av element har blitt utført ved bruk av flere analyse metoder. Et sett med analyse metoder var nytt for prøver analysert i 2008 og tidligere, mens et annet metode sett var nytt for prøver analysert i 2008 og senere. Geofysiske målinger ved bruk av induert polarisasjon (IP) i de mineraliserte horisontene, indikerte høyeste respons fra chalcocite, og naturlig gamma stråling indikerte et høyere innhold av feltspatt i den øvre mineraliserte horisonten.

Tidligere undersøkelser har spekulert i opprinnelsen til de to mineraliserte horisontene, enten at de er av a) sedimentær opprinnelse, eller b) at de er forårsaket av en tektonisk repetisjon i form av duplisering av en mineralisert horisont. De påpekte at det ikke er påvist strukturer som støtter teorien om en tektonisk repetisjon. Våre data indikerer stor likhet i sammensetningen av sporelement i de to horisontene, og støtter slik teorien om at det har skjedd en tektonisk repetisjon. Strukturgeologiske målinger gav imidlertid få holdepunkt for at det kan ha skjedd en duplisering. Videre undersøkelser synes nødvendig for å klargjøre opprinnelsen til de to horisontene i Nussir kobberforekomst.

Acknowledgments

Thanks to Associate Professor Kurt Aasly, at Department of Geology and Mineral Resources Engineering, NTNU, for supervision during this thesis. Thanks also to my co-supervisors, Associate Professor Steinar Løve Ellefmo, NTNU, and Professor Rune Berg-Edland Larsen, NTNU.

Thank to Nussir ASA for fundings during fieldwork, thin section preparation and micro probe analysis. Thank to Audun Sletten, Kjell Nilsen, Knut Emil Thomassen and Øystein Rushfelt at Nussir for their support, all their good stories, and a memorable field season in Repparfjorden.

Thank to the geophysical team at NGU, Einar Dalsegg, Harald Elvebakk and Jan Steinar Rønning, for introducing me to the geophysical measurement methods performed in Repparfjorden.

I would also like to thank Espen Torgersen and Håvard Smeplass for the many interesting and inspiring discussions.

Thank to my father Vidar Moen for guidance during the multivariate analysis using the SPSS software package.

Finally, thank to my family for their support and care in ups and downs during my work with the thesis.

Takk!

Contents

1	Introduction	1
2	Background	2
2.1	Previously work	2
2.2	Drill core analysis	2
2.3	Geophysical survey.....	5
2.4	Regional geology of Finnmark and the Repparfjord-Komagfjord tectonic window...	6
2.5	Sediment-hosted copper deposits	18
3	Materials and Methods	28
3.1	Optical microscopy and thin section preparation	28
3.2	Geological mapping.....	28
3.3	Drill core logging.....	28
3.4	Electron probe micro analyzer (EPMA)	29
3.5	Analyse data	30
3.6	Univariate statistics.....	30
3.7	Multivariate analysis (MVA) - Principle component analysis (PCA) and discrimination analysis (DA)	32
3.8	Geophysical measurements	36
4	Results	37
4.1	Geological mapping.....	37
4.2	Drill core re-logging	45
4.3	Comparison of the Upper and the Lower mineralized horizon in thin section.....	56
4.4	Micro probe analysis	62
4.5	Results of electron probe micro-analysis of sulphides (mass percent).....	70
4.6	Geochemical analysis	94
4.7	Multivariate analysis of trace elements in drill core samples.....	97
5	Drill hole geophysical logging	108
6	Discussion	111

7	Conclusions	117
8	Further work.....	118
9	References	119
10.	Appendix A	122
11.	Appendix B	128
12.	Appendix C	150
13.	Appendix D	158
14.	Appendix E.....	173

List of figures

Figure 1.	Overview map of the Nussir copper deposit.....	1
Figure 2.	(A) Map showing the geographic location of the two mineralized horizons. (B) Cross section.....	2
Figure 3.	Illustration of the JORC code of reserves	2
Figure 4.	Overview of the Achean provinces in the Fennoscandian Shield	7
Figure 5.	Early Paleoproterozoic rifting of the Fennoscandian Shield	8
Figure 6.	The regional setting of the Repparfjord-Komagfjord tectonic window.....	9
Figure 7.	Schematic lithostratigraphy of the Saltvatn Group.....	11
Figure 8.	Geological map of the Repparfjord window.....	13
Figure 9.	Detailed geological map of the central-eastern part of the Repparfjord Window. ...	15
Figure 10.	Magnetic total field map with interpreted geological structures	16
Figure 11.	Map showing the Nussir copper deposit	17
Figure 12.	Dextral ductile shearing in the Repparfjord Window.....	17
Figure 13.	Illustration of a sedimentary basin.....	19
Figure 14.	Effective stability of metal complexes and the stability fields for copper in solution	22
Figure 15.	The time period of the formation of the world's greatest SSC deposits.....	23
Figure 16.	Map showing the distribution of sediment-hosted stratabound copper deposits	24
Figure 17.	Simplified geologic map of the Central African Copperbelt	25
Figure 18.	Picture of a JEOL JXA-8500F Electron Probe Micro Analyzer (EPMA).....	30
Figure 19.	Illustration of the definition of the Nussir copper deposit in Zone 1, 2 and 3	32
Figure 20.	Example of eigenvalues.	35

Figure 21. An example of results of a Wilks' Lambda test.	36
Figure 22. Example of scatter plot of discriminant analysis	36
Figure 23. Geological map of the two mineralized horizon from profile 10 and westward	37
Figure 24. The picture shows an outcrop of the mineralized horizon	38
Figure 25. Picture shows the Upper mineralized horizon	38
Figure 26. The picture shows an example of the monomict dacitic Stangvatn conglomerate.	39
Figure 27. The picture shows the footwall slate with coarser layer of sandstone.	39
Figure 28. Picture shows the footwall slate containing layers of green mica	40
Figure 29. Hang wall slate.....	40
Figure 30. The picture shows the dolomite with clasts of jasper and quartz	41
Figure 31. The picture shows the dolomite with clasts of jasper and quartz	41
Figure 32. The picture shows the green tuffite containing pyroclasts.....	42
Figure 33. The picture shows the vulcanite.....	42
Figure 34. Geological map of the Nussir West with structural measurements	43
Figure 35. Geological map on top of the geological map made by Kjell Nilsen and Edward Iversen (1990)	44
Figure 36. Geological map with the location of diamond drill holes.....	45
Figure 37. The figure show the results from re-logging of the diamond drill core NUS-DD-13-004.....	49
Figure 38. The figure show the results from re-logging of the diamond drill core NUS-DD-13-012.....	51
Figure 39. The figure show the results from re-logging of the diamond drill core NUS-DD-13-003.....	53
Figure 40. The figure show the results from re-logging of the diamond drill core NUS-DD-13-002.....	55
Figure 41. Photomicrograph of thin section NUS_005.....	56
Figure 42. Photomicrograph of thin section NUS_005.....	57
Figure 43. Photomicrograph of thin section NUS_011	57
Figure 44. Photomicrograph of thin section NUS_018.....	58
Figure 45. Photomicrograph of thin section NUS_025	59
Figure 46. Photomicrograph of thin section NUS_031	60
Figure 47. Picture of thin section NUS_002.	62
Figure 48. Picture of the hang wall slate in thin section NUS_002	62
Figure 49. Picture of hang wall slate in thin section NUS_002	63

Figure 50. Sketch of thin section NUS_005.....	63
Figure 51. Picture of the Upper mineralized horizon in thin section NUS_005	64
Figure 52. Picture of the Upper mineralized horizon in thin section NUS_005	64
Figure 53. Picture of the Upper mineralized horizon in thin section NUS_005.....	65
Figure 54. Picture of the Upper mineralized horizon in thin section NUS_005	65
Figure 55. Sketch of thin section NUS_013.....	66
Figure 56. Picture of the Upper mineralized horizon in thin section NUS_013	66
Figure 57. Picture of thin section NUS_002.	70
Figure 58. Picture of hang wall slate in thin section NUS_002.	70
Figure 59. Sketch of thin section NUS_005.....	71
Figure 60. Picture of the Upper mineralized horizon in thin section NUS_005	71
Figure 61. Picture of thin section NUS_011 in the Lower mineralized horizon.....	72
Figure 62. Photomicrograph show analyse area NUS_011:1	72
Figure 63. Photomicrograph show analyse area NUS_011:1	73
Figure 64. Photomicrograph show analyse area NUS_011:3.	73
Figure 65. Picture of thin section NUS_018 in the Lower mineralized horizon.....	74
Figure 66. Photomicrograph show analyse area NUS_018:1	74
Figure 67. Photomicrograph show analyse area NUS_018:2	75
Figure 68. Photomicrograph show analyse area NUS_018:3	75
Figure 69. Picture of thin section NUS_025 in the Lower mineralized horizon.....	76
Figure 70. Photomicrograph show analyse area NUS_025:1	76
Figure 71. Photomicrograph show analyse area NUS_025:2	77
Figure 72. Picture of thin section NUS_031 in the Upper mineralized horizon	77
Figure 73. Photomicrograph show analyse area NUS_031:1	78
Figure 74. Photomicrograph show analyse area NUS_031:2	78
Figure 75. Scatter diagram of Cu/Fe-Cu ratio of WDS analysis in bornite.	85
Figure 76. Scatter diagram of Cu/S-Cu ratio of WDS analysis in bornite.	86
Figure 77. Scatter diagram of Co-Cu ratio of WDS analysis of bornite.	86
Figure 78. Scatter diagram of Cu-Ag ratio of WDS analysis in bornite	87
Figure 79. Scatter diagram of Cu-Zn ratio of WDS analysis in bornite.....	87
Figure 80. Scatter diagram of Cu/S-Cu ratio of WDS analysis in chalcocite	88
Figure 81. Scatter diagram of Cu-Ag ratio of WDS analysis in chalcocite	88
Figure 82. Scatter diagram of Zn-Cu ratio of WDS analysis in chalcocite.....	89
Figure 83. Scatter diagram of Cu-Fe ratio of WDS analysis in chalcocite.	89

Figure 84. Scatter diagram of Cu-Cu/Fe ratio of WDS analysis in chalcopyrite.....	90
Figure 85. Scatter diagram of Cu-Cu/S ratio of WDS analysis in chalcopyrite.....	91
Figure 86. Scatter diagram of Cu-Ag ratio of WDS analysis in chalcopyrite.....	91
Figure 87. Scatter diagram of Cu-Zn ratio of WDS analysis in chalcopyrite.	92
Figure 87. Ternary plot of Cu-Fe-S ratio in WDS analysis	93
Figure 89. Natural logarithm of mean values.....	95
Figure 90. Natural logarithm of standard deviation.	96
Figure 91. Multivariate comparison of the lateral variation within Zone 1	99
Figure 92. Histogram of the multivariate comparison of new and old samples in zone 1, 2 and 3.....	100
Figure 93. Scatter plot of multivariate comparison between zone 1, 2 and 3	102
Figure 94. Scatter plot in multivariate comparison of new and old samples within Zone 3). 104	
Figure 95. Scatter plot in multivariate comparison between new samples in Zone 1 (Profile 10 and westward) and Zone 2 (the Upper mineralized horizon).....	105
Figure 96. Scatter plot in multivariate comparison between new samples in Zone 1 (Profile 10 and westward) and Zone 3 (the Lower mineralized horizon)	106
Figure 97. Probability plot and histogram for the discriminant analysis of the comparison of the Upper mineralized horizon (Oreup) and the Lower mineralized horizon (Orelow).	107
Figure 98. Figure show the mineralization in the re-logged drill core NUS-DD-13-004 compared with IP-effect, resistivity and gamma radiation in drill hole log DD-13-004 Nussir, 5.9.2013.....	110

List of tables

Table 1. Overview of the laboratories performing geochemical analysis.....	4
Table 2. The histograms shows the sample length of drill core samples	33
Table 3. Description of nomenclatures in the multivariate analysis.	33
Table 4. Comparison of the Upper- and Lower mineralized horizon	61
Table 5. Table shows the predicted mineral composition of the analysed minerals by WDS .	67
Table 6. Results from WDS analysis	68
Table 7. Results from WDS analysis	69
Table 8. Results of electron probe micro-analysis in drill core NUS-DD-13-004.....	79
Table 9. Results of electron probe micro-analysis in drill core NUS-DD-13-004.....	79
Table 10. Results of electron probe micro-analysis in drill core NUS-DD-13-004.....	80
Table 11. Results of electron probe micro-analysis in drill core NUS-DD-13-002.....	81

Table 12. Results of electron probe micro-analysis in drill core NUS-DD-13-002.....	82
Table 13. Results of electron probe micro-analysis in drill core NUS-DD-13-003.....	83
Table 14. Results of electron probe micro-analysis in drill core NUS-DD-13-012.....	84
Table 15. Classification results from the multivariate comparison of the lateral variation within Zone 1 (Profile 10 and eastward)	98
Table 16. Classification results in multivariate comparison of new samples (1) and old samples (2) in Zone 1 (profile 10 and eastward).....	99
Table 17. Classification results in multivariate comparison of new and old samples in Zone 1, 2 and 3	100
Table 18. Classification results in the multivariate comparison of new samples from Zone 1, 2 and 3	101
Table 19. Classification results from the linear discriminant analysis of new drill core samples within Zone 2	103
Table 20. Classification results in the multivariate comparison of new and old samples within Zone 3 (Lower horizon)	103
Table 21. Classification results in the multivariate comparison between new samples in Zone 1 and Zone 2.....	104
Table 22. Classification results in the multivariate comparison between new samples in Zone 1 (Profile 10 and westward) and Zone 3 (Lower horizon).....	106
Table 23. Classification results from the multivariate comparison of the Upper mineralized horizon and the Lower mineralized horizon	107

1 Introduction

The Nussir copper deposit is a sedimentary-hosted copper deposit located in the Kvalsund Municipal, Finnmark County, Norway, and stretches from Repparfjorden in the east to the western part of the Nussir area (Figure 1).

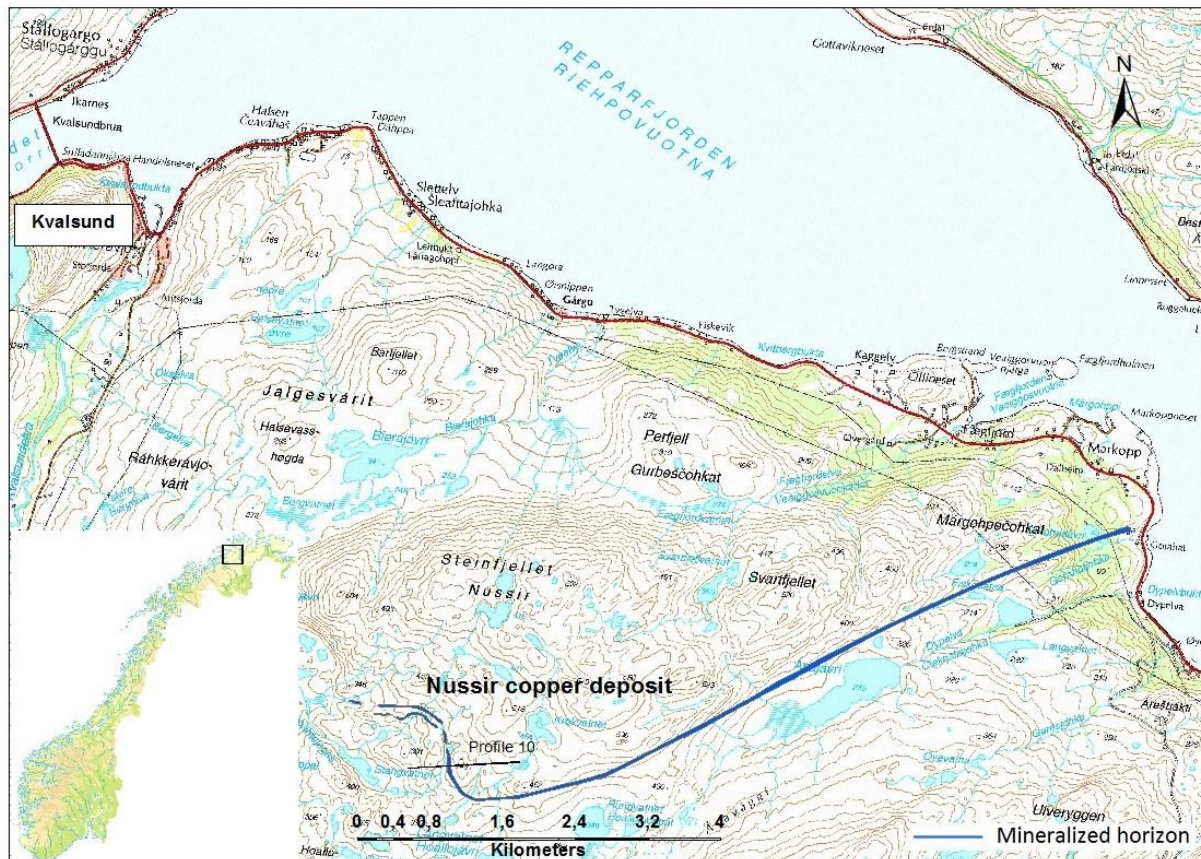


Figure 1. Overview map of the Nussir copper deposit with two mineralized horizons past Profile 10 in the western part of the Nussir area. The mineralized horizons is marked with blue lines.

In 1990, two dolomite- and calcite-rich mineralized horizons were detected past Profile 10 in the western part of the Nussir copper deposit. A further drilling campaign westward identified a continuation of the two mineralized horizons but seems to fade out (figure 1).

The origin and distribution of the two mineralized horizons was unclear. It has been speculated if this could have been caused by a tectonically phenomenon where folding or/and thrusting have created a repetition of the mineralized horizon, or if the two mineralized horizons was of a sedimentary origin.

The aim of this study was to compare the two mineralized horizons recorded in the western part of Nussir copper deposit. More specifically, to compare the Upper- and the Lower mineralized horizons from Profile 10 and westward (Figure 2). In order to compare the two mineralized horizons, geological mapping, drill core logging, thin section study, micro probe analysis, statistical analysis of chemical data and geophysical logging of drill cores were performed.

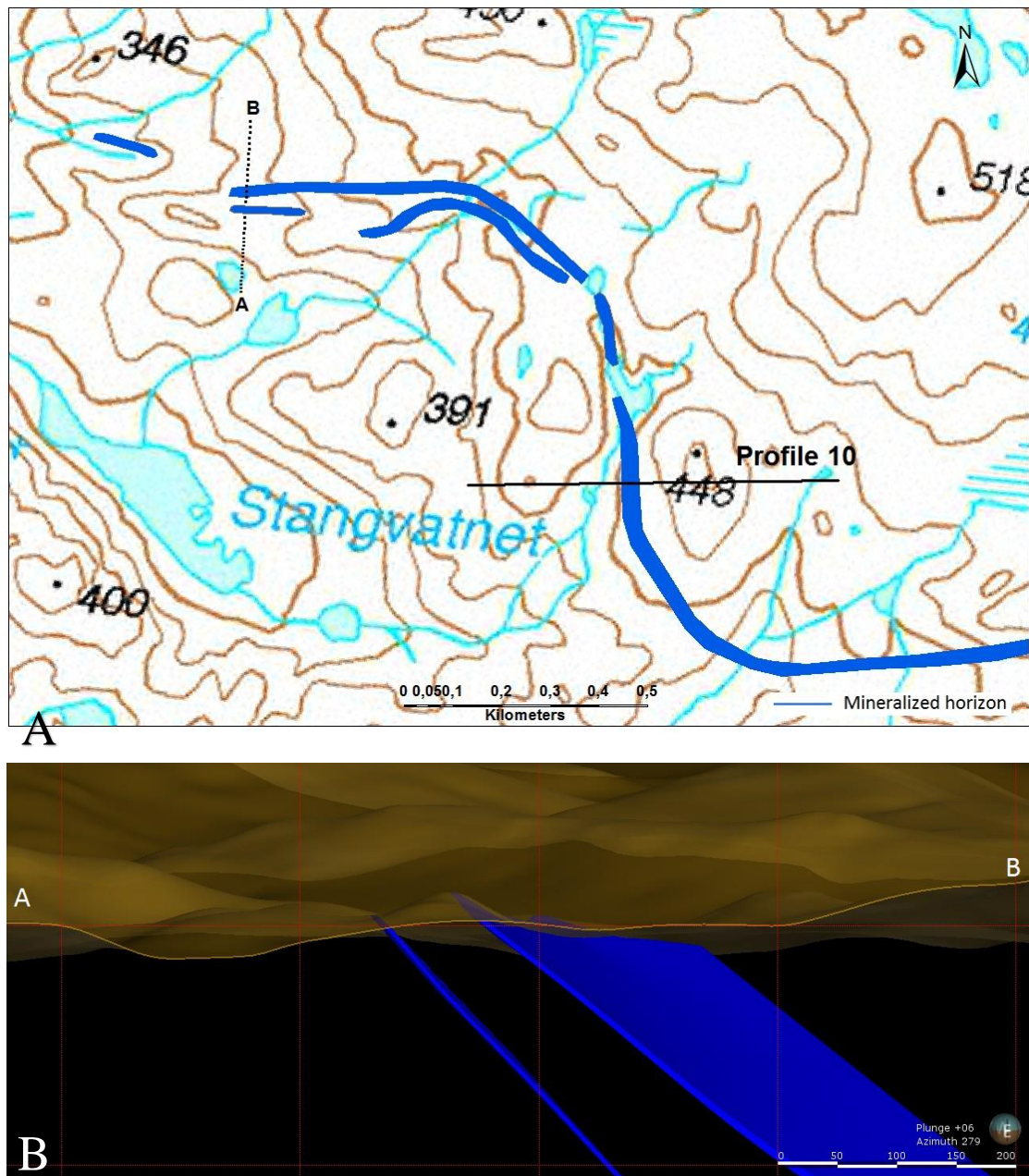


Figure 2. (A) Map showing the geographic location of the two mineralized horizons, the Upper- and the Lower horizons (marked with blue lines) from Profile 10 and westward. Map developed in Arcgis. (B) Cross section from dashed line (A) illustrate the appearance of the Upper- and Lower mineralized horizon steeply dipping (about 70°) toward NE. The mineralized horizons is about two meter thick with an apparent distance of about ten meters between, and the total length of the horizons is unknown. Figure developed in Leapfrog geo.

2 Background

2.1 Previously work

The Nussir copper company was established in 2005 (Nussir AS) and later registered as the Public Limited Company in 2007 (Nussir ASA). The company took over the exploration rights on the Nussir copper deposit in 2006. Between 2006 and 2013, Nussir ASA have been performing diamond drilling, percussion drilling (PD) and chip sampling (CH) in the area. Former investigation on the Nussir copper deposit was performed by ASPRO (AS Prospektering). ASPRO was the exploration department in the closed mine in Sydvaranger, and owned the exploration rights at the Nussir copper deposit from 1985 to 2006. Throughout this period, they conducted diamond drilling and surface surveys on the Nussir copper deposit. On the twenty-first of March, 2014, the Government and Modernization Ministry approved the zoning plan for Nussir in the Kvalsund municipality in Finnmark. This included a permission of fjord landfill and underground mining. The Nussir copper deposit is therefore accessible for mining activity, and fulfilled one of three steps of JORC code for reserves. A reserve is defined as a resource that is accessible, have economic and technological feasibility and where sufficient geological knowledge is collected (Figure 3). The accessibility of the Nussir copper deposit increased the efforts from investors, and ensured further research to fulfil the requirements in the JORC code.

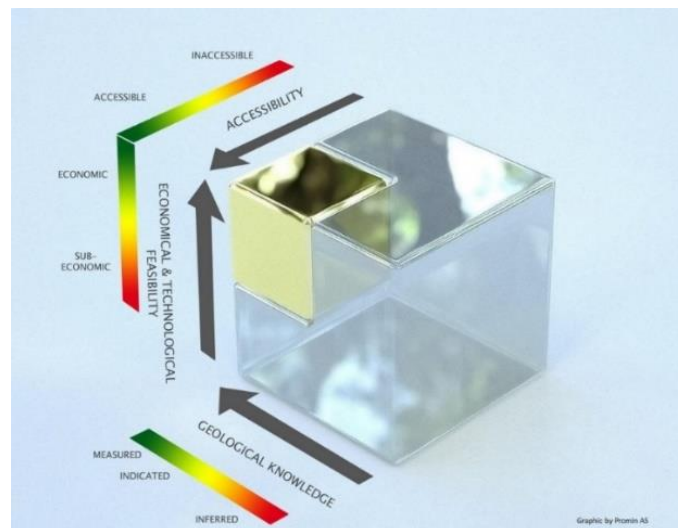


Figure 3. Illustration of the JORC code of reserves. Figure modified from JORC webpage (Joint Ore Reserves Committee of The Australasian Institute of Mining and Metallurgy 2012). The figure show that the three factors accessibility, economical & technological feasibility and geological knowledge must be met if a resource is to be classified as a reserve.

2.2 Drill core analysis

Geochemical analysis have been performed on drill core samples from diamond drilling (DD), percussion drill cores (PD) and chip samples (CH). The mineralized horizons were sampled by diamond drilling. The drill core samples analysed were usually around one meter in length. Drill cores were split longitudinal into two halves, crushed and pulverized. The geochemical data was registered in a drill hole database on a Excel spreadsheet. The company has recently updated the database (pers. med Audun Sletten). Some columns and rows in the spreadsheet were missing due to the different methods of analysis and number of analysed elements. Drill

cores analysed by OMAC include all the selected elements. Drill cores analysed by ALS have omitted the element boron (B), cerium (Ce), germanium (Ge), mercury (Hg), lithium (Li), niobium (Nb), rubidium (Rb), selenium (Se), tin (Sn), tantalum (Ta), tellurium (Te), yttrium (Y) and zirconium (Zr). An overview of laboratories, number of (diamond) drill holes, drill core samples and the analytical methods used in the analysis is shown in Figure 3. The drill holes analysed before 2002 was subject to unknown analytical methods where Cu, Au and Ag was the element analysed (Wheeler 2012). Pre-2002 analysis have a higher uncertainty and lower accuracy than analysis conducted in 2008 (Sandstad 2008). Aqua Regia digestion conducted by OMAC Laboratories is partial for the elements Al, Ba, Cr, K, Na, Sn, Sr, Ta, Ti, V and W, while Au, Pt and Pd were analysed by Fire Assay/AA and Fire Assay ICP. During the period 2006 to 2008, 20 percussion drill holes (PD) were analysed. In 2002 (63 samples) and 2008 (199 samples) drilled in 1990 were re-analysed (BH 90-003, 90-007, 90-008, 90-009, 90-010, 90-011, 90-017, 90-020 and 90-022) (Table 1.) due to unknown analytical methods and a higher degree of uncertainty. The re-analysed samples consisted of a few meters from each drill holes, where each sample represented a meter. Silver (Ag) was the only precious metal analysed in the re-analysed drill cores. Sample preparations at the laboratory ALS Chemex in Piteå were done through the following steps:

- Splitting of drill cores into two halves
- One-half crushed (70% < 2 mm)
- Riffle splitting of crushed sample
- Pulverising (85% < 75 µm).

Table 1. Overview of the laboratories performing geochemical analysis of drill cores from Nussir. The table lists the year of drilling, the number of (diamond) drill holes, the number of drill core samples, total meter analysed, and size of samples, analysed elements / number of elements, the analytical method, and the digestion method. The information is modified from Wheeler, A. (2012). "Resource estimation update." (Nussir project). *The columns marked with yellow colour represents re-analysed drill cores that were drilled in 1990 and re-analysed in 2002 and 2008. Re-analysed drill core samples consist of new samples, and do not correspond to the previous drill core samples.*

Laboratory	Year of drilling	Number of drill holes	Number of drill core samples	Total meter analysed (m)	Size of sample (m)	Analysed elements	Analytical method	Digestion method	
Mercury Analytical Ltd, Ireland	1984	8 channel samples from mineralised surface outcrop.						Unknown	Unknown
Mercury Analytical Ltd, Ireland	1985	6	Every meter or less	26.2	1	Cu, Au, Ag	Unknown	Unknown	
Mercury Analytical Ltd, Ireland	1986	2	Every meter or less	279.5	1	Cu, Au, Ag	Unknown	Unknown	
Caleb Brett Laboratories, England	1988	6	Every meter or less	205.57	1	Cu, Au, Ag	Unknown	Unknown	
OMAC Laboratories, Ireland	1990	22	567	893.4	1	Cu, Au, Ag	Unknown	Unknown	
OMAC Laboratories, Ireland	1990 Re-analysed in 2002	9	63	?	1	47	ICP	Aqua Regia digestion	
ALS Chemex laboratory, Sweden	1990 Re-analysed in 2008	4	199	?	1	46 +3	Four acid ICP-AES and 30 g Fire Assay ICP	Aqua Regia digestion	
OMAC Laboratories, Ireland	1995	4	58	79.6	1	Cu, Au, Ag	Unknown	Unknown	
OMAC Laboratories, Ireland	1996	4	66	66.5	1	Cu, Au, Ag	Unknown	Unknown	
OMAC Laboratories, Ireland	*2006-2008	20 and 9	832	*162.6	1	46	ICP-OES	Aqua Regia digestion	
OMAC Laboratories, Ireland	2008	9	407	?	01.feb	46 + 3	ICP-OES and Fire Assay/AA on 30 g samples	Aqua Regia digestion	
ALS Chemex laboratory, Sweden	2011	6	164	895.3	1	33 + 3	Four acid ICP-AES and 30 g Fire Assay ICP		
ALS Chemex laboratory, Sweden	2013	10	125	148.45	1	33 +and 3	Four acid ICP-AES and 30 g Fire Assay ICP		

* Samples analysed in 2006-2008 from 20 percussion drill holes and 9 diamond drill holes.

NGU (Sandstad 2008) carried out geochemistry correlation of elements in scatterplot and along drill holes. The analyses were based on XRF data from pre-2007 drill cores. The main goal of the work was to inspect any correlation between Cu and Ag, S, As, Co, Au and Fe. This correlation is valuable for the economic evaluation of the deposit, since correlation can provide an estimate of the behaviour and concentration of precious metals in mineralised zones (Sandstad 2008). Transition, alkali and alkaline metals were correlated with Cu to detect ore controlling factors and the potential for extending the mineralization. He concluded that there was no correlation between gold and copper, or copper and the platinum minerals.

2.3 Geophysical survey

NGU has performed geophysical surveys in cooperation with Nussir ASA. In the summer of 2007 and 2011, NGU conducted airborne magnetic, radiometric and electromagnetic geophysical surveys in a part of the Repparfjord tectonic window (Ofstad 2013). This survey covered an area of 1200 km². This was directed by a Hummingbird™ electromagnetic and magnetic helicopter survey system. Radiation were measured by a gamma spectrometer placed under the belly of the helicopter (Ofstad 2013). This data were gridded with a cell size of 50 x 50 m, and presented in a geophysical map with shaded relief in a scale of 1:50000. In 2007, 2011 and 2013, induced polarisation (IP) and resistivity were measured at the Nussir copper deposit in the Kvalsund Municipal. Charge potential (CP) in the copper minerals were measured to qualify the responds of this method. In addition, drill hole geophysical logging was measured in four holes (DD-11-004, DD-13-004, DD-13-008 and DD-13-011) (Dalsegg, Elvebakk et al. 2013).

2.4 Regional geology of Finnmark and the Repparfjord-Komagfjord tectonic window

2.4.1 The Fennoscandian Shield

The Fennoscandian Shield is situated in the north-western part of the East European Craton. It forms part of NW-Russia, Finland, Sweden and Norway. This shield contains old rocks from the Archean Eon (4 – 2,5 Ga), Palaeoproterozoic rocks (2,5 – 1,5 Ga), Meso- and Neoproterozoic rocks (1,5 – 0,5 Ga) and Phanerozoic rocks (500 – 340 Ma).

Formation of larger continents by converging and diverging activity, dominated the Archean Eon. This gave birth to several greenstone belts and plutonic rocks. Slabunov et al. divides the Archean rocks of Fennoscandia into four major Archean provinces: Karelian province, Belomorian province, Kola province and Murmansk province (Figure 4). These provinces has been affected by Paleoproterozoic orogenic activity (Hölttä, Balagansky et al. 2008). Eighty percent of the Fennoscandian shield area is dominated by the tonalite-trondjemite-granodiorite (TTG) rocks, with subordinate greenstone belts, paragneisses, granulite complexes and migmatitic amphibolites (Hölttä, Balagansky et al. 2008).

The Karelian province mainly consist of granite-greenstone belts (Gaál and Gorbatshev 1987). The greenstone belt unite are made up of about twenty larger and smaller belts, with a NNW-NW and NS trend. Achaean tonalities, trondjemite, granodiorites and granites surround this greenstone belts (Slabunov, Lobach-Zhuchenko et al. 2006). U-Pb measurements from zircons in the Karelian province have dated rock of 3.1 Ga (Lobach-Zhuchenko, Chekulayev et al. 1993).

Tonalite-trondjemite-granodiorite (TTG) gneisses of Neso- and Neoproterozoic age, three generation of seldom greenstone and paragneisses, dominate The Belomorian province. The oldest generation of greenstone is dated back to 2.88-2.82 Ga. It contains island arc-type basalt-andesite-dacite-rhyolite (BADR) series volcanic rocks and unit of greywackes interpreted as a fore-arc complex. The middlemost greenstones date to 2.8-2.78 Ga. They contain volcanic rock of calc-alkaline magma series with adakitic rocks, metagreywackes and basaltic komatiites. The youngest greenstone belt is 2.75-2.66 Ga and contain sedimentary sequence of polymictic conglomerates, and volcanic rocks of rhyodacitic to basaltic composition (Hölttä, Balagansky et al. 2008). Sutured Mesoarchean, Neoproterozoic and Paleoproterozoic rocks dominate the Kola area. This terrane collided with the Karelian province by subduction of oceanic crust.

The Kola province consist of TTG granitoids, diorites, enderbites (rock of charnockite series) and peraluminous metasedimentary rocks, greywackes and mudstones (Hölttä, Balagansky et al. 2008). The metasedimentary rocks are overlain by mafic volcanic rocks and calc-alkaline rocks “associated with tuffitic metaturbidites”, (Gaál and Gorbatshev 1987).

The Murmansk province contain rocks dated to 2.77-2.72 Ga and consist of TTG granitoids, diorites, enderbites and supracrustal rocks (Hölttä, Balagansky et al. 2008). The Archean bedrock were rifted and intruded by gabbro-norite and tholeiitic mafic dykes during the Palaeoproterozoic Eon. Fluvial and shallow water sedimentary rocks was accumulated in association with continental rifting and volcanic activity (Lahtinen 2012). Deep-water turbidites and carbonates was deposited in the Palaeoproterozoic Eon.

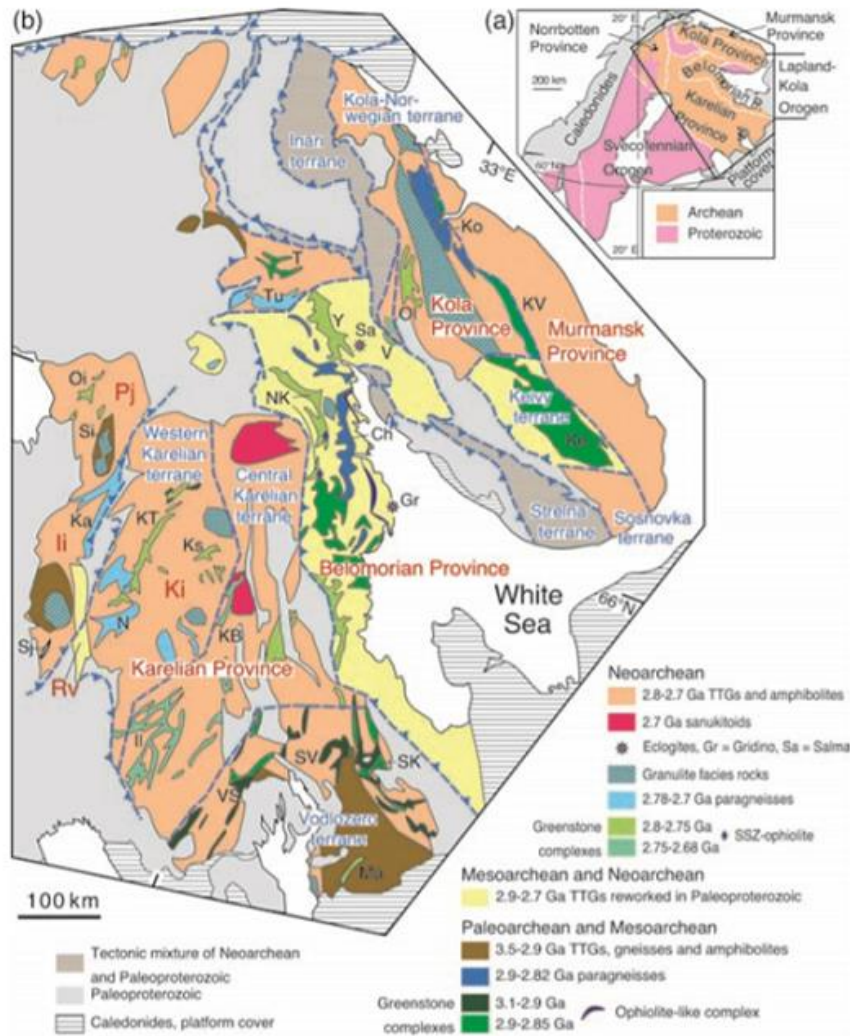


Figure 4. Overview of the Archean provinces in the Fennoscandian Shield (Hölttä, Balagansky et al. 2008).

Tectonic history and setting

NNE-SSW rifting of the Archean basement in Fennoscandia started in the Paleoproterozoic at 2.505 – 2.1 Ga. During the rifting of the crust in 2.1-2.04 Ga, the Kola Ocean and the Svecofennian Sea were formed (Lahtinen, Garde et al. 2008), Figure 5. Two main orogeny resulted from the Paleoproterozoic tectonic activity. A continent-continent collision built up the Lapland-Kola Orogeny (1.94-1.86 Ga) situated in N-E of the Fennoscandian shield. Consumption of repeating collisions of micro continents and subduction event with volcanic activity, lead to growth of igneous and sedimentary Paleoproterozoic rocks, and formed the Svecofennian Orogeny (1.92-1.79 Ga) placed in the southern part of the Fennoscandian Shield. The Paleoproterozoic rifting ended in 1.54 Ga when large batholites and plutons of granites formed (1.65-1.54 Ga) (Lahtinen, Garde et al. 2008).

The Paleoproterozoic plate tectonic events lead to the formation of a supercontinent (Lahtinen, Garde et al. 2008). Fennoscandia, Laurentia (Canadian Shield), Volgo-Uralia (part of the Russian craton west of Ural Mountains), Sarmatia (Ukraine and part of Russia) and probably Amazonia (eastern part of South Africa) composed the supercontinent, Rodinia.

The opening of the Kola Ocean and the Svecofennian Sea lead to eruption of MORB-type pillow basalt, and deposition of greywackes from turbidites at the continental shelf. The marine environment condition favoured deposition of calcium sulphate and stromatolites. Layered gabbro-norite and dike swarms were formed by intraplate rifting. Extension and erosion accumulated sediments in clastic sedimentary basins creating formations of polymict conglomerates and sandstones (Lahtinen, Garde et al. 2008).

During the early Paleozoic (540-400 Ma) (McKERROW, MAC NIOCAILL et al. 2000) the Caledonian Orogeny arose, a major continent-continent collision between Baltica and Laurentia, that had the greatest influence and impact to the western part of Fennoscandian Shield. Allochthonous thrust sheet were pushed towards and upon the margin of the Baltica continent. The Precambrian basement were reworked by folding and metamorphism, and the orogenic belt was probably at the same size as Himalaya today. The belt is divided into autochthon, parautochthon, lower, middle, upper and uppermost allochthonous.

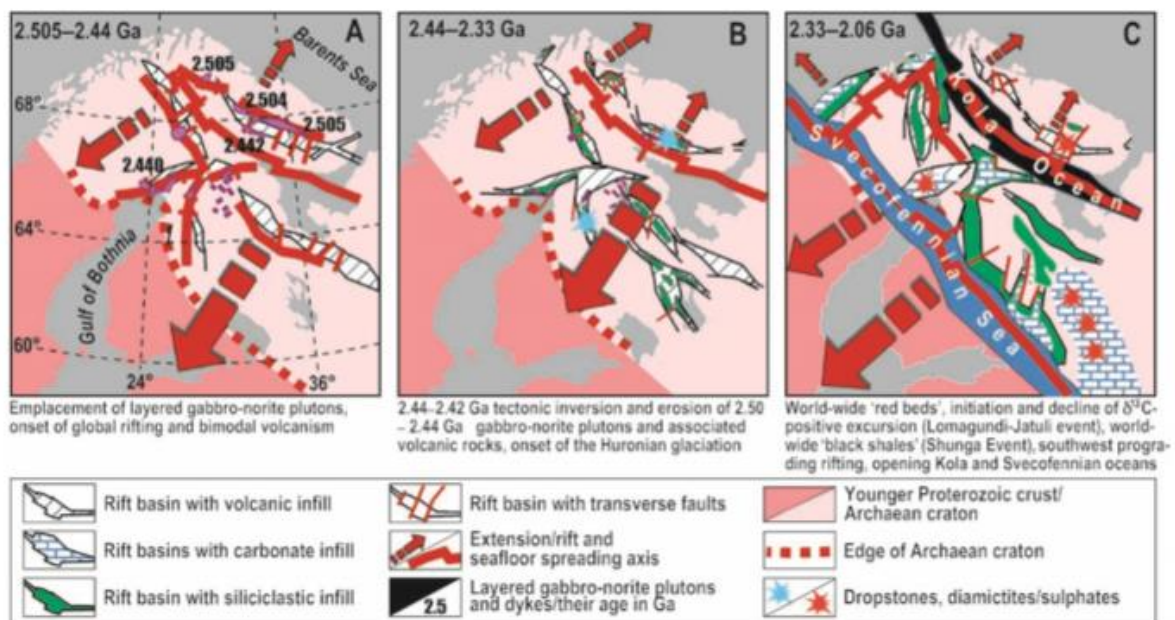


Figure 5. Early Paleoproterozoic rifting of the Fennoscandian Shield, forming the Svecofennian Sea and the Kola Ocean (Lahtinen, Garde et al. 2008).

2.4.2 Geology of the Repparfjord-Komagfjord tectonic window

The Caledonian thrust sheet covered the western part of Finnmark, Repparfjord and Komagfjord. Regional uplift along a SW-NE-axis increased the erosion of the allochthonous rocks in this area, and resulted in exposure of the underlying bedrock. A window into the Precambrian bedrock were created, hence the name of this geological feature. The exposed Precambrian bedrock lies in a larger anticline where the stratigraphic sequences is dipping towards NE.

The Repparfjord-Komagfjord tectonic window include a basement built up of 8 km thick sequence of sedimentary rocks of Paleoproterozoic age (2.5-1.6 Ga) overlain by sediments of Vendian age (650-543 Ma). The sedimentary units are overthrust by The Kalak Nappe Complex (Pharaoh, Ramsay et al. 1983).

Reitan (1963) was the first to study the bedrock in the Repparfjord-Komagfjord area. Later investigation by Pharaoh (Pharaoh, Ramsay et al. 1983) renamed the stratigraphic nomenclature and corrected knowledge of the basement rocks due to a better understanding of the formations and renamed localities. Pharaoh (Pharaoh, Ramsay et al. 1983) divide the basement rocks into four groups and eleven formation. Greenstone lavas, tuffs, continental and shallow marine sediments in the Raipas Supergroup, together with the intrusive group Raudfjell Suite composed by peridotites, norites and gabbros, constitute the Precambrian basement rocks in the Repparfjord-Komagfjord tectonic window. In addition to this, one formation of Vendian sediment overlies the Precambrian basement.

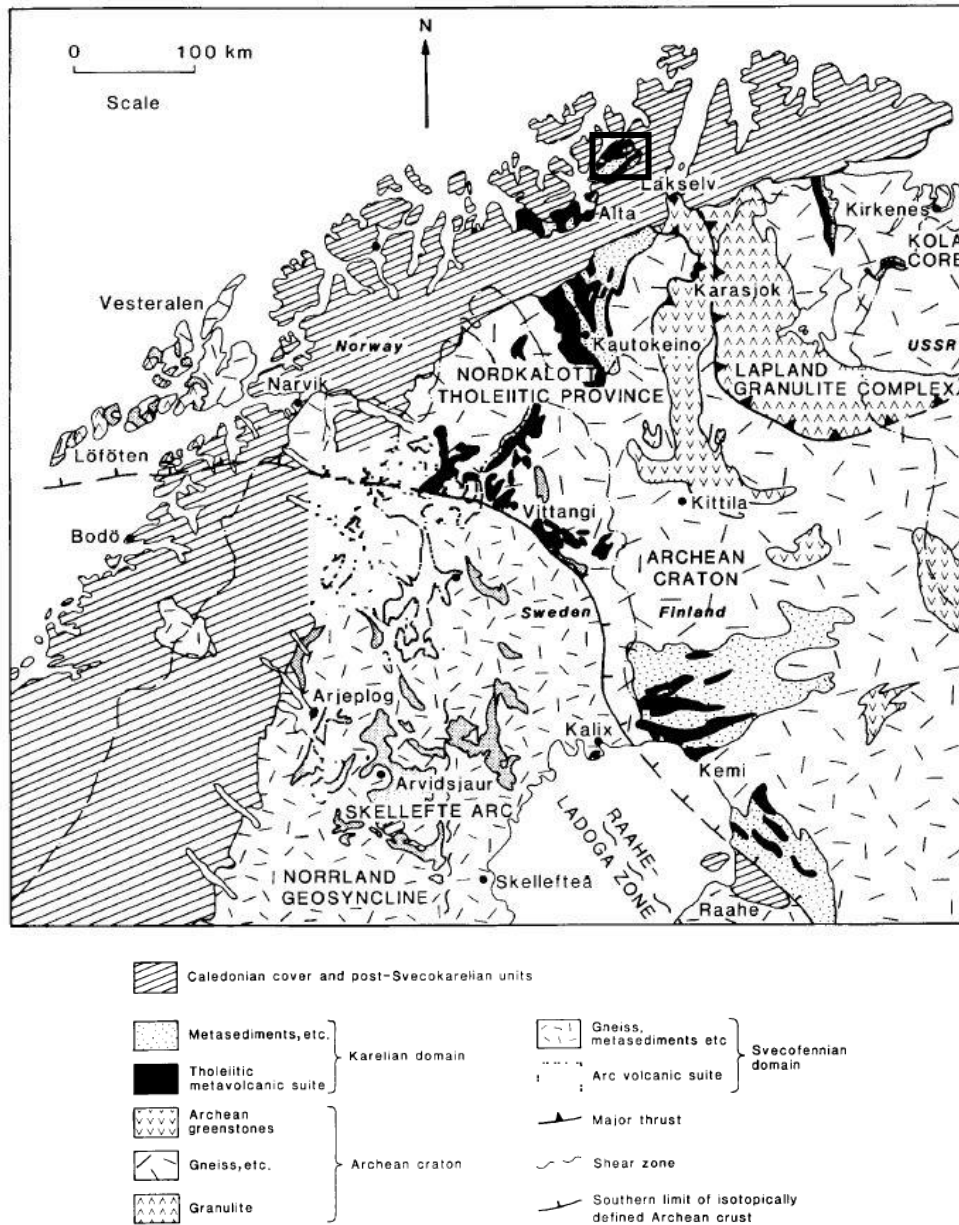


Figure 6. The regional setting of the Repparfjord-Komagfjord tectonic window (black square). Map of the Repparfjord-Komagfjord tectonic window modified from (Pharaoh 1985).

Stratigraphy of basement

The Holmvatn group is the lowest stratigraphic group resting on the bedrock. The Markfjell-, Båtdalselv- and Magerfjell Formation make up this Group. The stratigraphic feature is recognized by “polymict conglomerates, volcanoclastic sediments and feldspathic sandstone interbedded with metavolcanic horizons of basic and intermediate composition” (Pharaoh, Ramsay et al. 1983). They interpreted the polymict conglomerate of the Markfjell Formation to be accumulated sediments from a fault-bond source, where debris-flows supplied clastic material. Tuffaceous material from a pasmodic volcanic activity mixed with clast of greenstone covered the basal conglomerate. Pillow structures and sporadic carbonate indicate a subaqueous deposit environment.

The Saltvatn group contains the Ulveryggen/ Dåg’gejàkka-, Dypelv- and Stangvatn Formation. The lithostratigraphy of the Saltvatn Group is shown in Figure 7. The Ulveryggen Formation consists of feldspathic-quartz sandstone, polymict conglomerates with vein quartz and greenstone rounded pebbles in a quartz-rich sandy matrix. Ulveryggen conglomerates is covered by trough cross-bedded sandstone fining up into pale greenish or greyish siltstone. Dåg’gejàkka Formation consists of well-sorted white quartzitic metasandstone. The Dypelv Formation consists of sequences of green polymict conglomerates with metabasaltic lava, metatuffite and vein quartz pebbles. Dypelv conglomerates contains a greenstone fragmented and quartzo-feldspathic matrix, interbedded of thin sandstone layers. Purple polymict conglomerates with dacite pebbles and trough cross-bedded arkosic sandstone characterize the Stangvatn Formation. A dolomitic layer rich in calcite-veins, forms the upper part of the Stangvatn Formation, and hosts the Nussir copper deposit.

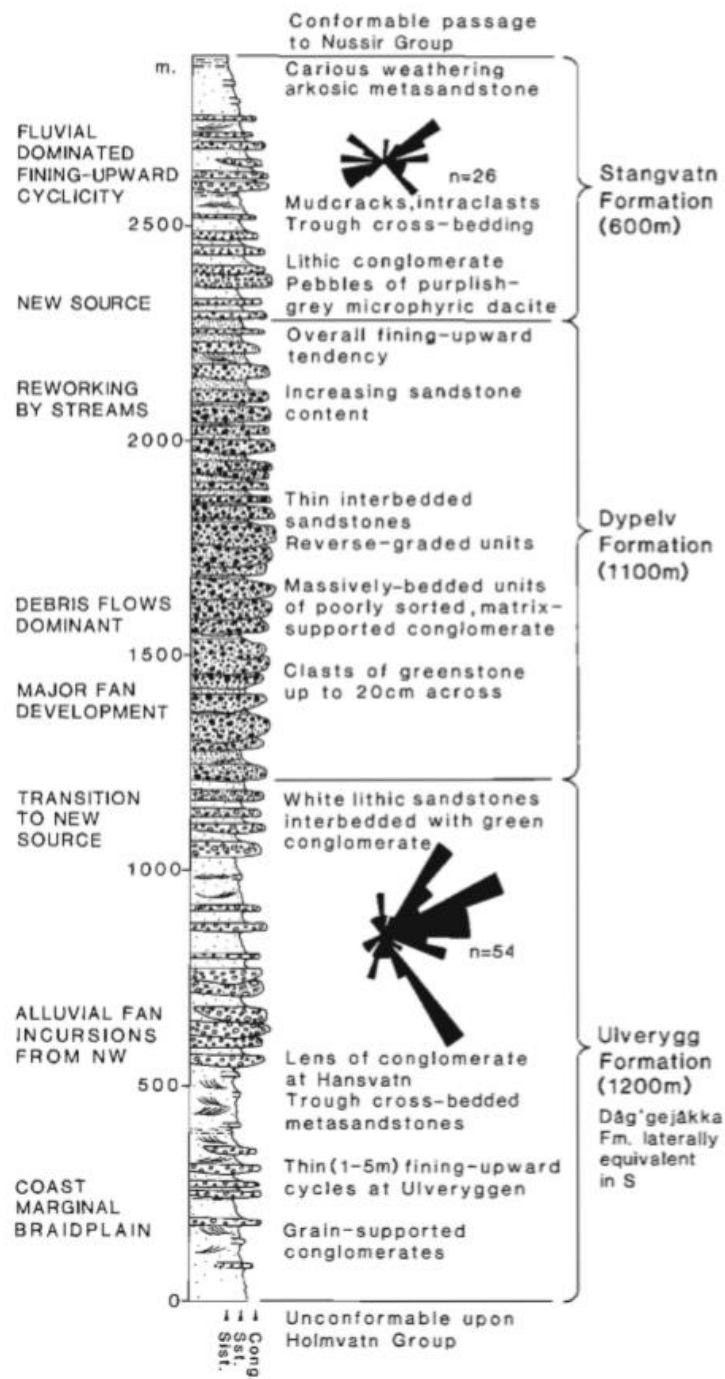


Figure 7. Schematic lithostratigraphy of the Saltvatn Group (Pharaoh, Ramsay et al. 1983).

The Ulveryggen- and Dåg'gejåkka Formation is interpreted by Pharaoh et al. (Pharaoh, Ramsay et al. 1983) as being sediments transported by rivers and rock fall in a fluvial/ alluvial environment. The Dypelv Formation seems to be of a close source because of the low degree of rounding of greenstone clasts, while the Stangvatn Formation stand out to be of a different provenance. Clasts of the Stangvatn Formation consist of an intermediate and acidic volcanic rock that is of unknown provenance and is considered absent in other places of Norway (Pharaoh, Ramsay et al. 1983).

The Nussir group consist of the Krokvatn- and Svartfjell Formation. The Krokvatn Formation is dominated by tuffaceous greenstones including thinner unites of metabasalts and a thin unite

of dolomite. The Svartfjell Formation consists of metabasalt lavas and thin horizons of metabasaltic tuff and meta-hyaloclastic breccia. Pharaoh et al. interpreted this group, dominated by tuffaceous greenstones and metabasalt, to be made of volcanic eruption in a subaqueous environment. The absence of sheeted dikes and the surrounding continental and shallow marine sediments, indicate that the Nussir Group is not of ophiolitic composition (Pharaoh 1985). The immobile elements Cr, Ni, Ti, Zr and Y, is used in a geochemical study and provide a basalt with a tholeiitic composition (Pharaoh 1985). Basaltic lavas have decreasing contents of vesiculars. This indicate a transgression of the sea level. Transportation and rework of volcanic material is most probably the origin of the hyaloclastic breccia.

The Porsa group divides into the Vargsund -, Kvalsund- and Bierajav'ri Formation. The Vargsund Formation includes stratigraphic units of "grain-supported conglomerate containing sub-angular pebbles of vein quartz and jasper" (Pharaoh, Ramsay et al. 1983) with a phyllitic matrix overlaid by thin layers of dolomite stromatolites and purplish shales. The Kvalsund Formation consist of dark graphitic slate rich in pyrite, while the Bierajav'ri Formation is made up of a mixture of green tuffs, slates, sandstone and horizons of carbonate. The presence of stromatolites and ripple sedimentary structures is interpreted to indicate a regression of the sea level and deposition of sediments from the Bierajav'ri Formation in a shallow water environment.

The Lomvatn Formation consist of sedimentary rocks of the Vendian age (650-543 Ma). The Lomvatn Formation unconformable overlies the Raipas Supergroup and has been truncated by the Kalak Thrust plane. The Lomvatn Formation consist of Hermannvatn Member and Saraby Member. The Hermannvatn Member is built up of "well-sorted, grain-supported quartz conglomerate" (Pharaoh, Ramsay et al. 1983) with well-rounded pebbles of vein quartz and metasandstone containing greenstone fragments and slate in-between. Upwards lies a well-bedded grey-greenish quartz arenite. The Saraby member lies at the top of the Lomvatn Formation and consist of parallel laminated shales and siltstones. Thin pale-gray and well sorted bands of feldspathic sandstone, interbed the shales and siltstones. The contact between the bands is sharp. The Lomvatn sediment is characterized by deformation by the Kalak Thrust plane and have taken up a phyllitic texture. Pharaoh et al. (1983) have interpreted the deposit environment to be a shallow marine environment due to accumulation of quartz and mature sandstone fining upward into parallel laminated clay and silt.

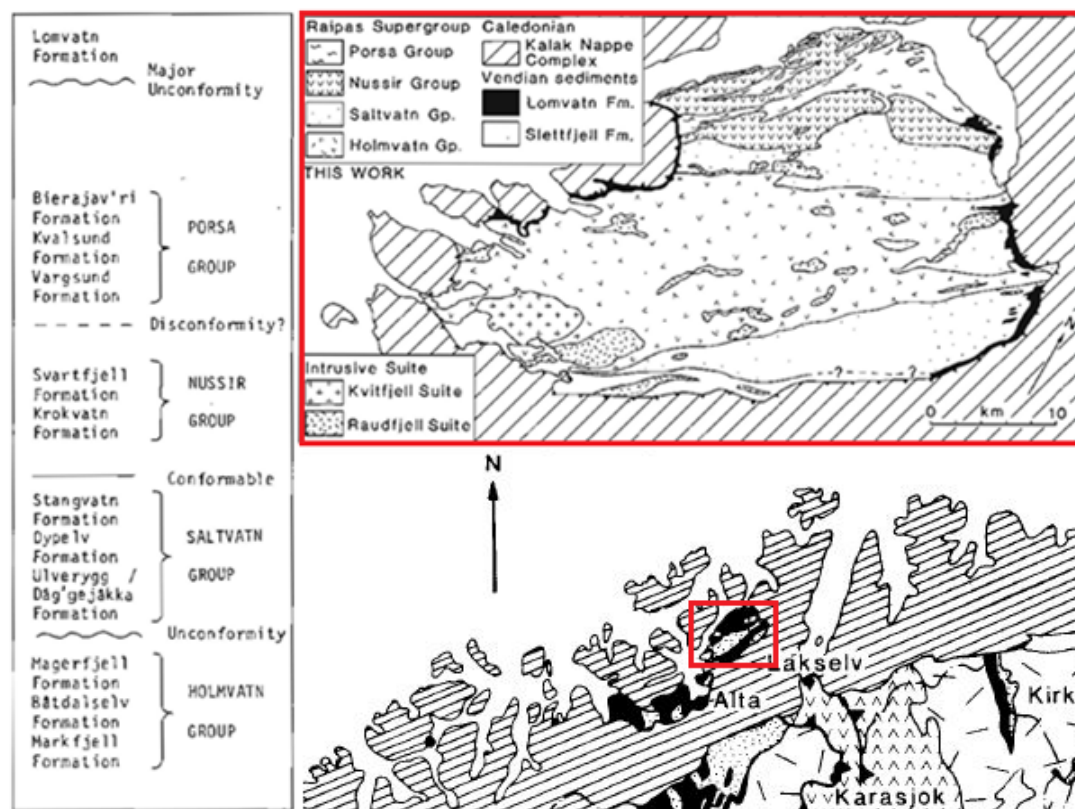


Figure 8. Geological map of the Repparfjord window illustrating the different lithostratigraphic interpretation proposed by Pharaoh et al. (1983, up to the right). Stratigraphic nomenclature of the groups and formation in the Repparfjord window proposed by Pharaoh et al. (1983, left).

Deposition environment

The metasedimentary rocks in the Repparfjord-Komagfjord were deposited in an intercontinental rift-basin environment. In the intracratonic rift episode, alluvial deposits, such as the Dypelv conglomerate and the Stangvatn conglomerate, filled the basin. Volcanic eruption of basalt and tuffites filled the basin together with continental and shallow marine sediments. Pillow basalt and turbidity sequences in tuffites, trough cross-bedded sandstone fining up into pale greenish or greyish siltstone, indicate the deposition in a subaqueous environment. The layers of dolomite probably formed in periods with low clastic sediment supply in calcareous saturated seawater. Dark graphitic slates rich in pyrite, sandstone fining upward into siltstone with stromatolites, indicated episodes of a change in the sea level (Pharaoh, Ramsay et al. 1983).

Structural geology of Repparfjord window

The Palaeoproterozoic bedrock in the Repparfjord Window were influenced by “multiphase deformation during the Svecokarelian and Caledonian orogeny” (Viola.G, Sandstad.J.S et al. 2008). A detailed geological map of the central-eastern part of the Repparfjord Window is shown in (Figure 9). The macro structure of the Repparfjord window is dominated by E/ENE-W/WSW trending fold in the Saltvatn Group and Nussir Group (Viola.G, Sandstad.J.S et al. 2008). Nussirjav’ri Thrust and the Skinnfjellet Thrust have separated the stratigraphical groups from the western part of the Repparfjord window (Figure 9).

The Dypelv conglomerate in the Holmvatn Group have an antiformal structure. It contains upright structures and have open to tight folds. These folds belong to the oldest deformation of the area

(Viola.G, Sandstad.J.S et al. 2008). An antifold with an axial trace trending towards SW-NE has folded the greenstones in the Skinnfjellet. These folds have been observed in smaller scale, and corresponds to the second oldest folding event of the bedrock (Viola.G, Sandstad.J.S et al. 2008). Younger folding structure are related to a dextral ductile shearing event, forming SSW-NNE trending folds plunging moderately towards northeast and striking ENE-WSW. This folding event have probably refolded the two older folding structures, causing the dominating folding pattern of the Nussir area (Viola.G, Sandstad.J.S et al. 2008). Folds that were created by the Caledonian Orogeny have been observed by Viola. et al. (2008) in the eastern area of the Repparfjord window, and represent the youngest folding event. Pharaoh et al. (1983) interpreted the sharp geological discontinuity dividing the Saltvatn Group and the Nussir Group towards the west, as a major thrust with a top-to-the-NW transport direction related to the Svecokarelian orogeny (Figure 9). Field work performed by Viola et al. (2008) indicated a top-to-the-NW shearing of the western side and a top-to-the-SE shearing of the eastern side of the greenstones in Skinnfjellet. According to Viola et al. (2008), the Nussir Group are separated from the Saltvatn Group by a fault contact. The Nussir Group forms the hang wall in a top-to-the-SE thrust fault. Macro structures in the Repparfjord window is visible in a total magnetic field, were the greenstones in the Nussir Group causes the strong magnetic anomalies (Figure 10). Labelling represent interpreted structures (Viola.G, Sandstad.J.S et al. 2008).

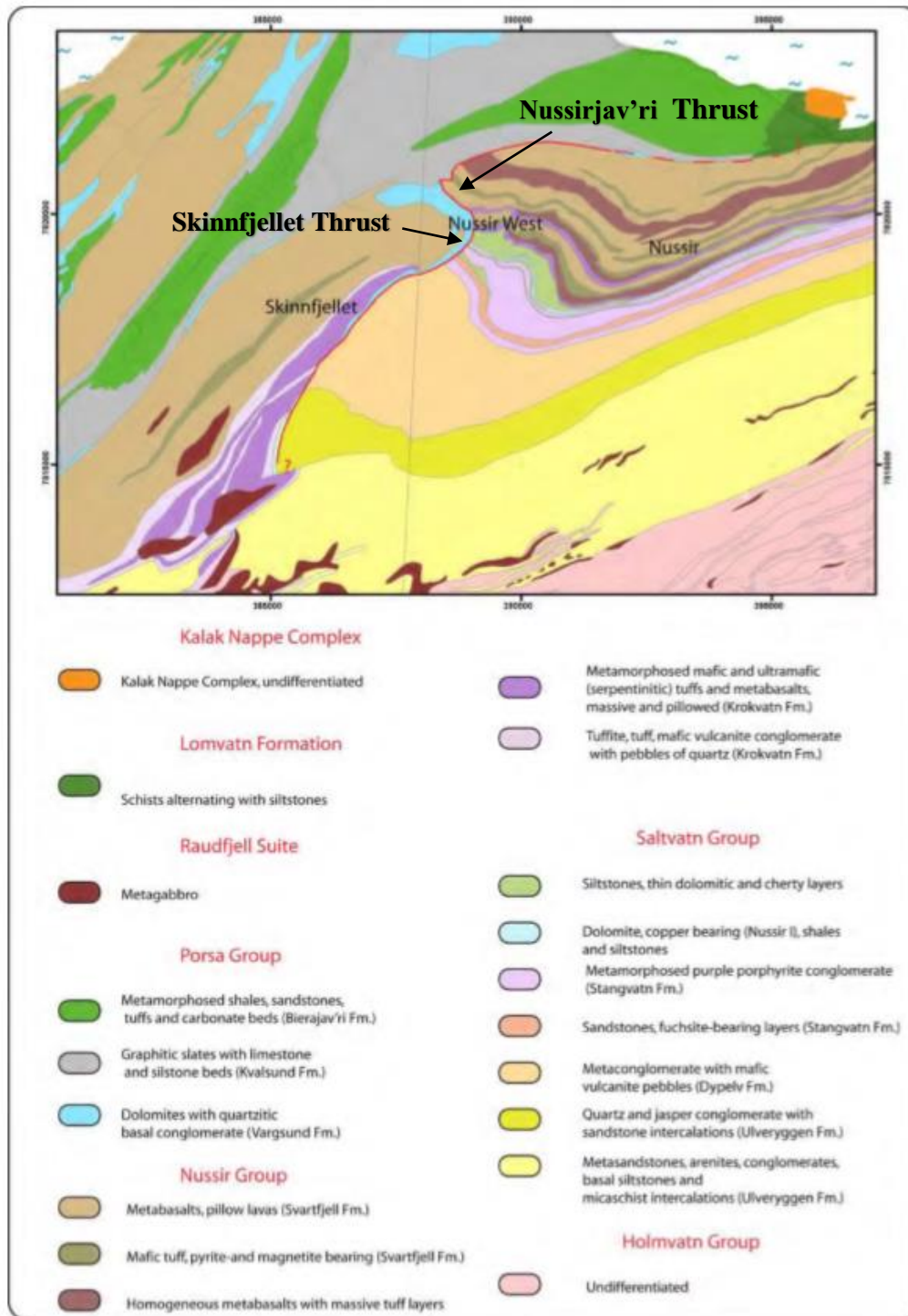


Figure 9. Detailed geological map of the central-eastern part of the Repparfjord Window. Map modified from Viola et. al (2008).

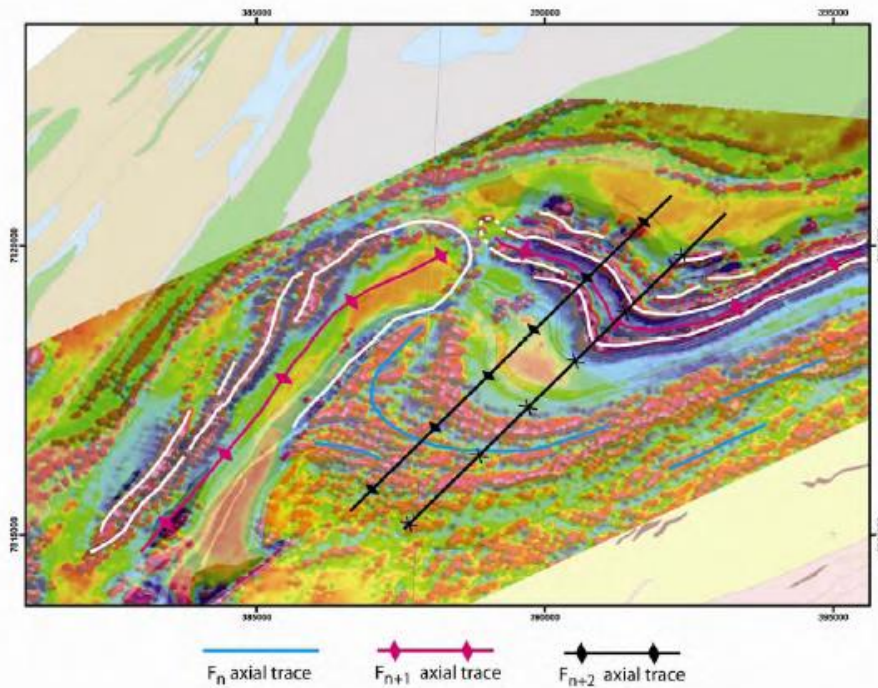


Figure 10. Magnetic total field map with interpreted geological structures is modified from Viola et al (2008). F_n is a designation of the age of the observed structures in the Repparfjord window. Additional numbers represent decreasing age of deformation structures.

Nussir copper deposit

The Nussir copper deposit is situated in the northwestern part of the Repparfjord Window, Finnmark, Northern Norway (Figure 11), located in the upper part of the Stangvatn Formation in the Saltvatn Group premeditated by the Nussir Group. The basement consists of metasedimentary- and volcanic rocks of the Precambrian to the Palaeoproterozoic age, with a formation of Venedian age on top. A detailed description is given in Table A24. The Nussir deposit is classified as a sediment-hosted stratabound copper deposit with occurrence of the copper minerals bornite, chalcocite, chalcopyrite, covellite and digente. Other sulphides such as malachite and pyrite occur. The copper deposit hosts accessory minerals of gold, silver, zinc, platinum and palladium (Andersen 1987). According to Andersen (1987), the Nussir copper deposit is of epigenetic origin. Oxidized and saline hydrothermal fluids transported sulphides in a half graben, and the changes in pH, Eh, temperature or pressure may be the reason to the precipitation of Cu-minerals (Andersen 1987). Another precipitation mechanism could have been the occurrence of a fine-grained slate at the top of the mineralized horizon, acting as a seal, preventing further migration of fluids through the metasedimentary rocks. According to Viola et al. (2008), the deposition of Cu-minerals is most probably syn-genetic with this dextral shearing (Viola.G, Sandstad.J.S et al. 2008). According to Viola et al. (2008) the mineralised horizons is located in a strain shadow, illustrated in Figure 12. The decreasing pressure in a strain shadow could be the triggering factor to precipitation of Cu-minerals from fluids. Hence, no studies or observed structures support a repetition of a strata created by folding or thrusting in the area containing two mineralised horizons. (Pharaoh, Ramsay et al. 1983, Viola.G, Sandstad.J.S et al. 2008).

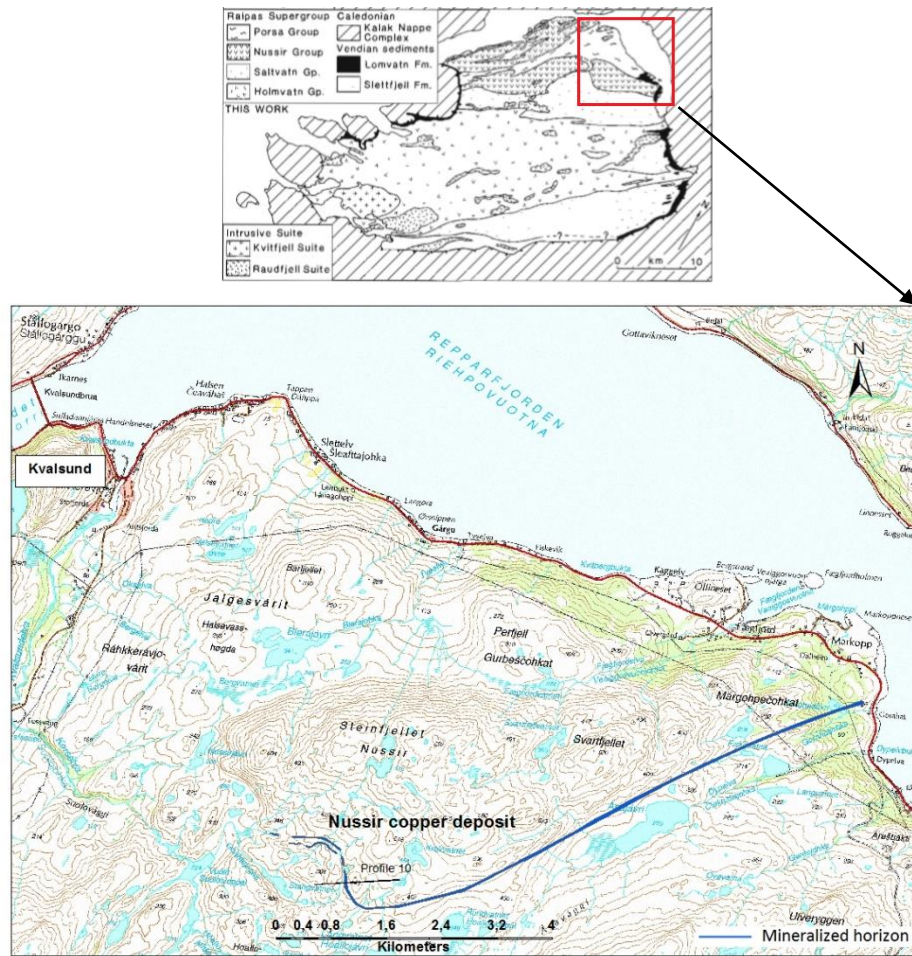


Figure 11. Map showing the Nussir copper deposit in the northwestern part of the Repparfjord Window, west of the Repparfjord and southeast of the Kvalsund municipal. Map (upper) was modified from (Pharaoh, Ramsay et al. 1983) and map (lower) was made in the arcgis software.

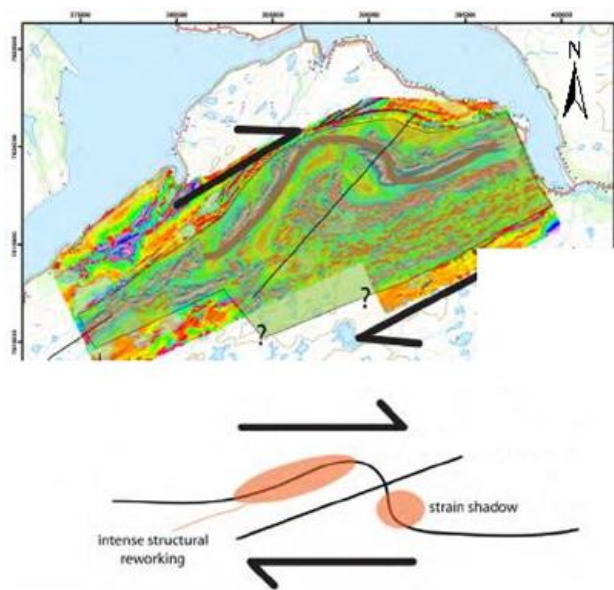


Figure 12. Dextral ductile shearing in the Repparfjord Window forming asymmetric fold. Strain shadow in the eastern fold limb, while intense structural reworking have affected the western fold limb. Figure modified from Viola et al. (2008).

2.5 Sediment-hosted copper deposits

2.5.1 Characteristics of sediment-hosted copper deposits

Sediment-hosted copper deposits is the term of sedimentary rock hosting valuable concentrations of copper and often associated metals as silver, cobalt, zinc, lead, and more seldom platinum-group elements, uranium, and vanadium (Zientek, Hammarstrom et al. 2010). Sediment-hosted copper deposits are associated to a narrow range of sedimentary layers in sedimentary sequences (stratabound). However, they are not restricted to sedimentary bedding (Cox, Lindsey et al. 2007). Additionally, copper deposits are structurally controlled. Fluids generated by tectonic activity in fractures and veins could transport sediment-hosted copper deposits. Copper occur as epigenetic or diagenetic deposits and is independent of igneous processes. Generally, all sediment-hosted copper deposits are hosted within either calcareous or dolomitic siltstone, shales and carbonate rocks of marine or lacustrine origin in a low-energy environment. The deposits also occur in sandstones, arkoses and conglomerates deposited in a high-energy environment. The source rock must have high permeability and consist of a copper bearing rock. A typical example of a good source rock is an oxidised and hematite-stable rock. The copper is transported by oxidised subsurface brines able to dissolve and transport copper, often in a chloride complex, and into a sedimentary rock with reducing condition where copper precipitates. Four criteria must be filled to form sedimentary-hosted copper deposits:

- Oxidized, hematite-stable copper source rock containing ferromagnesian minerals or mafic rock fragments: Early diagenetic fluids form iron oxides in red beds
- Source of sulphur: Reducing fluids convert hematite to pyrite, with hydrocarbons as an important source of reductants. Hydrocarbons and organic matter is probably the most important reductants in structurally controlled and vein copper deposits (SCRV).
- Basinal brine to mobilize and transport the copper and sulphur: Epigenetic copper-bearing saline fluids introduces along structural feeder zones where copper precipitates on contact with reductants in bleached bed.
- Stratigraphic or structural conditions generating precipitation: Physical trap as overburden layer with low permeability refusing brines to migrate further up in the sedimentary layers. Stratigraphic layer with reducing condition leads to precipitation.

An imagined sedimentary basin with the right condition to form a sediment-hosted stratabound copper deposit is shown in Figure 13. Intracontinental rifting can form a basin where clastic or volcanic sediments can accumulate, as the red bed illustrates in the figure above. In this situation, the red bed work as the source rock to copper- and other sulphides. Further infill of the basin with sediments such as sand and silt. Due to increasing sea level, carbonates and evaporates form. The sandy and silty sediments, together with the carbonate and evaporate, form a reservoir to the copper sulphides. The upper layer of sandstone, siltstone and shales form a seal to the basin (physical trap). In this way, the copper-rich brines are trapped into the basin, where it can circulate for centuries. Sediment-hosted copper deposits are divided into two subgroups:

- Sediment-hosted stratabound copper deposits (SSC)
- Structurally replacement and vein copper deposits (SCRV)

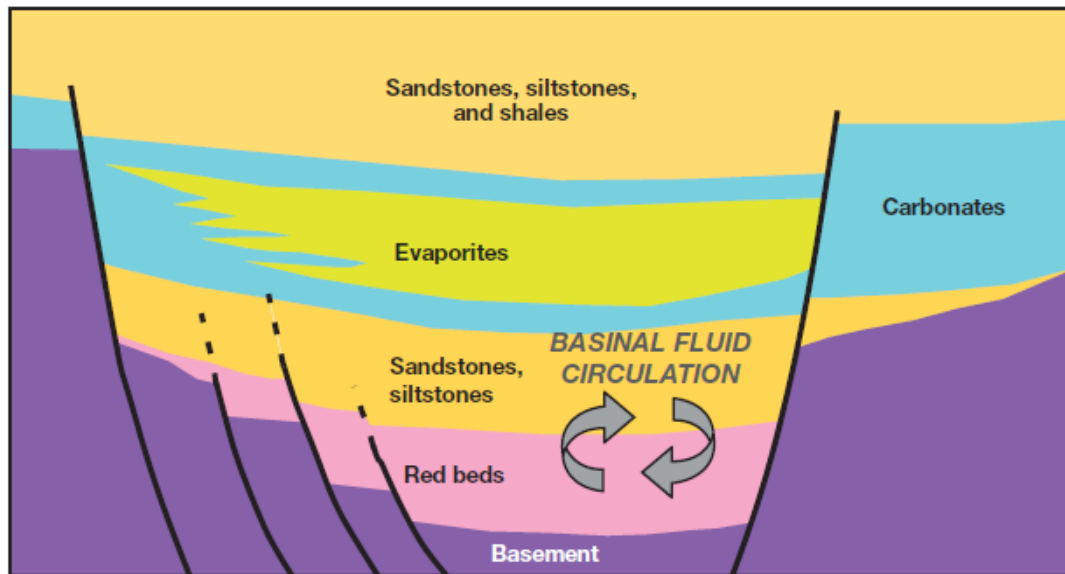


Figure 13. Illustration of a sedimentary basin with the right condition to form sediment-hosted copper deposit. Figure modified from (Hitzman, Selley et al. 2010).

Sediment-hosted stratabound copper deposits (SSC)

Michael et al. (2010) defines the sediment-hosted stratabound copper deposits (SSC) as; “Sediment-hosted stratabound copper mineralization consists of fine-grained copper- and copper-iron sulphide minerals that occur as stratabound to stratiform disseminations in siliciclastic or dolomitic sedimentary rocks. Ore minerals occur as cements and replacements, and less commonly, as veinlets. The concentration of sulphide minerals conforms closely, but not exactly, with the stratification of the host rocks. Typically, the ore zones comprise chalcocite and bornite. The deposits are characterized by zoning of ore minerals laterally along and across bedding, from pyrite, chalcopyrite, bornite, chalcocite, and to hematite. Deposits are hosted in black, grey, green, or white (reduced) sedimentary strata within and above a thick section of red (oxide) beds”.

The sediment-hosted stratabound copper deposits are divided into these three subgroup:

- Reduced-facies copper deposits
- Sandstone copper deposits
- Red bed copper deposits

The reduced-facies copper deposits are composed by marine or lacustrine shale, siltstone, mudstone or carbonaceous rock containing organic matter. Sandstone copper deposits are composed by coarser sediments like fine- to coarse-grained sandstone, well sorted grains and contain petroleum and/or sour gas (sulphuric gas). Red bed copper deposits are characterized by poorly to moderately sorted fluvial sandstone, often with conglomeratic composition and the content of carbonized plant fragments.

Structurally replacement and vein copper deposits (SCRV)

Structurally replacement and vein copper deposits (SCRV) deposits are replacements of already deposited sediment-hosted copper deposits. SCR.V is of epigenetic origin and often located in structurally disturbed, continental to restricted marine, rift-related sedimentary basins that host stratabound copper deposits. Other factors that are favourable in SCR.V deposits are the occurrence of evaporates and evidence of halokinesis, the formation of and movement of salt structures. Evidence of tectonic disruption and faults at high angles to bedding are particularly favourable (Michael L. Zientek 2010). A SCR.V deposits could form hundreds of million years later than sediment-hosted stratabound copper deposits situated in the same sedimentary basin and system. There is no direct link to igneous activity, but often, sedimentary basin contain rift-related volcanic rocks. SCR.V deposit differs from sediment-hosted stratabound copper deposits in the way that the structures are the main ore-controlling factor, while stratigraphy is the main controlling factor in sediment-hosted stratabound copper deposits. SCR.V deposits forms when hydrothermal fluids under high pressure and reducing condition reacts and decompose sediment-hosted copper deposits, that suddenly becomes activated by tectonic activity and transported into stratigraphic traps such as anticlines and oil field structural geometries. Halokinesis is one possible mechanism that provoke re-deposition of sediment-hosted copper deposits. Deposition environment is typically dominated by arid environment, continental clastic sequences (red bed), overlain by fine grained, organic-rich, marginal marine or lacustrine sediments. This type of fining-upward sequences, with siliciclastic sediment grade into shale and evaporites or carbonate and evaporites, is typical in rift-drift and rift-sag transgressive sequences. SCR.V deposits form massive, near monomineralitic veins of ore minerals of chalcocite-bornite or chalcopyrite-bornite-covellite. Mineralization is hosted in gangue minerals consisting of quartz, plagioclase, carbonate, potassium-feldspar, biotite, muscovite, barite, rutile, hematite and Mn-oxides. Often, the mineralization is in contact with siliciclastic walls in faults, fractures and brecciated rock, or is disseminated in porous sandstone containing structures trapping and generates brines into reductant-bearing strata. SCR.V deposits is hosted by phyllites, schist, marbles, calcareous siltstone, sandstone, conglomerates, thin marble beds, shales, and carbonate rock. The mineralization often occur between contrasting lithology. Characteristic of SCR.V-host rock is a high rock competency, since SCR.V deposits locate in brittle rock such as clastic unite. High permeability is necessary for the migration of brines and formation of SCR.V deposits. Typical minerals indicating hydrothermal alteration: feldspar, muscovite, chlorite, anhydrite, carbonate, quartz, tourmaline, scapolite, sodic amphiboles, and talc.

2.5.2 Geochemical processes in sediment-hosted stratabound copper deposits

The chemical properties controls the prevalence of sulphides and accessory minerals in SSC deposits. To form a SSC deposit, it is necessary with a source rock rich in metals. Typical source rock is a fertile volcanic rock, or a red bed sedimentary rock. Metals, in particular copper, are believed to leache from detrital minerals such as magnetite, biotite, hornblende, and pyroxene which themselves may have been derived from erosion of a fertile basement (Robb 2005). Red beds were formed in a period where the amount of free oxygen-atoms in the atmosphere was low. Iron cations could be transported by rivers and deposited in sedimentary rocks. Later oxidation of iron deposits gave the red characteristic colour. Circulation of hydrothermal fluids in iron-rich sedimentary rocks, generated adsorption of metals on ferromagnesian silica clasts.

Adsorption of metals at redbeds make them to a potentially source rock to sediment-hosted stratabound copper deposits. An oxidized brine is the replacement and transporting source in the formation of SSC deposits. These fluids is characterised by low temperature (75-220 °C), low pH and high salinity. Typically for SSC deposits is a thermally driven fluid flow in a rock with high permeability. When oxidised brine reacts with the source rock, ligands in the solution increase the solubility of metals. A ligand is a Lewis base able to donate an electron pair with a molecule or atom. These bases are negative charged elements, such as Cl^- , S^{2-} , O^{2-} . Ligands enhance formation of complexes with metals in solution by bonding. This is the most efficient way of transporting metals in a solution. Chloride is an important ligand for transporting metals, since it is characterized as a borderline base, a base able to bond with a wide range of metals. Cl^- form elongated ions with a bipolar electron distribution and bond to metals by sharing electron pairs. It form complexes with metals in oxidation conditions. Solubility of chloride-metal-complexes is strongly controlled by pH and Eh. Another important factor is the temperature. The relationship between the logarithmic scale of the equilibrium constant ($\log \beta_1$) and temperature in chloride complexes are illustrated in Figure 14 (left). The diagram miss the CuCl_2 complex, but ZnCl^+ - complex have approximately the same chemical properties as CuCl_2 . It is conspicuous that the stability of ZnCl^+ - complex increases with the increasing temperature. It is therefore necessary with a temperature near 200-300 °C to form a copper-chloride complex in a solution.

It requires a saline source to form Cl^- in solution. It could be descending seawater or an evaporitic rock. When the fluid condition changes and becomes more reduced, the chlorite-ligands will decrease the bonding mechanism and resulting in precipitation of metals. Decomposition of organic matter is an important reducing component. Soluble copper occurs in both Cu^+ and Cu^{2+} in soluble state. Cu^+ is the most dominant state in hydrothermal solutions. It forms stable Cu-chlorides, Cu-bisulfides and Cu-hydroxide complexes, but movement of Cu in hydrothermal solutions most often occurs as Cu-chloride (CuCl_2). If there is a high-sulphured environment, Cu-bisulfide is most abundant (Robb 2005). Copper (Cu^+) is dissolved in oxidised (high Eh) environment with middle to low pH. "Solubility of copper as a chloride complex under such conditions have been estimated to be as high as 35-100 ppm", (Robb, 2005). Copper precipitate in reducing condition with a higher pH value than during dissolution. This occurs because of instability of chloride ions in solution that form the bonding ligand to copper metals. The stability of different Cu components in a pH-Eh diagram is shown in Figure 14 (right). The Cu-chloride complex form a stable soluble phase when the fluid condition contain relatively high Eh (oxidizing) and low pH. As the diagram shows, Cu precipitate when a fluid reaches reducing condition with high pH and low Eh. In acidic, oxidizing and saline conditions, Ag, Zn, Pb and Au forms complexes with Cl^- ligands. When sulfides is dissolved into a oxidise brine, the remaining Fe-ions is left behind as goethite ($\text{FeO}(\text{OH})$).

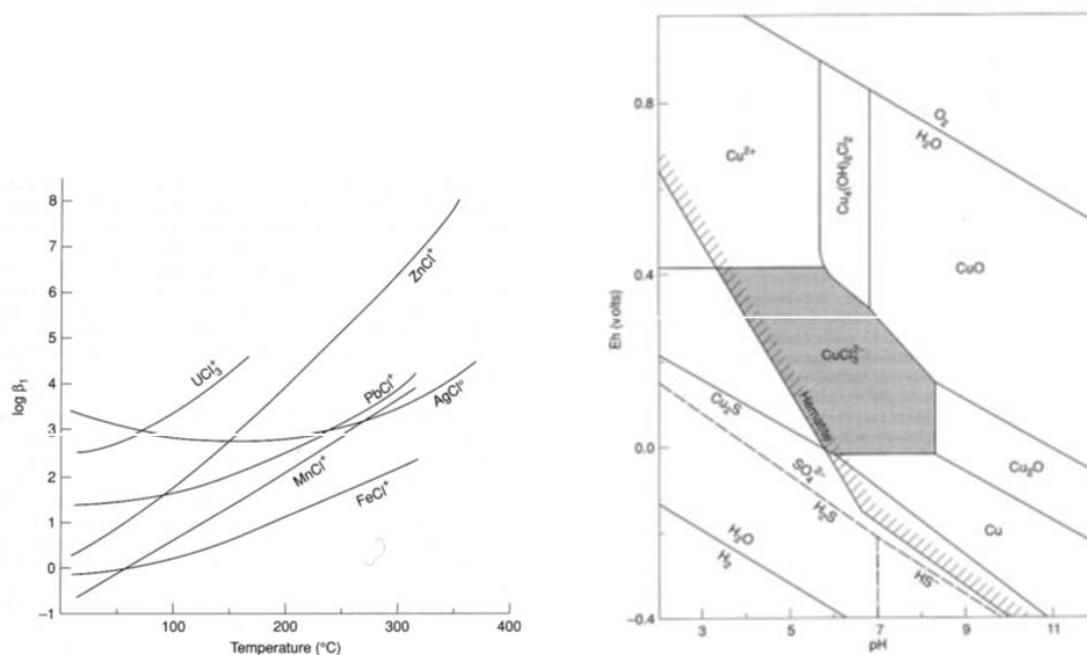


Figure 14. Diagram (left) illustrate the effective stability of metal complexes due to the equilibrium constant and temperature. β_1 is the equilibrium formation constant, a measure on the interaction between the reagents forming a complex. The copper-chloride complex is not present in this diagram, but act approximately in the same way as zinc-chloride complexes. As can be seen from the diagram, the different complexes have an increasing stability with increasing temperature, modified from (Robb 2005). Diagram (right) show the stability fields for copper in solution with given parameters of Eh (volts) and pH, modified from (Robb 2005).

Clay, silt and carbonaceous sediments acts as reducing components if they contain organic matter. Organic matter often contain high pH-values, but more important is the occurrence of diagenetic framboidal iron sulphides formed by bacterial reduction of sulphate to sulphide. Framboid is dead bodies of nannobacterial cells that precipitates iron sulphides (pyrite) in body chambers of fossils (Folk 2005). The copper minerals often replace pyrite sulphides. Carbonates contain relatively low concentration of copper compared to carbonaceous shales and pelagic clays. This indicates the importance of reducing conditions to precipitate copper in sediments. Effervescence, the transition from one liquid phase ($\text{H}_2\text{O} + \text{CO}_2$) into two separate phases of liquid and vapour, could also induce precipitation of metals from a brine. Effervescence occur when fluid pressure decreases under high isotactic pressure. When an upward migrating brine reach a reducing environment, precipitation of sulphides will theoretically form a vertical zoning. This zoning is lined up from the most copper-rich sulphide towards increasing iron- and sulphur content: Chalcocite (Cu_2S) \rightarrow bornite (Cu_5FeS_4) \rightarrow Chalcopyrite (CuFeS_2) \rightarrow Pyrite (FeS_2). Reducing environment destabilises metal-ligand complexes and the solubility of metals decreases. Chalcocite is the most copper-rich sulphide, and is the first sulphide to precipitate when a copper-rich brine reaches a reducing environment. The copper concentration decreases as the brine migrate upward and loses its metal-solubility capacity. Bornite is the second mineral precipitating, followed by chalcopyrite and pyrite. The iron- and sulphur content increases with decreasing copper content in the brine. Accessory metals as Ag, Au, Co, Pb and Zn precipitate together with the copper and often incorporate in the mineral-lattice of copper-sulphides. An evident indicator of an epigenetic deposit of copper sulphides, is a discordant mineralisation with bedding, and zoning (Maynard 1983).

2.5.3 Geological setting and mineralization

The most suitable settings to form SSC deposit is intercontinental basins situated at 20-30 degree from equator. These basins contain thick sequences of red beds formed by oxidation in hot and dry climate. Red beds formed in the Paleoproterozoic to Tertiary Era (Hitzman, Selley et al. 2010), when the vascular land plants showed up, supplying organic matter into sediments accumulated into the intracratonic basins. There is uncertainty connected to the time of precipitation, whether it is syngentetic or epigenetic. In the Neoproterozoic and the Permian time, glaciation events occurred. In glacial times, the composition of the oceans were rich in magnesium and sulphate, somewhat supplied the intracratonic basins with sulphur and magnesium-rich carbonates. Pulses of extension and calm periods characterises the depositional environment to SSC deposits. Period of extension causes accumulation of subareal fluvial and alluvial deposits, while in calmer periods, a progradational trend of turbidites grading upward into shallow water and coastal systems, and finally grades upward to alluvial environment. The larger known SSC deposits in the world have apparently formed in periods with supercontinents as Rodinia (Neoproterozoic) and Pangea (Perm-Triassic), periods with great tectonic breakup. Continental rifting and breakup lead to intense erosion and large amounts of clastic sediments present to accumulate in rift basins. The period of formation of the larger known SSC deposits in the world is illustrated in Figure 15.

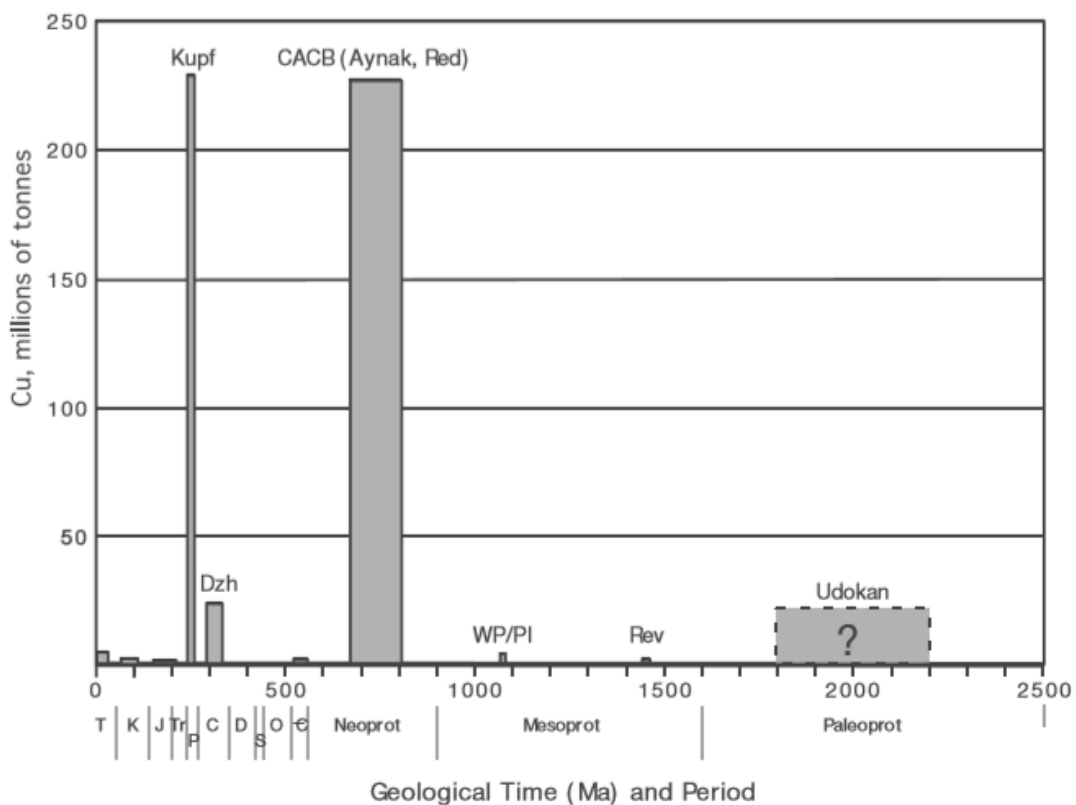


Figure 15. The time period of the formation of the world's greatest SSC deposits. Kupf: Kupferschiefer, Dzh: Dzhezkazgan, CACB (Aynak, Red): Central African Copperbelt, Aynak, Redstone, WP/PI: White Pine/ Presque Isle, Rev: Revett deposits, Udokan: Udokan. Columns give an index of the tonnage in every deposit. Figure modified from (Hitzman, Selley et al. 2010).

The most common copper minerals in SSC deposits are chalcocite, pyrite, bornite, chalcopyrite, digenite, djurleite and covellite. The copper minerals are disseminated and fine grained. The dissemination is often concentrated in coarse grain fractions. Copper minerals do also occurs in veins and cracks. Characteristic in SSC deposits is replacement of carbonaceous materials by copper minerals. Organic matter becomes altered by changing alginate to bitumen, or by oxidation to dissolve carbonate which is precipitated as calcareous rock. In diagenetic SSC deposits, chalcopyrite replace pyrite, bornite replace chalcopyrite and chalcocite replace bornite. Pyrite is also replaced by magnetite or hematite. This type of zonation is common in SSC deposits (Robb 2005).

2.5.4 Sediment-hosted copper deposits in the world

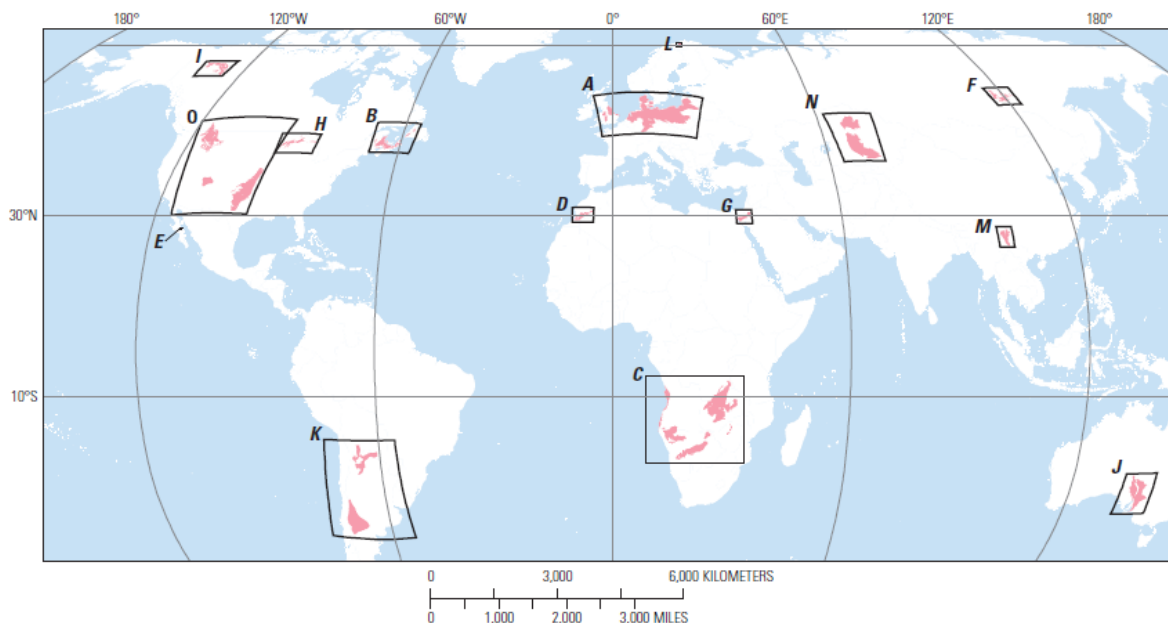


Figure 16. Map showing the distribution of sediment-hosted stratabound copper deposits in the world, modified from (Zientek, Hammarstrom et al. 2010). Black squares mark sediment-hosted copper deposits, and pink coloured areas represents basins. A. The Cheshire-Worcester basin, UK, and the Zechstein basin in the northern Europe. B. The Maritimes basin in Canada. C. Kwanza-, Otavi Mountain Land-, Northwest Botswana Rift/ Ghanzi-Chobe-, Deweras Group-, and Katanga basin located in the southern part of Africa. D. Anti Atlas basin in Morocco. E. Santa Rosalia basin in Mexico, F. Kodar-Udokan basin in Russia. G. Jafr-Tabuk-Sinai basin in Egypt, Israel and Jordan. H. Keewenawan rift basin in Canada and USA. I. Mackenzie Mountains basin in Canada. J. Stuart shelf and Willouran trough in Australia. K. Salta- and Neuquen basin in Argentina. L. Komagfjord-Repparfjord greenstone belt in Norway. M. Chuxiong- and the Dongchuan basin in China. N. Teniz- and Chu-Sarysu basin in Kazakhstan. O. Belt-Purcell-, Paradox- and the Permian basin in USA.

An overview of the distribution the sediment-hosted stratabound copper deposits in the world is given in Figure 16. The Nussir copper deposit (L) is small compared to other SSC deposits in the world. The next subsection describes The Central African Copperbelt, one of the world's largest SSC deposits (C).

The central African Copperbelt

The Central African copperbelt (CACB) is part of the Neoproterozoic Katangen basin. The Katangen copperbelt is located at the border between Zambia and the Democratic Republic of Congo (DRC) in the south of the central part of Africa. The Neoproterozoic Katangen basin host the greatest sediment-hosted stratiform copper-cobalt deposits in the world, with a total tonnage of 140 Mt copper and 6 Mt cobalt (Cailteux, Kampunzu et al. 2005). In addition, there are stratabound zinc-lead-copper deposits and copper-gold-silver deposits in veins in the Central African Copperbelt (Kampunzu, Cailteux et al. 2009).

The Katangan basin was filled by sedimentary and volcanic rocks before it closed and became deformed by the Lufilian Orogeny. Lufilian Orogeny is related to the breakup of the Rodinia and Gondwana supercontinents (880-512 Ma) (Kampunzu, Cailteux et al. 2009), forming a belt with a north-directed thrust-and fold arc. This arc is called the Lufilian Arc and is 150 km wide and 700 km long. A geological map of the Central African Copperbelt is shown in Figure 17. The Lufilian arc is located at the boundary between the Congo and Kalahari craton (Cailteux, Kampunzu et al. 2005).

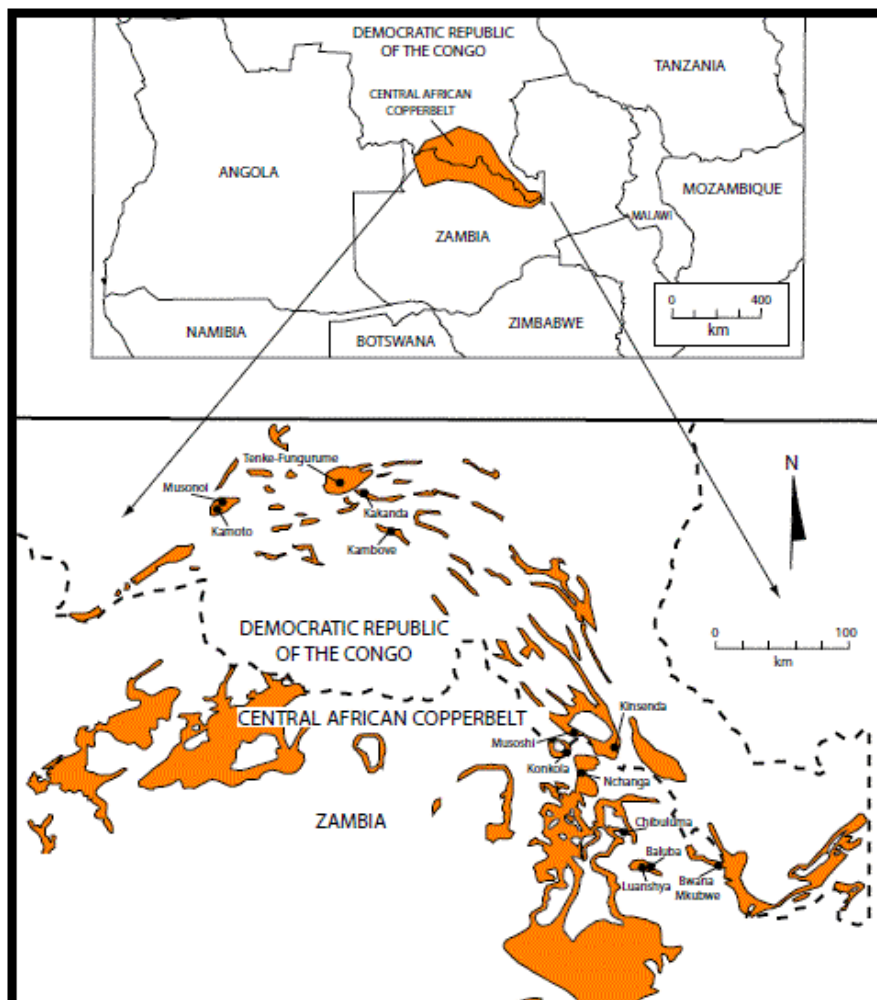


Figure 17. Simplified geologic map of the Central African Copperbelt. The Katanga Supergroup and some of the major mines is shown. Modified from (Cliff D. Taylor and Kirschbaum 2005).

The Katangan supracrustal sedimentary succession forms a 5-10 km thick sedimentary sequence that divides into three lithostratigraphic units, Roan, Nguba and Kundelungu Group. The Roan Group is composed by fluvial and lacustrine sediments, containing siliciclastic and carbonate sedimentary rock, and additionally volcanic and plutonic mafic rocks. The Roan Group is based by the “Roches Argilo-Talqueuses” (R.A.T) – and Mindola Subgroups. R.A.T is composed by red chlorite-rich dolomitic siltstones, dolomitic fine-grained sandstones, silty dolostones and dolomitic silty chloritites. Mindola is composed by scree-type boulder conglomerate, aeolian quartzite, fan conglomerates, arkoses and upward-fining sandstone sequences (Cailteux, Kampunzu et al. 2005). The Roan Group contains a lateral variation of sedimentary facies. The Nguba Group is made up of siliciclastic and carbonate sedimentary rocks with mafic igneous rock. These rocks were deposited into a proto-oceanic rift basin, similar to the Red Sea (Cailteux, Kampunzu et al. 2005). The Kundelungu Group is composed by molasses sequences that belong to syn- to post-orogenic sedimentary deposits. Today the Roan, Nguba and Kundelungu Group are part of allochthonous tectonic sheets.

The sediment-hosted stratiform copper-cobalt deposit occurs in the base of Roan Group. It is hosted by the Congolese facies of the Katangan sedimentary succession. The Congolese facies is an allochthonous unit composed by dolomites and dolomitic shales, situated at the base of the Mines/Musoshi Subgroup containing evaporate-rich sediments. Since the Roan Group show a lateral variation in sedimentary facies, the copper-cobalt deposits is divided into two successions, the Zambia-type and the Congo-type. The Zambia-type is located in Zambia and SE Congo. The host rock is made up by para-autochthonous siliciclastic rocks with the Mindola Subgroup in the base, and is located close to the basement terrain. The Congo-type deposit is located in Congo and is hosted by dolomites and dolomitic shales. The Congo-type includes a variant of the R.A.T rock in the base. The host rock form thrust sheets and nappes as a result of the Lufilian Orogeny. Carbonate units form the top of a lateral correlation between the mineralized succession in Congo and Zambia (Cailteux, Kampunzu et al. 2005).

Pre-lithification sedimentary structures, such as lamination and cross-bedding, show sign of controlling the disseminating of sulphides, and the mineralization is interpreted to have precipitated before compaction and consolidation of the host rock. Deformation of the mineralized host rock does also indicate a precipitation of copper-cobalt mineralization in a stage before the Lufilian Orogeny (Cailteux, Kampunzu et al. 2005). Despite to this, several generation of sulphides is indicated. Ore paragenesis indicates syngenetic, early diagenetic and late diagenetic processes that have formed mineralization of copper and cobalt. Cailteux et al. (2005) suggest that the source of precious metals is pre-Katangan continental rocks, including low-grade porphyry copper deposits, and copper-cobalt-nickel-bearing Archaean rocks of the Zimbabwe craton. Brines generated from seawater in sabkhas or hypersaline lagoons environment have transported mineralization from the source rock and into the host rock. Low crystallization temperature of sulphides, indicate a bacterial sulphate reaction releasing sulphur to growth of sulphides under reducing conditions. The controlling factors for precipitation of mineralization from saline brines probably were the change in Eh and pH condition, forming a more oxidized environment. Metamorphism and tectonic activities have remobilized mineralization. The richest copper-cobalt deposit is located along the southern side of the Lufilian arc, and indicates a tectonic controlling process after deposition of the copper and cobalt mineralization. The deposition of sediment-hosted stratabound zinc-lead-copper deposits is of epigenetic origin. The vein type copper-gold-silver deposits are of post-tectonic and

hydrothermal origin (Kampunzu, Cailteux et al. 2009). This mineralization is connected to the remobilization of sulphides after compaction and consolidation of the host rock.

In the Nchanga deposit in the CACB, two mineralized horizon is described (Upper Orebody and Lower Orebody) to be part of the intracratonic Katangan sedimentary basin with a maximum age determination given by an 877 ± 11 Ma U–Pb geochron for the Nchanga Red Granite (Armstrong et al. 1999) situated below Katangan rocks. The Upper- and Lower Orebody are hosted by an arkosic unit within the base of overlying shales (McGowan, Roberts et al. 2006) and were the Upper Orebody contains mineralization of copper and cobalt, and the Lower Orebody contain mineralization of copper. A study of the $\delta^{34}\text{S}$ concentration between the Upper- and Lower Orebody, have given $+12.1\pm 3.3$ (n=65) in the Upper Orebody and $+5.2\pm 3.6$ (n=23) for the Lower Orebody (McGowan, Roberts et al. 2006). Petrographic observations of the SSC deposit in Nchanga, support a epigenetic origin with a sulfide mineral paragenesis of diagenetic pyrite followed by chalcopyrite, bornite, and carrollite, with late chalcocite (McGowan, Roberts et al. 2006).

3 Materials and Methods

3.1 Optical microscopy and thin section preparation

A fourth part of drill cores, with a length of about 7 cm, was sampled from Nussir ASA drill cores using a rock saw. A total of 32 samples were taken from drill core NUS-DD-13-002 (6 samples), NUS-DD-13-003 (6 samples), NUS-DD-13-004 (14 samples) and NUS-DD-13-012 (6 samples). Then the thin section laboratory at NTNU prepared samples into polarized thin sections. From this, 29 thin sections were prepared, 6 samples from NUS-DD-13-002, 6 samples from NUS-DD-13-003, 12 samples from NUS-DD-13-004, and 6 samples from NUS-DD-13-012 respectively.

The conducted optical microscope Nikon Eclipse E400 POL, with 2.5x, 5x, 10x, 20x and 50x objectives, and 10x ocular, were used in the study of thin sections. ProgRes® CT3, Jenoptik were used to make photomicrographs of thin section. Pictures of whole thin sections were taken using the Olympus Stylus 1030SW digital camera.

32 thin sections from drill core NUS-DD-13-004, NUS-DD-13-002, NUS-DD-13-003 and NUS-DD-13-012 was studied in polarization microscope with the intent to compare the Upper mineralized horizon and the Lower mineralized horizon with regards to the mineralization and zonation. 32 thin sections in each of the mineralized horizon was compared. Further, thin sections from the Upper- and Lower mineralized horizon was compared. The metasedimentary rocks is described in Appendix C.

3.2 Geological mapping

Geological mapping were performed using Garmin GP60 GPS, Silva Ranger 15TDCL compass, Panasonic Toughbook computer, Olympus Stylus 1030SW digital camera, and traditional notebooks. The two mineralized horizons was mapped from Profile 10 and westward in profiles perpendicular to the strike direction. Dip and dip direction was measured in the footwall slate, the Upper- and Lower mineralized horizon if possible, and in the hang wall slate. The mineralized horizons were exposed from Profile 10 and westward until both horizons disappear beneath overburden materials. In the area missing outcrops of the mineralized horizons, the footwall slate and the hang wall slate were mapped until the Nussirjav'ri Thrust. Coordinates from the GPS and the Toughbook were registered in the software SIGMA (System for Integrated Geoscience Mapping), and imported into the ArcGIS software from ESRI.

3.3 Drill core logging

Four diamond drill cores from Nussir ASA were re-logged (NUS-DD-13-004, NUS-DD-13-002, NUS-DD-13-003, NUS-DD-13-012). Intervals of great interest, around and in the mineralized horizons were logged in more detail.

3.4 Electron probe micro analyzer (EPMA)

WDS analysis were performed by electron micro probe-analyser on thin sections from (diamond) drill holes. Oxides and sulphides was analysed qualitatively to detect mineral composition of unknown minerals in the light microscope and to measure concentration of elements in the Upper- and Lower mineralized horizon. The analysed mineral grains was marked with the same label as the thin section and with a number describing the area of the analysis (Table D73, Table D74 and Table D80-Table D82).

A quantitative analyse of eight polished thin section were run by the electron probe micro analyser (EPMA) located at NTNU. EPMA, also called electron probe, detect microscopic features that is undetectable in the light microscope and give a quantitative measurement of elements in a selected point of a polished thin section. Electron probe measures quantitative values of elements by wavelength-dispersive x-ray spectrometer (WDS). The EPMA used at NTNU, is a JEOL JXA-8500F Electron Probe Micro Analyser (Figure 18). A high performance thermal field emission electron probe micro analyser combines high Scanning Electron Microscopy (SEM) resolution with high quality x-ray analysis of submicron areas. JEOL JXA-8500F contains five Wavelength Dispersive x-ray Spectrometers (WDS) and Energy Dispersive x-ray Spectrometer (EDS). This instrument is able to analyse five elements WDS, 16 elements EDS, and collect image signals from backscatter and secondary electron detectors. The WDS is run with high probe current and small probe diameter. The WDS analysis is able to direct extreme element analysis of sub-micron areas.

The system is automated and controlled by a powerful sun workstation system. The EPMA is able to analyse elements with atomic number 4 (Be) to 92 (U), and wavelengths from 0.087 to 9.3 nm. Secondary electron image resolution (SEI) is 3.0 (WD11 mm, 30 kV), and the backscattered electron image (BEI) include topography and composition image (JEOL 2011). X-rays with 15 kilo voltage (kV) acceleration voltage were used in WDS analysis of selected points at thin sections. There were performed point analysis and mapping of minerals measured as percent of oxides (mass oxides %) and as percent of sulphides (mass sulphides %). The utilized standards are given in Table D78 and Table D79. Selection of element in the WDS analysis is based on the appearing minerals observed in light microscope and common elements in copper sulphides. The thin sections were coated by conducting carbon paint to conduct electrons from the micro probe. The mineral composition of analysed minerals were calculated by the formula calculation given in (Deer, Howie et al. 1992).



Figure 18. Picture of a JEOL JXA-8500F Electron Probe Micro Analyzer (EPMA), (JEOL 2011).

3.5 Analyse data

The trace elements analysed by Nussir ASA is shown in Table B25. The analysis of elements from Nussir ASA contain values below the detection limit (censored data), somewhat is normal in chemical analysis of ore samples (Clemens, Filzmoser et al. 2008). According to Helsel (2006), the exclusion of the censored data gives a strong upward bias. He also points out that substitution of censored data with a constant will distort all statistical testing of a data set. Despite the recommendations of (Helsel 2006), censored data was excluded from the database. This was to preserve the natural variation in the data set, something that was important to investigate the natural variation of elements in the Upper- and Lower mineralized horizons. The short time limit of this thesis was also a reason to exclude censored data. Finding a good substitution method for this data set would require great amount of statistical study, and was considered slightly outside the scope of this thesis.

The percussion drill holes (PD) and chip sampling (CH) was executed from the excel spreadsheet containing all the analyse data, since these samples were taken by a different sample method than diamond drilling. In the comparison of mean value and standard deviation, samples from the Upper mineralized horizon and the Lower mineralized horizon were used.

3.6 Univariate statistics

Univariate statistics, statistics for data with one variable, for the Upper mineralized horizon and the Lower mineralized horizon were given using the software ioGAS-64 as mean, standard deviation, variance, max value, minimum value, and number of counts. In the univariate comparison of the Upper- and Lower horizon, only mean and standard deviation.

Mean values of the Upper- and Lower mineralized horizon were compared in a scatterplot where the Upper horizon constituted the y-axis, and the Lower horizon constituted the x-axis. Natural logarithm was used to give a better view of the plotted values.

The mean value is given in Formula 1. Mean (\bar{X}) is the sum of observations ($\sum X_i$) divided by the total number of observations (n). Mean is sensitive to outliers. If the sample contains one observation with an extreme high value, the predominant observations would lie below the

mean value. Mean values are therefore best suited when the observations in a sample form a normal distribution.

$$\mu = \frac{\sum \chi^i}{n}$$

Formula 1. Mean (μ) of a number of samples (n) with a total value (χ^i).

Variance is the squared deviation of the mean value. σ^2 is the variance for a population.

$$\sigma^2 = \frac{1}{N} \sum_{i=1}^N (\bar{x} - \mu)^2$$

Formula 2. Variance (σ^2) for a population. Sample value (x), mean (μ), and number of samples (n).

Standard deviation of the Upper- and Lower mineralized horizon were compared in a scatterplot where the Upper horizon constituted the y-axes, and the Lower horizon constituted the x-axes. Natural logarithm was used to give a better view of the plotted values. Standard deviation is a measure of the distribution of observation around the mean value in a sample.

$$\sigma = \sqrt{\frac{1}{n} \sum_{i=1}^N (\bar{x}i - \mu)^2}$$

Formula 3. Standard deviation (σ), Number of samples (N), Value of samples (X_i), mean value (μ).

The mean values and the standard deviation were correlated in a scatterplot. Correlation describes the linear relationship between two or more variables. In a correlation analysis, the value of a variable is tested against another variable to see if they correlate linear. A correlation coefficient give a measure between 0-1, where 1 indicate total correlation, while a value of 0 indicate no correlation.

The chemical analysis formed a non-normal distribution, and the test is therefore classified as non-parametric test. The variables do not form a frequency curve with one major peak, but several.

3.7 Multivariate analysis (MVA) - Principle component analysis (PCA) and discrimination analysis (DA)

Multivariate analysis using Principle Component Analyses (PCA) and linear discriminant function analysis (DA) were used to test for vertical differences between the Upper and Lower mineralized horizon. There were also performed a lateral comparison between and within Zone 1, Zone 2 and Zone 3. Each zone represents drill core samples from drill holes from different part of the Nussir copper deposit. Zone 1 included samples from drill holes east of Profile 10. Zone 2 include samples from the Upper mineralized horizon west of Profile 10, and Zone 3 include samples from the Lower mineralized horizon located west of Profile 10 (Figure 19). Drill holes from Zone 1, Zone 2 and Zone 3 were numbered 1-53 (stratum number) to distinguish between each drill hole. An overview of the nomenclature used in the multivariate analysis is given in Table 3. The statistic testing was performed using SPSS ver.21. Analysis below detection limit and missing data were excluded from the PCA and linear discriminant analysis, as recommended in “Statistical data analysis explained“ (Clemens, Filzmoser et al. 2008). To get a good PCA model, every selected element should have data for each sample to get a representative group covariance matrix (Clemens, Filzmoser et al. 2008). Records showing a factor scores above 3.0 or below -3.0, were classified as outliers and excluded from the further analysis. In the lateral comparison within and between Zone 1, Zone 2 and Zone 3, the drill core analysis with copper content 0.1 % or higher were classified to belong to the mineralized horizon.

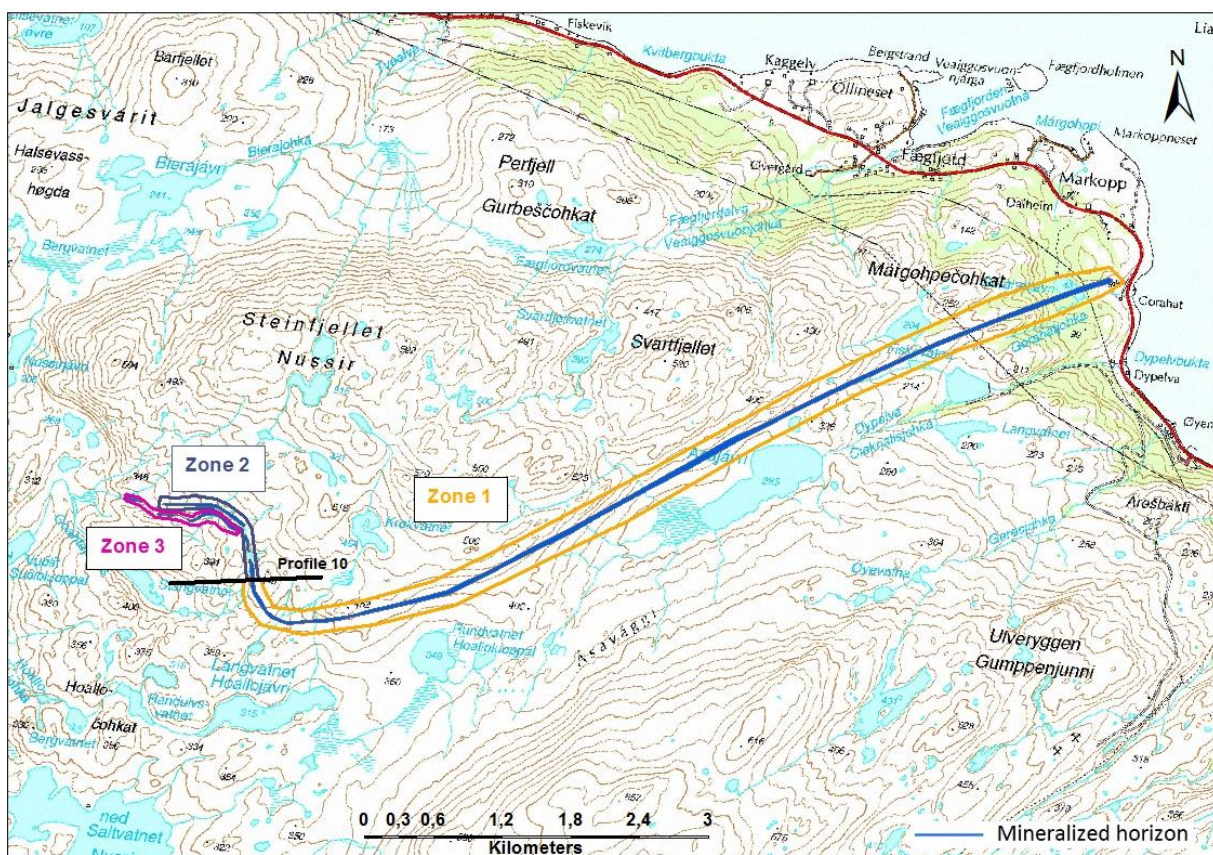
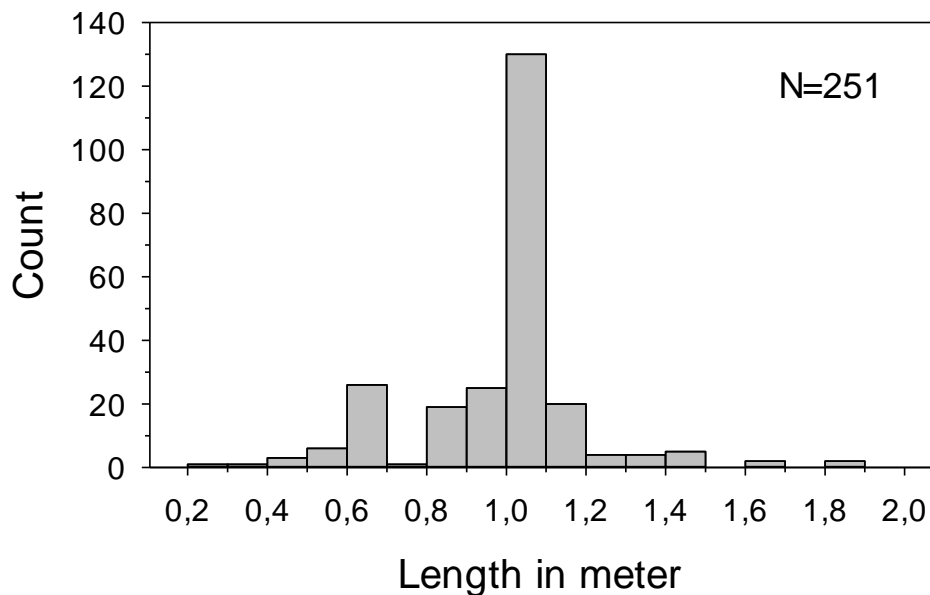


Figure 19. Illustration of the definition of the Nussir copper deposit in Zone 1, 2 and 3 used in the multivariate comparison.

Table 2. The histograms shows the sample length of drill core samples, with the specific length. Data from 251 analysed samples was used in the multivariate analysis.



3.7.1 Nomenclature

A sample record is in this case, in connection to the quantitative trace element analysis, the analysis of one-half of a nearly one meter long drill core from one borehole. Number of samples from each borehole varies depending on the thickness of the ore bearing strata. The different terms used in the multivariate analysis are described in .

Table 3.

Table 3. Description of nomenclatures in the multivariate analysis.

The Upper mineralized horizon	Mineralized horizon located highest up in the stratigraphy from profile 10 and westward.
The Lower mineralized horizon	Mineralized horizon located lower in the stratigraphy than the Upper mineralized horizon from profile 10 and westward.
Zone 1	Mineralized horizon stretching from east to profile 10.
Zone 2	The Upper mineralized horizon.
Zone 3	The Lower mineralized horizon.
Stratum number	Each (diamond) drill hole were given a number from 1 – 53 to separate drill holes.
New samples	Samples from (diamond) drill hole NUS-DD-08-014 and younger. Classified as 1 in the multivariate analysis.
Old samples	Samples from (diamond) drill hole NUS-DD-08-013 and older. Classified as 2 in the multivariate analysis.

3.7.2 Principle component analysis (PCA)

PCA reduces the dimensionality of a data set containing a large number of variables without taking away the natural variation in the data set. Dimension reduction make new variables, Principle Components (PC1, PC2, PC3 etc.), were PC1 represents the direction of maximum variance (Esbensen, Guyot et al. 2002). The PCs represent the dimensions that each element appears. The PCs spread on ten or more dimension (function), but often four factors explain the major variation of the data set. The PCs is uncorrelated to preserve the natural variation. PCA construct a statistical model of the data set and the new variables, PCs. In this PCA test, a linear discriminant function analysis was used.

Recommended parameter setting when producing PCA model (Austin 2014):

- Ratio of samples to variables should be at least 5:1, meaning that number of variables should be one fifth of number of samples.
- Variables should have correlations greater than 0.30.
- When testing for communality, values should be equal or larger than 0.5.
- The rotated component matrix should have one value larger than 0.4. If more than one excide this value the element should be excluded.
- Kaiser-Meyer-Olkin Measure (K-M-O) indicates the sampling adequacy of a variable, and is a measure of the correlation and partial correlation in a variable and range from 0-1. K-M-O should be 0.5 or higher. K-M-O values of 0.5-0.6 is considered good while higher values is considered very good. Values below 0.5 make the model improprie for a PCA analysis.
- Bartlett's Test of Sphericity gives an identification of the suitability of the PCA model.. Approx. Chi-Square, DF (degree of freedom) and significant values is included in the Bartlett's test. High Chi-Square values and a significant value <0.05 is an indication of a good model.
- Eigenvalues describes the components forming the PCA model. Figure 20 shows an example of eigenvalues. The initial eigenvalue is described by:
 - The total eigenvalue describe how much discriminating ability a function possesses. The eigenvalue should have a total >1.
 - Percent of variance is the proportion of discriminating ability of the selected variables found in a given component. If the percent of variance in component 1 is 77%, it accounts for 77% of the discriminating ability of the discriminating variables.
 - Cumulative % is representing the proportion of variance in the original variables that is accounted for in the factor solution. If the cumulative in the first component is 45 %, the first component explains 45% of the total variation in the dataset. If the second component is 76%, the first two components explain 76% of the total variation.
 - The canonical correlation describes the correlation between variables.

The extraction sums of squared loading describes the components with a total eigenvalue >1. The rotation sums of squared loading describe the eigenvalues after a rotation of the components have been made. The components are rotated to get the best fitt to the linear model.

Function	Eigenvalue	% of Variance	Cumulative %	Canonical Correlation
1	,110 ^a	77,5	77,5	,315
2	,032 ^a	22,5	100,0	,176

a. First 2 canonical discriminant functions were used in the analysis.

Figure 20. Example of eigenvalues.

- The rotated component matrix shows a PCA model where the components (dimension vectors) is rotated to get the best-suited orientation in relation to the variables. The rotated component matrix plot give an overview of how much each variable appears in the different components. Variables should have 0.4 or more in just one component. If a variable exceed this, having 0.4 or more in two components, it contribute too much in two components, and weakens the PCA model.
- Regression factor scores values above or below 3.0 were considered as outliers and excluded for further application in the linear discriminant analysis.

3.7.3 Discriminant analysis

A linear discriminant function analysis predicts the likelihood as member of groups. Definition of descriptive statistics of a discriminant analysis is given below. Good procedures performing Multivariate analysis and discriminant analysis using the software program SPSS is given on the internet. A good description is given by (Austin 2014)¹.

Wilks' Lambda gives an indication of the correlation with a null hypothesis that the canonical correlation associated with the functions (components) are all equal to zero. Figure 21 show an example of the results from a Wilks' Lambda test.

- Test of function is the included functions in a given test with the null hypothesis that the canonical correlation associated with the function are all equal to zero. If there are more than one test of function, the first and second function is tested with each other and so on.
- Wilks' Lambda is a multivariate statistic calculation. Wilks' Lambda is the product of the values of $(1 - \text{canonical correlation}^2)$. By using the examples in Figure 20 and Figure 21, Wilks' Lambda for test of function 1 through 2 is: $(1 - 0.315^2) \times (1 - 0.176^2) = 0.873$. This value means that 87,3 % of the variation is not explained.
- Chi-square is testing the canonical correlation of the null hypothesis, in other word, if the given function is equal to zero, there is no correlation between the functions.
- Df – degree of freedom for the given function. Df is based on the number of groups present in the categorical variable and the number of continuous discriminant variables.

Sig. – significant value is the probability value (p-value) associated with the Chi-square statistic of a given test. If the p-value is lower than alpha, often set to 0.05, the null hypothesis fails, and must be rejected. This means that the functions correlates.

¹ www.utexas.edu/.../PrincipalComponentAnalysis_Outliers_Validation_Reliability.ppt

Wilks' Lambda				
Test of Function(s)	Wilks' Lambda	Chi-square	df	Sig.
1 through 2	,873	32,018	6	,000
2	,969	7,427	2	,024

Figure 21. An example of results of a Wilks' Lambda test.

A scatter plot or other type of graphic illustration could present the discriminant analysis. Figure 22 show an example of a scatter plot with graphs of the results from a discriminant analysis.

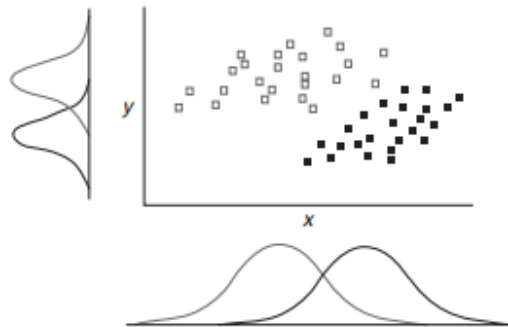


Figure 22. Example of scatter plot of discriminant analysis. The variables form two groups. The graphs illustrate the degree of overlap between the two groups. figure modified from (Agresti 1996).

3.8 Geophysical measurements

Geophysical measurements in drill holes performed by NGU in 2013 in cooperation with Nussir ASA were used to compare induced polarization (IP), resistivity and natural gamma radiation with observed mineralization in drill hole NUS-DD-13-004. Re-logged drill core with observation of the mineralization in thin sections from drill core samples, was compared to investigate the geophysical response from the mineralization. Harald Elvebakk (NGU) provided the geophysical data.

Natural gamma radiation differs in unequal rock types. Natural gamma radiation in a drill hole shows the change in geology and give well response on rock contacts. The change in natural gamma radiation is often caused by different content of potassium, uranium or thorium. The total gamma radiation is measured in cps (counts per second) with API-standard (Dalsegg, Elvebakk et al. 2013).

The resistivity is measured in Short Normal (SN) and Long Normal (LN). SN with a pol/pol-electrode configuration and electrode distance 0.4 m, measures the resistivity close to the drill hole wall, while LN have an electrode distance 1.6 m and measures the resistivity some decimetre out from the drill hole (Dalsegg, Elvebakk et al. 2013). The resistivity measurements is corrected to the conductivity of water in the drill hole, drill hole diameter and the diameter of the probe (Dalsegg, Elvebakk et al. 2013).

The IP-effect is measured when alternating current of 110 ms is induced in to the drill hole wall and turned off in 110 ms. The ratio between IP-voltage and current voltage in the time when the current is induced into the ground, give a IP-effect measured in percent (Dalsegg, Elvebakk et al. 2013).

4 Results

4.1 Geological mapping

The geological map shows the interpreted rock boundaries based on field observations (circles with representative lithology-colour), geological map from Kjell Nilsen and Edward Iversen (1990), Figure E128, and magnetic map (Appendix E).

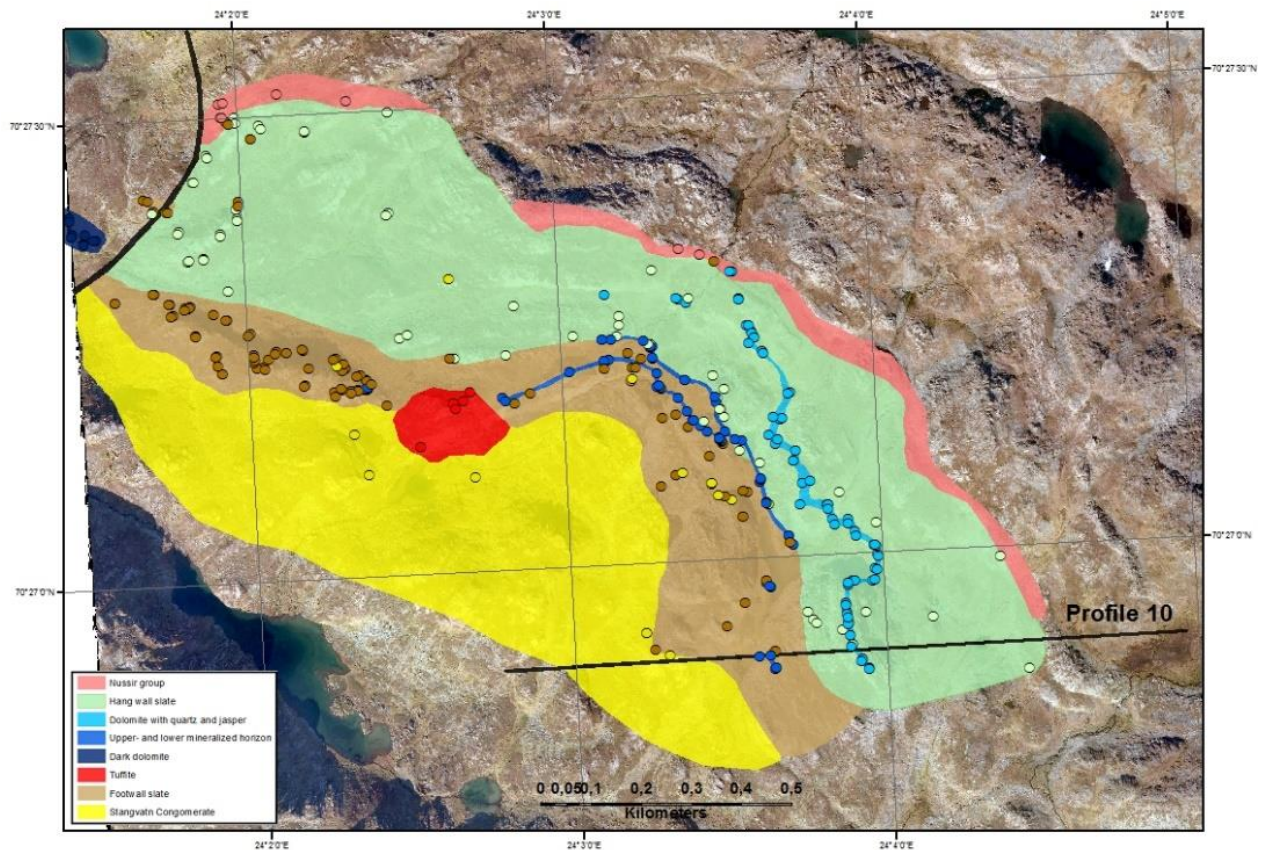


Figure 23. Geological map of the two mineralized horizons from profile 10 and westward to the Skinnfjellet Thrust (Pharaoh, Ramsay et al. 1983) (black line up to the left). Observation points (circles) form the basis for the interpreted geological map. Areas with few or absence of observation points, the rock boundaries are drawn on basis of the geological map of Nussir (Nilsen and Iversen 1983), and geophysical map of magnetically survey (Appendix E).

The Upper- and Lower mineralized horizons were exposed from profile 10 and westward until both of the horizons disappeared and became covered by overburden material (Figure 23). The mineralized horizons occurred as blocks and fracture-dominated outcrops with brown weathered surface with veins of quartz and calcite (Figure 24). The mineralized horizon was about two meter thick and dipped steeply towards NE. The outcrop showed generally a mineralization of bornite and malachite. Tight folds with fold axis: $47 \rightarrow 044$ and fold axial plane: $312/76$ were observed in the Upper mineralized horizon (Figure 25). The Lower mineralized horizon was observed from Profile 10 and westward until it reached a body of tuffite (Figure 23). Few blocks of mineralized slate was observed at the western side of the tuffite.



Figure 24. The picture shows an outcrop of the mineralized horizon composed by dolomite with veins of quartz and calcite. Hammer as scale. Photo: Kjersti Moen



Figure 25. Picture shows the Upper mineralized horizon composed by dolomite with veins of calcite and quartz. The dolomite formed a tight fold, fold axis: $47 \rightarrow 044$, fold axial plane: $312/76$. Rock hammer as scale. Photo: Kjersti Moen.

The Stangvatn conglomerate was a monomict conglomerate with dacitic clasts in varying size with normal grading (Figure 26). The conglomerate contained sandstone layers and veins of quartz. The intensity of the sandstone layers increased upward in the Stangvatn conglomerate, and graded into the overlying footwall slate (Figure 27). The footwall slate was situated above the Stangvatn conglomerate and beneath the Lower mineralized horizon, and was composed by arkosic sandstone with layers of green mica (Figure 27 and Figure 28). The footwall slate was carbonate-rich in the boundary of the Lower mineralized horizon. Structural measurements indicated that the footwall slate dipped towards NE, were the dip varied from 40-80 °. A fining-up sequence in the footwall slate made it difficult to distinguish it from the overlying hag wall slate.



Figure 26. The picture shows an example of the monomict dacitic Stangvatn conglomerate. The conglomerate contains sandstone layers and veins of quartz. Photo: Kjersti Moen.

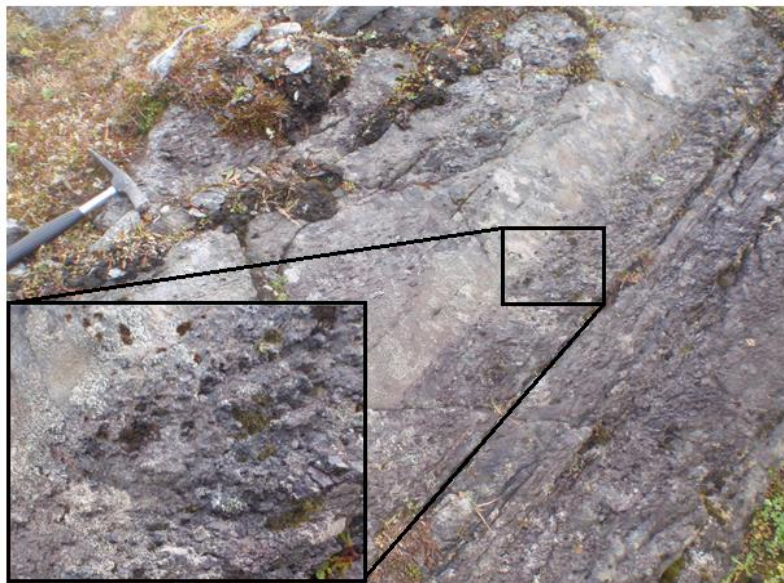


Figure 27. The picture shows the footwall slate with coarser layer of sandstone. The square show a coarser sandstone layer. Photo: Kjersti Moen.

The hang wall slate was situated above the Lower mineralized horizon, and was composed by a light-coloured slate. The hang wall slate was rich in carbonate, especially near the Upper mineralized horizon. Structurally measurements indicated dip direction towards NE with dip varying from 40-80 °. An un-mineralized dolomitic rock with clasts of jasper and quartz was situated in the hang wall slate. This dolomite was exposed along the field area from profile 10 and westward (Figure 23). The un-mineralized dolomite followed about the same distribution as the Upper- and Lower mineralized horizon, but at a higher level in the stratigraphy.



Figure 28. Picture shows the footwall slate with layers of green mica. Photo: Kjersti Moen.

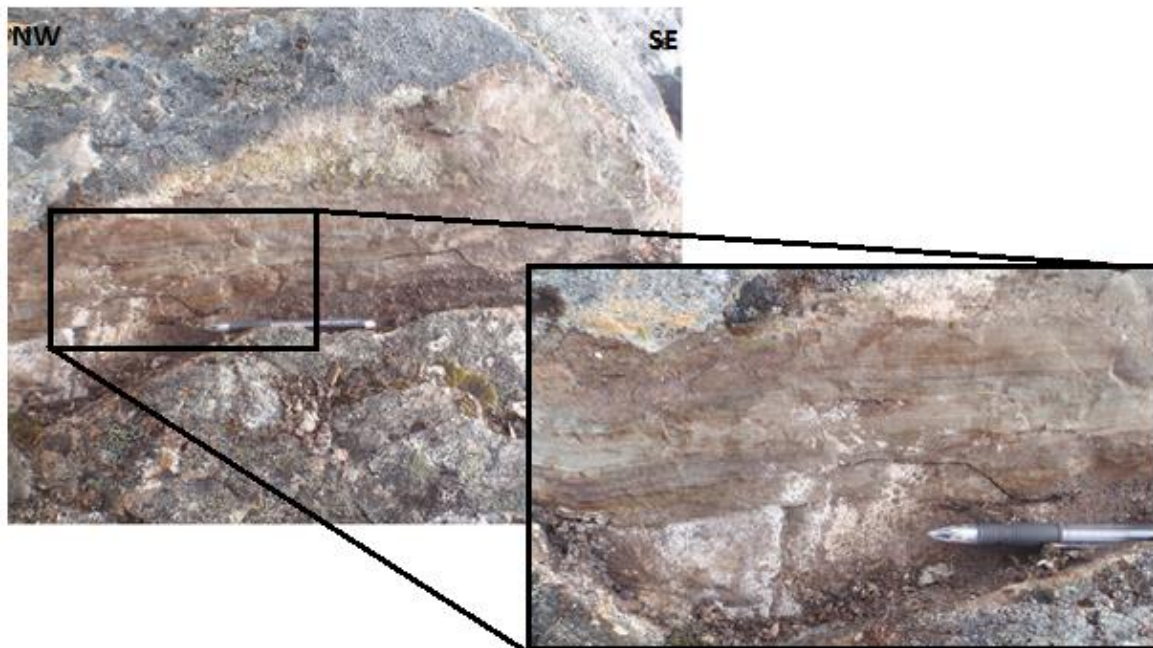


Figure 29. Hang wall slate. The black frame show sedimentary lamination in the fine-grained hang wall slate. Photo: Kjersti Moen.



Figure 30. The picture shows the dolomite with clasts of jasper and quartz. The dolomite was situated in the hang wall slate. It followed about the same distribution as the Upper- and Lower mineralized horizon, but at a higher level in the stratigraphy. Hammer as scaling (black circle). Photo: Kjersti Moen.



Figure 31. The picture shows the dolomite with clasts of jasper and quartz. Photo: Kjersti Moen.

A body of tuffite was observed in the field area (Figure 23) and were composed by fine-grained tuffitic sediments with light-coloured pyroclasts (Figure 32). The tuffite cut the stratigraphic sequences of the surrounding rocks (Stangvatn conglomerate and the footwall slate).

A fine-grained vulcanite with magnetite-rich lamella was situated above the hang wall slate (Figure 23). The vulcanite contained dark grey colour with black lamellas (Figure 33). An unmineralized dolomite was observed west of the Skinnfjellet Thrust. The fresh surface showed a dark grey colour. Structural measurements indicated an overall dip direction towards NNE with dip varying from 40-80 ° and a bedding dipping towards NW in the eastern field area with dip around 60-80° (Figure 34). In the western part of the Nussir West, the structural measurements were somewhat limited to get a complete understanding of the structural development. However, the dip direction changed and showed a dip direction towards ESE with dip varying from 50-90° indicated folding of the bedrock.



Figure 32. The picture shows the green tuffite containing light pyroclasts. Hammer as scaling. Photo: Kjersti Moen.



Figure 33. The picture shows the vulcanite located above the hang wall slate and containing magnetite-rich lamella (white frame). Hammer as scaling (white circle). Photo: Kjersti Moen.

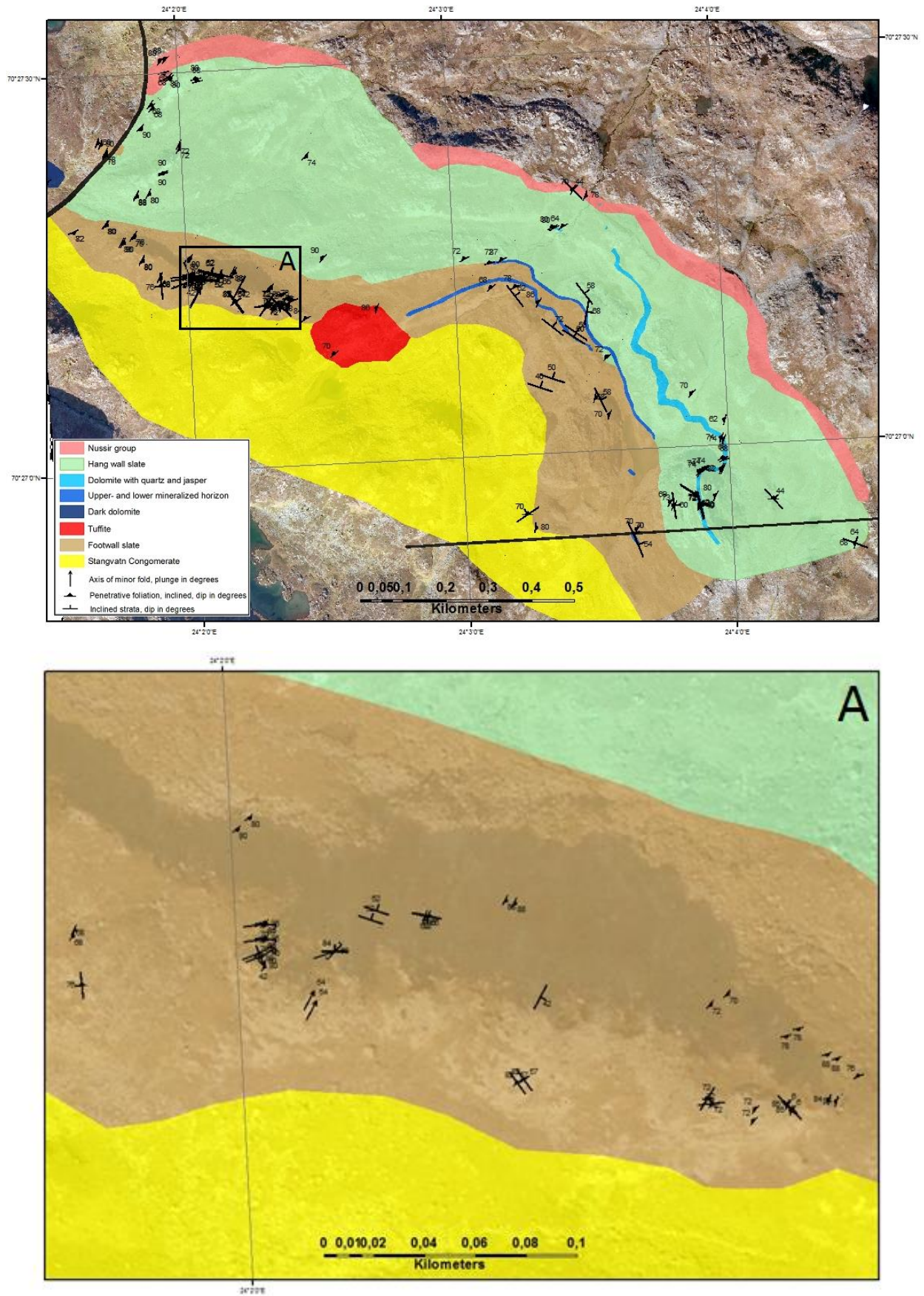


Figure 34. Geological map of the Nussir West with structural measurements. Map developed in Arcgis.

The geological map were compared with the geological map made by Nilsen and Iversen (1990) (Appendix E), and showed that the geological map fitted well with the geological map from Nilsen and Iversen (1990), Figure 35. They interpreted the further distribution of the two mineralized horizon westward. This was not performed in the geological map since observation of the mineralized horizon was absence in the westernmost area.

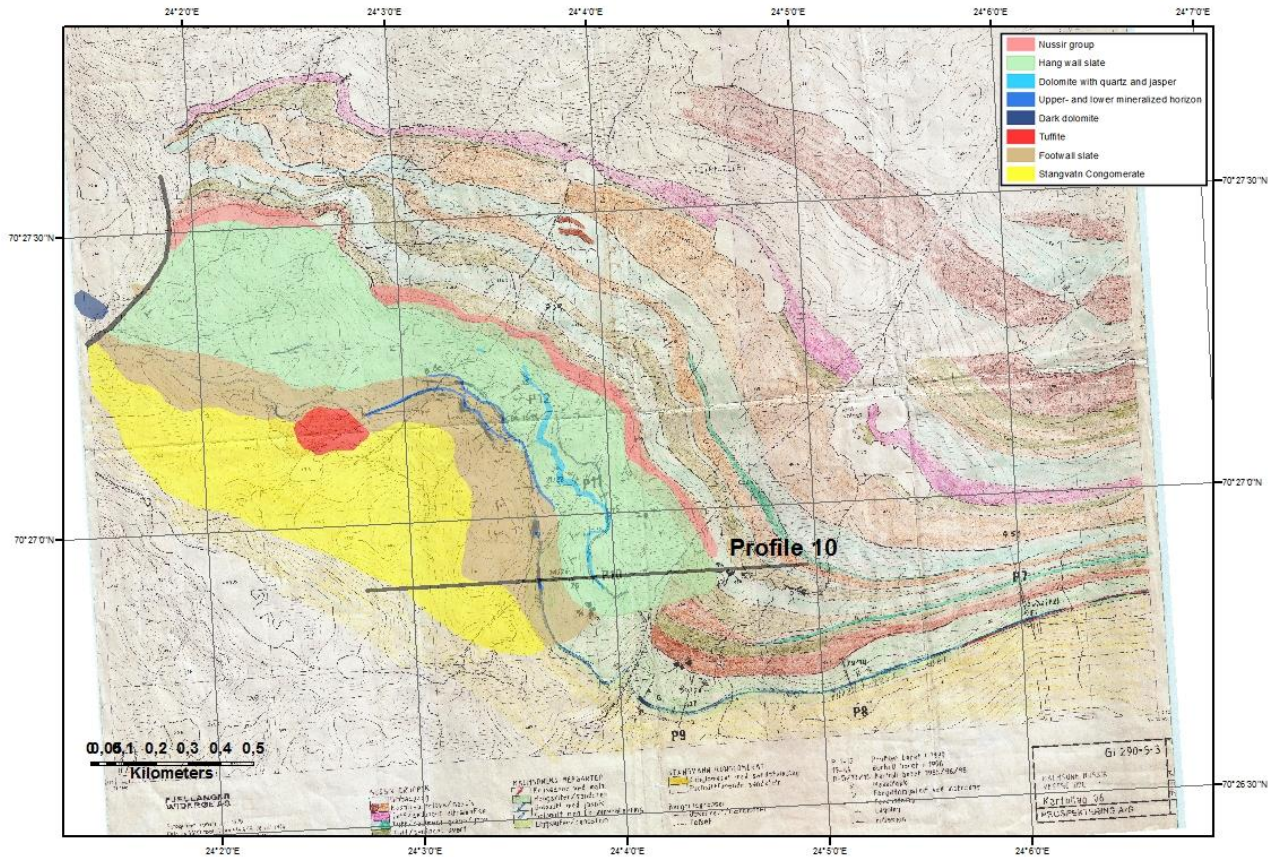


Figure 35. Geological map on top of the geological map made by Kjell Nilsen and Edward Iversen (1990). The geological map show about the same rock boundaries as map from Kjell Nilsen and Edward Iversen (1990). The mineralized horizon was not drawn west of the tuffite because of the absence of outcrops in the area.

4.2 Drill core re-logging

Four diamond drill cores were re-logged (NUS-DD-13-004, NUS-DD-13-002, NUS-DD-13-003, NUS-DD-13-012). Results from re-logging are given in Figure 37, Figure 38, Figure 39 and Figure 40. The drill core logs show the lithological sequences, intervals classified as ore by Nussir ASA based on geochemical analysis and drill core descriptions. Drill core samples observed in thin sections were added to the drill core logs. The location of drill cores is shown in Figure 36.

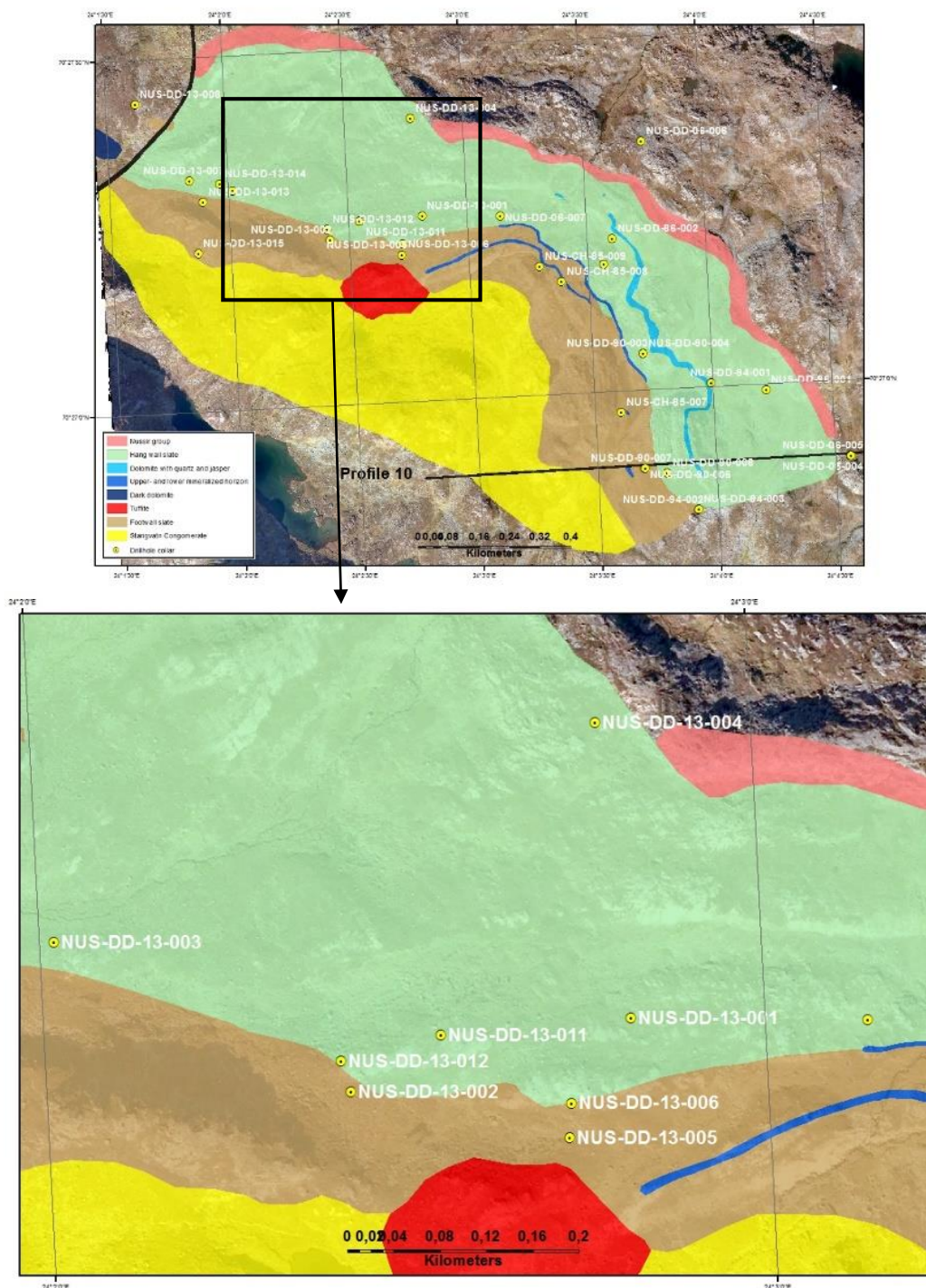
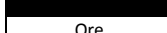
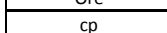
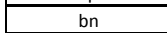
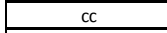
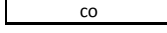


Figure 36. Geological map with the location of diamond drill holes in the western part of Nussir West. Drill cores from drill hole NUS-DD13-004, NUS-DD13-002, NUS-DD13-003 and NUS-DD-13-012 were re-logged.

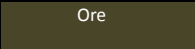
The re-logging of drill core NUS-DD-13-004 indicated that the drill core cut through carbonate-rich slate where calcite occurs in veins and spots (Figure 37). The drill core contained the Upper mineralised horizon (379.6-390.15 m) and the Lower mineralized horizon (407.76-412.5 m). Observations of dacitic clasts in the slate beneath the Lower mineralization were interpretation as an indication of the occurrence of the footwall slate. The mineralization occurred in the slate above and beneath the dolomite-rich layers, and in the dolomite in the Upper- and Lower mineralized horizon. The lower part of the drill core cut through a dark coloured fine laminated magnetic tuff (416.4-420.26 m, 420.62-425.2 m) and a green coloured laminated tuff (420.26-420.62 m).

The re-logging of drill core NUS-DD-13-012 (Figure 38) indicated that the drill core cut through the Upper mineralized horizon due to the fine-grained slate beneath the mineralized horizon and the location where the drill core was drilled (Figure 36). Like drill core NUS-DD-13-004, a carbonate-rich slate were observed where calcite occurred in vein and spots. The re-logging of drill core NUS-DD-13-003 indicated that the drill core cut through a dolomite-rich mineralized horizon surrounded by carbonate-rich slate (Figure 39). Clast of dacite were observed in the Lower part of the drill core about 9.22 m beneath the mineralized horizon. Nussir ASA defined the mineralized horizon as the lower mineralized horizon. The re-logging of drill core NUS-DD-13-002 indicated that the drill core cut through a mineralized horizon hosted by carbonate-rich slate (Figure 40). The dolomite layer seen in the three other drill cores were not observed. Thick veins of quartz and calcite cut through the slate with some mineralization of chalcopyrite. Mineralization in the relogged drill cores were association to dark vein and veins and spots of calcite in the dolomite, hang wall slate and the footwall slate. Minor amount of pyrite were observed in the footwall- and hang wall slate, and a green coloured slate were observed in the hang wall slate and in the footwall slate.

Drill core NUS-DD-13-004,

	CLY + CRB (carbonate-rich slate)
	CLY (Slate)
	CRB (Carbonate)
	TUMT (Magnetite laminated tuff)
	TUF (Green tuffite, not magnetic)
	BRK (Broken rock)
	Ore > 0.1 % Cu
	cp Chalcopyrite
	bn Bornite
	cc Chalcocite
	co Covellite

Northing: 7819477.921
 Easting: 389763.401
 Elevation: 401.969 m
 Azimuth: 178°
 Dip: 80°
 Total length: 436.6 m

Depth from (m)	Depth to (m)	Thickness (m)	Lithology	Description	Thin section (interval (m))	Mineralization in thin sections
378	379.6	1.6		Dark slate with carbonate veinlets and spots. Thick carbonate vein (379,36 m)		
379.6	380.3	0.7	Ore 	Dark slate. Decreasing amount of carbonate spots.	NUS_002 (380.04-380.14)	cp + bn (disseminated)
380.3	380.72	0.42	Ore 	Dark slate with thick veinlets of carbonate. Disseminated chalcopyrite.		
380.72	380.92	0.2		Broken rock		
380.92	381.65	0.73	Ore 	Green-coloured slate with dark alteration traces. Carbonate-rich veinlets and spots hosts mineralization of chalcopyrite and bornite.		
381.65	384.84	3.19	Ore 	Carbonate rich rock with minor slate, hosting disseminated chalcopyrite. Increasing mineralization of bornite and chalcopyrite from 384,30 m.	NUS_003 (381.6-381.7)	bn + cp (disseminated)
384.84	386.4	1.56	Ore 	Green-colored slate with bands of dark slate. Carbonate-rich spots and veinlets hosts disseminated chalcopyrite.	NUS_005 (384.58-384.69)	bn + cp (disseminated and veins)

386.4	388.45	2.05	Ore	Green-coloured carbonate with slate sections. Carbonate-rich veinlets and spots hosts disseminated chalcopyrite.		
388.45	390.15	1.7	Ore	Carbonate with veinlets of slate and carbonate. Disseminated chalcopyrite hosted by slate-rich layers.	NUS_006 (388.1-388.16)	cp (disseminated and veins)
390.15	391.33	1.18		Dark slate with dark alteration traces and carbonate-rich veinlets that host mineralization of chalcopyrite.	NUS_007 (390.6-390.66)	cp + cc (disseminated and veins)
391.33	392.54	1.21		Carbonate-rich slate hosting mineralization of chalcopyrite and pyrite.		
392.54	393	0.46		Dark slate with carbonate-rich veinlets and spot.		
393.12	400.54	7.42		Dark slate with carbonate-rich veinlets and spots.		
400.54	401.9	1.36		Ligth colored slate with layers of dark slate, containing carbonate-rich veinlets and spots.	NUS_008 (399.16-399.27)	cp (disseminated)
401.9	407.76	5.86		Dark slate with carbonate-rich veinlets and spots.		

407.76	410.15	2.39	Ore	Carbonate with slate-rich layers hosting mineralization of chalcopyrite.	NUS_009 (407.68-407.75)	cp (disseminated and veins)
					NUS_010 (408.03-408.09)	cp (disseminated and veins)
					NUS_011 (409.65-409.72)	bn + cp + cc (disseminated and veins)
410.15	410.47	0.32				
410.47	412.5	2.03	Ore	Carbonate with slate-rich layers hosting mineralization of chalcopyrite.		
					NUS_012 (411.84-411.9)	bn + cp + cc (disseminated and veins)
412.5	416.4	3.9		Chlorite-colored slate with carbonate-rich veinlets and spots containing. Dacitic clasts.	NUS_013 (412.53-412.6)	cp (disseminated)
416.4	420.26	3.86				
				Magnetite laminated tuff with carbonate-rich veinlets and spots.		
420.26	420.62	0.36				
420.62	425.2	4.58				
				Green tuffite with carbonate-rich veinlets and spots. Not magnetic.		
				Magnetite laminated tuff with carbonate-rich veinlets and spots, and veinlets of epidote.		

Figure 37. The figure show the results from re-logging of the diamond drill core NUS-DD-13-004. Drill core samples observed in thin section were added to the drill core log.

Drill core NUS-DD-13-012

	CLY + CRB (Carbonate-rich slate)
	CLY (Slate)
	CRB (Carbonate)
ORE	> 0.1 % Cu
cp	Chalcopyrite
bn	Bornite
cc	Chalcocite
py	Pyrite

Northing: 7819207.452
 Easting: 389512.862
 Elevation: 342.868 m
 Azimuth: 181.58°
 Dip: 45°
 Total length: 51 m

Depth from (m)	Depth to (m)	Thickness (m)	Lithology	Drill core description	Thin section (interval (m))	Mineralization in thin sections
3.9	4.06	0.16		Green-coloured rock.		
4.06	7.4	3.34		Dark slate with carbonate-rich veinlets and spots.		
7.4	10.75	3.35		Carbonate-rich slate.	NUS_027 (8.9-8.98)	cp (disseminated)
10.75	13.2	2.45	ORE	Slate-rich carbonate hosting mineralization of bornite and malachite.	NUS_028 (11-11.05)	cp (disseminated)
					NUS_029 (12.02-12.07)	bn + cc + py (disseminated and veins)
					NUS_030 (12.33-12.39)	cp + bn + cc + py (disseminated and veins)
					NUS_031 (13-13.07)	cp + bn + cc (disseminated and veins)
13.2	38	24.8		Slate with carbonate-rich veinlets and spots.	NUS_032 (17.95-18)	bn + cp + cc (disseminated and veins)

			Shortened log			
38	42	4		Green-grey coloured slate.		
42	46,6 (end of hole)	4.6		Dark slate with carbonate-rich veinlates and spots.		

Figure 38. The figure show the results from re-logging of the diamond drill core NUS-DD-13-012. Drill core samples observed in thin section were added to the drill core log. The drill core interval is shortened in the figure since the interval 13.2-38 m showed about the same lithology.

Drill core NUS-DD-13-003

	CLY + CRB (carbonate-rich slate)
	CLY (Slate)
	CRB (Carbonate)
Ore	> 0.1 % Cu
cp	Chalcopyrite
bn	bornite
cc	chalcocite
co	covellite

Northing: 7819335.465
 Easting: 389280.463
 Elevation: 312.378 m
 Azimuth: 208°
 Dip: 50°
 Total length: 161.8 m

Depth from (m)	Depth to (m)	Thickness (m)	Lithology	Drill core description	Thin section (interval (m))	Mineralization in thin sections
133.57	134.7	1.13		Dark slate with lighth-coloured layers parallel with the foliation. Carbonate-rich veinlets and spots.		
134.7	141.88	7.18		Slate with alteration traces.	NUS_021 (139.42-139.48)	No mineralization
141.88	146.13	4.25	Ore	Carbonate with slate-rich layers containing mineralization of chalcopyrite and bornite.	NUS_022 (141.93-142)	cp (disseminated and veins)
					NUS_023 (142.82-142.9)	cp (disseminated and veins)
					NUS_024 (144.62-144.7)	cp + bn + cc + co (disseminated and veins)
					NUS_025 (146-146.07)	bn + cp + cc + co (disseminated and veins)

145.13	152.2	7.07		Carbonate-rich slate.	NUS_026 (149.58-149.64)	cp (disseminated and veins)
152.2	154.35	2.15		Dark slate with carbonate-rich veinlets and spots.		
154.35	155.35	1		Dark slate with carbonate-rich veinlets and spots. Dacite clasts.		

Figure 39. The figure show the results from re-logging of the diamond drill core NUS-DD-13-003. Drill core samples observed in thin section were added to the drill core log.

Drill core NUS-DD-13-002

CLY + CRB (Slate rich in carbonate)
CLY (Slate)
QTZ (Thick quartz veins)
ORE > 0.1 % Cu
cp Chalcopyrite
bn Bornite
cc Chalcocite
py Pyrite

Northing: 7819181.78
 Easting: 389522.83
 Elevation: 344.846 m
 Azimuth: 180°
 Dip: 55°
 Total length: 154.15 m

Depth from (m)	Depth to (m)	Thickness (m)	Lithology	Description	Thin section (interval (m))	Mineralization in thin sections
55.02	58.55	3.53		Dark homogeneous slate with carbonate-rich veinlets and spots. Mineralization of pyrite in veins and as disseminated grains.	NUS_015 (57.84-57.9)	cp (disseminated)
58.55	62.45	3.9		Dark slate with carbonate-rich veinlets and spots, containing dissemination of pyrite.	NUS_016 (62.36-62.42)	cp (disseminated)
62.45	63.8	1.35	ORE	Carbonate-rich slate with mineralization of bornite and chalcopyrite.	NUS_017 (63.59-63.67)	cp + bn + cc + py (disseminated and veins)
63.8	64.7	0.9	ORE	Slate with carbonate-rich veinlets and spots. Mineralization of chalcopyrite and bornite in slate-rich layers.		
64.7	65.8	1.1	ORE	Grey-brown coloured slate with carbonate-rich veinlets and spots hosting mineralization of bornite and chalcopyrite.	NUS_018 (65.08-65.15)	cp + bn + cc + py (disseminated and veins)

65.8	74.9	9.1		Dark slate with carbonate-rich veinlets and spots hosting mineralization of chalcopyrite.	NUS_019 (65.9-65.97)	cp + py (disseminated and veins)
					NUS_020 (72.9-72.98)	cp + py (disseminated and veins)
74.9	75.58	0.68		Carbonate-rich slate.		
75.58	76	0.42		Dark slate with carbonate-rich veinlets and spots hosting mineralization of chalcopyrite.		
76	76.85	0.85		homogeneous quartzite.		
76.85	78.06	1.21		Green-coloured slate with carbonate-rich veinlets and spots hosting mineralization of chalcopyrite.		
78.06	78.88	0.82		Two thick veins of quartzite with carbonate, hosting mineralization of chalcopyrite.		
78.88	88	9.12		Green-coloured slate with carbonate and quartzite-rich veinlets hosting disseminated pyrite.		

Figure 40. The figure show the results from re-logging of the diamond drill core NUS-DD-13-002. Drill core samples observed in thin section were added to the drill core log.

4.3 Comparison of the Upper and the Lower mineralized horizon in thin section

4.3.1 Description of thin sections from drill core NUS-DD-13-004

The location of drill core NUS-DD-13-004 is shown in Figure 36. The drill core cut through the hanging wall slate, the Upper mineralized horizon, mid wall slate, Lower mineralized horizon, footwall slate and the tuffite (Figure 37). The Upper mineralized horizon contained mineralization of chalcopyrite, bornite, chalcocite and covellite. Chalcopyrite and bornite occurred in veins and as disseminated grains. Chalcocite formed myrmekitic inclusions in bornite and chalcopyrite, and occurred in association to covellite at rims in grains of bornite and chalcopyrite. The vertical zonation from top of the Upper mineralized horizon was chalcopyrite, bornite, chalcocite, covellite. Within deeper sections, chalcopyrite was the dominating sulphide. The Lower mineralized horizon contained mineralization of chalcopyrite, bornite, chalcocite, covellite and pyrite. Chalcopyrite and bornite was the dominating sulphide, while only one grain of pyrite was observed. In the upper section of the Lower mineralized horizon, chalcopyrite form the mineralization. With increasing depth, bornite, chalcopyrite, chalcocite and covellite was the dominating sulphides. In the lower sections of the drill core, chalcopyrite, bornite, chalcocite, pyrite and covellite was dominating. In the lowest part of the mineralized horizon, chalcopyrite dominated. An example of the host rock and mineralization in the Upper mineralized horizon is shown in Figure 41 and Figure 42. An example of host rock and mineralization in the Lower mineralized horizon is shown in Figure 43.

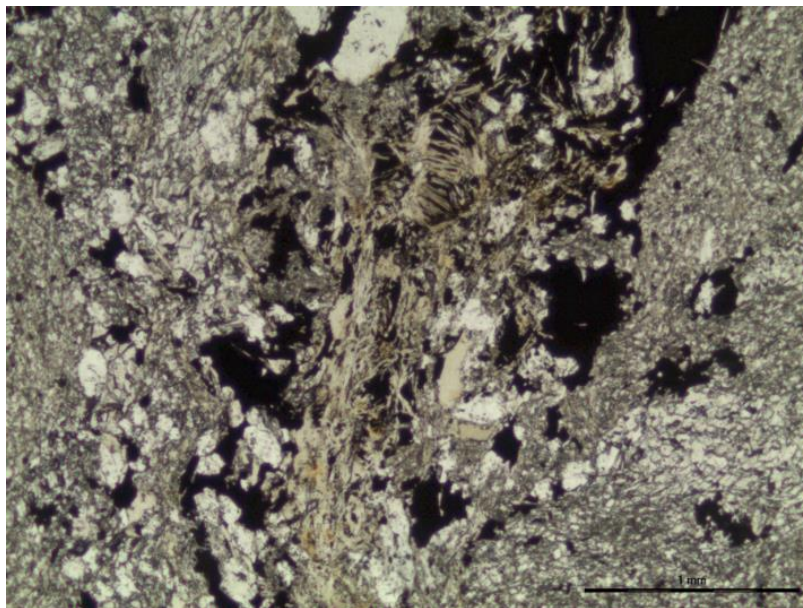


Figure 41. Photomicrograph of thin section NUS_005 in drill core NUS-DD-13-004, in polarized light. It shows the Upper mineralized horizon. The matrix consisted of fine-grained dolomite and mica. Chlorite and biotite was located around veins of sulphides. Dark spots represents opaque sulphide minerals. Photo: Kjersti Moen.

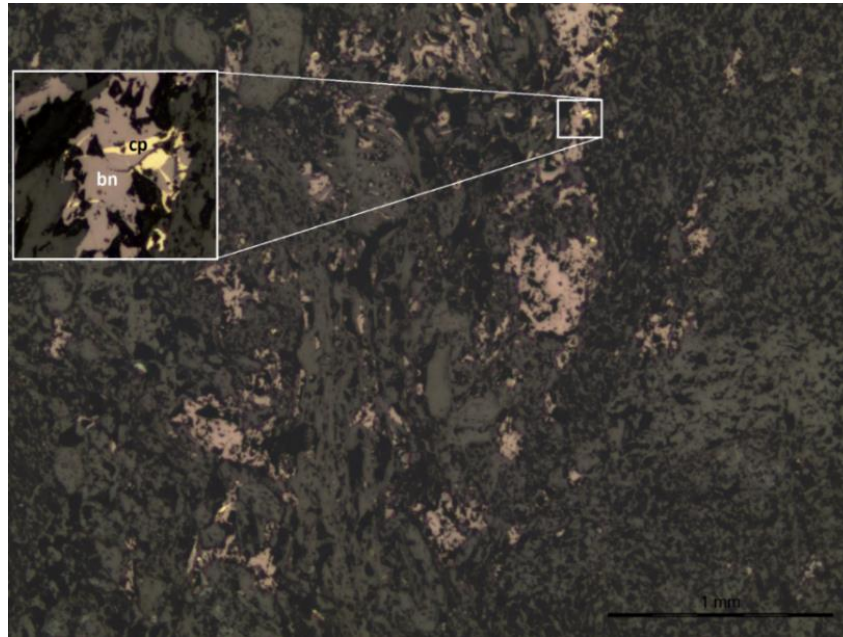


Figure 42. Photomicrograph of thin section NUS_005 in drill core NUS-DD-13-004, in reflected light. It shows the Upper mineralized horizon, with mineralization of bornite and chalcopyrite. The picture represents the same area shown in Figure 41. Marked area shows mineralization of bornite (bn) and chalcopyrite (cp). The mineralization occurred in veins and as disseminated grains. Photo: Kjersti Moen.

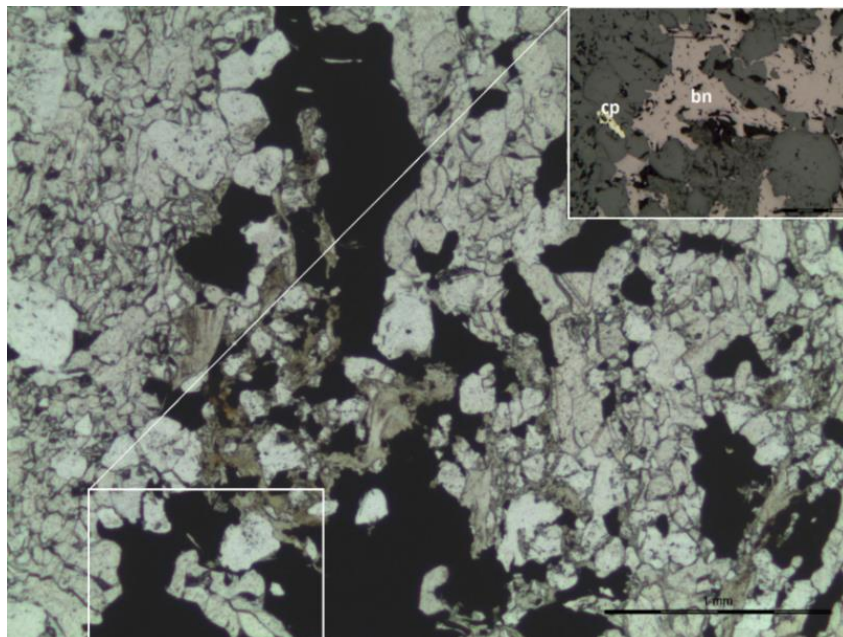


Figure 43. Photomicrograph of thin section NUS_011 in drill core NUS-DD-13-004, in plane polarised light. It shows the Lower mineralized horizon in plane polarised light. Veins were dominated by calcite, with mineralization of biotite and chlorite. The area marked by frame in reflected light, shows the mineralization of bornite (bn) and chalcopyrite (cp). Photo: Kjersti Moen.

4.3.2 Thin sections from drill core NUS-DD-13-002

The location of drill core NUS-DD-13-002 is shown in Figure 36. NUS-DD-13-002 cuts through what was interpreted as hanging wall slate, lower mineralized horizon and the footwall slate, Figure 40. The lithology of the metasedimentary rocks is described in Appendix III. The lower mineralized horizon contained mineralisation of bornite, chalcopyrite, chalcocite and covellite. Bornite and chalcopyrite is the dominating sulphides, and chalcocite and covellite occurs in association with bornite and chalcopyrite (Figure 44).

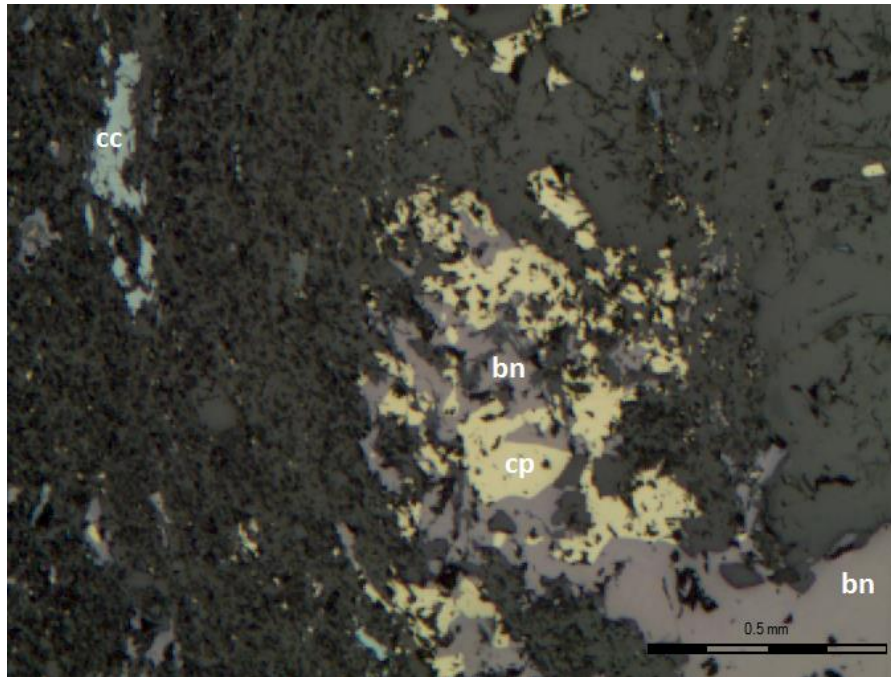


Figure 44. Photomicrograph of thin section NUS_018 in drill core NUS-DD-13-002, in reflected light. It shows an example of mineralization in the Lower mineralized horizon. Bornite (bn), chalcopyrite (cp) and chalcocite (cc) occurred as disseminated grains and in veins. Photo: Kjersti Moen.

4.3.3 Thin sections from drill core NUS-DD-13-012

The location of drill core NUS-DD-13-012 is shown in Figure 36. The drill core cut through what was interpreted as hanging wall slate, Upper mineralized horizon and the footwall slate, Figure 38. Lithology of the metasedimentary rocks is described in Appendix III. The Upper mineralized horizon contained mineralization of bornite, chalcopyrite, chalcocite and covellite. Bornite and chalcopyrite was the dominating sulphide and occurred in veins and as disseminated grains, Figure 45.

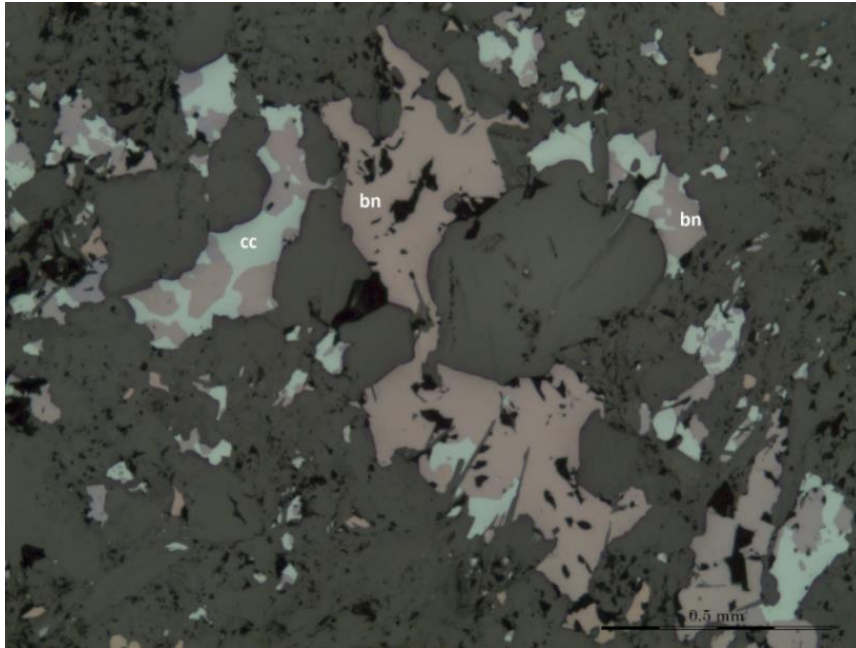


Figure 45. Photomicrograph of thin section NUS_025 in drill core NUS-DD-13-012, in reflected light. It shows an example of mineralization in the Upper mineralized horizon. Bornite (bn) and chalcocite (cc) occurred as disseminated grains and in veins. Photo: Kjersti Moen.

4.3.4 Thin sections from drill core NUS-DD-13-003

The location of drill core NUS-DD-13-003 is shown in Figure 36. The drill core cut through what was interpreted as hanging wall slate, Lower mineralized horizon and the footwall slate, Figure 39. Lithology of the metasedimentary rocks is described in Appendix III. The Lower mineralized horizon contained mineralization of bornite, chalcopyrite and chalcocite. Bornite and chalcocite was the dominating sulphide. Bornite, chalcopyrite and chalcocite occurred in veins and as disseminated grains. Chalcocite were associated with grains of bornite (Figure 46).



Figure 46. Photomicrograph of thin section NUS_031 in drill core NUS-DD-13-003, in reflected light. It shows an example of mineralization in the Lower mineralized horizon. Bornite (bn), chalcopyrite (cp) and chalcocite (cc) occurred as disseminated grains and in veins. Chalcopyrite (cp) and chalcocite (cc) formed inclusions in the bornite grain (bn). Photo: Kjersti Moen.

4.3.5 Comparison within and of the Upper- and Lower mineralized horizon

A comparison between all the studied thin sections from the Upper- and Lower mineralized horizons, is shown in Table 4. The comparison of the mineralization along the Upper mineralized horizon, showed similarities between thin sections from drill core NUS-DD-13-012 and NUS-DD-13-004 (Table 4). However, drill core NUS-DD-13-012 contained a higher concentration of chalcocite, and showed a lower concentration of chalcopyrite, compared to NUS-DD-13-004. The comparison of the mineralization along the Lower mineralized horizon, indicated similarities between thin sections from drill core NUS-DD-13-002, NUS-DD-13-003 and NUS-DD-13-004 (Table 4). However, drill core NUS-DD-13-003 contained a higher amount of chalcocite, and covellite was absent. Grains of bornite in drill core NUS-DD-13-003 appeared with a dark-purple colour and with a light-purple colour.

The comparison of thin sections from the Upper- and the Lower mineralized horizon, showed a high degree of similarity with the thin sections from drill core NUS-DD-13-012 and NUS-DD-13-003. Pyrite were only observed in the Upper mineralized horizon.

Table 4. Comparison of the Upper- and Lower mineralized horizon. Drill cores, thin section and mineralization in given thin sections is shown. Blue-coloured part represents observations in the Upper mineralized horizon, and white-coloured part represents observations in the Lower mineralized horizon. cp = chalcopyrite, bn = bornite, cc = chalcocite, co =covellite, py = pyrite.

Drill core	NUS-DD-13-012				
Thin section	NUS_029	NUS_029	NUS_030	NUS_031	NUS_032
Mineralization	cp	bn, cp, cc, co	cp, bn, cc, co	cp, bn, cc, py	cp, bn, cc
Drill core	NUS-DD-13-004				
Thin section	NUS_003	NUS_005	NUS_006	NUS_007	
Mineralization	cp, bn	cp, bn, cc, co	cp, bn	cp	
Drill core	NUS-DD-13-002				
Thin section	NUS_016	NUS_017	NUS_018	NUS_019	NUS_020
Mineralization	cp	bn, cp, cc, co	cp, bn	cp, bn	cp
Drill core	NUS-DD-13-003				
Thin section	NUS_022	NUS_023	NUS_024	NUS_025	NUS_026
Mineralization	cp	cp, bn	bn, cc	bn, cc	cp, cc
Drill core	NUS-DD-013-004				
Thin section	NUS_010	NUS_011	NUS_012	NUS_013	
Mineralization	cp	bn, cp, cc, co	bn, cp, cc, co	cp	

4.4 Micro probe analysis

4.4.1 Results of electron probe micro-analysis of minerals (mass oxide)

Minerals were analysed by WDS analysis in an electron micro-analyzer to detect the mineral composition of unknown minerals and the composition of the matrix. Results from WDS analysis is given in Table 6-7, Figure 47-56, Table D75 and Table D76.

The mineral grains in drill core NUS-DD-13-004 (No. 2-4), Figure 47 and Figure 48, indicated a mineral of biotite-phlogophite concentration (Table 5).

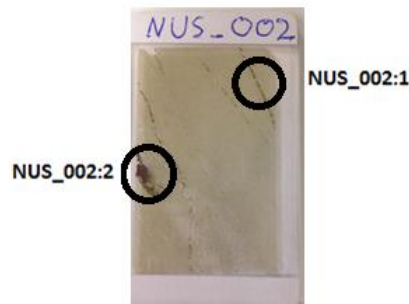


Figure 47. Picture of thin section NUS_002. Black circle mark the analyzed area (area of thin section, NUS_002:1 and NUS_002:2). Photo: Kjersti Moen.



Figure 48. Picture of the hang wall slate in thin section NUS_002, in plan polarized light. White circles mark the selected spot in the matrix (NUS_002:1.1, No. 5-12) and mineral grains (NUS_002:1.2, No.2-4). Photo: Kjersti Moen.

WDS analysis of the matrix in the hang wall slate in drill core NUS-DD-13-004 (No. 5-12 in Table D75) and Figure 47 and Figure 48, indicated minerals of plagioclase, chlorite and alkali feldspar composition (Table 5). A scanning map shows the point analysis of the matrix in the hang wall slate (Figure D119).

WDS analysis of a mineral grains in drill core NUS-DD-13-004 (No. 13-15 in Table D75), Figure 47 and Figure 49, indicated a mineral of chloritic composition (Table 5).



Figure 49. Picture of hang wall slate in thin section NUS_002, plan polarized light. Circles mark the analysed spot of minerals (selected spot, NUS_002:2.1, No. 13-15, and NUS_002:2.2, No. 16-18). Photo: Kjersti Moen.

WDS analysis of minerals in the hang wall slate in NUS-DD-13-004 (No. 16-18 in Table D75 and Table D76), Figure 47 and Figure 49, indicated a mineral composition of chlorite (Table 5). This mineral was classified as a biotite in the light microscope.

WDS analysis of a mineral in the Upper mineralized horizon in NUS-DD-13-004 (No. 25-27 in Table D75 and Table D76), Figure 50 and Figure 51, indicated a mineral with the composition of sphene (titanite), (Table 5).

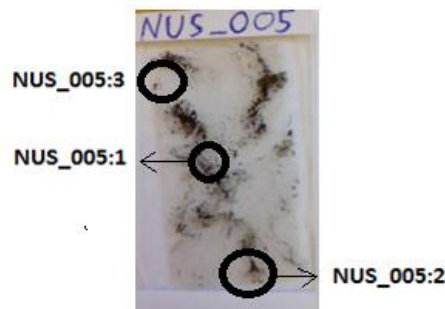


Figure 50. Sketch of thin section NUS_005. Black circle mark the area analysed (area of thin section, NUS_005:1, NUA_005:2 and NUS_005:3). Photo: Kjersti Moen.

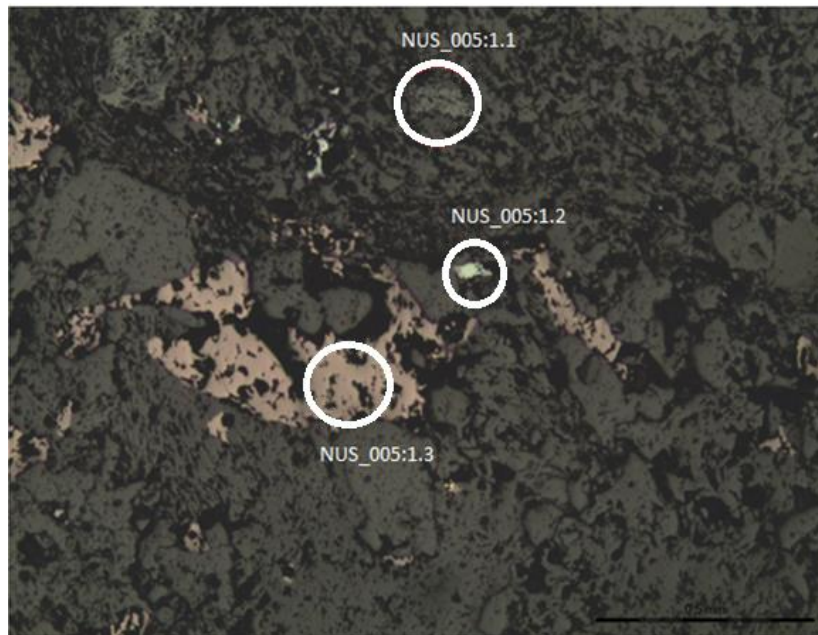


Figure 51. Picture of the Upper mineralized horizon in thin section NUS_005, reflected light. White circles mark the analysed spot of minerals (selected spot, NUS_005:1.1, No. 25-27). The two other marked areas is described later in this section. Photo: Kjersti Moen.

WDS analysis of a mineral in the hang wall slate in NUS-DD-13-004 (No. 34-36 in Table D76), Figure 50 and Figure 52, indicated a mineral of chloritic composition (Table 5).

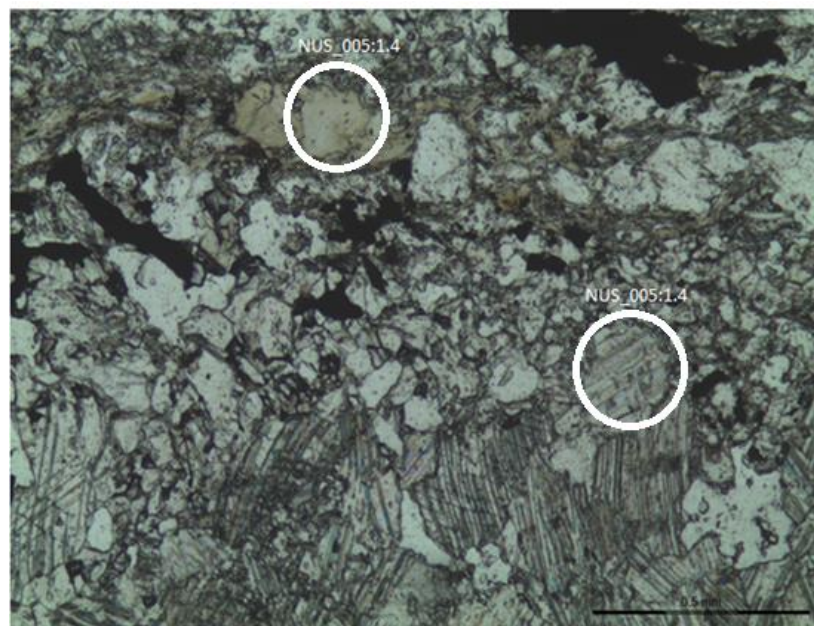


Figure 52. Picture of the Upper mineralized horizon in thin section NUS_005, plan polarized light. White circles mark the analysed spot of minerals (selected spot, NUS_005:1.4, No.34-36, and NUS_005:1.5, No.37-39). Photo: Kjersti Moen.

WDS analysis of mineral grains in the Upper mineralized horizon in NUS-DD-13-004 (No. 37-39 in Table D76), Figure 50 and Figure 52, indicated a mineral of calcitic composition (Table 5).

The micro probe analysis of the matrix in the Upper mineralized horizon in drill core NUS-DD-13-004 (Figure 50 and Figure 53) is given in Table 6 and Table 7. The qualitative WDS analysis indicated a feldspar-rich matrix (No. 43-49 and 51) and the occurrence of a calcite grain in analyse number 50 (Table 5). Analyse number 43-51 is shown in a scatter map (Figure D120) and in scanning map (Figure D121), and indicated the occurrence of calcite in analyse number 50.

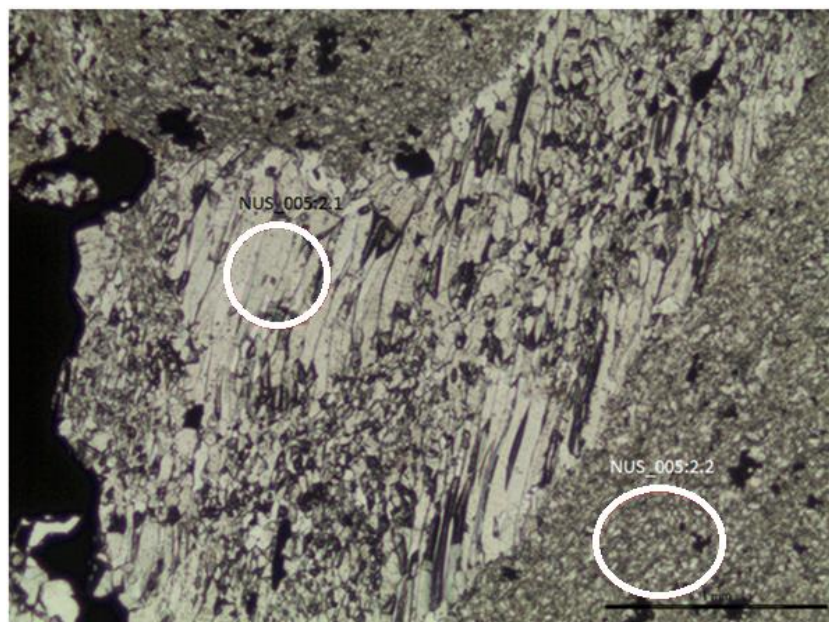


Figure 53. Picture of the Upper mineralized horizon in thin section NUS_005, plan polarized light. White circles mark the analysed spot of minerals (selected spot, NUS_005:2.1, No.40-42, and NUS_005:2.2, No.43-49 and 51). Photo: Kjersti Moen.



Figure 54. Picture of the Upper mineralized horizon in thin section NUS_005, plan polarized light. White circle mark the analysed spot of minerals (selected spot, NUS_005:3.1, No.52-54). Photo: Kjersti Moen.

WDS analysis of a mineral grains in the footwall slate in drill core NUS-DD-13-004 (No. 58-60 in Table D76), Figure 55 and Figure 56, indicated a mineral of chloritic composition (Table 5).

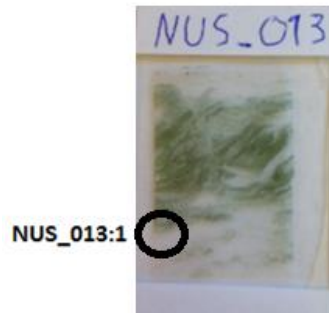


Figure 55. Sketch of thin section NUS_013. Black circle mark the area analysed (area of thin section, NUS_013:1.). Photo: Kjersti Moen.

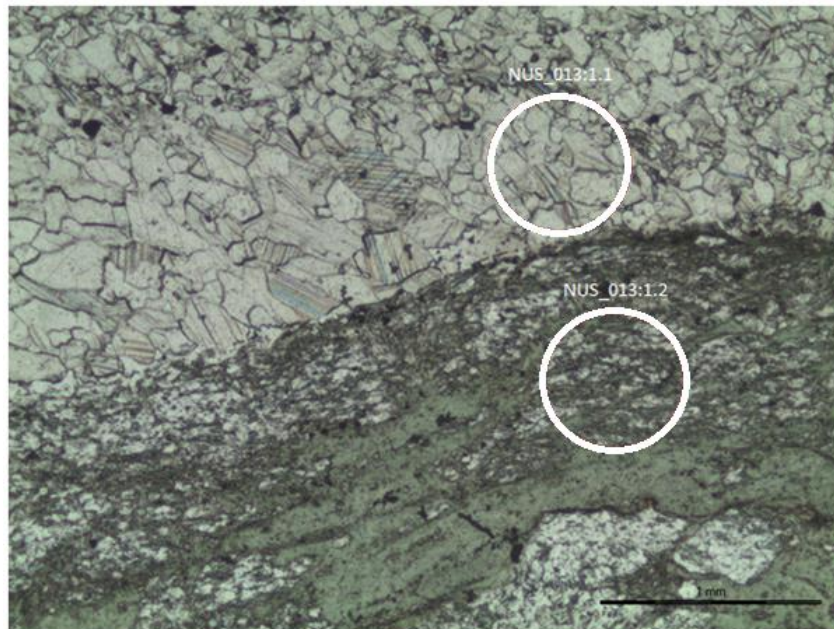


Figure 56. Picture of the Upper mineralized horizon in thin section NUS_013, plan polarized light. White circles mark the analysed spot of minerals (selected spot, NUS_013:1.1, No.55-57, and NUS_013:1.2, No.58-60). Photo: Kjersti Moen.

WDS analysis of carbonate grains in the Upper mineralized horizon and in the footwall slate in drill core NUS-DD-13-004 is given in Table 7 (No. 40-41, Figure 53, No. 52-54, Figure 54, and No. 55-57, Figure 56). The analysis indicated carbonate-minerals of calcitic composition (Table 5).

Table 5. Table shows the predicted mineral composition of the analysed minerals by WDS.

No.	Mineral	Formula
2-4	Biotite-phlogopite	$K_2(Mg, Fe^{2+})_{6-4}(Fe^{3+}, Al, Ti)_{0-2}[Si_{6-5}Al_{2-3}O_{20}](OH, F)_4$
5	Plagiocalse	Na $[AlSi_3O_8]$ – Ca $[Al_2Si_2O_8]$
6-9	Chlorite	$(Mg, Fe^{2+}, Fe^{3+}, Mn, Al)^{12}[(Si, Al)_8O_{20}](OH)_{16}$
10-12	Alkali feldspar	$[KAlSi_3O_8-NaAlSi_3O_8]$
13-15	Chlorite	$(Mg, Fe^{2+}, Fe^{3+}, Mn, Al)^{12}[(Si, Al)_8O_{20}](OH)_{16}$
16-18	Chlorite	$(Mg, Fe^{2+}, Fe^{3+}, Mn, Al)^{12}[(Si, Al)_8O_{20}](OH)_{16}$
25-27	Sphene (titanite)	Ca Ti $[SiO_4]$ (O, OH, F)
34-36	Chlorite	$(Mg, Fe^{2+}, Fe^{3+}, Mn, Al)^{12}[(Si, Al)_8O_{20}](OH)_{16}$
37-39	Calcite	$CaCO_3$
43-49	Alkali feldspar	$[KAlSi_3O_8-NaAlSi_3O_8]$
51		
50	Calcite	$CaCO_3$
40-41	Calcite	$CaCO_3$
52-54		
55-57		
58-60	Chlorite	$(Mg, Fe^{2+}, Fe^{3+}, Mn, Al)^{12}[(Si, Al)_8O_{20}](OH)_{16}$

Table 6. Results from WDS analysis (analyse number 43-51, thin section NUS_005, area NUS_005:2.2, point NUS_005:2.2.1-NUS_005:2.2.9) performed in micro probe-analyser. The element-concentrations is give in Wt %.

No.	Al ₂ O ₃	F	K ₂ O	Cr ₂ O ₃	SiO ₂	Na ₂ O	CaO	MnO	MgO	TiO ₂	FeO	SrO	Total	Comment
43	17.923	0.008	14.996	0	65.49	0.36	0.072	0.032	0.03	0.053	0.104	0	99.065	NUS-005:2. 2.1
44	17.715	0.016	15.496	0.024	66.066	0.393	0.151	0.019	0.055	0	0.086	0	100.014	NUS-005:2. 2.2
45	17.765	0	11.706	0	67.974	1.333	0.079	0	0.01	0.027	0.064	0	98.958	NUS-005:2. 2.3
46	18.49	0	0.225	0	70.877	8.368	0.325	0	0.041	0	0.052	0	98.378	NUS-005:2. 2.4
47	0.593	0	0.16	0.015	98.468	0.196	0.064	0.033	0.04	0	0.037	0.024	99.63	NUS-005:2. 2.5
48	18.287	0.026	0.18	0	70.168	8.013	0.434	0.02	0.02	0.006	0.022	0	97.165	NUS-005:2. 2.6
49	18.469	0	0.171	0.009	70.321	7.686	0.416	0.025	0.003	0	0.038	0	97.138	NUS-005:2. 2.7
50	0.475	0	0.157	0	1.315	0.185	55.032	2.127	0.333	0	0.296	0	59.92	NUS-005:2. 2.8
51	17.884	0.004	15.556	0	66.555	0.213	0.12	0.04	0.078	0	0.048	0	100.496	NUS-005:2. 2.9

Table 7. Results from WDS analysis in analyse number 40-42 and 52-57 in thin section NUS_005 and NUS_013 performed in micro probe-analyser (Figure 53 and Figure 54 and Figure 56). The element-concentrations is give in Wt %.

No.	Al ₂ O ₃	F	K ₂ O	Cr ₂ O ₃	SiO ₂	Na ₂ O	CaO	MnO	MgO	TiO ₂	FeO	SrO	Total	Comment
40	0.041	0.015	0	0.022	0	0	53.387	1.719	0.298	0	0.229	0	55.705	NUS-005:2. 1.1
41	0.098	0.081	0.013	0.003	0	0.004	52.109	1.558	0.269	0	0.191	0	54.292	NUS-005:2. 1.2
42	0	0	0	0	0	0	56.522	2.401	0.454	0	0.247	0	59.624	NUS-005:2. 1.3
52	0.008	0.03	0	0.015	0	0	56.538	1.773	0.378	0	0.199	0	58.928	NUS-005:3. 1.1
53	0	0.005	0	0	0	0.023	56.807	1.613	0.425	0	0.198	0	59.069	NUS-005:3. 1.2
54	0	0	0.008	0.012	0	0	55.112	1.539	0.417	0	0.175	0	57.263	NUS-005:3. 1.3
55	0	0	0	0.044	0	0	56.257	1.392	0.391	0.01	0.755	0	58.849	NUS-013:1. 1.1
56	0	0	0	0.018	0	0.012	57.828	1.19	0.396	0.012	0.709	0	60.165	NUS-013:1. 1.2
57	0.027	0	0	0.001	0	0.027	55.993	1.043	0.21	0.013	0.504	0	57.818	NUS-013:1. 1.3

4.5 Results of electron probe micro-analysis of sulphides (mass percent)

The results from the WDS analysis is given in Table 8, Table 9, Table 10, Table 11, Table 13 and Table 14.

4.5.1 Drill core NUS-DD-13-004 (Upper mineralized horizon)

The WDS analysis in micro probe-analysis in drill core NUS-DD-13-004 in thin section NUS_002, indicated mineralization of bornite and chalcopyrite (No. 19-24, Figure 57 and Figure 58, Table 8).

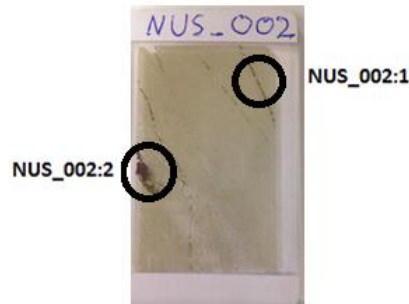


Figure 57. Picture of thin section NUS_002. Black circle mark the area analysed (area of thin section, NUS_002:1 and NUS_002:2). Photo: Kjersti Moen.

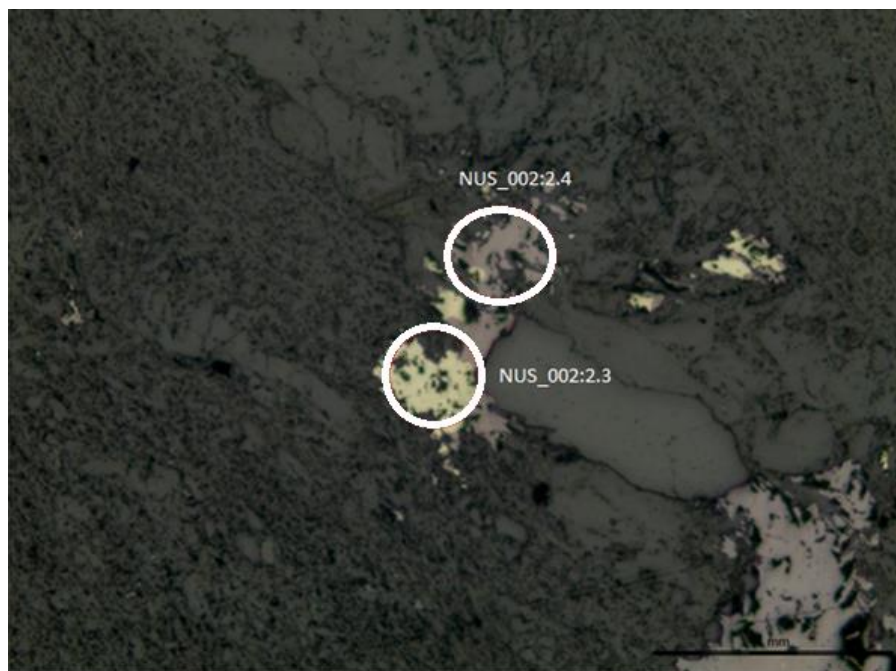


Figure 58. Picture of hang wall slate in thin section NUS_002, reflected light. White circles mark the analysed spot of minerals (selected spot, NUS_002:2.3, No. 19-21, and NUS_002:2.4, No. 22-24). Photo: Kjersti Moen.

Analysis of thin section NUS_005 (Figure 59 and Figure 60, Table 9), indicated mineralization of bornite (No.30-33) and chalcocite (No.28-29). The chalcocite contained the highest concentration of gold (Au) and silver (Ag), except of the relative high concentrations of gold in the bornite (0.562%, No. 33). Palladium occurred with a very low concentration in the copper sulphides (0-0.084 %) and platinum was not detected.

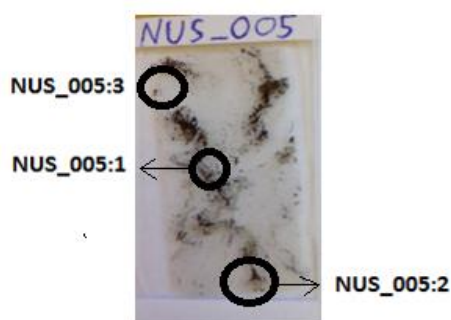


Figure 59. Sketch of thin section NUS_005. Black circle mark the area analysed (area of thin section, NUS_005:1, NUA_005:2 and NUS_005:3). Photo: Kjersti Moen.

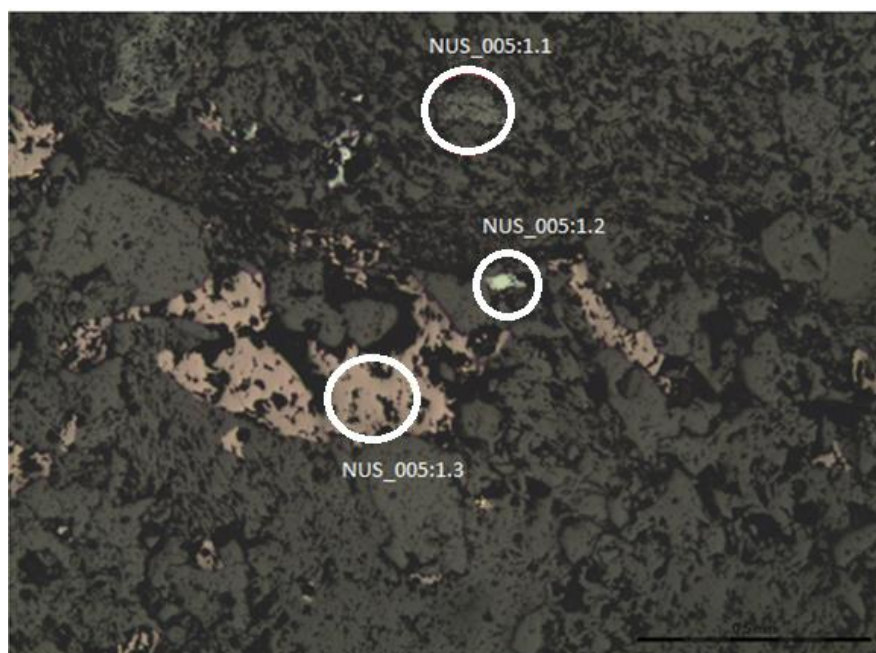


Figure 60. Picture of the Upper mineralized horizon in thin section NUS_005, reflected light. White circles mark the analysed spot of minerals (selected spot, NUS_005:1.2, No. 28-29, and NUS_005:1.3, No. 30-33). Photo: Kjersti Moen.

4.5.2 Drill core NUS-DD-13-004 (Lower mineralized horizon)

The WDS analysis in micro probe-analysis in drill core NUS-DD-13-004 in thin section NUS-011 (Figure 61, Figure 62, Figure 63 and Figure 64), indicated mineralization of bornite (No.76-81, 88-93 and 97-99), chalcopyrite (No.85-87) and chalcocite (No. 82-84 and 94-96),

Table 10. The analysis of bornite showed a varying content of silver and a grain of bornite (No.91.93) showed a concentration of 1.926-2.141 mass percent Ag. Gold and platinum was undetected. The analysis showed low concentration of palladium (0-0.013 %) and mercury (0-0.562 %). The analysis of chalcopyrite (No.85-87) contained value of iron (11.515-11.654 %), sulphur (25.541-25.744 %) and copper (62.019-3.148 %), and indicated a composition of bornite. Analysis of what was classified as chalcopyrite in No.82-84 and 94-96, indicated a composition of bornite. A scanning map of point NUS_011:3.1 indicated that the grain of chalcocite contained silver-rich lamellas and minor amount of gold and mercury (Figure D122 and Figure D123).

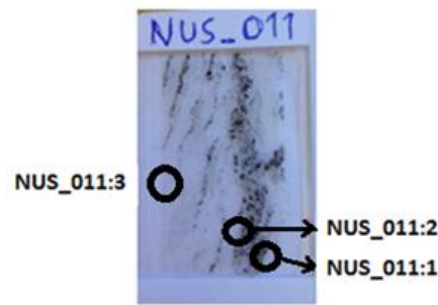


Figure 61. Picture of thin section NUS_011 in the Lower mineralized horizon in drill core NUS-DD-13-004. Black circles mark the areas analysed in micro probe-analyser (NUS_011:1, NUS_011:2, NUS_011:3). Photomicrographs show the analysed spots in each area (Area NUS_011:1: Figure 63, area NUS_011:2: Figure 62 and area NUS_011:3: Figure 64). Photo: Kjersti Moen.

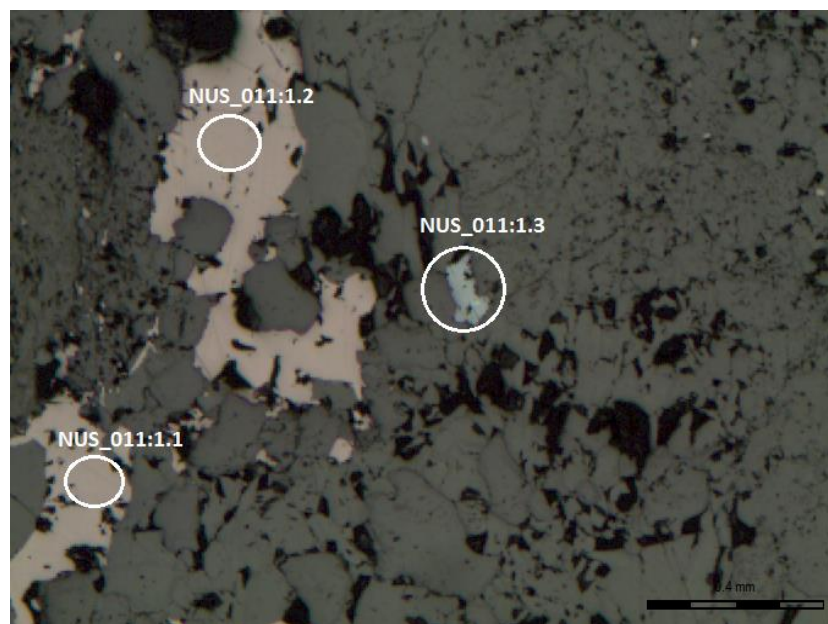


Figure 62. Photomicrograph show analyse area NUS_011:1 (Figure 61) in thin section NUS_011 in the Lower mineralized horizon in drill core NUS-DD-13-004. White circles mark the analysed sulphide grains (NUS_011:1.1, NO.76-78, NUS_011:1.2, No. 79-81, NUS_011:1.3, No.82-84). Photo: Kjersti Moen.

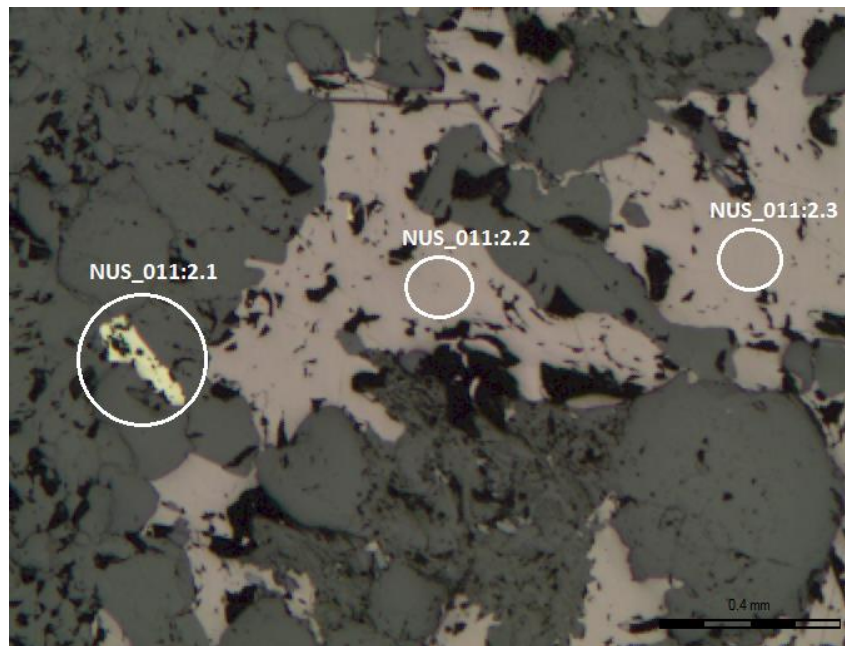


Figure 63. Photomicrograph show analyse area NUS_011:1 (Figure 61) in thin section NUS_011 in the lower mineralized horizon in drill core NUS-DD-13-004. White circles mark the analysed sulphide grains (NUS_011:2.1, No.85-87, NUS_011:2.2, No. 88-90, NUS_011:2.3, No.91-93). Photo: Kjersti Moen.

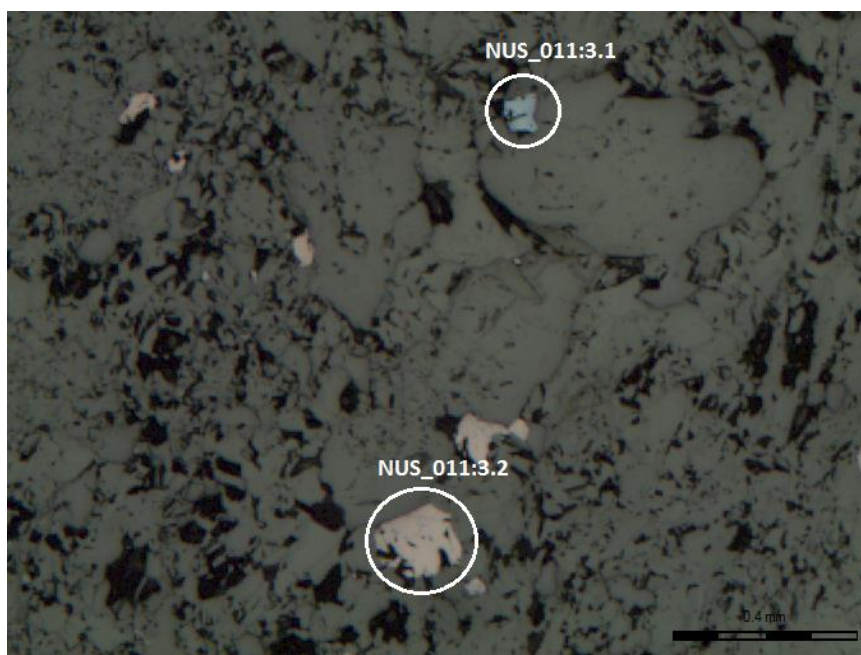


Figure 64. Photomicrograph show analyse area NUS_011:3 (Figure 61) in thin section NUS_011 in the Lower mineralized horizon in drill core NUS-DD-13-004. White circles mark the analysed sulphide grains (NUS_011:3.1, No. 94-96, and NUS_011:3.2, No. 97-99). Photo: Kjersti Moen.

4.5.3 Drill core NUS-DD-13-002 (Lower mineralized horizon)

The WDS analysis in micro probe-analysis in drill core NUS-DD-13-002 in thin section NUS-018 (Figure 65, Figure 66, Figure 67 and Figure 68), Table 10, indicated the mineralization of bornite (No.106-111, 121-123 and 127-129), chalcopyrite (No.103-105, 112-117, 124-126 and 130-132) and chalcocite (100-102 and 118-120). EDS measurements indicated disseminated grains of lead-composition in and surrounding grains of bornite. A scanning map of the mineralized vein in area NUS_018:3, showed two types of sulphides (chalcopyrite and bornite), Figure D124 and Figure D125. Mineral grains with a high density (heavy metals), was detected in the micro probe survey by EDS, and indicated a high concentration of molybden. Disseminated grains of lead was detected in association to grains of bornite.

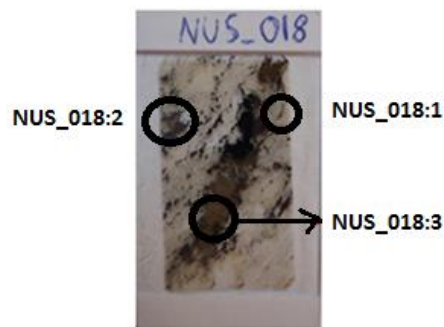


Figure 65. Picture of thin section NUS_018 in the Lower mineralized horizon in drill core NUS-DD-13-002. Black circles mark the areas analysed in micro probe-analyser (NUS_018:1, NUS_018:2, NUS_018:3). Photomicrographs show the analysed spots in each area (Area NUS_018:1: Figure 66, area NUS_018:2: Figure 67 and area NUS_018:3: Figure 68). Photo: Kjersti Moen.

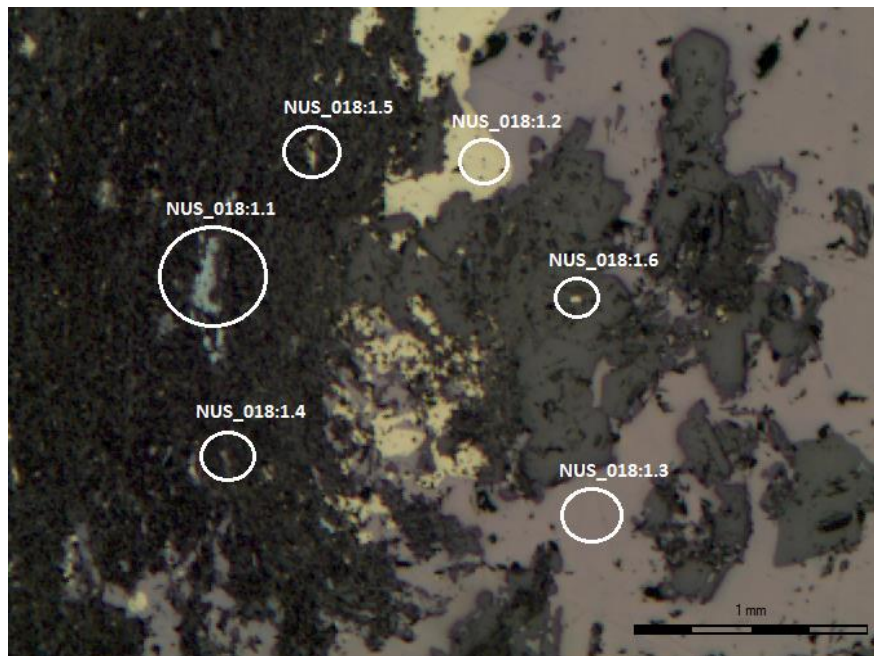


Figure 66. Photomicrograph show analyse area NUS_018:1 (Figure 65) in thin section NUS_018 in the Lower mineralized horizon in drill core NUS-DD-13-002. White circles mark the analysed sulphide grains (NUS_018:1.1, No. 100-102, NUS_018:1.2, No. 103-105, NUS_018:1.3, No. 106-108, NUS_018:1.4, No. 109-111, NUS_018:1.5, No. 112-114). Photo: Kjersti Moen.

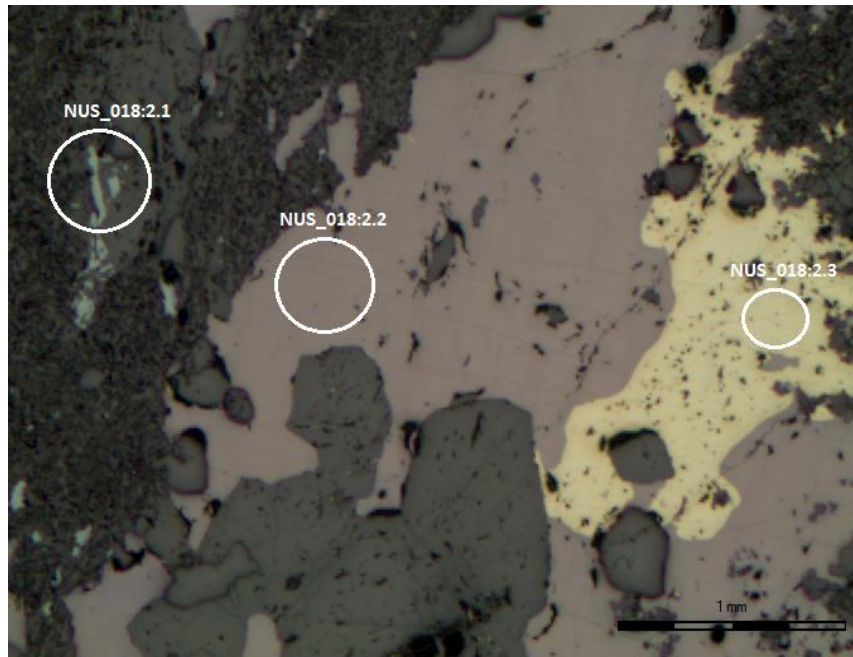


Figure 67. Photomicrograph show analyse area NUS_018:2 (Figure 65) in thin section NUS_018 in the Lower mineralized horizon in drill core NUS-DD-13-002. White circles mark the analysed sulphide grains (NUS_018:2.1, No. 118-120, NUS_018:2.2, No. 121-123, and NUS_018:2.3, No. 124-126). Photo: Kjersti Moen.

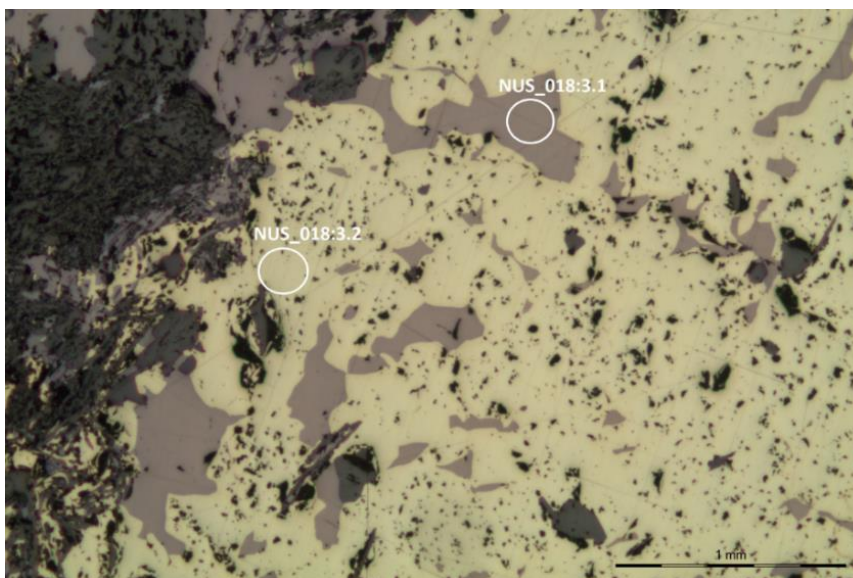


Figure 68. Photomicrograph show analyse area NUS_018:3 (Figure 65) in thin section NUS_018 in the Lower mineralized horizon in drill core NUS-DD-13-002. White circles mark the analysed sulphide grains (NUS_018:3.1, No. 127-129, and NUS_018:3.2, No. 130-132). Photo: Kjersti Moen.

4.5.4 Drill core NUS-DD-13-003 (Lower mineralized horizon)

The WDS analysis in micro probe-analysis in drill core NUS-DD-13-003 in thin section NUS-025 (Figure 69, Figure 70 and Figure 71, Table 10), indicated mineralization of bornite (No. 136-138 and 142-147) and chalcocite (No. 133-135, 139-141 and 148-153). Grains of bornite was observed with a light purple colour (No. 136-138) and with a dark purple colour (No. 142-147). The analysis showed no difference in the element concentration between bornite grains with the different colour. Analysis of chalcocite gave a high concentration of copper (78.458-79.752 %) and silver (0.277-0.483 %). A scanning map was taken of the disseminated mineralization of bornite and chalcocite in point NUS_025:1.3 and NUS_025:1.4, shown in Figure 70 (Figure D126 and Figure D127). No significant differences was detected in the content of silver, gold, mercury or zinc, in the grains of bornite and chalcocite.

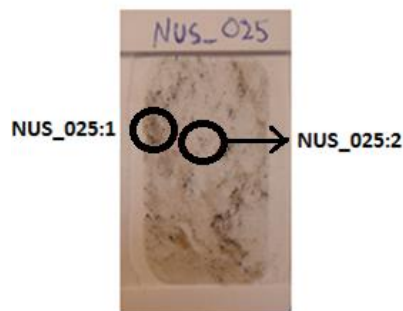


Figure 69. Picture of thin section NUS_025 in the Lower mineralized horizon in drill core NUS-DD-13-003. Black circles mark the areas analysed in micro probe-analyser (NUS_025:1 and NUS_025:2). Photomicrographs show the analysed spots in each area (Area NUS_025:1: Figure 70 and area NUS_025:2: Figure 71). Photo: Kjersti Moen.

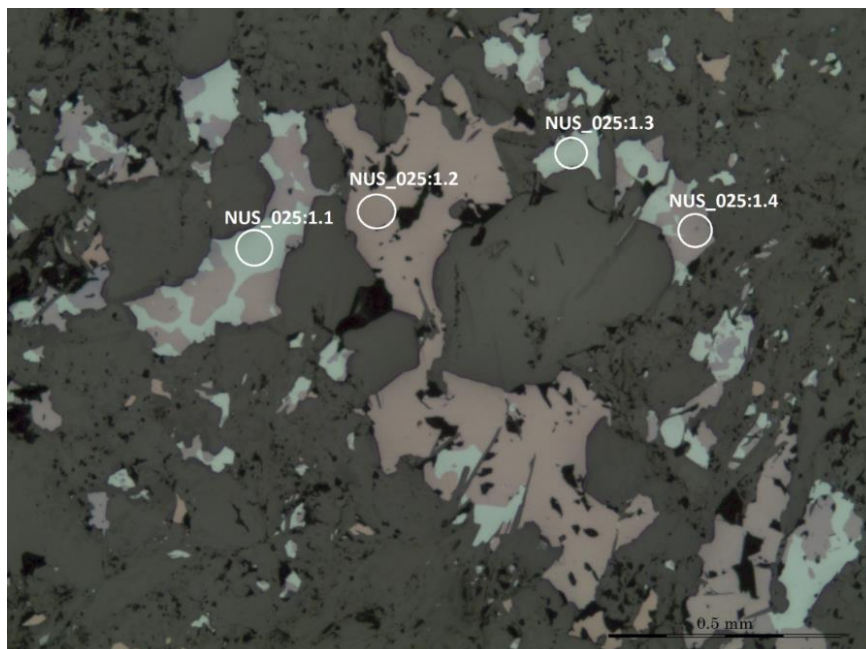


Figure 70. Photomicrograph show analyse area NUS_025:1 (Figure 69) in thin section NUS_025 in the Lower mineralized horizon in drill core NUS-DD-13-003. White circles mark the analysed sulphide grains (NUS_025:1.1, No. 133-135, and NUS_025:1.2, No. 136-138). Photo: Kjersti Moen.

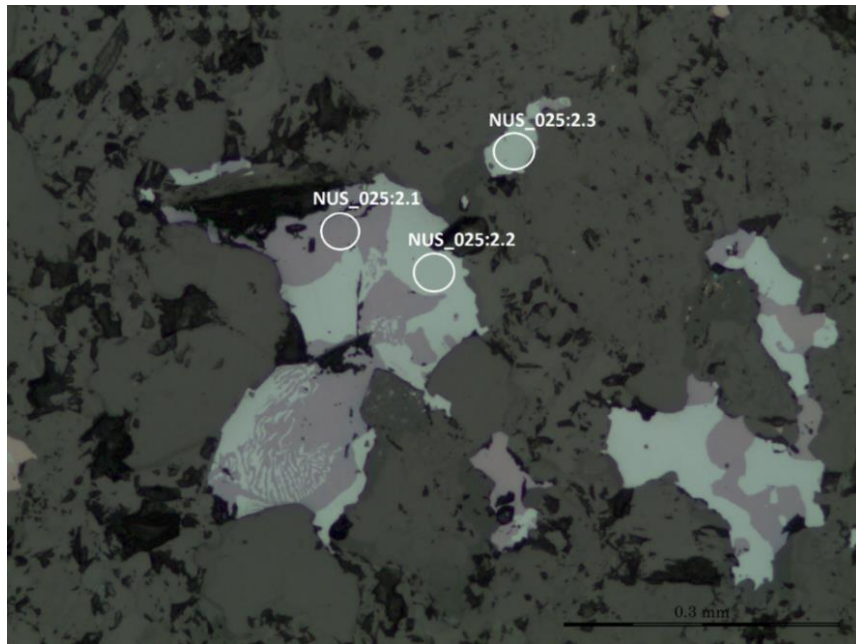


Figure 71. Photomicrograph show analyse area NUS_025:2 (Figure 69) in thin section NUS_025 in the Lower mineralized horizon in drill core NUS-DD-13-003. White circles mark the analysed sulphide grains (NUS_025:2.1, No. 145-147, NUS_025:2.2, No. 148-159, and NUS_025:2.3, 151-153). Photo: Kjersti Moen.

4.5.5 Drill core NUS-DD-13-012 (Upper mineralized horizon)

The WDS analysis in micro probe-analysis in drill core NUS-DD-13-012 in thin section NUS-031 (Figure 72, Figure 73 and Figure 74, Table 10), indicated mineralization of bornite (No. 154-156), chalcopyrite (No. 164-169) and chalcocite (No. 157-159). A sulphide mineral, undetected in the polarized microscope, indicated an unknown bismuth-rich sulphide. EDS measurement of the sulphides indicated concentration of molybden, sulphur, copper and lead.

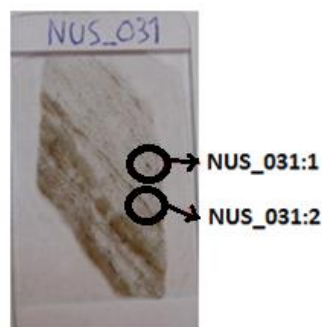


Figure 72. Picture of thin section NUS_031 in the Upper mineralized horizon in drill core NUS-DD-13-012. Black circles mark the areas analysed in micro probe-analyser (NUS_031:1 and NUS_031:2). Photomicrographs show the analysed spots in each area (Area NUS_031:1 in Figure 73 and area NUS_031:2 in Figure 74). Photo: Kjersti Moen.

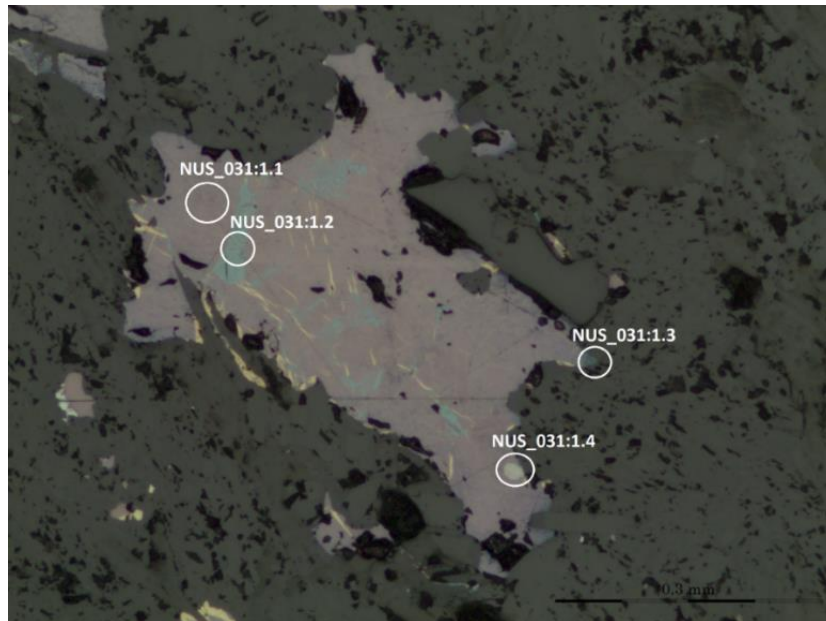


Figure 73. Photomicrograph show analyse area NUS_031:1 (Figure 72) in thin section NUS_031 in the Upper mineralized horizon in drill core NUS-DD-13-012. White circles mark the analysed sulphide grains (NUS_031:1.1, No. 154-156, NUS_031:1.2, No. 157-159, NUS_031:1.3, No. 160, and NUS_031:1.4, No. 161-163). Photo: Kjersti Moen.

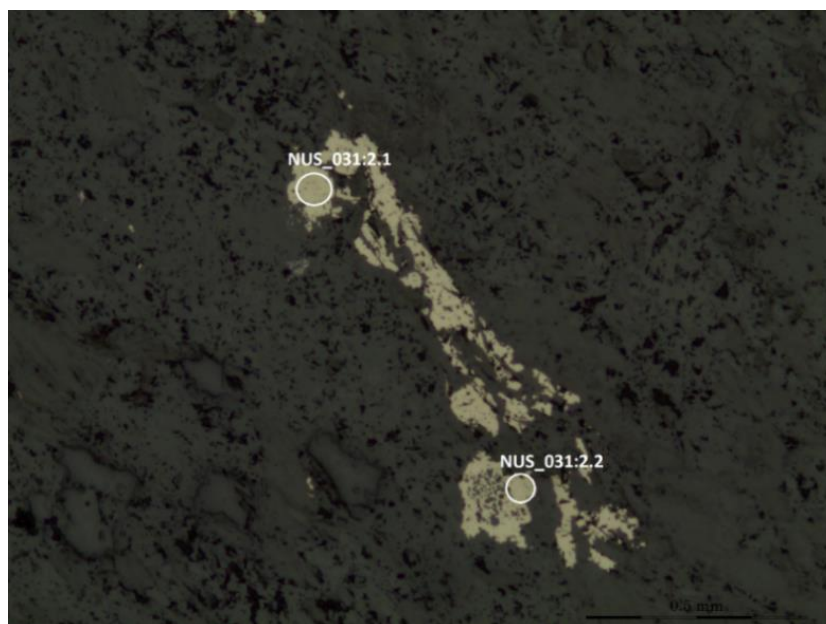


Figure 74. Photomicrograph show analyse area NUS_031:2 (Figure 72) in thin section NUS_031 in the Upper mineralized horizon in drill core NUS-DD-13-012. White circles mark the analysed sulphide grains (NUS_031:2.1, No. 164-166, and NUS_031:2.2, No. 167-169). Photo: Kjersti Moen.

Table 8. Results of electron probe micro-analysis in drill core NUS-DD-13-004 in thin section NUS_002 of chalcopyrite (No.19-21) and bornite (No.22-24). The element-concentrations is give in Wt %.

No.	Mg	S	Cr	As	Pd	Fe	Ag	Co	Te	Ni	Sb	Cu	Zn	Pt	Au	Total	Comment
19	0.003	32.772	0	0	0	33.016	0.002	0.008	0	0	0	34.227	0.058	0	0.133	100.22	NUS-002:2. 3.1
20	0.011	34.379	0.022	0.008	0.027	33.114	0.047	0.039	0	0	0	34.285	0.006	0	0	101.94	NUS-002:2. 3.2
21	0.004	34.798	0	0	0.016	33.435	0.042	0.051	0	0	0	34.398	0.088	0	0	102.83	NUS-002:2. 3.3
22	0	25.818	0.013	0.058	0	12.556	0.196	0.031	0	0	0.097	62.806	0.121	0	0	101.7	NUS-002:2. 4.1
23	0.071	25.845	0.004	0.031	0.008	12.577	0.239	0.045	0	0	0	63.318	0	0	0	102.14	NUS-002:2. 4.2
24	0.068	25.793	0	0.005	0.084	12.512	0.133	0	0	0.001	0.012	62.894	0.089	0	0	101.59	NUS-002:2. 4.3

Table 9. Results of electron probe micro-analysis in drill core NUS-DD-13-004 in thin section NUS_005 of chalcocite (No.28-29) and bornite (No.30-33). The element-concentrations is give in Wt %.

No.	Mg	S	Cr	As	Pd	Fe	Ag	Co	Te	Ni	Sb	Cu	Zn	Pt	Au	Total	Comment
28	0.022	20.672	0	0	0	0.073	0.246	0.009	0	0	0	78.308	0.073	0	0.113	99.516	NUS-005:1. 2.1
29	0.055	20.604	0	0	0	0.07	0.355	0	0	0.014	0	78.199	0	0	0.239	99.536	NUS-005:1. 2.2
30	0.054	25.225	0	0	0.032	11.281	0.304	0	0	0	0.136	62.299	0.072	0	0	99.403	NUS-005:1. 2.3
31	0	25.784	0	0.021	0	12.44	0.186	0	0	0	0.128	63.453	0.158	0	0.049	102.22	NUS-005:1. 3.1
32	0.015	26.258	0	0.074	0	12.614	0.181	0.047	0	0	0.137	62.493	0.198	0	0	102.02	NUS-005:1. 3.2
33	0	26.117	0	0	0	12.497	0.211	0.032	0	0	0.066	62.752	0.119	0	0.562	102.36	NUS-005:1. 3.3

Table 10. Results of electron probe micro-analysis in drill core NUS-DD-13-004 in thin section NUS_011 of bornite (No.85-87, 88-93 and 94-99) and chalcopyrite (No. 76-84). The element-concentrations is give in Wt %.

No.	Y	As	S	V	Ti	Cr	Bi	Fe	Pd	Co	Ag	Ni	Te	Cu	Mo	Zn	Sn	Pt	Pb	Au	Hg	W	Total
76	0.033	0.005	34.378	0	0.006	0	0.012	30.285	0	0.078	0	0	0	34.218	0.421	0.118	0.011	0	0	0	0.129	0	99.694
77	0	0	33.897	0	0	0	0	30.406	0	0.079	0.002	0	0	34.014	0.343	0.082	0.049	0	0.025	0	0.09	0	98.987
78	0	0	34.316	0.016	0	0	0.031	30.183	0.002	0.049	0	0	0	33.957	0.384	0.006	0	0	0	0	0.223	0	99.167
79	0.03	0.026	25.427	0	0	0.006	0	11.53	0	0.028	0.106	0	0	62.153	0.296	0.023	0	0	0.102	0	0	0	99.727
80	0.001	0	25.453	0	0	0	0	11.479	0	0.007	0.075	0.005	0	62.961	0.312	0.073	0	0	0.093	0	0.261	0	100.72
81	0.009	0.007	25.393	0.027	0	0.045	0	11.639	0	0.037	0.086	0	0	62.931	0.253	0.1	0	0	0.127	0	0.478	0	101.132
82	0.001	0	25.585	0	0.018	0.041	0	11.575	0	0.002	0.074	0	0	62.668	0.303	0.07	0.035	0	0.008	0	0	0	100.38
83	0	0	25.303	0.021	0	0.004	0.088	11.433	0	0.018	0.082	0	0	62.864	0.312	0.06	0	0	0	0	0	0	100.185
84	0.015	0	25.361	0.022	0.004	0	0.031	11.7	0	0.004	0.102	0	0	62.887	0.35	0.041	0.013	0	0	0.073	0.338	0	100.941
85	0.027	0	25.744	0.035	0	0	0.025	11.603	0	0.028	0.112	0	0	62.019	0.261	0.093	0	0	0.059	0	0.073	0	100.079
86	0	0.002	25.541	0.005	0	0	0	11.515	0.013	0	0.083	0	0	62.702	0.341	0	0	0	0	0	0	0	100.202
87	0.018	0	25.713	0	0.006	0.022	0	11.654	0	0.059	0.065	0	0	63.148	0.371	0.012	0	0	0	0	0.091	0	101.159
88	0	0	25.704	0.033	0	0	0	11.541	0.013	0	0.096	0	0	62.981	0.236	0	0.024	0	0.076	0	0	0	100.704
89	0	0.001	25.549	0.04	0.014	0.024	0.075	11.598	0.006	0	0.056	0	0	62.924	0.332	0.009	0	0	0.11	0	0.507	0	101.245
90	0	0.007	25.355	0.004	0	0.009	0	11.594	0	0	0.142	0	0	62.673	0.198	0	0	0	0.161	0	0.481	0	100.624
91	0.002	0	24.949	0	0	0.027	0.125	11.19	0	0.018	2.001	0	0	61.381	0.159	0	0.037	0	0.127	0	0.562	0	100.578
92	0	0	24.895	0.007	0.006	0	0	11.039	0.009	0.008	1.926	0	0	61.387	0.256	0.06	0	0	0	0	0	0	99.593
93	0	0.006	25.018	0	0.001	0.013	0	10.92	0.006	0.032	2.141	0	0	60.844	0.265	0	0	0	0.042	0	0	0	99.288
94	0.024	0	24.922	0	0	0.001	0	10.895	0.001	0	2.422	0.028	0	60.259	0.279	0.041	0.033	0	0	0	0	0	98.905
95	0	0	25.299	0	0	0.023	0	11.125	0	0	1.827	0	0	60.897	0.224	0.014	0.093	0	0.128	0	0.568	0	100.198
96	0.011	0	25.077	0	0	0.002	0	10.841	0.004	0.021	2.888	0.01	0	59.997	0.309	0.076	0.038	0	0	0	0	0	99.274
97	0.021	0.011	25.041	0	0	0.007	0	11.54	0	0.029	0.04	0	0	61.963	0.333	0.097	0	0	0	0	0	0	99.082
98	0.036	0.006	25.538	0.017	0.009	0	0	11.579	0.007	0	0.023	0.005	0	63.017	0.194	0.058	0.024	0	0	0	0.318	0	100.831
99	0.011	0	25.742	0	0	0.031	0	11.574	0.009	0.017	0.041	0.036	0	63.052	0.417	0.071	0.002	0	0.101	0	0	0	101.104

Table 11. Results of electron probe micro-analysis in drill core NUS-DD-13-002 in thin section NUS_018 of bornite (No.106-111, 121-123 and 127-129), chalcopyrite (No. 103-105, 113-117, 124-126 and 130-132) and chalcocite (No. 100-102 and 118-120). Table 1:2. The element-concentrations is give in Wt %.

No.	Y	As	S	V	Ti	Cr	Bi	Fe	Pd	Co	Ag	Ni	Te	Cu	Mo	Zn	Sn	Pt	Pb	Au	Hg	W	Total
100	0	0.011	19.839	0	0	0.024	0	0.032	0.001	0.013	2.018	0	0	77.344	0.18	0.143	0	0	0.112	0	0	0	99.717
101	0	0	20.237	0	0	0	0	0.054	0	0	1.331	0	0	76.037	0.257	0.062	0	0	0	0	0.125	0	98.103
102	0	0	20.535	0	0.003	0.014	0	0.043	0	0.002	1.072	0	0	77.663	0.21	0.1	0	0	0	0	0.228	0	99.87
103	0.005	0.01	34.395	0	0	0	0	30.663	0.001	0.025	0.007	0	0	33.989	0.448	0.063	0.038	0	0	0	0.186	0	99.83
104	0.019	0.005	34.604	0.005	0	0	0	30.489	0	0.072	0.011	0	0	33.963	0.375	0.035	0	0	0.115	0	0	0	99.693
105	0.006	0	34.431	0	0	0.025	0	30.497	0	0.05	0.009	0.005	0	34.136	0.542	0.043	0	0	0.066	0	0	0	99.81
106	0.009	0	26.064	0.029	0	0.017	0.056	11.445	0	0.021	0.288	0	0	62.189	0.257	0.083	0	0	0.085	0	0.171	0	100.714
107	0.027	0	26.029	0.005	0	0	0	11.513	0.005	0.051	0.32	0.027	0	62.32	0.265	0	0.011	0	0.144	0	0	0	100.717
108	0.013	0	25.66	0	0	0.009	0.013	11.677	0	0	0.245	0	0	62.186	0.232	0.038	0	0	0	0	0	0	100.073
109	0.014	0	34.003	0.034	0	0	0	29.633	0	0.019	0.028	0.004	0	34.32	0.517	0.038	0.011	0	0.033	0	0.018	0	98.672
110	0	0.002	25.652	0.033	0	0.026	0	11.492	0	0	0.119	0	0	61.51	0.318	0.098	0.066	0	0.196	0	0	0	99.512
111	0	0	25.356	0	0.02	0	0	11.166	0	0.012	0.101	0	0	61.386	0.161	0.121	0	0	0	0	0.564	0	98.887
112	0	0.004	26.228	0	0	0.005	0	11.287	0	0.007	0.115	0	0	59.58	0.261	0.024	0	0	0	0	0.336	0	97.847
113	0.01	0.003	34.048	0	0.001	0.008	0	29.946	0.001	0.049	0.032	0	0	33.676	0.416	0.029	0.002	0	0.016	0	0	0	98.237
114	0	0	34.034	0.002	0	0.021	0	29.987	0	0.096	0.031	0	0	33.809	0.379	0.032	0	0	0.164	0	0	0	98.555
115	0	0	33.942	0.011	0.01	0	0	29.734	0.005	0.078	0.028	0	0	33.494	0.375	0.04	0	0	0	0	0	0	97.717
116	0	0	34.064	0	0.005	0.019	0.104	29.734	0	0.048	0.024	0	0	33.47	0.358	0.062	0.022	0	0	0	0	0	97.91
117	0	0.005	34.017	0	0	0	0	29.927	0.008	0	0.038	0.002	0	33.407	0.383	0.054	0	0	0	0	0	0	97.841
118	0	0	20.519	0	0.017	0.009	0	0.044	0	0	0.398	0.016	0	78.476	0.181	0.06	0.076	0	0	0	0.139	0	99.935

Table 12. Results of electron probe micro-analysis in drill core NUS-DD-13-002 in thin section NUS_018 of bornite (No.106-111, 121-123 and 127-129), chalcopyrite (No. 103-105, 113-117, 124-126 and 130-132) and chalcocite (No. 100-102 and 118-120). Table 2:2. The element-concentrations is give in Wt %.

No.	Y	As	S	V	Ti	Cr	Bi	Fe	Pd	Co	Ag	Ni	Te	Cu	Mo	Zn	Sn	Pt	Pb	Au	Hg	W	Total
119	0	0	20.282	0	0	0.02	0	0.02	0.025	0.015	0.39	0	0	78.953	0.125	0.037	0	0	0	0	0	0	99.867
120	0	0.028	19.701	0.015	0	0	0	0.046	0	0.061	0.465	0	0	79.789	0.212	0.137	0.024	0	0	0	0	0	100.478
121	0	0.007	25.853	0	0	0.012	0.025	11.567	0	0.007	0.34	0.032	0	61.926	0.329	0.032	0	0	0.042	0	0.223	0	100.395
122	0.027	0.03	25.821	0	0	0	0	11.68	0	0.016	0.294	0	0	62.021	0.266	0.067	0	0	0	0	0	0	100.222
123	0.008	0.026	25.947	0.008	0	0.018	0.094	11.677	0.004	0.035	0.389	0	0	61.594	0.253	0.132	0	0	0.025	0	0	0	100.21
124	0	0.011	34.707	0	0	0	0	30.781	0	0.009	0.025	0	0	34.095	0.372	0.041	0.063	0	0.016	0	0	0	100.12
125	0.02	0	34.52	0	0	0.05	0	30.431	0	0.047	0.044	0.011	0	34.281	0.522	0.007	0	0	0.107	0	0.182	0	100.222
126	0	0.002	34.882	0	0.009	0.016	0	30.566	0.014	0.072	0	0	0	34.271	0.253	0.044	0.009	0	0.321	0	0	0	100.459
127	0.007	0	25.936	0	0.021	0.019	0	11.642	0	0.059	0.177	0	0	62.827	0.393	0.029	0	0	0	0	0.004	0	101.114
128	0	0.019	26.192	0.01	0	0	0	11.702	0	0.037	0.21	0	0	62.027	0.397	0.061	0.004	0	0.059	0	0	0	100.718
129	0.006	0.012	25.799	0.001	0.002	0.008	0.013	11.76	0.004	0.035	0.2	0	0	62.231	0.313	0.104	0	0	0	0	0.205	0	100.693
130	0	0.015	34.408	0	0	0	0	30.331	0.005	0.018	0	0	0	34.188	0.445	0.058	0.052	0	0.041	0	0.054	0	99.615
131	0	0	34.601	0.012	0	0.013	0	30.646	0	0.099	0.007	0.008	0	34.243	0.372	0.046	0.002	0	0	0	0.05	0	100.099
132	0	0	34.504	0	0	0.013	0	30.62	0.009	0.045	0.036	0.012	0	34.232	0.458	0.046	0	0	0	0	0.325	0	100.3

Table 13. Results of electron probe micro-analysis in drill core NUS-DD-13-003 in thin section NUS_025 of bornite (No.136-138 and 142-147) and chalcocite (No. 133-135, 139-141 and 148-153). The element-concentrations is give in Wt %.

No.	Y	As	S	V	Ti	Cr	Bi	Fe	Pd	Co	Ag	Ni	Te	Cu	Mo	Zn	Sn	Pt	Pb	Au	Hg	W	Total
133	0	0	20.402	0	0.022	0.002	0.006	0.057	0	0.029	0.244	0	0	79.244	0.211	0.091	0.024	0	0	0	0	0	100.332
134	0.016	0	20.471	0.006	0	0	0	0	0.008	0	0.249	0.015	0	79.551	0.319	0.083	0.061	0	0.061	0	0.305	0	101.145
135	0.017	0	20.296	0	0	0	0	0.113	0	0	0.277	0	0	79.286	0.25	0.119	0.026	0	0	0	0	0	100.384
136	0.015	0	25.746	0	0.022	0.003	0	11.305	0.003	0.038	0.087	0	0	62.54	0.368	0.028	0	0	0	0	0.314	0	100.469
137	0	0.005	25.839	0	0.014	0.02	0	11.538	0.011	0.016	0.1	0	0	62.755	0.377	0.074	0.024	0	0	0	0.027	0	100.8
138	0	0	25.663	0	0	0	0	11.498	0	0.036	0.1	0	0	62.676	0.373	0.052	0	0	0.06	0	0.114	0	100.572
139	0	0.011	20.444	0	0.016	0.028	0	0.016	0	0	0.405	0.007	0	79.54	0.186	0.129	0	0	0	0	0	0	100.782
140	0	0	20.553	0.028	0	0	0	0.028	0.006	0.019	0.389	0.023	0	79.762	0.177	0.125	0.02	0	0	0	0.108	0	101.238
141	0	0	20.364	0.031	0.022	0.017	0.058	0.102	0.007	0	0.372	0.001	0	79.3	0.22	0.041	0.066	0	0.087	0	0.121	0	100.809
142	0	0	25.45	0.004	0.002	0.031	0	11.262	0.011	0.024	0.127	0	0	63.202	0.28	0.003	0	0	0	0	0.009	0	100.405
143	0	0.005	25.682	0	0.027	0	0	11.339	0.003	0.037	0.156	0	0	63.004	0.373	0.084	0.015	0	0.017	0	0	0	100.742
144	0.018	0.003	25.791	0.015	0	0.015	0	11.241	0	0	0.165	0	0	62.65	0.361	0.103	0	0	0.068	0	0.573	0	101.003
145	0	0.005	25.672	0	0	0.015	0	11.225	0	0.043	0.174	0	0	62.971	0.34	0.063	0	0	0	0	0	0	100.508
146	0.01	0	25.589	0	0	0	0	11.115	0	0.048	0.171	0	0	63.113	0.344	0.057	0	0	0.213	0	0.092	0	100.752
147	0.001	0	25.741	0	0.008	0	0	11.087	0	0.011	0.17	0	0	63.225	0.293	0.057	0.011	0	0.119	0.003	0	0	100.726
148	0.002	0.003	20.736	0.016	0	0	0	0.104	0	0.02	0.468	0.001	0	79.662	0.203	0.092	0	0	0.32	0	0	0	101.627
149	0	0.011	20.673	0.03	0	0	0	0.118	0.01	0.004	0.461	0.034	0	79.283	0.22	0.094	0	0	0	0	0	0	100.938
150	0.018	0	20.52	0.005	0	0	0	0.064	0.012	0.056	0.428	0.012	0	79.752	0.328	0.03	0.103	0	0.13	0	0	0	101.458
151	0.024	0	20.9	0.004	0.016	0.003	0	0.019	0	0.01	0.401	0	0	78.458	0.246	0.12	0	0	0	0	0.169	0	100.37
152	0	0.003	20.637	0.02	0	0.007	0	0.015	0.02	0.045	0.483	0	0	79.147	0.207	0	0.024	0	0	0	0	0	100.608
153	0	0	20.662	0.017	0.018	0.009	0	0	0.011	0	0.38	0.012	0	78.477	0.337	0.155	0	0	0.087	0	0	0	100.165

Table 14. Results of electron probe micro-analysis in drill core NUS-DD-13-012 in thin section NUS_031 of bornite (No.154-156), chalcopyrite (No. 164-169), chalcocite (No.157-159), covellite (No. 160) and ??(No. 161-163). The element-concentrations is give in Wt %.

No.	Y	As	S	V	Ti	Cr	Bi	Fe	Pd	Co	Ag	Ni	Te	Cu	Mo	Zn	Sn	Pt	Pb	Au	Hg	W	Total
154	0.032	0	25.916	0	0	0.012	0.013	11.668	0.015	0.001	0.041	0	0	61.691	0.225	0.11	0.004	0	0	0.131	0	0	99.859
155	0.01	0	25.841	0.006	0.003	0.005	0	11.513	0	0	0.02	0.013	0	62.539	0.187	0.008	0.024	0	0.111	0	0.268	0	100.548
156	0.012	0	25.992	0.019	0.004	0	0	11.62	0	0.004	0.058	0.014	0	62.322	0.369	0.015	0.086	0	0.128	0	0.136	0	100.779
157	0	0	22.461	0	0	0.004	0	1.102	0.001	0	0.278	0	0	60.936	0.157	0.026	0	0	0	0	0	0	84.965
158	0.046	0.103	21.551	0	0	0	0.21	0.812	0.009	0	0.163	0	0	76.897	0.193	0.064	0.072	0	0	0	0	0	100.12
159	0	0	21.977	0	0	0.029	0	0.656	0	0	0.084	0	0	77.884	0.231	0.038	0	0	0.017	0	0	0	100.916
160	0	0	25.92	0.002	0.001	0.041	0	11.646	0	0	0.013	0	0	60.646	0.445	0.02	0	0	0.177	0	0	0	98.911
161	0.104	0	19.511	0	0	0.027	44.643	0.867	0	0.056	0.051	0.023	0	38.527	0.244	0.032	0.009	0	0	0	0.516	0	104.61
162	0.14	0	19.693	0.014	0	0.058	41.576	0.709	0	0.025	0.011	0.042	0	41.418	0.144	0.036	0.038	0	0	0	0.141	0	104.045
163	0.079	0	19.68	0.019	0.005	0.052	42.198	0.705	0	0	0.034	0	0	41.146	0.253	0.021	0.018	0	0	0	0.293	0	104.503
164	0	0.083	33.877	0	0	0.006	0	29.173	0	0.089	0.035	0	0	32.56	0.41	0.058	0	0	0.182	0	0	0	96.473
165	0	0.124	33.676	0	0	0.014	0	29.789	0.008	0.077	0.041	0	0	33.02	0.357	0.049	0.007	0	0.174	0	0.134	0	97.47
166	0	0.048	34.074	0	0	0.002	0	29.516	0	0.073	0.056	0	0	34.287	0.427	0.074	0	0	0.19	0	0	0	98.747
167	0	0.002	34.473	0	0	0	0	30.3	0	0.066	0.022	0	0	34.085	0.423	0.022	0.052	0	0	0	0.14	0	99.585
168	0	0	34.205	0	0	0	0	30.309	0.012	0.062	0	0	0	34.244	0.464	0.021	0.014	0	0	0	0.457	0	99.788
169	0.002	0	33.671	0	0	0.029	0.006	29.506	0	0.097	0.051	0.009	0	34.616	0.288	0.022	0.002	0	0.696	0	0.447	0	99.442

4.5.6 Comparison of WDS analysis of sulphides in the Upper- and Lower mineralized horizon

WDS analysis of bornite, chalcocite and chalcopyrite in the Upper- and Lower mineralized horizons, was compared in scatter diagrams. The comparison of copper and copper/iron ratio in the WDS analysis of bornite in the Upper- and Lower mineralized horizons, showed a variation in the copper concentrations in the Lower mineralized horizon, and a lateral variation in the Upper mineralized horizon (Figure 75). The copper concentration was higher in the Upper mineralized horizon, compared to the Lower mineralized horizon. The concentration of copper in the Lower mineralized horizon showed a greater variation. The copper-iron ratio in the Upper mineralized horizon was spread into two groups. The analysis from the Upper mineralized horizon and that plotted most to the left, was analysis of the bornite in drill core NUS-DD-13-004 in thin section NUS_002 and NUS_005 (Table 8 and Table 9, No. 22-24 and 31-33). Analysis from the Upper mineralized horizon that plotted to the right in the scatter plot was analysis from drill core NUS-DD-13-004 (Table 9, No.30) and from drill core NUS-DD-13-012 (Table 13, No. 136-138, 142-147).

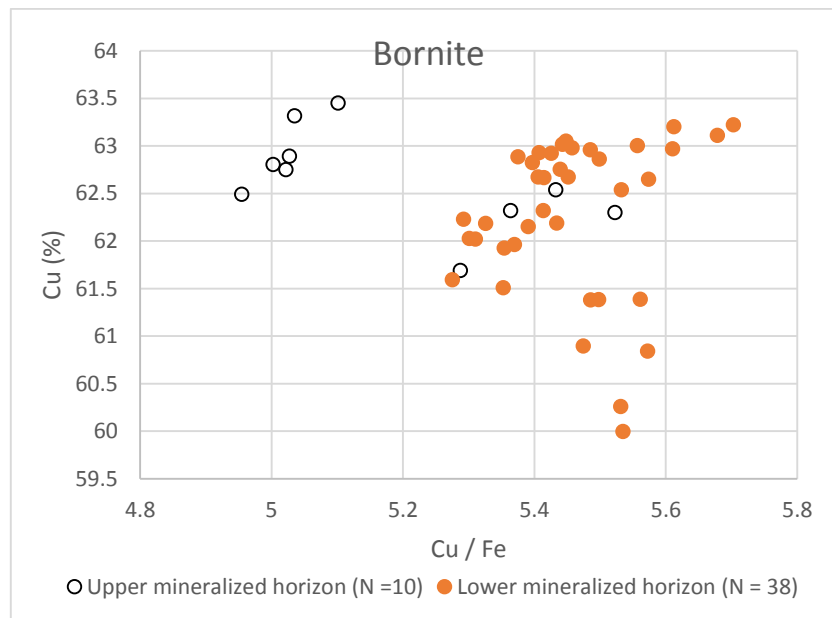


Figure 75. Scatter diagram of Cu/Fe-Cu ratio of WDS analysis in bornite in the Upper (unfilled circle) and the Lower (filled circle) mineralized horizon.

The comparison of copper/sulphur ratio and copper concentration in WDS analysis of bornite, showed a spread in the copper concentration in the Lower mineralized horizon, and some variation in the copper/sulphur concentration in the two mineralized horizons (Figure 76).

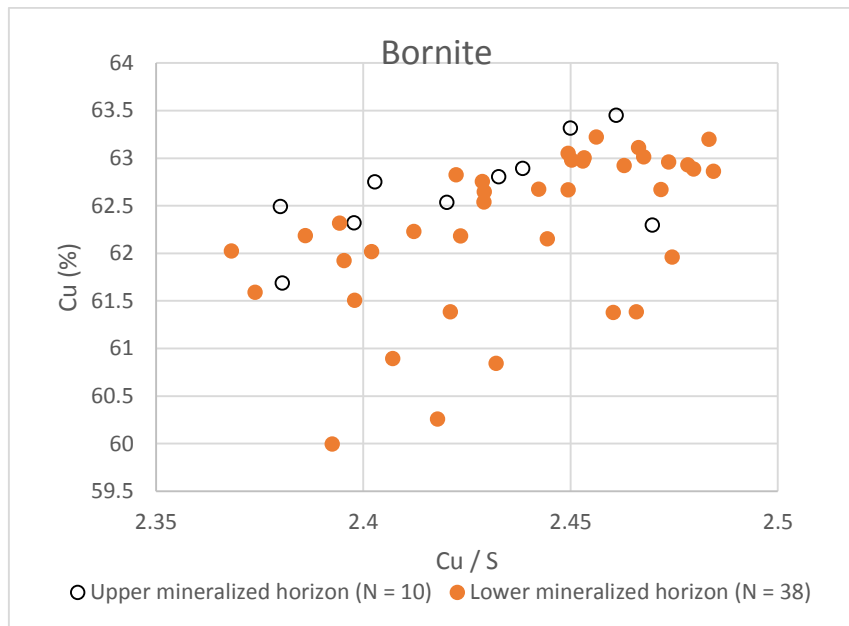


Figure 76. Scatter diagram of Cu/S-Cu ratio of WDS analysis in bornite in the Upper (unfilled circle) and the Lower (filled circle) mineralized horizon.

The comparison of the copper and the cobalt from WDS analysis of borite in the Upper- and Lower mineralized horizons, showed some variation in the copper concentrations in the Lower mineralized horizon and some variation in the cobalt concentrations in the two mineralized horizons (Figure 77).

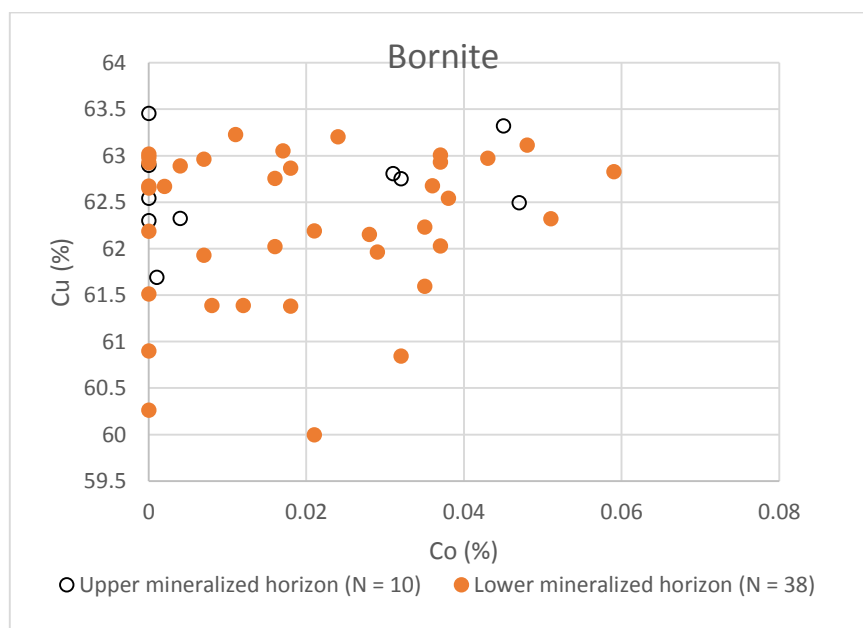


Figure 77. Scatter diagram of Co-Cu ratio of WDS analysis of bornite in the Upper (unfilled circle) and the Lower (filled circle) mineralized horizon.

The comparison of copper/iron ratio and silver from WDS analysis, gave an indication of a higher silver concentration in the bornite grains in the Lower mineralized horizon (Figure 78). The values with the greatest silver concentration in the Lower mineralized horizon, was analysed in drill core NUS-DD-13-004 in thin section NUS_011 (Table 10, No.91-96). The value from the Lower mineralized horizon that plotted to the left, was analyses from drill core NUS-DD-13-002 in thin section NUS_018 (Table 11, No. 100).

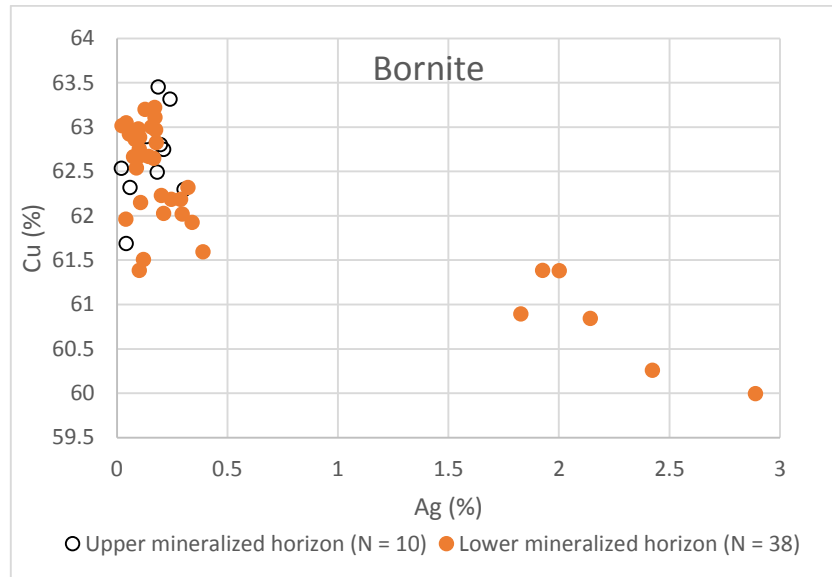


Figure 78. Scatter diagram of Cu-Ag ratio of WDS analysis in bornite in the Upper (unfilled circle) and the Lower (filled circle) mineralized horizon.

The comparison of copper-zinc concentrations from the WDS analysis of bornite in the Upper- and Lower mineralized horizon indicated some spread of the zinc concentrations in both the Upper- and Lower mineralized horizons (Figure 79).

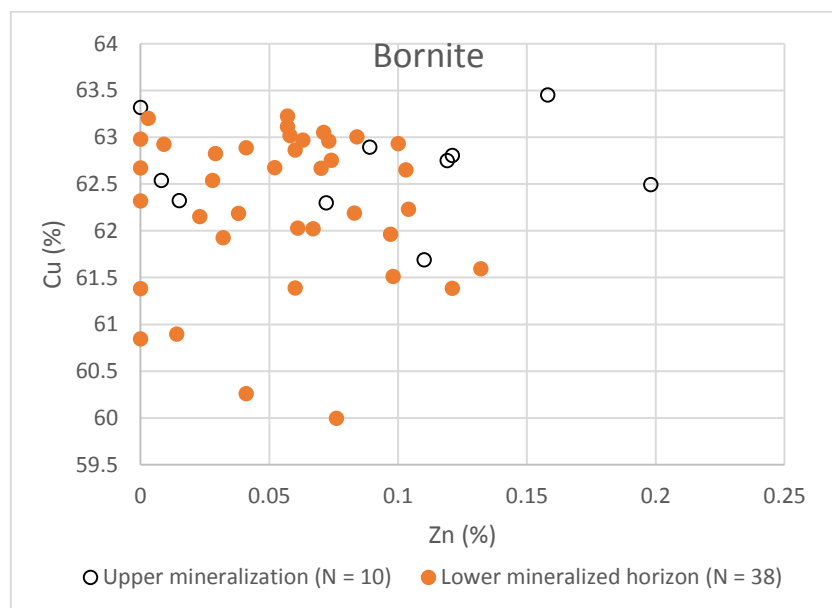


Figure 79. Scatter diagram of Cu-Zn ratio of WDS analysis in bornite in the Upper (unfilled circle) and the Lower (filled circle) mineralized horizon.

The comparison of the copper/sulphur ratio and the copper concentration from WDS analysis of chalcocite in the Upper- and Lower mineralized horizons, indicated similarities (Figure 80). Sample that plotted most to the left, was analysed in drill core NUS-DD-13-003 in thin section NUS_031 (Table 14, No.157).

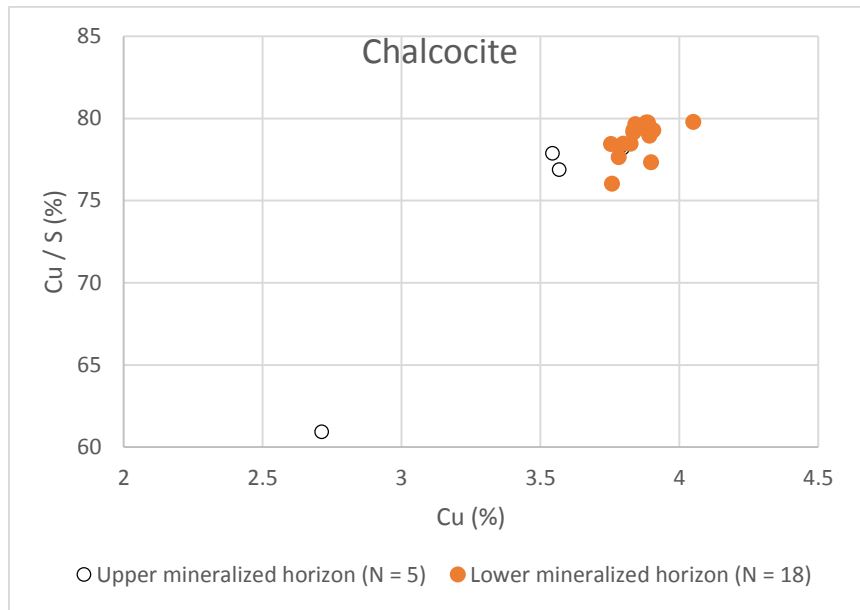


Figure 80. Scatter diagram of Cu/S-Cu ratio of WDS analysis in chalcocite in the Upper (unfilled circle) and the Lower (filled circle) mineralized horizon.

Comparison of the copper/sulphur ratio and the silver concentration from WDS analysis in the Upper- and Lower mineralized horizon, showed spread in the silver concentration in the Lower mineralized horizon and a stable concentration of silver in the Upper mineralized horizon (Figure 81). The copper/sulphur ratio in the Lower mineralized horizon varies.

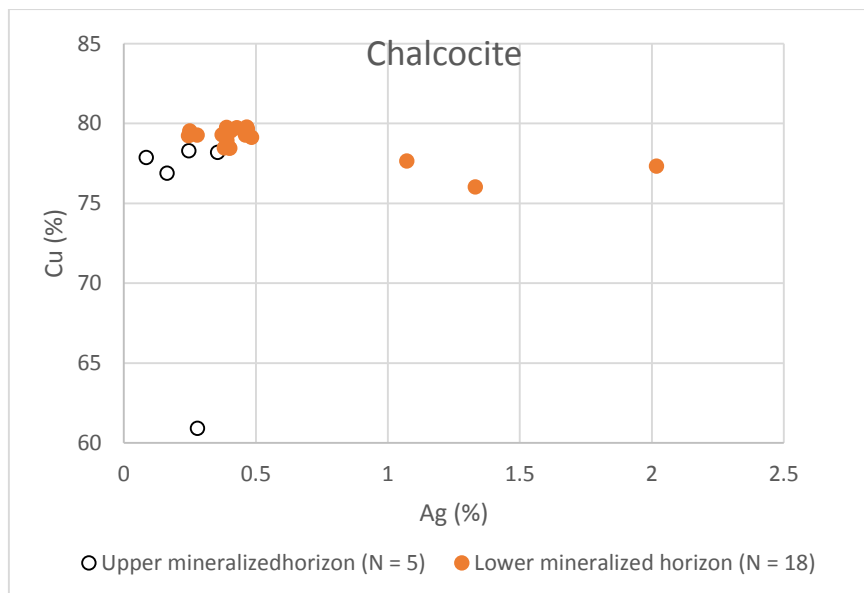


Figure 81. Scatter diagram of Cu-Ag ratio of WDS analysis in chalcocite in the Upper (unfilled circle) and the Lower (filled circle) mineralized horizon.

The comparison of Zn-Cu ratio from the WDS analysis in chalcocite in the Upper- and the Lower mineralized horizons, indicated variation of zinc (Figure 82).

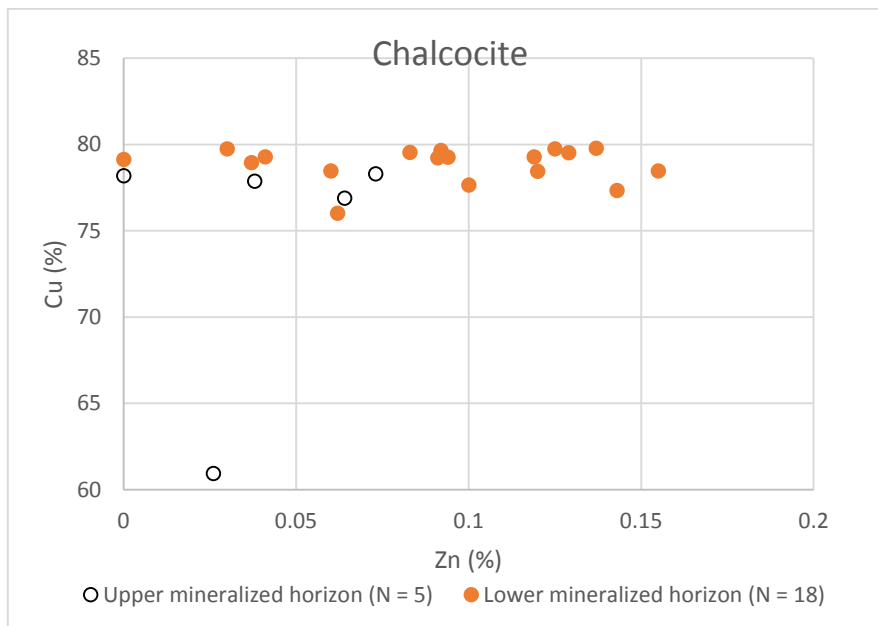


Figure 82. Scatter diagram of Zn-Cu ratio of WDS analysis in chalcocite in the Upper (unfilled circle) and the Lower (filled circle) mineralized horizon.

The comparison of Cu-Fe ratio from the WDS analysis in chalcocite in the Upper- and Lower mineralized horizons indicated higher concentrations of iron in the Upper mineralized horizon (Figure 83).

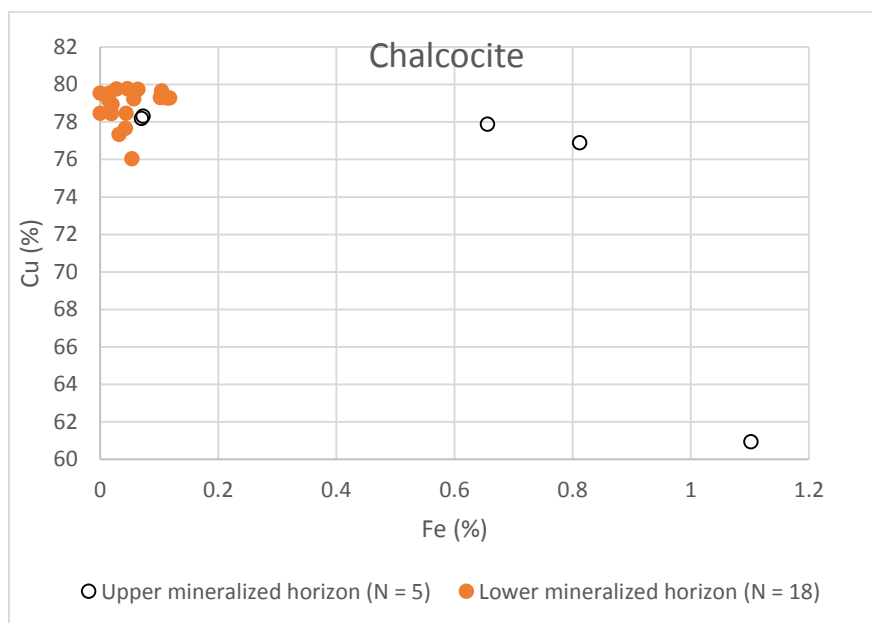


Figure 83. Scatter diagram of Cu-Fe ratio of WDS analysis in chalcocite in the Upper (unfilled circle) and the Lower (filled circle) mineralized horizon.

The comparison of the copper/iron-copper ratio from WDS analysis of the chalcopyrite in the Upper- and Lower mineralized horizons, indicated a higher concentration of iron in the Upper mineralized horizon, while the copper concentration showed a greater spread in the Lower mineralized horizon (Figure 84). The number of samples from the Upper mineralized horizon was low (N = 3), but indicated differences between the chalcopyrite grains analysed in the Upper horizon, with the grains analysed in the Lower mineralized horizon.

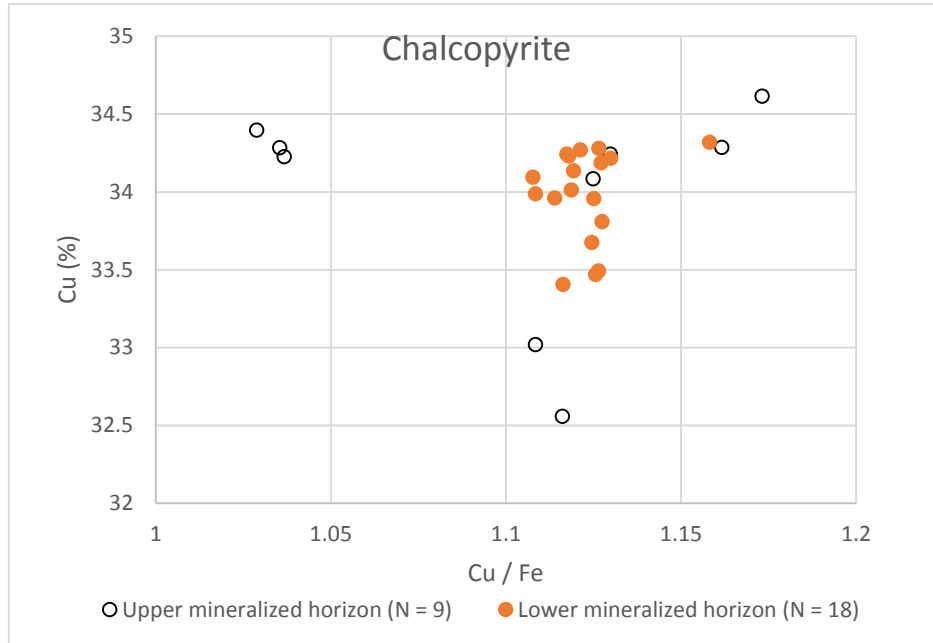


Figure 84. Scatter diagram of Cu-Cu/Fe ratio of WDS analysis in chalcopyrite in the Upper (unfilled circle) and the Lower (filled circle) mineralized horizon.

The comparison of the copper-copper/sulphur ratio from the WDS analysis of chalcopyrite in the Upper- and Lower mineralized horizons indicated a greater spread in the sulphur concentrations in the Upper mineralized horizon (Figure 85).

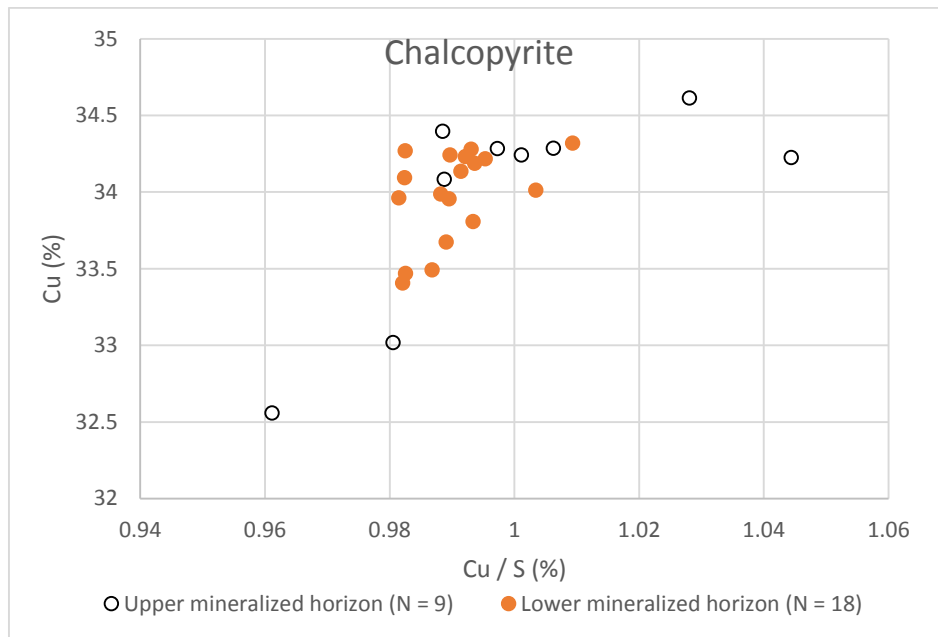


Figure 85. Scatter diagram of Cu-Cu/S ratio of WDS analysis in chalcopyrite in the Upper (unfilled circle) and the Lower (filled circle) mineralized horizon.

The comparison of the copper-silver ratio from the WDS analysis of chalcopyrite in the Upper- and Lower mineralized horizons indicated that the silver concentration varied in both horizons (Figure 86).

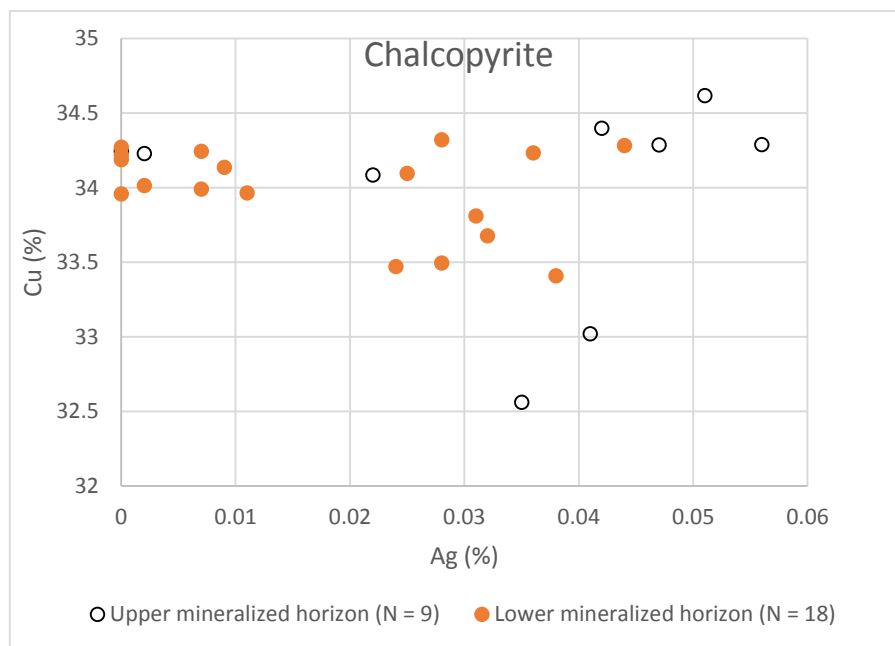


Figure 86. Scatter diagram of Cu-Ag ratio of WDS analysis in chalcopyrite in the Upper (unfilled circle) and the Lower (filled circle) mineralized horizon.

The comparison of the copper-zinc ratio from the WDS analysis of chalcopyrite in the Upper- and Lower mineralized horizons indicated that the concentration of zinc varied in the two horizons (Figure 87).

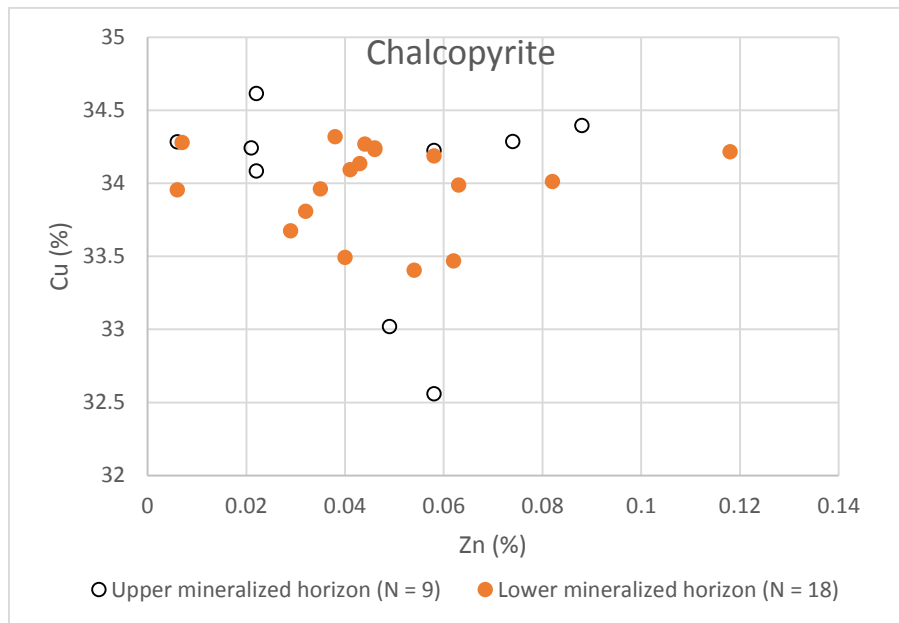


Figure 87. Scatter diagram of Cu-Zn ratio of WDS analysis in chalcopyrite in the Upper (unfilled circle) and the Lower (filled circle) mineralized horizon.

The WDS analysis of bornite, chalcocite and chalcopyrite from the Upper- and Lower mineralized horizons, was plotted in a Cu-Fe-S ternary diagram to compare the distribution of the analysis (Figure 88). The WDS analysis from the two horizons showed an overall similarity, with some deviation of the concentration in chalcocite in the Lower mineralized horizon.

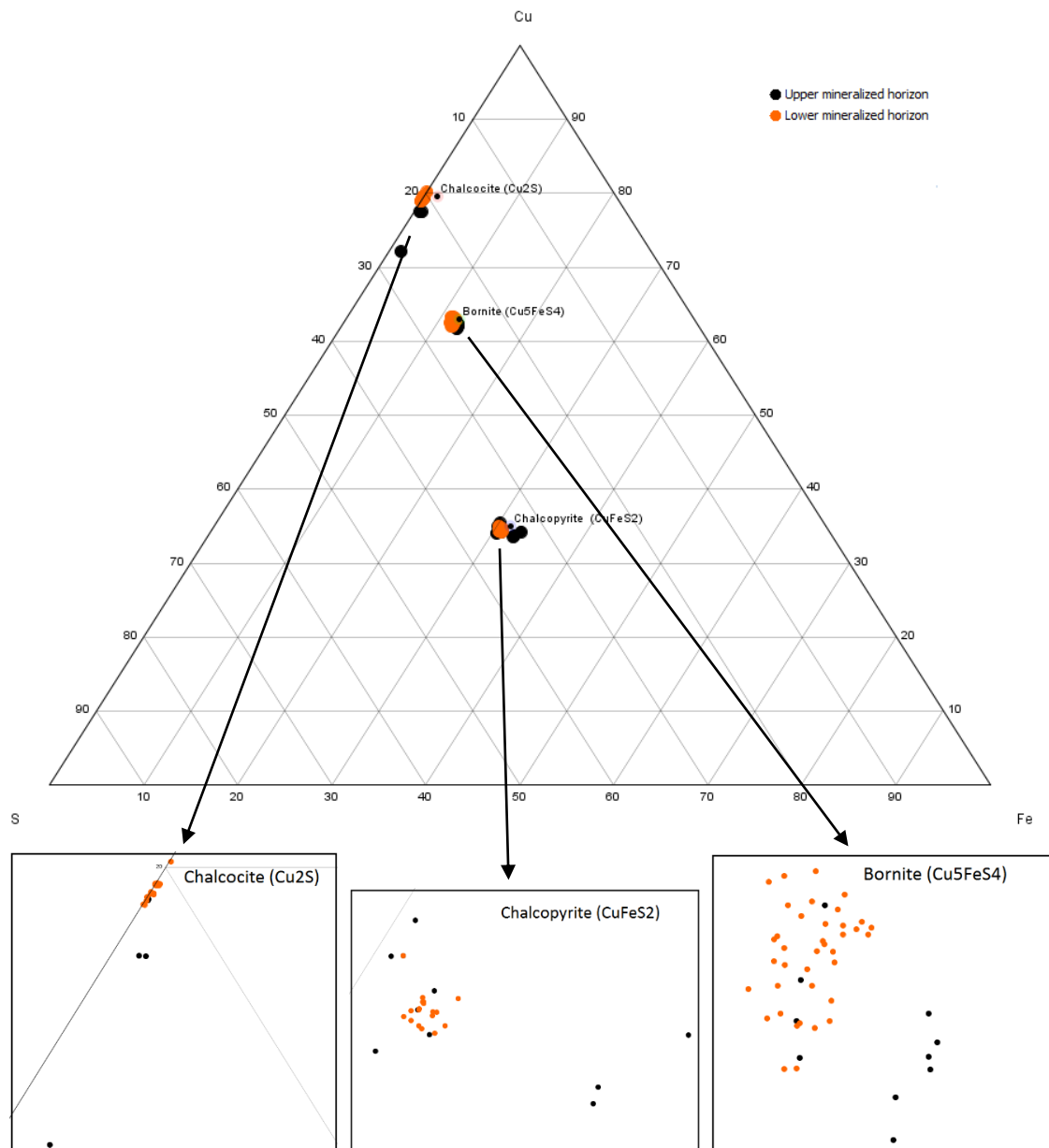


Figure 88. Ternary plot of Cu-Fe-S ratio in WDS analysis of bornite, chalcocite and chalcopyrite in the Upper (black) and the Lower (orange) mineralized horizon.

4.6 Geochemical analysis

4.6.1 Univariate statistic comparison between the Upper- and Lower mineralized horizon

Univariate statistics were performed in the Upper- and Lower mineralized horizons (Table B26-Table B34) from drill holes with the location given in Figure B99. Analysed elements with values below the detection limit, was excluded from the analysis and applied to tungsten, germanium, selenium, niobium, tellurium, tantalum, thallium and tin. The number of samples in the Upper mineralized horizon was about 146, and the number of analysis in the Lower mineralized horizon was about 30. The number of samples in the elements, bismuth, arsenic, yttrium, rubidium, thorium, boron, cerium, mercury and lithium, was only 1-5 in the Lower mineralized horizon. In the Upper mineralized horizon, the number of these elements was 21-146.

The mean values in the Upper mineralized horizon and the Lower mineralized horizon, was plotted in a scatter plot (Figure 89), and showed good correlation between the two mineralized horizons. The mean values of manganese and uranium showed the highest ppm values, and manganese contained the mean value of $(4378 \pm 2290 \text{ ppm}, 30)$ (mean \pm SD, N) in the Lower mineralized horizon, and $(4578 \pm 2970 \text{ ppm}, 102)$ in the Upper mineralized horizon. The difference of 200 ppm, indicated a relatively low difference between the Upper- and the Lower mineralized horizons. Uranium contained the mean values $(1210 \pm 1934 \text{ ppm}, 7)$ in the Lower mineralized horizon, and $(19 \pm 49 \text{ ppm}, 31)$ in the Upper mineralized horizon. The uranium mean value differed with 1191 ppm. The maximum value in one sample in the Lower mineralized horizon was 4040 ppm, and indicated that the mean value in the Lower mineralized horizon was strongly influenced by this high value.

Phosphorus, strontium, vanadium, lead, aluminium and scandium was located at the right side of the trend line, lying between the Upper mineralized horizon and the Lower mineralized horizon. Vanadium showed values of $(187 \pm 391 \text{ ppm}, 30)$ in the Lower mineralized horizon and $(28 \pm 377 \text{ ppm}, 33)$ in the Upper mineralized horizon. The difference was 159 ppm. Lead were plotted to the right of the trend line and contained the mean value $(46 \pm 108 \text{ ppm}, 29)$ in the Lower mineralized horizon, and $(24, 40 \text{ ppm}, 94)$ in the Upper mineralized horizon. The difference was 22 ppm. Strontium contained a mean value of $(225 \pm 102 \text{ ppm}, 30)$ in the Lower mineralized horizon and $(122 \pm 100 \text{ ppm}, 102)$ in the Upper mineralized horizon. The mean content of phosphorus was $(266 \pm 170 \text{ ppm}, 30)$ in the Lower mineralized horizon and $(162 \pm 223 \text{ ppm}, 102)$ in the Upper mineralized horizon. The aluminium content was $(4 \pm 2 \%, 5)$ in the Lower mineralized horizon and $(2 \pm 3 \%, 58)$ in the Upper mineralized horizon. The content of scandium in the Lower mineralized horizon was $(5 \pm 3 \text{ ppm}, 30)$ and $(4 \pm 4 \text{ ppm}, 98)$ in the Upper mineralized horizon. Aluminium, phosphorus and scandium plotted on the right side of the trend line.

Platinum, chromium, palladium and arsenic plotted left of the trend line. The mean value in palladium was $(11 \pm 1 \text{ ppb}, 30)$ in the Lower mineralized horizon and $(44 \pm 1 \text{ ppb}, 102)$ in the Upper mineralized horizon. The mean value varied with 33 ppb. Platinum contained the concentration $(41 \pm 36 \text{ ppb}, 7)$ in the Lower mineralized horizon, and $(135 \pm 377 \text{ ppb}, 33)$ in the Upper mineralized horizon. The difference was 94 ppb. Platinum and palladium showed a positive correlation, and plotted on the left side of the trend line. The mean value of arsenic was $(5 \pm 0 \text{ ppm}, 1)$ in the Lower mineralized horizon and $(37 \pm 47 \text{ ppm}, 29)$ in the Upper mineralized horizon. The mean value of the Lower mineralized horizon should be treated with caution since

the number of count were only 1. Chromium contained a mean value of $(41 \pm 26 \text{ ppm}, 30)$ in the Lower mineralized horizon and $(91 \pm 71 \text{ ppm}, 102)$ in the Upper mineralized horizon. The resulting elements was concentrated close to the trend line and was locate at the right side of the trend line.

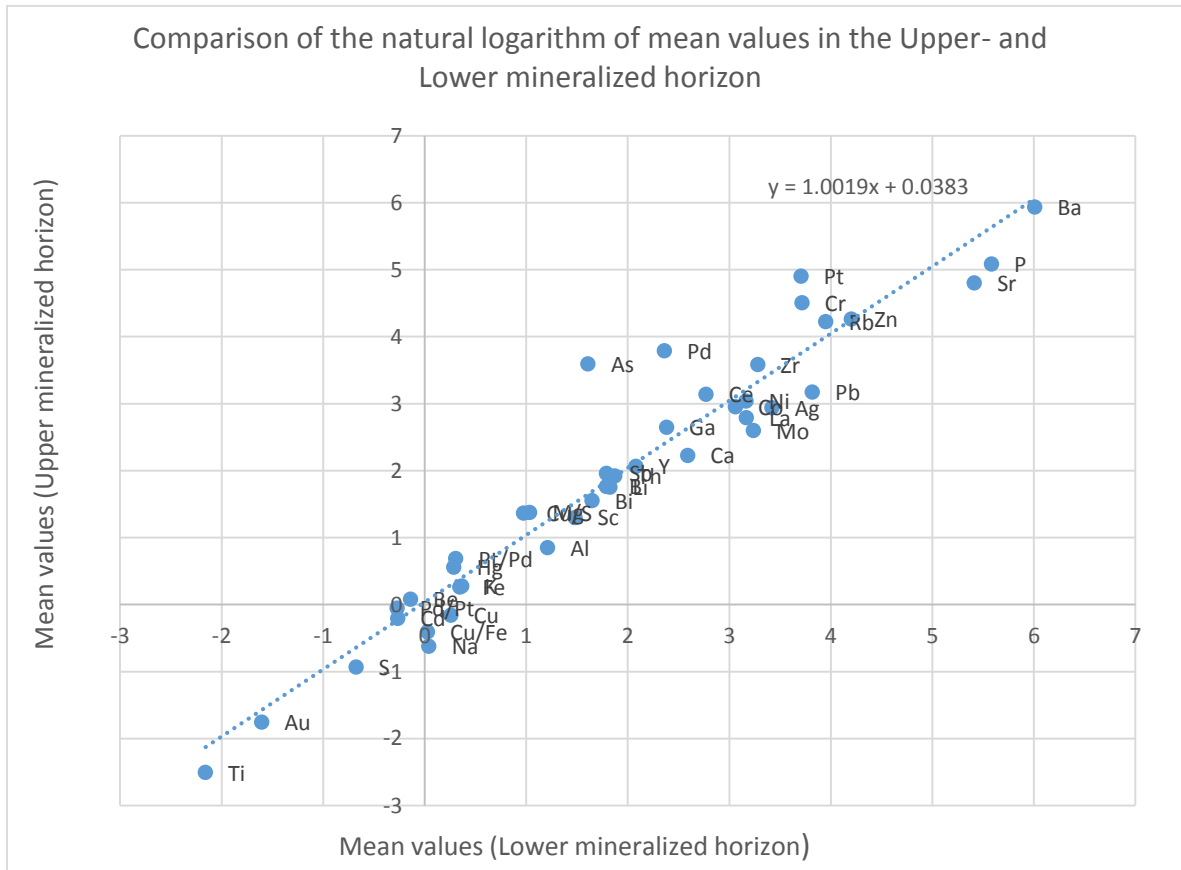


Figure 89. Natural logarithm of mean value of element concentrations in the Upper mineralized horizon and the Lower mineralized horizon. To enhance the visibility in the plot, the relatively high values of manganese, uranium and vanadium was left out.

4.6.2 Univariate comparison of standard deviation in the Upper mineralized horizon and the Lower mineralized horizon

The standard deviation of elements in the Upper mineralized horizon and the Lower mineralized horizon showed a linear correlation (Figure 90), and indicate an overall similarity of the standard deviation.

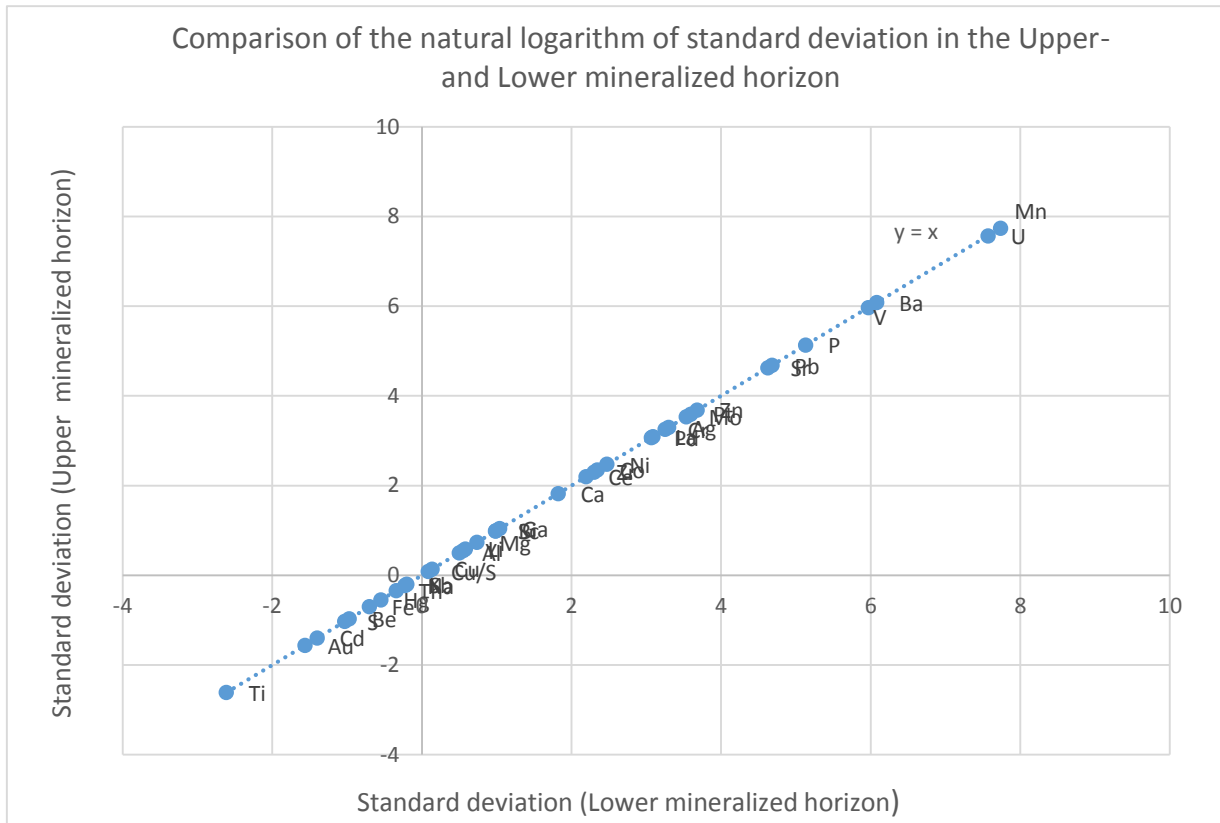


Figure 90. Natural logarithm of standard deviation of element concentrations in the Upper mineralized horizon and the Lower mineralized horizon.

4.7 Multivariate analysis of trace elements in drill core samples

4.7.1 Multivariate comparison of the lateral variation within Zone 1 (profile 10 and eastward)

The lateral variation within and between drill core samples in Zone 1-3 was compared by multivariate analysis. 7 of 125 samples were classified as outliers and therefore excluded from the PCA model. The results indicated that there may be some differences between the samples (the significance for Wilks' Lambda gave a value < 0.05 in Function 1 through 4 and 2 through 4, and significant value > 0.05 in Function 3 through 4 and Function 4, Table B47) and the classification showed that samples was distributed in two groups (Table 15). The distribution of samples is shown in Figure 91, and indicated differences between samples in Zone 1.

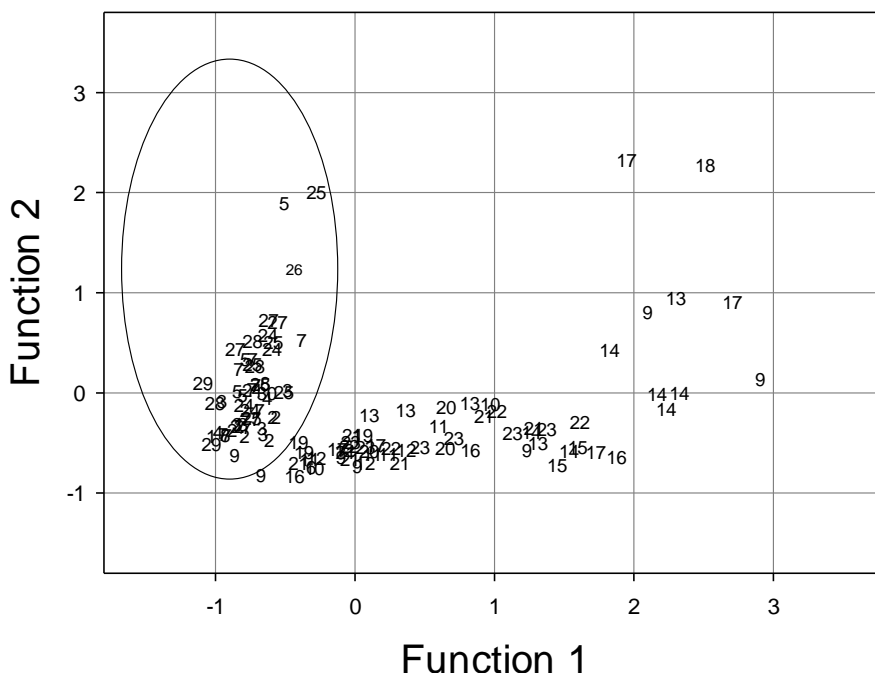


Figure 91. Multivariate comparison of the lateral variation within Zone 1 (profile 10 and eastward). The scatter plot show a split and grouping of the samples from Zone 1. Function 1 and Function 2 in Zone 1 is plotted. Details for the stratum numbers is given in Table B41 and Table B42. The circle indicate data from the analyses made in 2008 or earlier.

4.7.2 Multivariate comparison of new samples and old samples in Zone 1 (profile 10 and eastward)

The distribution of samples in Zone 1 was further investigated by dividing the samples in new and old samples. New samples and old samples was correctly classified and gave a Wilks' Lambda (Table B49) with significant value < 0.000. New samples was 100% correctly classified and 98.2 % of the old samples was correctly classified (Table 16), and indicate two grouping in samples from Zone 1.

Table 16. Classification results in multivariate comparison of new samples (1) and old samples (2) in Zone 1 (profile 10 and eastward). The classification results show that 100 % of new samples was correct classified and 98.2 % of old samples was correct classified.

Classification Results^a

		Predicted Group Membership		Total
		1,00	2,00	
Original	Count	62	0	62
		1	55	56
	%	100,0	,0	100,0
		1,8	98,2	100,0

a. 99,2% of original grouped cases correctly classified.

4.7.3 Multivariate comparison of new and old samples in zone 1, 2 and 3.

New and old samples from Zone 1, 2 and 3 was compared in multivariate analysis. The PCA model was good (Table B50-Table B53). The comparison of new and old samples from Zone 1, 2 and 3 gave Wilks' Lambda with significant value < 0.000 (Table B54). 99.2 % of new samples was correct classified and 97.3 % of old samples was correct classified (Table 17). The distribution of new and old samples is shown in histogram (Figure 92), and indicate differences between new and old samples in Zone 1, 2 and 3.

Table 17. Classification results in multivariate comparison of new and old samples in Zone 1, 2 and 3. The split parameters represents new samples = 1, and old samples = 2.). 99.2 % of new samples was correct classified and 97.3 % of old samples was correct classified.

		Ny_gammel	Predicted Group Membership		Total
			1	2	
Original	Count	1	125	1	126
		2	3	110	113
	%	1	99,2	,8	100,0
		2	2,7	97,3	100,0

a. 98,3% of original grouped cases correctly classified.

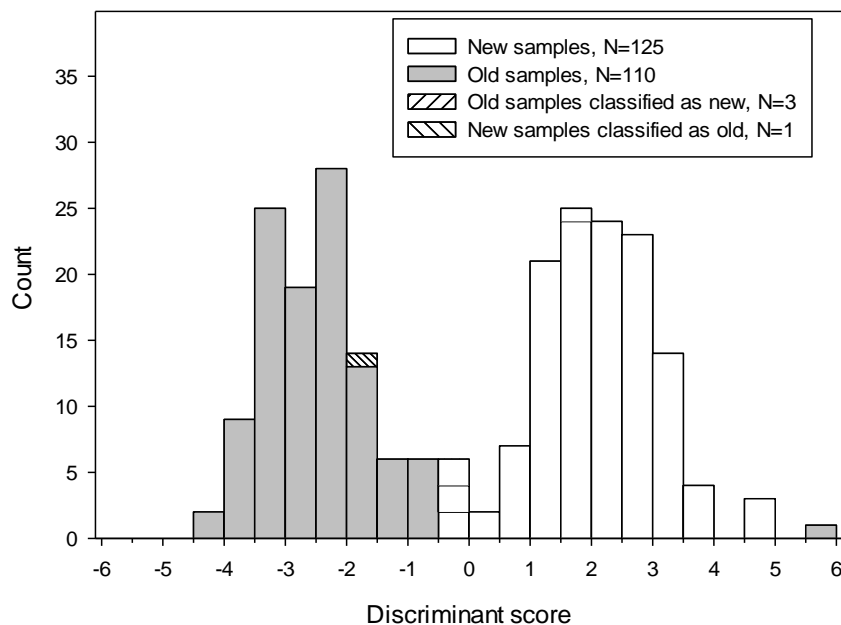


Figure 92. Histogram of the multivariate comparison of new and old samples in zone 1, 2 and 3. The histogram show the distinction between new and old samples. The distribution of samples along Function 1 and Function 2 (discriminant score) is shown along the x-axes. Number of samples (counts) is shown along the y-axes. New samples is marked by white column and old samples is marked by blue column. Overlapping samples is marked by hatched column.

4.7.4 Multivariate comparison of new samples from Zone 1, 2 and 3.

New samples from Zone 1, 2 and 3 was compared in multivariate analysis. The samples was random classified (Wilks' Lambda gave significant value > 0.05 , Table B56). From the new samples in Zone 1, 97.1 % of the samples was correctly classified. 17.5 % of the samples from Zone 2 was correctly classified and 0 % of the samples from Zone 3 was correctly classified (Table 18). The distribution of new samples from Zone 1, 2 and 3 is shown in scatter plot (Figure 93), and indicate similarity.

Table 18. Classification results in the multivariate comparison of new samples from Zone 1, 2 and 3. From the new samples in Zone 1, 97.1 % of the samples was correct classified. 17.5 % of the samples from Zone 2 was correct classified and 0 % of the samples from Zone 3 was correct classified.

		Sone_nr	Predicted Group Membership			Total
			1,0	2,0	3,0	
Original	Count	1,0	67	2	0	69
		2,0	33	7	0	40
		3,0	17	0	0	17
	%	1,0	97,1	2,9	,0	100,0
		2,0	82,5	17,5	,0	100,0
		3,0	100,0	,0	,0	100,0
Cross-validated ^b	Count	1,0	66	3	0	69
		2,0	35	5	0	40
		3,0	17	0	0	17
	%	1,0	95,7	4,3	,0	100,0
		2,0	87,5	12,5	,0	100,0
		3,0	100,0	,0	,0	100,0

a. 58,7% of original grouped cases correctly classified.

b. Cross validation is done only for those cases in the analysis. In cross validation, each case is classified by the functions derived from all cases other than that case.

c. 56,3% of cross-validated grouped cases correctly classified.

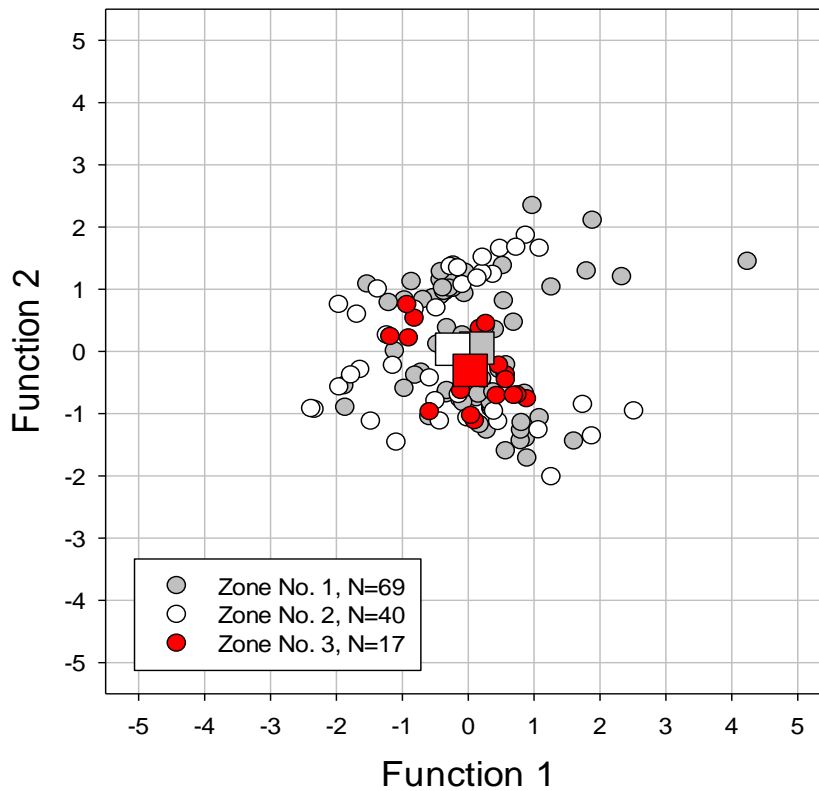


Figure 93. Scatter plot of multivariate comparison between zone 1, 2 and 3 using new samples. The scatter plot shows the high degree of overlap between new samples from Zone 1, 2 and 3. New samples from Zone 1 (blue), 2 (white) and 3 (red) is marked by circles and the mean value of each zone is marked by a square. Samples is plotted along Function 1 (x-axes) and Function 2 (y-axes). The two functions explains most of the variation of the multivariate analysis.

4.7.5 Multivariate comparison of new samples within Zone 2 (the Upper mineralized horizon)

The new samples from Zone 2 was compared. The PCA model showed a Kaiser-Meyer-Olkin of 0.792 and is considered a good model (Table B57-Table B59). The results indicate similarities between the new samples from Zone 2 (Wilks' Lambda < 0.05 for function 1 through 3, but > 0.05 for function 2 through 3 and 3, Table B60), and 54.1 % of the samples was correctly classified (Table 19).

Table 19. Classification results from the linear discriminant analysis of new drill core samples within Zone 2. The actual and predicted membership of a total of 37 samples from 7 strata is shown. The results are given in number and percent. The overall classification gave 54,1 % correct classification.

Classification Results^a

		Predicted Group Membership							Total
Sjiktnummer		29	32	34	35	36	37	39	
Original	Count	29	32	34	35	36	37	39	
		3	0	1	0	1	0	0	5
		1	7	0	0	0	2	0	10
		0	1	0	2	0	0	3	6
		1	0	2	3	0	0	0	6
		0	0	0	0	2	0	0	2
		0	0	0	0	0	3	0	3
	0	1	1	1	0	0	2	5	
	%	29	32	34	35	36	37	39	
		60,0	,0	20,0	,0	20,0	,0	,0	100,0
		10,0	70,0	,0	,0	,0	20,0	,0	100,0
		,0	16,7	,0	33,3	,0	,0	50,0	100,0
		16,7	,0	33,3	50,0	,0	,0	,0	100,0
		,0	,0	,0	,0	100,0	,0	,0	100,0
		,0	,0	,0	,0	,0	100,0	,0	100,0
		,0	20,0	20,0	20,0	,0	,0	40,0	100,0

a. 54,1% of original grouped cases correctly classified.

4.7.6 Multivariate comparison of new and old samples within Zone 3 (the Lower mineralized horizon)

New and old samples from Zone 3 was compared in multivariate analysis. The PCA model showed a Kaiser-Meyer-Olkin of 0.768 and is considered a good model, Table B61-Table B63. The results indicate differences between new and old samples from Zone 2 (Wilks' Lambda < 0.05 for function 1 through 2, but > 0.05 in function 2, Table B64). Scatter plot of function 1 and 2 (Figure 95) indicate the difference between the new (samples from stratum number 5 and 33) and old (samples from stratum 30, 31 and 38). The new samples on the left side while the old one is on the right side. 70.0 % of the samples was correctly classified, Table 20.

Table 20. Classification results in the multivariate comparison of new and old samples within Zone 3 (Lower horizon). 70.0 % of the samples was correct classified.

Classification Results^a

		Predicted Group Membership					Total
Sjiktnummer		5	30	31	33	38	
Original	Count	5	30	31	33	38	
		2	0	0	1	0	3
		0	4	2	0	0	6
		0	2	3	0	0	5
		1	0	0	4	0	5
	0	0	0	0	0	1	
	%	5	30	31	33	38	
		66,7	,0	,0	33,3	,0	100,0
		,0	66,7	33,3	,0	,0	100,0
		,0	40,0	60,0	,0	,0	100,0
		20,0	,0	,0	80,0	,0	100,0
		,0	,0	,0	,0	100,0	100,0

a. 70,0% of original grouped cases correctly classified.

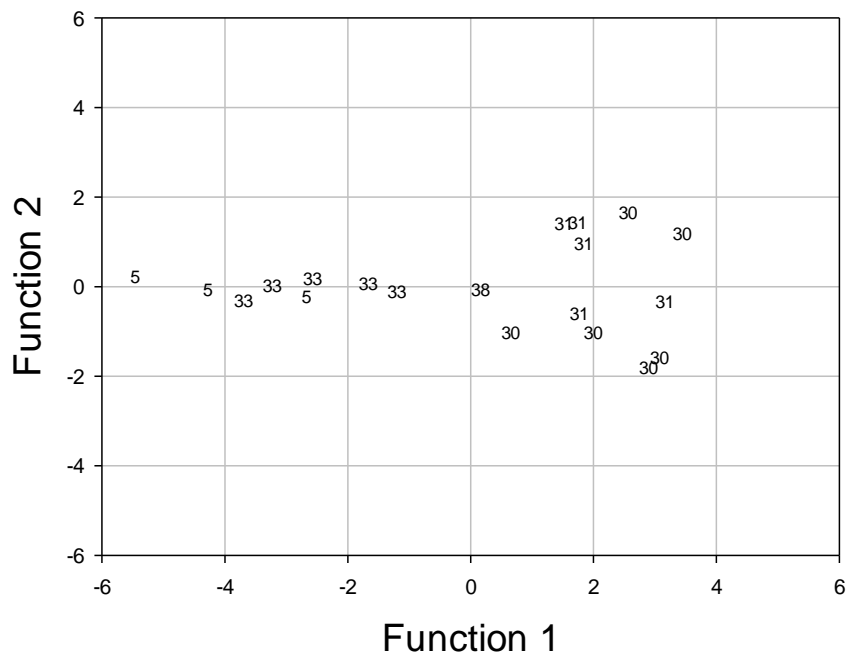


Figure 94. Scatter plot in multivariate comparison of new and old samples within Zone 3 (the Lower mineralized horizon). Stratum number (Table B41-Table B42) is plotted along Function 1 and Function 2. Scatter plot show the apparently grouping of samples in Zone 3.

4.7.7 Multivariate comparison between new samples in Zone 1 (Profile 10 and westward) and Zone 2 (the Upper mineralized horizon)

New samples from Zone 1 and Zone 2 was compared in multivariate analysis. The PCA model is given in Table B65-Table B67. The model was considered good with a Kaiser-Meyer-Olkin of 0.717 (Table B66). There is some differences between samples in Zone 1 and Zone 2 (Wilks' Lambda gave significant value < 0.05 , Table B68), and 86.2 % of samples in Zone 1 was correctly classified, and 66.7 % of samples in Zone 2 was correctly classified (Table 21). However, the distribution of samples along Function 1 and Function 2 indicate a relative high degree of overlap between the two zones (Figure 95).

Table 21. Classification results in the multivariate comparison between new samples in Zone 1 and Zone 2. 86.2 % of samples in Zone 1 was correct classified, and 66.7 % of samples in Zone 2 was correct classified.

Classification Results^a

		Sone_nr	Predicted Group Membership		Total
			1,0	2,0	
Original	Count	1,0	50	8	58
		2,0	12	24	36
	%	1,0	86,2	13,8	100,0
		2,0	33,3	66,7	100,0

a. 78,7% of original grouped cases correctly classified.

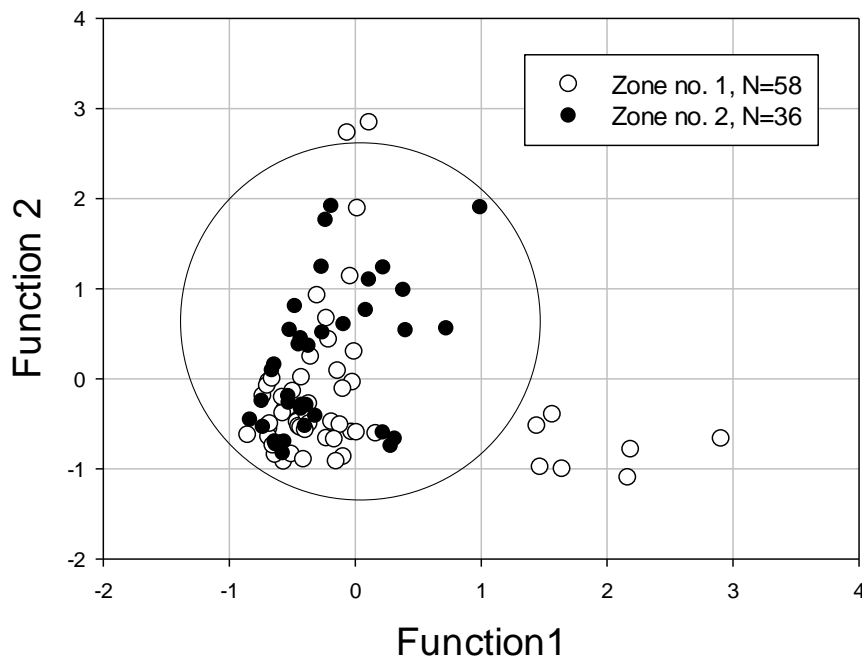


Figure 95. Scatter plot in multivariate comparison between new samples in Zone 1 (Profile 10 and westward) and Zone 2 (the Upper mineralized horizon). The scatter plot show high degree of overlap between new samples in Zone 1 and Zone 2. New samples from Zone 1 (white) and new samples from Zone 2 (black) plot along Function 1 and Function 2 that explains the most of the variation in of new samples in Zone 1 and Zone 2. Area with highest sample density is marked by a large circle. Stratum number 19 and 20 have value > 2 along the y-axes. Stratum number 13, 17, 18 and 21 have value > 1 along the x-axes.

4.7.8 Multivariate comparison between new samples in Zone 1 (Profile 10 and westward) and Zone 3 (the Lower mineralized horizon)

New samples from Zone 1 and Zone 3 was compared in multivariate analysis. The PCA model is given in Table B69-Table B71. The model was considered good with a Kaiser-Meyer-Olkin of 0.780 (Table B72). There is some differences between samples in Zone 1 and Zone 3 (Wilks' Lambda gave significant value < 0.05 , Appendix II, Table 76), and 93.7 % of samples in Zone 1 was correctly classified, and 66.7 % of samples in Zone 3 was correctly classified (Table 22). However, the distribution of samples along Function 1 and Function 2 indicate a relative high degree of overlap between the two zones (Figure 96).

Table 22. Classification results in the multivariate comparison between new samples in Zone 1 (Profile 10 and westward) and Zone 3 (Lower horizon). 93.7 % of samples in Zone 1 was correct classified, and 66.7 % of samples in Zone 3 was correct classified

Classification Results^a

		Sone_nr	Predicted Group Membership		Total
			1,0	3,0	
Original	Count	1,0	59	4	63
		3,0	4	8	12
	%	1,0	93,7	6,3	100,0
		3,0	33,3	66,7	100,0

a. 89,3% of original grouped cases correctly classified.

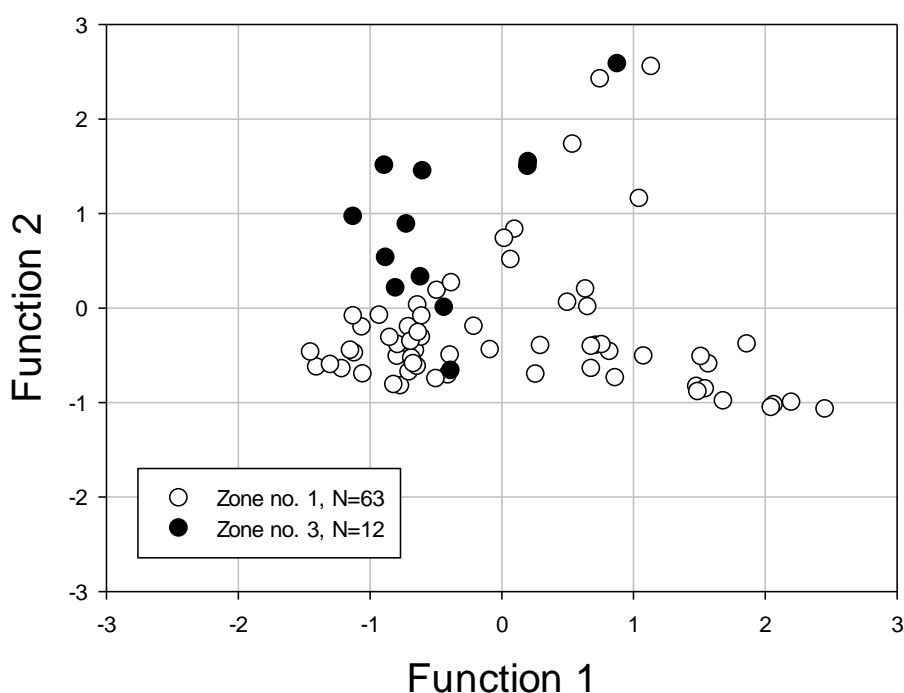


Figure 96. Scatter plot in multivariate comparison between new samples in Zone 1 (Profile 10 and westward) and Zone 3 (the Lower mineralized horizon). The scatter plot shows that new samples from Zone 1 and Zone 3 overlaps. New samples from Zone 1 (white) and new samples from Zone 3 (black) plot along Function 1 and Function 2 that explains the most of the variation in of new samples in Zone 1 and Zone 3.

4.7.9 Multivariate comparison of the Upper and the Lower mineralized horizon

The Upper- and Lower mineralised horizons was compared by multivariate analysis. The PCA model is given in Table B36-Table B38. The model was considered good with a Kaiser-Meyer-Olkin of 0.736, Table B37. The results indicated that there may be some differences (the significance for Wilks' Lambda gave a value < 0.05 , Table B39, and the classification showed that 72.7 % of samples from the Upper mineralized horizon was correctly classified, while 72.2 % of samples from the Lower mineralized horizon was correctly classified (Table 23). The probability plot and the histogram indicated high degree of overlap between the Upper- and the Lower mineralized horizon (Figure 91).

Table 23. Classification results from the multivariate comparison of the Upper mineralized horizon and the Lower mineralized horizon. 72.7 % of samples from the Upper mineralized horizon was correct classified, while 72.2 % of samples from the Lower mineralized horizon was correct classified

Classification Results^a

		oreup_orelow	Predicted Group Membership		Total
			1	2	
Original	Count	1	24	9	33
		2	5	13	18
	%	1	72,7	27,3	100,0
		2	27,8	72,2	100,0

a. 72,5% of original grouped cases correctly classified.

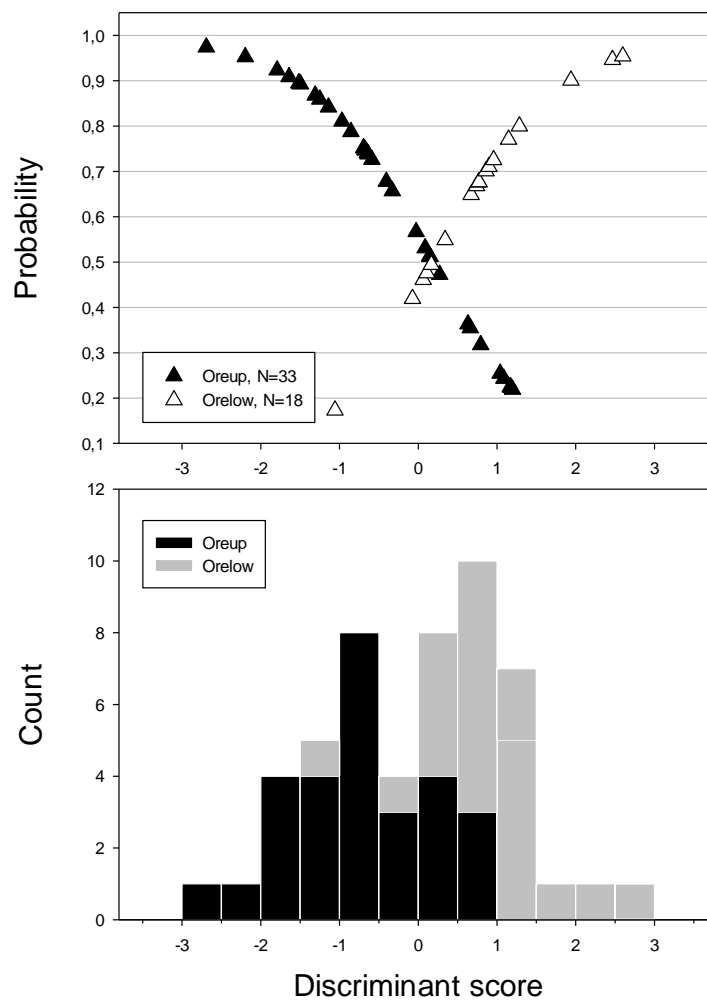


Figure 97. Probability plot and histogram for the discriminant analysis of the comparison of the Upper mineralized horizon (Oreup) and the Lower mineralized horizon (Orelow).

5 Drill hole geophysical logging

Drill hole geophysical logging performed by NGU in corporation with Nussir ASA, were compared to re-logged drill cores with the observed mineralization in thin sections. IP-effect, resistivity and gamma radiation from drill hole log DD-13-004 Nussir, 5.9.2013 (Dalsegg, Elvebakk et al. 2013), were compared with the mineralization in drill hole NUS-DD-13-004 (Figure 98). A complete description of the re-logged drill core NUS-DD-13-004 is given in Figure 37.

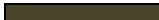
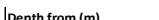
The natural gamma radiation gave a higher response at the Upper mineralized horizon (ore: 397.6-380.72 m and 380.92-390.15 m) than the Lower mineralized horizons (ore: 407.76-412.5 m). The natural gamma radiation generally decreased along the dolomite- and calcite rich mineralized horizon, despite at the interval 386-389 m. The carbonate-rich slate at the interval 413-416 m gave low natural gamma radiation in the Lower mineralized horizon.

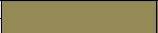
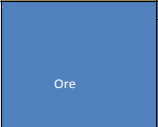
The SN resistivity gave a similar resistivity in the Upper and Lower mineralized horizon, while the LN resistivity showed a higher resistivity in the Upper mineralized horizon. The SN resistivity decreased in the mineralized horizons. The LN resistivity varied and showed minor connection to the mineralized horizons. Interval 382-384 m gave an increased LN resistivity in the mineralized horizon. The carbonate-rich slate in interval 391-405 m, showed high resistivity (> 10000 ohmm). The LN resistivity curve showed a straight line in this area since the resistivity probe have a maximum limit of 10000 ohmm (Dalsegg, Elvebakk et al. 2013).

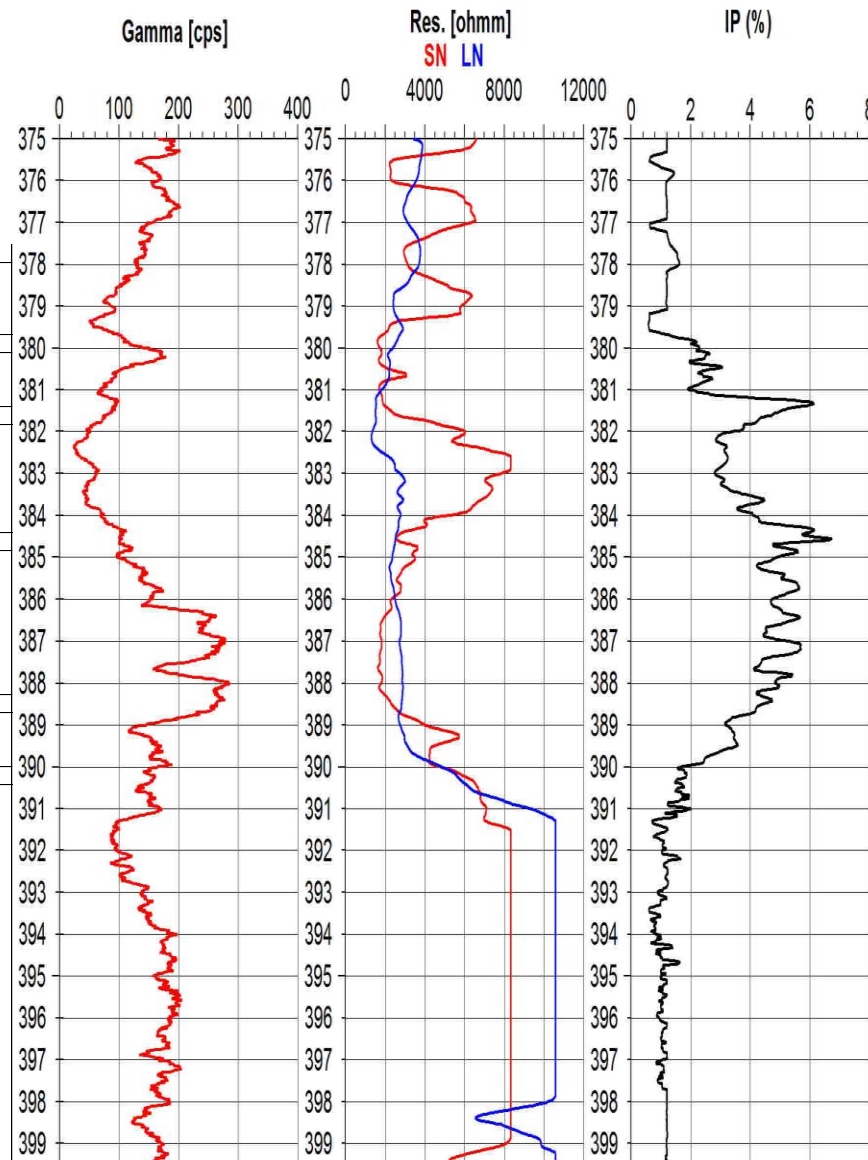
The observed mineralization in thin sections fitted well to the measured IP-effect. The Upper- and Lower mineralized horizon gave about the same IP-response, despite a higher peak in the Lower mineralized horizon. The peak was placed in the interval where mineralization of bornite, chalcopyrite and chalcocite was observed in thin sections. The Upper mineralized horizon (397.6-380.72 m and 380.92-390.15 m) gave the strongest IP-effect in the carbonate-rich slate and slate that surrounded the dolomite and calcite-rich rock (carbonates). Both mineralization as disseminated grains and in veins showed good IP-effect.

5.9.2013

Drill core NUS-DD-13-004

	CLY + CRB (Slate rich in carbonate)
	CLY (Slate)
	CRB (Carbonate)
	TUMT (Magnetite laminated tuff)
	TUF (Green tuffite, not magnetic)
	BRK (Broken rock) + NGU sample 393-393,12 m
	Ore
	cp Chalcocopyrite
	bn Bornite
	cc Chalcocite
	co Covellite

Depth from (m)	Depth to (m)	Lithology	Mineralization in thin sections (interval m)
378	379.6		
379.6	380.3	Ore	cp + bn (disseminated) (380.04-380.14)
380.3	380.72	Ore	
380.72	380.92		
380.92	381.65	Ore	bn + cp (disseminated) (381.6-381.7)
381.65	384.84		bn + cp (disseminated and in veins) (384.58-384.69)
384.84	386.4	Ore	
386.4	388.45		
388.45	390.15	Ore	cp (disseminated an in veins) (388.1-388.16)
390.15	391.33		cp + cc (disseminated and in veins) (390.6-390.66)
391.33	392.54		
392.54	393		
393.12	400.54		



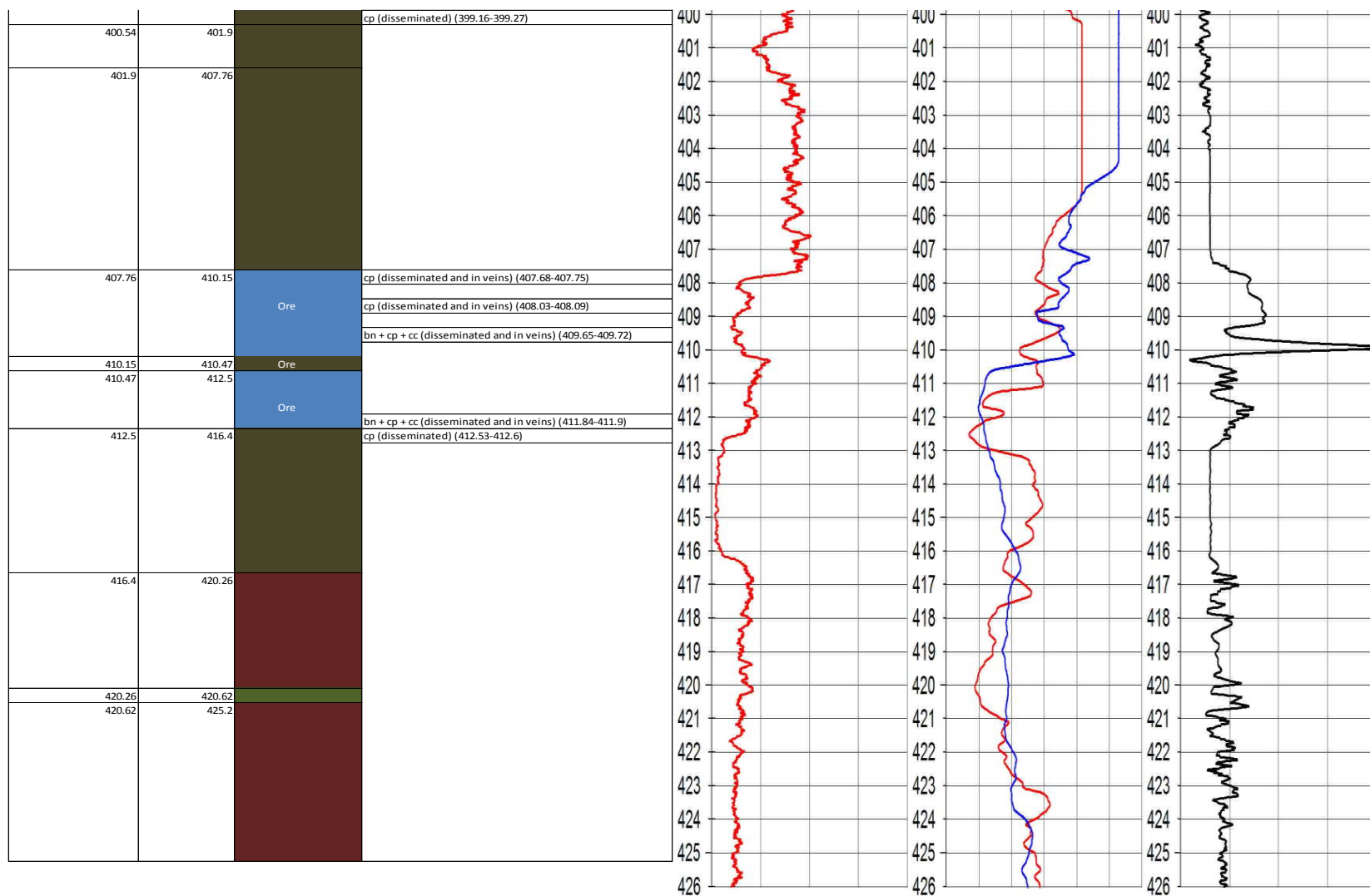


Figure 98. Figure show the mineralization in the re-logged drill core NUS-DD-13-004 compared with IP-effect, resistivity and gamma radiation in drill hole log DD-13-004 Nussir, 5.9.2013 (Dalsegg, Elvebakk et al. 2013).

6 Discussion

In this study, two mineralized horizons in the Nussir copper deposit were compared. The mineralized horizon was found by diamond drilling conducted by Nussir ASA in the western part of Nussir West in Kvalsund Municipality, Finnmark County. The Nussir copper deposit is hosted by sedimentary and volcanic rock of Precambrian- Palaeoproterozoic age (2.5-1.6 Ga) that was deposited in an intracratonic half graben. It is classified as sediment-hosted stratabound copper deposit where bornite, chalcocite and chalcopyrite occurs as disseminated grains in a dolomitic rock with mineralization along veins and spots of calcite.

To compare the two mineralized horizons, geological mapping, re-logging of diamond drill cores, thin section study of core samples, micro probe analysis of thin sections, chemical analysis and correlation of geophysical measurements in drill holes have been done.

The Nussir copper deposit is situated in the northwestern part of the Repparfjord window (Figure 11), and are located in the upper part of the Stangvatn Formation in the Saltvatn Group (Figure 7). The basement rocks consist of metasedimentary- and volcanic rocks of Precambrian to Palaeoproterozoic age (2.5-1.6 Ga), deposited in a intracratonic half graben (Pharaoh, Ramsay et al. 1983). The Nussir copper deposit are classified as a sediment-hosted stratabound copper deposit (SSC), and constitute one of fifteen known SSC deposits in the world (Figure 16). Observation in thin section from drill core samples and from re-logging of the Upper- and Lower mineralized horizon, showed that copper sulphides occurred as disseminated grains and in veinlets, restricted to two dolomite-rich layers hosting the copper sulphides. The dolomite-rich layers are underlain by a dacitic conglomerate (Stangvatn conglomerate), that probably have been the source rock of the copper sulphides, fining upward to an arkosic sandstone layer (footwall slate). A fine-grained sandstone layer is situated in between the Upper- and Lower mineralized horizon (mid wall slate) and a fine-grained siltstone layer is situated above the dolomite-rich layers (hang wall slate) (Figure 37). This corresponds well with the definition of Michael et al. (2010) for sediment-hosted stratabound copper deposits (SSC) (Zientek, Hammarstrom et al. 2010).

Diamond drill cores from drill holes NUS-DD-13-004, NUS-DD-13-002, NUS-DD-13-003 and NUS-DD-13-012 were re-logged, an overview of the localities of each drill hole is shown in Figure 36. The re-logging of drill cores indicated that the Lower mineralized horizon changed from being hosted by a dolomite-rich rock in drill core NUS-DD-13-004, to become rich in slate further west in drill core NUS-DD-13-002 (Figure 40). Nussir ASA has earlier regarded drill core NUS-DD-13-012 to be from the Upper mineralized horizon and NUS-DD-13-003 from the Lower mineralized horizon. However, the two drill cores showed similarity in the amount of chalcocite and bornite with minor chalcopyrite (Table 4). This could indicate that the two drill cores belonged to the same lithological horizon. Re-logging of the Upper- and Lower mineralized horizon showed that both of the horizons decrease in thickness toward west from drill core NUS-DD-13-004 (Figure 16-19), somewhat could indicate an increasing deformation in the westernmost part of the Nussir West. The Lower horizon seems to pinch out towards west.

Geological map (Figure 23) corresponded well with previously compiled map (Nilsen and Iversen, 1990), despite that they not have interpreted the mineralized horizon further towards west on the geological map (Figure E128). Their interpretation of the distribution of the Lower

mineralized horizon to the west, indicated that it bended around the tuffite and continued until Skinnfjellet Thrust. In the spring of 2013 there were drilled in the tuffite (NUS-DD-13-005) clarify whether the Lower mineralized horizon was located under tuffite. Drill hole log showed that the borehole did not pass through the lower mineralized horizon, but a un-mineralisert slate (Nussir 2013). The mineralized blocks observed west of tuffite may indicate that the Lower horizon continues west of tuffite. The Lower mineralized horizon was not observed further westward. This could have been caused by overburden matter, or that the horizon has picked out. Increased degree of deformation in the western part of Nussir may also have led to faulting of the two mineralized horizons.

The scope of the structural geological measurements were limited. Minor folds with the foldaxes towards NNE, NE and SSE, and a change in the dip direction in the footwall slate was indicated (Figure 34). It was also observed minor faults that were not marked on the geological map of structural measurements (Figure 13). On the geological map from Nilsen & Iversen (1990), the Upper mineralized dolomite were not drawn further west from the most westerly outcrop, since borehole further west (NUS-DD-13-003) only cut through one mineralized horizon (Figure E128).

Re-logging of drill core (NUS-DD-13-003) indicated similarity to the boreholes from the Upper mineralized horizon (NUS-DD-13-012 and NUS-DD-13-004) (Figure 47 and Figure 48), and may indicate that it is the Upper mineralized horizon that continues westward. The sulphide minerals in the Upper- and Lower mineralized horizon showed larger variation in concentration of copper in bornite in the Lower mineralized horizon compared to the Upper mineralized horizon (Figure 85). At the same time, the total copper concentration in bornite was somewhat higher in the Upper mineralized horizon, while silver in bornite and chalcocite showed a higher concentration in the Lower mineralized horizon (Figure 78 and Figure 81). Wavelength-dispersive X-ray spectrometer (WDS) analysis of chalcopyrite showed a higher iron concentration in the Upper mineralized horizon than in the Lower horizon (Figure 84). Thin sections from drill core NUS-DD-13-004 were made at an earlier date than the others and Chalcopyrite oxidizes in contact with air to form sulfates of iron and copper and may have caused a concentration of iron in the sample. Sandstad (2008) investigated borehole BH 60 (NUS-DD-06-007) (Figure 46), and recorded a higher Cu / Fe ratio, a higher total copper concentration and magnesium concentration in the Upper mineralized horizon than in the Lower mineralized horizon. Their results indicated a difference in the composition of the host rock in the Upper and the Lower mineralized horizon. Analyses of the host rock in the hanging wall slate; the Upper mineralized horizon and the footwall slate indicated that the content of calcite was high (52-57 %) with relatively low concentration of magnesium (0.2-0.4 %), Table 6 and Table 7. Manganese may have substituted for magnesium in dolomite and calcite. The higher Cu / Fe content in the Upper mineralized horizon recorded by Sandstad (2008) corresponded to our results on the composition of bornite, chalcocite and chalcopyrite (Figure 75, Figure 83 and Figure 84). The investigations of the host rock was not fully adequate, but the re-logging indicated that the Upper mineralized horizon consisted of a cleaner dolomite (Figure 37 and Figure 38), which correlated with a higher magnesium content than the Lower horizon, that showed a higher slate content (Figure 37 and Figure 40).

Differences in trace element composition between the Upper- and Lower mineralized horizon were investigated using both univariate and multivariate statistical analyzes. The mean and standard deviation for each of the elements indicated a high degree of similarity between the

two mineralized horizons (Figure 89 and Figure 90). However, the large difference in the number of measurements and measured values for each element gave a limited impression of differences and similarities between the mineralized horizons (Table B26-Table B34).

The univariate analysis was considered inadequate for comparison the trace element composition in the mineralized horizons. A multivariate analysis was therefore employed. 50 different trace elements were used in the comparison between and within the mineralized horizons (Zone 1 (east of Profile 10) and Zone 2 and 3 (both in the west of Profile 10) (Table B25).

The multivariate analysis of Zone 1 indicated differences between the new and old analysis (assay values) (Figure 91). Samples analyzed before 2008 was different from the recent analyse values. The difference was also evident in the analysis based on the cores from all three zones together (Zone 1, 2 and 3) (Table 17 and Figure 92). However, in a previous study, Sandstad (2008) did a univariat analysis of the concentration of calcium, magnesium and copper in the diamond drill cores from the borehole NUS-DD-06-007 (Zone 2 and 3). His analysis was based on the old analysis and recorded a higher concentration of magnesium in the Upper mineralized horizon (Zone 2), and a higher concentration of calcium in the Lower mineralized horizon (Zone 3). Analysis of the lateral variation along the mineralized horizon from east to west showed differences between new and old samples when performing a multivariate analysis based on 21 different trace elements (Figure 92). In 2009, Nussir ASA conducted a comparison of samples analyzed by the ALS Laboratory and from the OMAC laboratory (Wheeler 2012). Samples analyzed by the ALS laboratory were sent to the OMAC laboratory and vice versa for a comparison of the measured values of copper gehalten. The comparison showed that the accuracy of the two laboratories was sufficient for good resource estimation. In 2012, 1,443 analyzes from 1990. They found that Half Relative Absolute Difference (HARD) was 31%, proportion misclassified was 7.6%, while the correlation coefficient between the analyses from 1990 and re-analysis was 95.7%. The samples were analyzed by Mercury Analytical or Caleb Brett Laboratories, and re-analyzed for copper grade. The result indicated that the samples analyzed by OMAC Laboratories and ALS had good correlation. An overview of the analytical methods utilized are shown in Table 1. Analysis methods seem to form distinct groupings between samples from 2008 (NUS-DD-08-014) and younger from older samples analyzed. Differences between analytical methods utilized are thus the likely cause of the differences between new and old samples. This should be taken into account in the further use of the data from these chemical analyses.

A lateral comparison of new samples from Zone 1, 2 and 3 were conducted to investigate if the chemical composition varied from east to west. The analysis showed high degree of similarity in the chemical composition. Likewise showed the lateral variation in the Upper mineralized horizon in the west (Zone 2) high degree of similarity with the mineralized horizon in the east (Zone 1) (Figure 95). Comparison between Zone 1 and the Lower mineralized horizon (Zone 3) also indicated similarity even though the number of samples from Zone 3 were relatively few (Figure 96). The results indicated that the two mineralized horizons in the west (Zone 2 and Zone 3) had the same chemical composition as Zone 1 in the east. This may indicate that the two mineralized horizons in the west (Zone 2 and Zone 3) belong to the same stratigraphic mineralised layer.

Thin sections analysis of the drill core samples from the Upper- and Lower mineralized horizon showed a high degree of similarities in zonation and occurrence of copper sulphides (Table 4). Bornite and chalcopyrite was the dominating sulphides in the upper part of the mineralized horizon, while bornite, chalcocite and chalcopyrite were the major sulphide in the central part. Chalcopyrite and minor bornite occurred in the lower part of the mineralized horizon. Chalcopyrite and bornite observed in the core of sulphide minerals, contained chalcocite along cracks and rims of bornite and chalcopyrite. This could indicate a replacement of chalcopyrite and bornite by chalcocite, which is typical in SSC deposits (Robb 2005). Sandstad (2010) performed thin section observation of drill core samples from four drill holes in the eastern part of the Nussir copper deposit (H0810:NUS-DD-08-010, H0811: NUS-DD-08-011, H0814:NUS-DD-08-014 and H0821:NUS-DD-08-021) by using polarization microscope and scanning electron microscope (SEM). He concluded that the major copper sulphides (bornite and chalcocite) were of syngenetic or diagenetic origin, were accessory minerals as chalcopyrite, covellite, wittichenite, carrollite and cinnabar have replaced and/or exsolved from the major copper sulphides. Sandstad (2010) remark that the accessory minerals could have been of epigenetic growth. Andersen (1987) have correlated the Nussir copper deposit to the two major SSC deposits Kupferschiefer in Central Europe and particular The Central African Copper Belt (CACB) located at the border between Zambia and the Democratic Republic of Congo. In the Nchanga deposit in the CACB, two mineralized horizon is described (Upper Orebody and Lower Orebody) to be part of the intracratonic Katangan sedimentary basin with a maximum age determination given by an 877 ± 11 Ma U–Pb geochron for the Nchanga Red Granite (Armstrong et al. 1999) situated below Katangan rocks. The Upper- and Lower Orebody are hosted by an arkosic unit within the base of overlying shales (McGowan, Roberts et al. 2006) and were the Upper Orebody contains mineralization of copper and cobalt, and the Lower Orebody contain mineralization of copper. A study of the $\delta^{34}\text{S}$ concentration between the Upper- and Lower Orebody, have given $+12.1 \pm 3.3$ (n=65) in the Upper Orebody and $+5.2 \pm 3.6$ (n=23) for the Lower Orebody (McGowan, Roberts et al. 2006). Petrographic observations of the SSC deposit in Nchanga, support a epigenetic origin with a sulfide mineral paragenesis of diagenetic pyrite followed by chalcopyrite, bornite, and carrollite, with late chalcocite (McGowan, Roberts et al. 2006). The study performed by McGowan, Robert et al. (2006) shed light on the occurrence of two ore bodies diversified stratigraphically in a SSC deposit that have been classified as epigenetic with differences in the composition of the host rock and sulphides. The great similarities in thin section observation of the Upper- and Lower mineralized horizon in the Nussir copper deposit could support an epigenetic origin of the Nussir copper deposit if the mineralized horizon was one horizontal layer, were hydrothermal fluids migrated upward in a sedimentary basin. The occurrence of two mineralized horizon seems to be contrary to an epigenetic origin.

When oxidized fluids migrate upward into a sedimentary strata along grain boundaries and pore space, the metal carrying capacity in fluids decreases rapidly when they reach a reducing environment, such as dolomite or a calcite-rich slate. Therefore, it is unlikely that fluids have been able to transport metals through and passed the reducing host rock of the Lower mineralized horizon, and then precipitates copper sulphides in exactly the same way in the host rock of the Upper mineralized horizon. The occurrence of sulphides as disseminated grains and growth along veins could, support an epigenetic origin, if larger faults or crushed breccia have worked as drainage of the hydrothermal fluids. The absence of observed faults and crushing

zones in Nussir west, oppose this view. If the copper minerals are of syngenetic or diagenetic origin and not of epigenetic origin, as suggested by (Sandstad 2010) oppose the view that the two mineralized horizons are of sedimentary origin.

By geological mapping of the Nussir copper deposit from Profile 10 and west, it was striking that the Stangvatn Formation followed a stratigraphic sequence, as illustrated in the lithostratigraphy of the Stangvatn Formation (Figure 7). The Stangvatn conglomerate in the bottom was overlaid by sandstone layers (footwall slate), and the Lower mineralized horizon was overlaid by new sandstone layers (mid wall slate). Further up, a siltstone layer (hanging wall slate) covered the Upper mineralized horizon (Figure 32). Structural measurements indicated that all the layers in succession had a dip against NE, and was folded in an anticline fold with a fold axis NE-SW (Figure 44). However, structures indicated that the succession was faulted or folded further than the macroscopic NE-SW fold. The structural measurements were somewhat limited and did not give a good overview of the structural development west towards Skinnfjellet fault. Based on studies conducted by (Reitan 1963) it has previously been speculated that the two mineralized horizons were caused by a thrust fault towards NE as the basis for the formation of duplex structures. Reitan (1963) assessed the contact between Saltvatn Group and Nussir Group as tectonic, where Saltvatn Group has been pushed up and over the Nussir Group. Later studies by Pharaoh et al. (1983) concluded that there is weak evidence of such a tectonic contact. Viola et al. (2008) performed structural and ore geological surveys and interpretation of geophysical data from the western part of Repparfjorden. They pointed out that there were non-structural measurements that could support a thrust fault towards NE between Nussir Group and Saltvatn group. This may indicate that the two mineralized horizons not have been able to repeat in form of a duplex structure associated with a NE thrust. They believed instead that the structural measurements gave indications of a tectonic contact where Nussir group forms hanging wall with top to the SE transport direction above the Saltvatn Group. Viola et al. (2008) concluded that the formation of Nussir copper deposit could have been formed in connection with the synkinematic fluids that migrated down in shear zones at the escarpment of Nussir group towards SE in the formation of Skinnfjellet Thrust. This contradicts the impression of great similarities between the Upper- and Lower mineralized horizon. The results from the mineral zonation and chemical analyses indicated that the two mineralized horizons was equal. According to previous studies of SSC deposits, it was unlikely that similar mineral zonation as observed in the Upper- and Lower mineralized horizons could be formed if they were of sedimentary origin (pers.med. Rune Berg Larsen).

Hydrothermal fluids precipitate sulphides as they reached a reducing barrier. With the short distance between the Upper- and Lower horizon, they do not seem to be of sedimentary origin. Viola et al (2008) states that Nussir west have been subjected to a dextral ductile deformation (see Figure 14), which could have caused a thrust fault of the mineralized horizon in form of a duplex structure. The comparison of the two mineralized horizons showing a high degree of similarity between the Upper- and Lower mineralized horizons may indicate that the mineralized dolomite-containing layers was deposited as a lateral sedimentary unit where oxidized epigenetic fluids subsequently circulated via cracks associated with tectonic activity. In this way, copper minerals could have replaced diagenetic pyrite and deposited sulphides as fluids encountered the reducing barrier of the dolomite-rich layer. Subsequent dextral deformation could result in a duplex structure in which the western part of Nussir ore was pushed upon the other. Arguments as the similarity in the mineralization of sulphides, the

chemical analysis and the apparent similarity between the drill core NUS-DD-13-012 and NUS-DD-13-003. The observed slate-bearing mineralized horizon in drill core NUS-DD-13-002 suggests that it formed a sulphide-bearing slate that was located below the copper-bearing dolomite layer. The absence of observed duplex structures by geological mapping and thin section observations, and the fact that the underlying Stangvatn conglomerate not were observed in the Upper mineralized horizon, indicates that the two mineralized horizons in the western part of Nussir copper deposit have formed as two sedimentary layers. It seems necessary to do further and and more detailed studies of the Nussir deposit to clarify its origin.

Drill hole geophysical logg from NGU of drill core log of NUS-DD-13-004, indicated good induced polarization effect (IP-effect) from the Upper- and Lower mineralized horizons (Figure 98). The greatest peaks in the IP-effect was centred in the area where chalcocite were observed in thin section in the drill core samples. This corresponded well with the standard chargeability of sulphide minerals were chalcocite have chargeability 13.3 ms, while the chargeability of chalcopyrite is 9.4 ms and 6.3 ms in bornite (Jones 2007). The natural gamma radiation showed differences between the Upper- and Lower mineralized horizon, and could indicate that the host rock of the Upper mineralized horizon contains a higher concentration of feldspar minerals or that the natural gamma radiation marked a lithological boundary (Figure 90).

7 Conclusions

- In this study, two mineralized horizons in the Nussir copper deposit in Kvalsund Municipality, Finnmark County, were compared. The mineralized horizons (The Upper mineralized horizon and the Lower mineralized horizon) was found by diamond drilling conducted by Nussir ASA in the western part of Nussir West.
- Geological mapping, re-logging of diamond drill cores, thin section study of core samples, micro probe analysis of thin sections, analysis of data from chemical analysis of the mineralized sections and correlation of geophysical measurements in drill holes have been performed.
- Several different methods have been employed when analysing the chemical composition of drill core samples. In particular, one set of methods was utilized for the samples analysed before 2008, and another set for the samples from 2008 and later. This was strongly indicated when doing multivariate analysis on data from different drill holes. These differences should be taken into account in further use of the data.
- Trace element composition of drill core data analysed before or after 2008 indicated great similarities between the two mineralized horizons and between these and the area in the east.
- Wavelength-dispersive X-ray spectrometer analysis supported a sedimentary origin of the Nussir copper deposit, but the geochemical processes that have formed the sediment-hosted strata bound copper deposits could not have precipitated copper sulphide with the same mineral-zonation as observed in the Upper- and Lower mineralized horizons.
- Re-logging, thin section observation and the analysis of trace element composition of drill cores supported the theory of a tectonic origin of the Upper- and Lower mineralized horizon. Dextral deformation could have thrust the sulphide-bearing dolomite towards east and formed duplex structures of the mineralized horizon. The absence of observed duplex structures contradicts a tectonic repetition of the Nussir copper deposit.
- Further investigation to determine the origin of the Upper- and Lower mineralized horizons seems necessary.

8 Further work

The Nussir copper deposit should be dated to performe a comparison to the other sediment-hosted stratabound copper deposits in the world.

Fluid inclusions in quartz and calcite in veins should be studied to get a better understanding of the chemical properties of the copper-bearing fluids that have transported the sulphides.

The δS -concentration from the Upper- and Lower mineralized horizon should be compared.

9 References

Agresti, A. (1996). "An introduction to categorical data analysis John Wiley and Sons." Inc., Publication.

Andersen, M. C. (1987). Kvalsund Cu- (Ag, Au)- forekomst. Resultater av diamoantboring 1986 og forslag til mineraliserings modell.

Austin, T. U. o. T. a. (2014). "Principal Component Analysis." from [www.utexas.edu/.../PrincipalComponentAnalysis Outliers Validation](http://www.utexas.edu/.../PrincipalComponentAnalysis%20Outliers%20Validation) Reliability.ppt.

Cailteux, J. L. H., A. B. Kampunzu, C. Lerouge, A. K. Kaputo and J. P. Milesi (2005). "Genesis of sediment-hosted stratiform copper–cobalt deposits, central African Copperbelt." Journal of African Earth Sciences **42**(1–5): 134-158.

Clemens, R., P. Filzmoser, R. Garrett and R. Dutter (2008). Statistical data analysis explained, Wiley.

Cliff D. Taylor, K. J. S., Jeff L. Doebrich, Greta J. Orris, Paul D. Denning, and M. J. Kirschbaum (2005). "Geology and Nonfuel Mineral Deposits of Africa and the Middle East " Open-File Report 2005–1294-E

Cox, D. P., D. A. Lindsey, D. A. Singer, B. C. Moring and M. F. Diggles (2007). "Sediment-Hosted Copper Deposits of the World: Deposit Models and Database." USGS.

Dalsegg, E., H. Elvebakk and J. S. Rønning (2013). Geofysiske bakke- og borehullsmålinger ved Nussir i 2013 Kvalsund kommune, Finnmark.

Deer, W. A., R. A. Howie and J. Zussman (1992). An introduction to the rock-forming minerals. England, Pearson Education Limited.

Esbensen, K. H., D. Guyot, F. Westad and L. P. Houmoller (2002). Multivariate data analysis: in practice: an introduction to multivariate data analysis and experimental design, Multivariate Data Analysis.

Folk, R. (2005). "Nannobacteria and the formation of framboidal pyrite: Textural evidence." Journal of Earth System Science **114**(3): 369-374.

Gaál, G. and R. Gorbatshev (1987). "An Outline of the precambrian evolution of the baltic shield." Precambrian Research **35**(0): 15-52.

Helsel, D. R. (2006). "Fabricating data: How substituting values for nondetects can ruin results, and what can be done about it." Chemosphere: 6.

- Hitzman, M. W., D. Selley and S. Bull (2010). "Formation of Sedimentary Rock-Hosted Stratiform Copper Deposits through Earth History." Economic Geology **105**(3): 627-639.
- Hölttä, P., V. Balagansky, A. A. Garde, S. Mertanen, P. Peltonen, A. Slabunov, P. Sorjonen-Ward and M. Whitehouse (2008). "Archean of Greenland and Fennoscandia." Episodes **31**(1): 13-19.
- JEOL (2011). "Electron Beam Microprobes Analyzers (EPMA)."
- Joint Ore Reserves Committee of The Australasian Institute of Mining and Metallurgy, A. I. o. G. a. M. C. o. A. J. (2012). "Australasian Code for Reporting of Exploration Results, Mineral Resources and Ore Reserves." The JORC Code, 2012 Edition. from http://www.jorc.org/docs/JORC_code_2012.pdf
- Jones, F. (2007). "Chargeability." Retrieved 06/28/2007, from <http://www.eos.ubc.ca/ubcgif/iag/foundations/properties/2physprop-iag.htm>.
- Kampunzu, A. B., J. L. H. Cailteux, A. F. Kamona, M. M. Intiomale and F. Melcher (2009). "Sediment-hosted Zn–Pb–Cu deposits in the Central African Copperbelt." Ore Geology Reviews **35**(3–4): 263-297.
- Lahtinen, R. (2012). "Main geological features of Fennoscandia." Geological Survey of Finland Special Paper 53: 13-18.
- Lahtinen, R., A. A. Garde and V. A. Melezhik (2008). "Paleoproterozoic evolution of Fennoscandia and Greenland." Episodes **31**(1): 20.
- Lobach-Zhuchenko, S. B., V. P. Chekulayev, S. A. Sergeev, O. A. Levchenkov and I. N. Krylov (1993). "Archaean rocks from southeastern Karelia (Karelian granite greenstone terrain)." Precambrian Research **62**(4): 375-397.
- Maynard, J. B. (1983). Geochemistry of sedimentary ore deposits.
- McGowan, R., S. Roberts and A. Boyce (2006). "Origin of the Nchanga copper–cobalt deposits of the Zambian Copperbelt." Mineralium Deposita **40**(6-7): 617-638.
- McKERRROW, W. S., C. MAC NIOCAILL and J. F. DEWEY (2000). "The Caledonian Orogeny redefined." Journal of the Geological Society **157**(6): 1149-1154.
- Ofstad, V. B., Janusz Koziel, Rolf Lynum, Alexei Rodionov (2013). Helicopter-born magnetic, electromagnetic and radiometric geophysical survey in Repparfjord area, ALta and Kvalsund, Finnmark, NGU.

- Pharaoh, T. (1985). "Volcanic and geochemical stratigraphy of the Nussir Group of Arctic Norway—an early Proterozoic greenstone suite." Journal of the Geological Society **142**(2): 259-278.
- Pharaoh, T., D. Ramsay and O. Jansen (1983). "Stratigraphy and structure of the northern part of the Repparfjord-Komagfjord Window, Finnmark, Northern Norway." NORGES GEOLOGISKE UNDERSØKELSE BULLETIN(68): 1-&.
- Reitan, P. H. (1963). The geology of the Komagfjord tectonic window of the Raipas suite Finnmark, Norway. Oslo, Universitetsforlaget.
- Robb, L. (2005). Hydrothermal ore-forming processes, Blackwell publishing.
- Sandstad, J. S. (2008). "Geochemistry of drill cores from the Nussir copper deposit, Kvalsund, Finnmark, Northern Norway " NGU report 2008 055.
- Sandstad, J. S. (2010). Microscope and SEM (scanning electron microscope) investigations of thin sections from the Nussir copper deposits. NGU Report 2010.025, Geological Survey of Norway.
- Slabunov, A. I., S. B. Lobach-Zhuchenko, E. V. Bibikova, V. V. Balagansky, P. Sorjonen-Ward, O. I. Volodichev, A. A. Shchipansky, S. A. Svetov, V. P. Chekulaev, N. A. Arestova and V. S. Stepanov (2006). "The Archean of the Baltic Shield: Geology, Geochronology, and Geodynamic settings." Geotectonics **40**(6): 409-433.
- Viola.G, Sandstad.J.S, Nilsson.L.P and Heincken.B (2008). Structural and ore geological studies in the northwestern part of the Repparfjord Window, Kvalsund, Finnmark, Norway.
- Wheeler, A. (2012). "Resource estimation update." (Nussir project).
- Zientek, M. L., J. M. Hammarstrom and K. M. Johnson (2010). "Descriptive Models, Grade-Tonnage Relations, and Databases for the Assessment of Sediment-Hosted Copper Deposits- With Emphasis on Deposits in the Central African Copperbelt, Democratic Republic of the Congo and Zambia." USGS Scientific Investigations Report 2010-5090-J: 154.

10. Appendix A

Description of the sedimentary stratigraphy of the Repparfjord-Komagfjord tectonic window

Table A24. Stratigraphy of northern part of the Repparfjord-Komagfjord Window, modified after (Pharaoh, Ramsay et al. 1983)

Caledonian Orogeny(Kalak Nappe Complex)		
Lomvatn Formation (Vendian age 650 – 543 Ma)		
Upper Saraby Member	Shales and siltstones, small amount of sandstone Strongly affected by Caledonian deformation with a distinctly phyllitic appearance	Interpretation Strong Caledonian deformation.
Lower Saraby Member	Shales and siltstones interbedded with feldspathic sandstone band Parallel-laminated shale and siltstones Well sorted sandstone Sharp contact between sandstone beds and siltstone Ripple cross-lamination in sandstone	Hermannvatn Member is associated with a shallow marine transgression. The variability in thickness of the Hermannvatn Member is possibly a reflection of irregularities in the palaeotopography. The Lomvatn Formation is of Vanadian-Cambrian age and underlies the Caledonian thrust sheet, Kalak Nappe Complex.
Hermannvatn Member	Quartz conglomerate and quartz-feldspathic arenites Well sorted and grain-supported conglomerate Well-bedded pale grey-greenish quartz arenite Cross-bedding	
Angular Unconformity (Svecokarelian orogeny)		
Porsa Group		
Bierjav'ri Formation	Green tuffaceous volcanic lithologies, grey slates, sandstone and thin carbonate horizons Lower part is dominated by greenish-colored sediments of volcanoclastic origin Contains fragments of dolomitic carbonate probably eroded from the underlying Vargsund Formation Upper part consist of grey slates with thin sandstones, carbonates and volcanoclastic units Horizons of bluish-grey micritic limestone containing simple, low amplitude domes and unbranched short columnar stromatolites Represent the highest level of the Raipas Supergroup exposed in the Komagfjord window	Interpretation Sedimentary structure and lithofacies suggest that the entire sequence became deposited in shallow water. Pillow lavas of the Nussir Group underlies the sediments. Pillow lavas were probably erupted in deep water. It seems likely that the basin of deposition suffered shallowing prior to deposition of the Porsa Group. The presence of a well-developed basal

Kvalsund Formation	<p>Greyish-black graphitic slate or phyllite</p> <p>Locally rich in pyrite</p> <p>Formation reflects considerable thickening of the sequence in the hinges of macroscopic Svecokarelian folds, and strong attenuation on their limbs</p>	<p>conglomerate may even imply erosion of the substrate, although angular discordance is difficult to demonstrate.</p> <p>Palaeoenvironmental indicator in the Vargsund Formation is the</p>
Vargsund Formation	<p>Grain-supported conglomerate</p> <p>Containing sub-angular pebbles of vein quartz and jasper in fine-grained, phyllitic matrix</p> <p>Cobbles of acid gneiss is found in the conglomerate</p> <p>The basal conglomerate is relatively thin and discontinuous</p> <p>The conglomerate passes up into a sequence of thinly interbedded limestones, dolomite and purplish shales</p> <p>The dolomite is coarsely crystalline as a consequence of recrystallization during deformation</p> <p>Ripple- and parallel-lamination are occasionally found</p> <p>Beds of planar cross-bedded quartzitic sandstone up to 60cm thick occur within the dolomite at certain horizon</p> <p>Stomatolites is found in the dolomite</p>	<p>Formation is the widespread development of algal stromatolites throughout the district. The Vargsund Formation most likely deposited in shallow water.</p> <p>The Kvalsund Formation was probably deposited in slightly deeper water, in a basin with sluggish circulation promoting euxinic condition (anoxic).</p> <p>The Bierajav'ri Formation marked a return to condition of more active marine circulation. This environment was periodically disturbed by the influx of volcanoclastic material.</p> <p>The sediments in the upper part of the formation are mostly shales and stromatolitic carbonates indicating a shallow-water environment with low current energy.</p>
Disconformity		
Nussir Group		
Svartfjell Formation	<p>Metabasaltic lavas</p> <p>Matabasaltic lavas exposed in the cores of prominent anticlinal structures in the Vargsund district, forming the hills of Stortinden, Segelnesfjellet, Skinnfjellet and Nussir</p> <p>Most lavas show pillow texture, non-vesiculare and plagioclase-microphyric</p>	<p>Interpretation</p> <p>Primary textures in lavas and tuffs indicate an origin by extrusive volcanism in a subaqueous environment.</p> <p>Tuffs and tuffites of Krokvatn Formation</p>

	Units of unpillowed metabasalt,, and local thin gorizons of metabasaltic tuff and meta-hyaloclastite breccia	interpret as aquagene tuffs generated by the fragmentation of chilled basaltic lava in a submarine environment.
Krokvatn Formation	<p>Tuffaceous greenstones</p> <p>Interbedded by with thinner units of metabasalt</p> <p>Only exposed along the southern flank of Nussir</p> <p>Graded lithic sandstones with clastic material of mafic volcanogenic origin, interbedded with finer-grained material form the same source</p> <p>Thin lenses of quartz grains in the lithic sandstone is derived from a non-volcanic source and may have erosional bases</p> <p>Parallel and ripple lamination in the finer sediments</p> <p>Serpentinous fragmental lithology's</p> <p>A thin unit of dolomite (3 m thick) is interbedded with the tuffites near the base of the formation in the west</p> <p>Pillow texture</p> <p>Sedimentary texture show that the rocks is right-way-up</p>	<p>The spectrum from hyaloclastic breccia to poorly bedded tuff and well-bedded, graded tuffite is considered to represent increased sedimentary reworking of the fragmented basalt with distance from the source area.</p> <p>The early vesicular lavas interbedded with tuffites containing a dolomite horizon may have been erupted in relatively shallow water.</p> <p>The later lavas are non-vesicular and probably erupted in deeper water.</p>
Conformable – Nussirjav'ri thrust		
Saltvatn Group		
Stangvatn Formation	<p>Purple polymict conglomerates and arkosic sandstones</p> <p>Clasts of microphyric lavas of dacitic composition</p> <p>The source of these clast has not so far been recognized within the Precambrian and northern Norway</p> <p>3 major fining upward cycles</p> <p>At the base of each cycle, a grain-supported conglomerate fine upwards into thinner interbedded units of trough cross-bedded arkosic sandstone</p> <p>Weathering nature of these arkosic metasandstone is a consequence of their carbonate cement</p> <p>Two major paleocurrent direction, paleoslope towards north</p>	<p>Interpretation</p> <p>Saltvatn Group locally oversteps the Magerfjell Formation to rest upon the Båtdalselv Formation. This is believed to be the consequence of an erosional unconformity.</p> <p>Sequence of clastic sediments deposited under predominantly fluvial condition.</p> <p>The Ulverygg Formation appears deposited by braided streams flowing from a siliceous source area to the west and north, probably fault-bounded.</p> <p>Lenoid bodies of</p>
Dypelv Formation	<p>Green polymict conglomerates</p> <p>Interbeds of sandstones</p>	

	<p>Pebbles, cobbles and boulders of metabasaltic lava, metatuffite and vein quartz</p> <p>Rare pebbles of quartzite, jasper, dolomite and intermediate volcanic rocks</p> <p>Sub-rounded – sub-angular clasts in poorly sorted schistose matrix composed of greenstone fragments and quartzo-feldspathic material.</p> <p>Reverse grading in some of the conglomerates</p> <p>An overall fining-upward tendency of the whole assemblage</p> <p>Thickness variation, reflecting deformation, thickening in the hinge of the Nussir structure and strong attenuation on its limbs</p>		<p>conglomerate suggest locally distortion of alluvial fans.</p> <p>The Dypelv Formation reflects the change to a new source area, dominated by greenstone volcanic.</p> <p>Coarse conglomerate and poor sorting indicate that this source was rather closer than Ulverygg formation sediments.</p> <p>Matrix-supported conglomerates in the lower part of the sequence is probably generated as volcanoclastic debris flows in a terrestrial environment.</p> <p>It suggest that some of the conglomerates is fanconglomerate created by subaerial mudflows on alluvial fans.</p> <p>Interbedded sandstones probably became deposited by braided streams reworking the surface of the fan, a process that became increasingly important towards the upper part of the formation.</p> <p>Stangvatn Formation reflects a change of provenance, this time to a southerly source area dominated by intermediate and acid volcanic rocks.</p> <p>The large-scale cyclicity may reflect rejuvenation of the source by tectonic uplift.</p> <p>Ulveryggen vs Doggeelv: Ulveryggen is interpreted as less mature sediment deposited in floodplains and minor alluvial fans</p>
<p>1 Ulveryggen Formation</p> <p>2 Dåg’gejåkka – doggeelv Formation</p>	<p>1 White or grey, lithic, feldspathic and quartzitic sandstones and polymict conglomerate (1000m thick).</p> <p>Massive lensoid bodies of conglomerate</p> <p>Sub-rounded to rounded pebbles of vein quartz and greenstone</p> <p>Quartz rich sandy matrix</p> <p>Fining upward cycles</p> <p>Coarse-grained trough cross-bedded sandstone that fine upward into pale greenish or greyish siltstone</p> <p>Paleocurrent direction towards NE-SE</p> <p>Scour-and-fill in the unconformity</p>	<p>2 White quartzitic metasandstone</p> <p>Well sorted with impurities as mica and sodic feldspar</p> <p>Pebbly lenses with clasts of vein quartz, chert and occasionally acid banded gneiss</p> <p>Parallel bedding and planar cross-bedding, transport towards the south-west</p> <p>Overlain with strong angular unconformity by the much less deformed Lomvatn Formation</p> <p>1 and 2 forming a major anticlinale fold with the Holmvatn Group in the core</p> <p>Correlation between 1 and 2</p>	

		<p>flanking a fault-bounded upland to the north-west. Most of the sediments became deposited in braided stream channels widening across a coast-marginal braidplain.</p> <p>South-west of ulveryggen the more mature sandstones of the Doggeelv formation appear to have been deposited in a shallow marine environment dominated by persistent long-shore drift towards the south-west.</p>
Unconformity (tectonic unconformity)		
Holmvatn Group (Precambrian 4600 – 541 Ma)		
Magerfjell Formation	<p>Metabasaltic lava</p> <p>Pillow texture</p> <p>Tholeiitic composition</p>	<p>Interpretation</p> <p>Deformation and metamorphism during the Svecokarelian Orogeny hinders sedimentary facies interpretation.</p> <p>Poor sorting, matrix-supported conglomerate and the absence of sedimentary structures suggests that they may have originated as debris-flow deposits.</p> <p>Boulder of gneiss and granite implies nearby source composed of these lithologies possible created by faulting.</p> <p>Spasmodic volcanism during formation of Holmvatn Group, creation of tuffaceous matrix and greenstone clasts in the conglomerate, overlain by tuffs and lava.</p> <p>The presence of sporadic carbonate, pillow-structure and minor cross bedding in</p>
Båtdalselv Formation	<p>Quartzo-feldspathic schists</p> <p>Cross-bedding</p> <p>Upper part dominated by amphibolitic schist</p> <p>Thin beds of dolomite</p> <p>These lithologies were probably lavas and tuffs of basaltic and andesitic composition</p>	
Markfjell Formation	<p>Polymict greenstone conglomerate</p> <p>Lowest unite of Precambrian stratigraphy</p> <p>Interbeds containing poorly sorted volcanoclastic sediments and metavolcanics</p> <p>Matrix consist of quartzo-feldspatic clastic material with mixture of volcanogenic material</p>	

		<p>sediments could indicate a subaqueous deposit environment.</p> <p>Local absent of the Magerfjell Formation is here considered as a consequence of the unconformity at the base of the Doggeelv Formation.</p>
--	--	--

11. Appendix B

Geochemical analysis – univariate statistics

Table B25. Elements, nomenclature and unite of analysed elements in drill core samples.

Elements	Nomenclature	Unit
Aluminium	Al	%
Antimony	Sb	ppm
Asimut	As	ppm
Barium	Ba	ppm
Beryllium	Be	ppm
Bismuth	Bi	ppm
Boron	B	ppm
Cadmium	Cd	ppm
Calcium	Ca	%
Cerium	Ce	ppm
Chromium	Cr	ppm
Cobalt	Co	ppm
Cooper	Cu	%
Cooper/Sulphur	Cu/S	%
Gallium	Ga	ppm
Germanium	Ge	ppm
Gold	Au	ppm
Iron	Fe	%
Lanthanum	La	ppm
Lead	Pb	ppm
Lithium	Li	ppm
Magnesium	Mg	%
Manganese	Mn	ppm
Mercury	Hg	ppm
Molybdenum	Mo	ppm
Nickel	Ni	ppm
Niobium	Nb	ppm
Palladium	Pd	ppb
Phosphorus	P	ppm
Platinum	Pt	ppb
Potassium	K	%
Rubidium	Rb	ppm
Scandium	Sc	ppm
Selenium	Se	ppm
Silver	Ag	ppm
Sodium	Na	%
Strontium	Sr	ppm
Sulphur	S	%
Tantalum	Ta	ppm
Tellurium	Te	ppm
Thallium	Tl	ppm
Thorium	Th	ppm
Tin	Sn	ppm
Titanium	Ti	%
Tungsten	W	ppm
Uranium	U	ppm
Vanadium	V	ppm
Yttrium	Y	ppm
Zinc	Zn	ppm
Zirconium	Zr	ppm

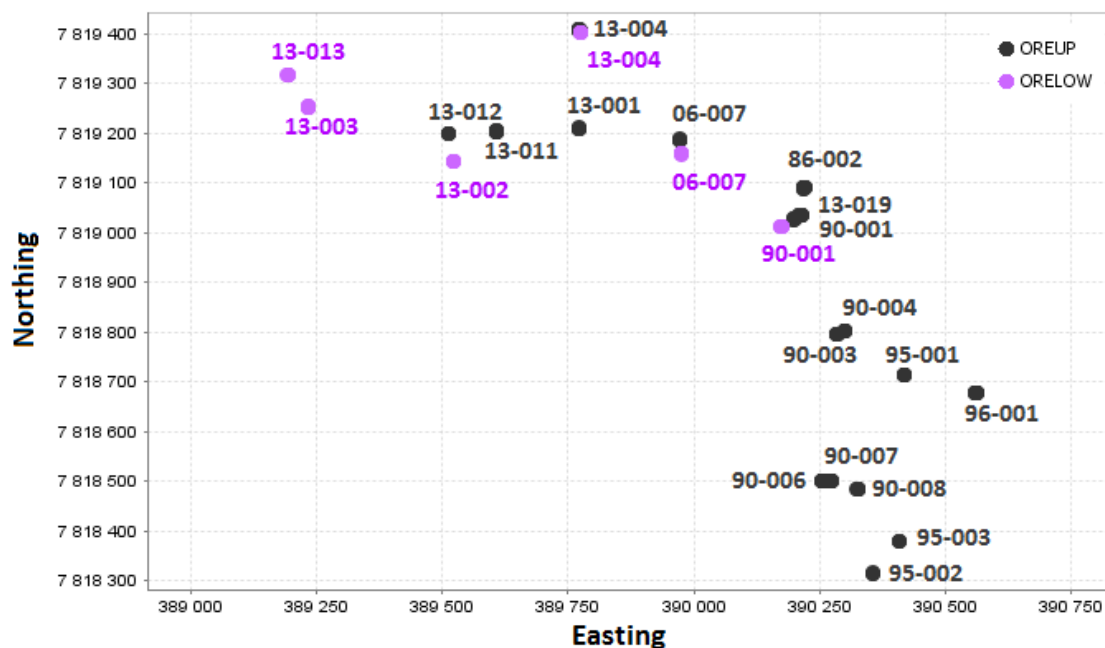


Figure B99. Attribute map showing the surface location of boreholes included in the unimodal statistical survey of the Upper mineralized horizon (dark grey) and the Lower mineralized horizon (purple). Map derived from ioGAS-64.

Table B26. Unimodal statistics of elements in samples from the Upper mineralized horizon (Oreup) and the Lower mineralized horizon (Orelow), 1:9. Table derived from ioGAS-64.

Unimodal statistics		Li ppm	Ag ppm	Bi ppm	Sb ppm	Pb ppm	As ppm
ORELOW	Count Numeric	5	32	5	7	29	1
	Min	4	0.6	2	5	4	5
	Max	8	101	8	7	432	5
	Mean	6.2	30.5520147	5.2	6	45.5517241	5
	Median	6	25.6	4	6	15	5
	Variance	3.2	730.99771	7.2	0.66666667	11574.1133	0
	Standard.Dev.	1.78885438	27.0369693	2.68328157	0.81649658	107.583053	0
OREUP	Count Numeric	55	109	19	8	94	29
	Min	2	0.5	2	6	2	5
	Max	21	76	14	9	272	162
	Mean	5.78181818	18.9412399	4.73684211	7.125	23.9255319	36.3793103
	Median	5	14.5	3	7	15.5	17
	Variance	13.7292929	314.235154	10.6491228	1.26785714	1583.91913	2180.74384
	Standard.Dev.	3.70530605	17.7266792	3.26329937	1.12599163	39.7984815	46.6984351

Table B27. Unimodal statistics of elements in samples from the Upper mineralized horizon (Oreup) and the Lower mineralized horizon (OreLOW), 2:9. Table derived from ioGAS-64.

Unimodal statistics		S pc	Cd ppm	Ba ppm	Ca pc	Zn ppm	Mo ppm
ORELOW	Count Numeric	30	12	30	30	30	27
	Min	0.02	0.5	50	0.88	20	2
	Max	1.26	1.4	2110	23.37	156	180
	Mean	0.50866667	0.76666667	407.166667	13.3383333	66.9	25.4814815
	Median	0.46	0.7	210	14.8	48	18
	Variance	0.1269154	0.06060606	190720.489	38.0366557	1566.16207	1171.25926
	Standard.Dev.	0.35625188	0.24618298	436.715569	6.16738646	39.5747656	34.2236652
OREUP	Count Numeric	93	17	102	102	102	83
	Min	0.01	0.5	14	0.17	15	1
	Max	1.82	1.8	4150	27.7	533	104
	Mean	0.39483871	0.81764706	378.588235	9.30441176	71.1568627	13.4819277
	Median	0.23	0.7	98.5	10.38	51.5	10
	Variance	0.17031003	0.13279412	398769.413	40.4866982	5960.72763	229.862474
	Standard. Dev.	0.41268636	0.36440927	631.481918	6.36291585	77.2057487	15.1612161

Table B28. Unimodal statistics of elements in samples from the Upper mineralized horizon (Oreup) and the Lower mineralized horizon (OreLOW), 3:9. Table derived from ioGAS-64.

Unimodal statistics		Na pc	Be ppm	P_ pm	Sn ppm	Au ppm	Sr ppm
ORELOW	Count Numeric	29	13	30	0	33	30
	Min	0.02	0.5	0.025		0.003	26
	Max	2.5	1.7	690		0.764	395
	Mean	1.04241379	0.86923077	266.006833		0.20063636	224.633333
	Median	1.06	0.8	260		0.15	262
	Variance	0.63248325	0.14230769	28579.6879		0.04375799	10417.3437
	Standard. Dev.	0.79528816	0.37723692	169.05528		0.2091841	102.065389
OREUP	Count Numeric	101	31	102	1	131	102
	Min	0.01	0.5	0.015	25	0.002	4
	Max	3.1	2.2	850	25	4.34	445
	Mean	0.53861386	1.08709677	162.277667	25	0.17372261	122.107843
	Median	0.04	0.9	0.065	25	0.06025444	104
	Variance	0.63396606	0.24182796	49841.8606	0	0.21208976	9906.55261
	Standard. Dev.	0.79621986	0.49176006	223.252907	0	0.46053205	99.5316664

Table B29. Unimodal statistics of elements in samples from the Upper mineralized horizon (Oreup) and the Lower mineralized horizon (OreLOW), 4:9. Table derived from ioGAS-64.

Unimodal statistics		Co ppm	Pd ppb	K pc	Ni ppm	Rb ppm	Th ppm
ORELOW	Count Numeric	30	26	30	30	2	2
	Min	8	1	0.35	10	52	6
	Max	40	79	3.53	53	52	7
	Mean	21.3333333	10.602047	1.441	23.7333333	52	6.5
	Median	18	2	1.28	20.5	52	6.5
	Variance	108.505747	461.126563	0.65713345	140.409195	0	0.5
	Standard. Dev.	10.4166092	21.4738577	0.81063768	11.8494386	0	0.70710678
OREUP	Count Numeric	102	68	102	102	5	32
	Min	2	1	0.08	5	51	5
	Max	118	1200	5.16	52	96	13
	Mean	19.254902	44.346425	1.31990196	20.9411765	68.4	6.84375
	Median	14	3.76675212	0.78	20	53	7
	Variance	393.577946	27964.0726	1.70025445	126.194525	509.3	2.45866935
	Standard.Dev.	19.838799	167.224617	1.30393805	11.2336337	22.567676	1.56801446

Table B30. Unimodal statistics of elements in samples from the Upper mineralized horizon (Oreup) and the Lower mineralized horizon (OreLOW), 5:9. Table derived from ioGAS-64.

Unimodal statistics		Mg pc	Se ppm	Zr ppm	Pt ppb	V ppm	U ppm
ORELOW	Count Numeric	30	0	5	7	30	7
	Min	0.6		13	6	4	7
	Max	6.64		40	87	1380	4040
	Mean	2.81133333		26.6	40.7142857	187.066667	1209.57143
	Median	1.785		26	24	33	150
	Variance	4.33968782		99.3	1313.90476	152888.685	3741967.95
	Standard.Dev.	2.08319174		9.96493853	36.2478242	391.009827	1934.4167
OREUP	Count Numeric	102	0	58	33	102	31
	Min	0.14		10	2.00528582	2	5
	Max	8.43		99	1920	141	282
	Mean	3.9672549		36.1206897	134.751292	27.6078431	18.5483871
	Median	4.24		33	12	18	7
	Variance	6.68924387		351.862371	142346.923	864.082314	2438.72258
	Standard.Dev.	2.58635726		18.7579949	377.288911	29.3952771	49.3834241

Table B31. Unimodal statistics of elements in samples from the Upper mineralized horizon (Oreup) and the Lower mineralized horizon (OreLOW), 6:9. Table derived from ioGAS-64.

Unimodal statistics		Ti pc	B ppm	Ce ppm	Cr ppm	Al pc	Y ppm
ORELOW	Count Numeric	30	1	5	30	30	5
	Min	0.0149279	6	9	12	0.41	5
	Max	0.34	6	30	118	7.13	9
	Mean	0.11542571	6	16	41.1333333	3.35433333	8
	Median	0.1	6	11	31	3.51	9
	Variance	0.00533038	0	80.5	665.154023	2.7142254	3
	Standard.Dev.	0.07300948	0	8.97217922	25.7905801	1.64749064	1.73205081
OREUP	Count Numeric	102	7	58	102	102	58
	Min	0.00252111	5	6	7	0.12	6
	Max	0.41	8	49	379	8.27	24
	Mean	0.0818269	5.85714286	23.1724138	90.9117647	2.34068627	7.9137931
	Median	0.04240769	6	20	77	1	7
	Variance	0.00931715	1.14285714	120.496068	5022.73471	5.75372131	6.6415608
	Standard.Dev.	0.09652538	1.06904497	10.9770701	70.8712545	2.39869158	2.57712258

Table B32. Unimodal statistics of elements in samples from the Upper mineralized horizon (Oreup) and the Lower mineralized horizon (OreLOW), 7:9. Table derived from ioGAS-64.

Unimodal statistics		Ga ppm	La ppm	Fe pc	Hg ppm	Tl ppm	Mn ppm
ORELOW	Count Numeric	24	30	30	3	0	30
	Min	10	6	0.57	1		378
	Max	20	100	2.29	2		7230
	Mean	10.8333333	23.7666667	1.41366667	1.33333333		4377.56667
	Median	10	20	1.4	1		4787
	Variance	7.97101449	479.771264	0.24517575	0.33333333		5245077.36
	Standard.Dev.	2.82329851	21.9036815	0.49515225	0.57735027		2290.21339
OREUP	Count Numeric	35	102	102	12	1	102
	Min	5	5	0.51	1	10	40
	Max	30	30	3.03	4	10	10266
	Mean	14.1428571	16.3039216	1.30519608	1.75	10	4577.7549
	Median	10	18	1.27	1.5	10	5166
	Variance	33.0672269	37.3423607	0.20366679	0.93181818	0	8819991.69
	Standard.Dev.	5.75041102	6.11083961	0.45129457	0.9653073	0	2969.84708

Table B33. Unimodal statistics of elements in samples from the Upper mineralized horizon (Oreup) and the Lower mineralized horizon (OreLOW), 8:9. Table derived from ioGAS-64.

Unimodal statistics		Cu pc	Cu/S pc	Te ppm	Sc ppm	W ppm	Ge ppm
ORELOW	Count Numeric	35	30	0	30	0	0
	Min	7.90E-05	0.0037137		1		
	Max	4.49	3.80851064		14		
	Mean	1.29643672	2.65142137		4.4		
	Median	0.985	2.97857143		4		
	Variance	1.30860838	1.18520528		7.14482759		
	Standard.Dev.	1.14394422	1.08867133		2.67298103		
OREUP	Count Numeric	146	93	0	98	0	0
	Min	3.00E-04	0.18952984		1		
	Max	4.2	97.2544932		18		
	Mean	0.85759804	3.9345348		3.68367347		
	Median	0.66026783	2.3475		2		
	Variance	0.69745216	114.697007		11.9504523		
	Standard.Dev.	0.83513601	10.7096689		3.45694263		

Table B34. Unimodal statistics of elements in samples from the Upper mineralized horizon (Oreup) and the Lower mineralized horizon (OreLOW), 9:9. Table derived from ioGAS-64.

Unimodal statistics		Ta ppm	Nb ppm	Pt/Pd ppb	Pd/Pt ppb	Cu/Fe pc
ORELOW	Count Numeric	0	0	7	7	30
	Min			0.93670886	0.6091954	9.99E-05
	Max			1.64150943	1.06756757	2.48066298
	Mean			1.35797943	0.76343867	1.02742539
	Median			1.44444444	0.69230769	1.05887215
	Variance			0.06511305	0.02866257	0.43767194
	Standard.Dev.			0.25517259	0.16930024	0.66156779
OREUP	Count Numeric	0	32	33	33	102
	Min		5	0.20252025	0.12339449	1.43E-04
	Max		7	8.10408944	4.93777778	3.18072289
	Mean		6.09375	1.99094092	0.94931738	0.66608075
	Median		6	1.55555556	0.64285714	0.52071213
	Variance		0.41028226	2.80202284	0.82263081	0.44399132
	Standard.Dev.		0.64053279	1.67392438	0.90698997	0.66632674

Multivariate analysis – comparison of the Upper- and Lower mineralized horizon

Table B35. Boreholes (BHID) included in the vertical comparison between the Upper- and the Lower mineralized horizon. Table show the depth-interval of mineralized horizon in each borehole.

BHID	Depth	
	From (m)	To (m)
NUS-DD-06-007	24.3	29
NUS-DD-06-007	79.5	82.3
NUS-DD-13-001	17	21.8
NUS-DD-13-002	62.5	68
NUS-DD-13-003	142.6	146.7
NUS-DD-13-004	379.6	392
NUS-DD-13-004	407.7	412.5
NUS-DD-13-010	8.2	13.5
NUS-DD-13-011	24	30
NUS-DD-13-012	11.5	13.2
NUS-DD-13-013	7.4	11.4
NUS-DD-13-013	22.3	23.4
NUS-DD-13-019	44.6	50
NUS-DD-90-002	44	50
NUS-DD-90-003	40	45
NUS-DD-90-004	59	66
NUS-DD-90-006	40	48
NUS-DD-90-007	48	60
NUS-DD-96-001	355	363

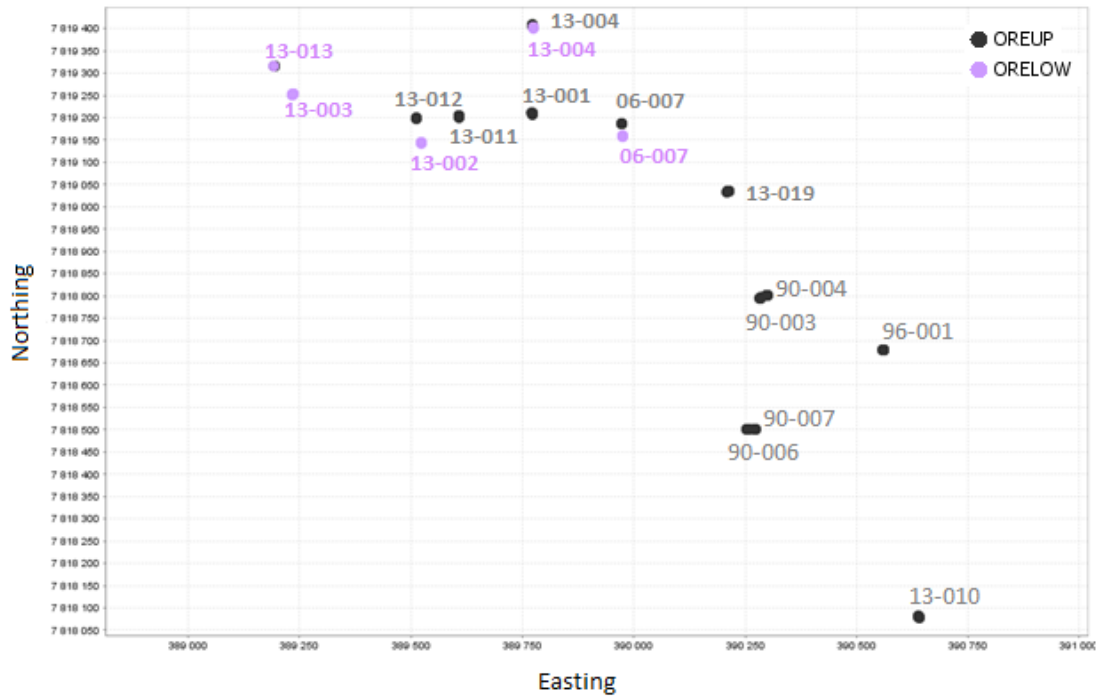


Figure B100. Attribute map showing the surface location of the included drill holes in the multivariate comparison between Upper mineralized horizon (Oreup, dark grey) and the Lower mineralized horizon (Orelow, purple). Map derived from ioGAS-64.

Table B36. Selected elements and descriptive statistics in the PCA model.

Descriptive Statistics			
	Mean	Std. Deviation	Analysis N
Al_prosent	3,2880494	2,25448588	53
Ca_prosent	10,532294	7,4967848	53
K_prosent	1,6116056	1,26860406	53
P_ppm	23.37748030	22.00060739	53
Sc_ppm	4,3543867	3,50179677	53
Sr_ppm	146,6986273	131.4114743	53
Cu_prosent	1.494873817	1.011657897	53
Ag_ppm	25,4239101	20,19348677	53
Co_ppm	18,0585608	14,81540394	53
Fe_prosent	1,3646650	,54008882	53

Table B37. Kaiser-Meyer-Olkin (KMO) and Bartlett's test in PCA mode.

KMO and Bartlett's Test		
Kaiser-Meyer-Olkin Measure of Sampling Adequacy.		,736
Bartlett's Test of Sphericity	Approx. Chi-Square	369,733
	df	45
	Sig.	,000

Table B38. Rotated component matrix of the first four components in PCA model.

Rotated Component Matrix^a

	Component			
	1	2	3	4
Al_prosent	,944	-,041	,047	,150
Ca_prosent	-,269	,843	-,192	-,084
K_prosent	,906	-,254	,047	,082
P_ppm	,958	,020	,085	,040
Sc_ppm	,916	-,135	,123	,114
Sr_ppm	,001	,919	-,053	-,068
Cu_prosent	,248	-,235	,294	,775
Ag_ppm	,045	,016	-,002	,948
Co_ppm	-,009	-,099	,922	,000
Fe_prosent	,201	-,124	,831	,224

Extraction Method: Principal Component Analysis.

Rotation Method: Varimax with Kaiser Normalization. ^a

a. Rotation converged in 5 iterations.

Table B39. Statistics of the discriminant analysis of the regression factor score.

Wilks' Lambda

Test of Function(s)	Wilks' Lambda	Chi-square	df	Sig.
1	,727	15,011	4	,005

Table B40. Classification results of discriminant analysis. Results given in counts and presents. 1 = Upper mineralized horizon, 2 = Lower mineralized horizon.

Classification Results^a

		Predicted Group Membership		Total
		1	2	
Original	Count	1	2	
		24	9	33
		5	13	18
	%	1	2	
		72,7	27,3	100,0
		27,8	72,2	100,0

a. 72,5% of original grouped cases correctly classified.

Multivariate analysis – comparison of the lateral variation between and within Zone 1, Zone 2 and Zone 3

Table B41. Boreholes (BHID) included in multivariate comparison of the lateral variation between and within Zone 1, 2 and 3 (hypothesis 2), Table 1:2. Depth interval, zone number and stratum number is given for each borehole.

BHID	Depth		Zone	Stratum number
	From (m)	To (m)		
NUS-DD-06-001	415	417	1	1
NUS-DD-06-002	505	512.5	1	2
NUS-DD-06-004	438.1	442.2	1	3
NUS-DD-06-007	24.3	29	2	4
NUS-DD-06-007	79.5	82.3	3	5
NUS-DD-08-001	196	198	1	6
NUS-DD-08-003	160.2	166	1	7
NUS-DD-08-003	174.2	177.1	1	8
NUS-DD-08-006	207.6	210.9	1	9
NUS-DD-08-011	134.5	144.3	1	10
NUS-DD-08-013	374	377.6	1	11
NUS-DD-08-014	320.2	339.9	1	12
NUS-DD-08-014	347.5	353.5	1	13
NUS-DD-08-015	422.9	425.6	1	14
NUS-DD-08-019	456.1	360	1	15
NUS-DD-08-020	485.4	488.7	1	16
NUS-DD-08-021	120.4	128.8	1	17
NUS-DD-08-023	124.2	129.9	1	18

Table B42. Boreholes (BHID) included in multivariate comparison of the lateral variation between and within Zone 1, 2 and 3 (hypothesis 2), Table 2:2. Depth interval, zone number and stratum number is given for each borehole.

NUS-DD-08-025	30.4	34	1	19
NUS-DD-08-026	93.5	95.7	1	20
NUS-DD-08-027	99.1	103.1	1	21
NUS-DD-08-029	140.5	145.2	1	22
NUS-DD-08-030	111.9	114.5	1	23
NUS-DD-11-001	120	123	1	24
NUS-DD-11-002	147	150	1	25
NUS-DD-11-004	452.6	459.8	1	26
NUS-DD-11-005	314	318	1	27
NUS-DD-11-006	541.4	552	1	28
NUS-DD-13-001	17	21.8	2	29
NUS-DD-13-002	62.5	68	3	30
NUS-DD-13-003	142.6	146.7	3	31
NUS-DD-13-004	379.6	392	2	32
NUS-DD-13-004	407.7	412.5	3	33
NUS-DD-13-010	8.2	13.5	2	34
NUS-DD-13-011	24	30	2	35
NUS-DD-13-012	11.5	13.2	2	36
NUS-DD-13-013	7.4	11.4	2	37
NUS-DD-13-013	22.3	23.4	3	38
NUS-DD-13-019	44.6	50	2	39
NUS-DD-90-002	44	50	2	40
NUS-DD-90-003	40	45	2	41
NUS-DD-90-004	59	66	2	42
NUS-DD-90-006	40	48	2	43
NUS-DD-90-007	48	60	2	44
NUS-DD-90-009	23	28	1	45
NUS-DD-90-012	77	92	1	46
NUS-DD-90-013	55	61	1	47
NUS-DD-90-015	74	75	1	48
NUS-DD-90-020	94	97	1	49
NUS-DD-90-021	86	100	1	50
NUS-DD-90-023	23	25	1	51
NUS-DD-90-026	90	91	1	52
NUS-DD-96-001	355	363	2	53

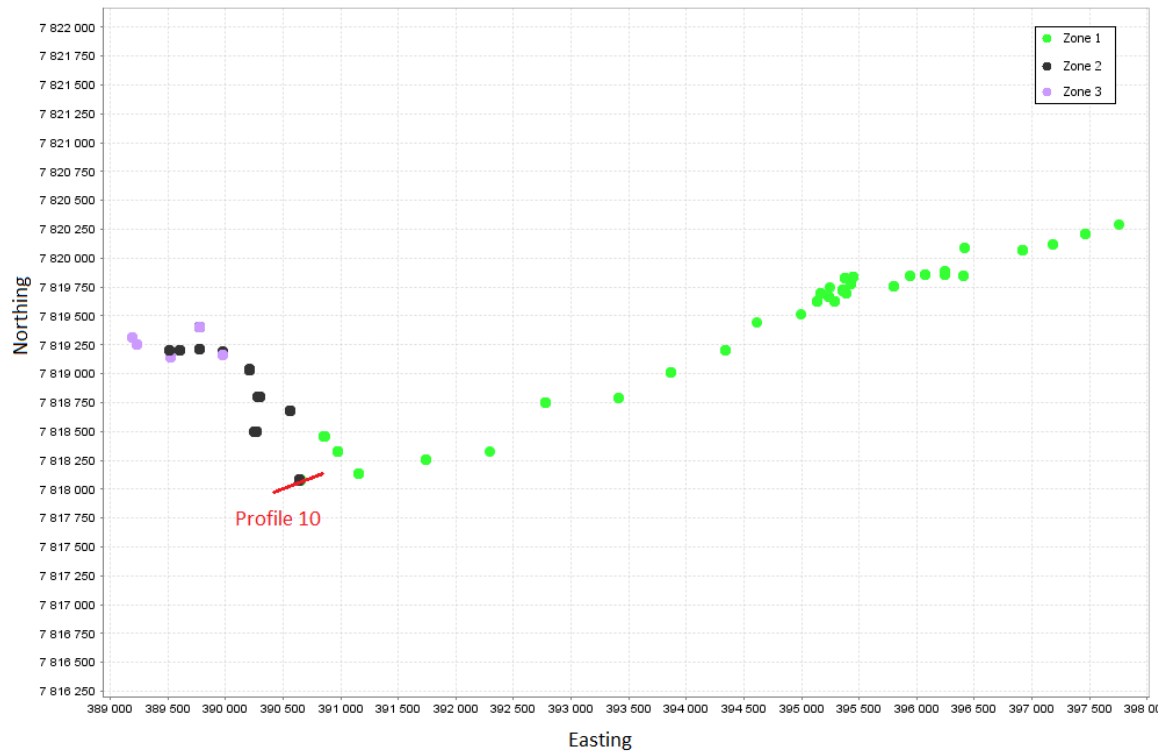


Figure B101. Attribute map showing the surface location of drill holes included in the lateral multivariate comparison between and within Zone 1 (green), 2 (dark grey) and 3 (purple). Profile 10 mark the boundary between Zone 1 and Zone 2 and 3. Map derived from ioGAS-64.

Multivariate analysis – comparison of the lateral variation within Zone 1 (Profile 10 and westward)

Table B43. Descriptive statistics in multivariate comparison of the lateral variation within Zone 1 (profile 10 and eastward).

Descriptive Statistics			
	Mean	Std. Deviation	Analysis N
Ag_ppm	12,2891982	15,38386584	125
Au_ppm	,1784701	,33465491	125
Al_prosent	2.690949921	2.247859436	125
Ba_ppm	791.3798293	924.9532677	125
Cr_ppm	143.4753255	185.8994972	125
K_prosent	1.488640995	1.245583809	125
Ni_ppm	45.26101569	90.10344925	125
P_ppm	193,46325	246,083788	125
S_prosent	.3982829364	.4053277793	125
Sc_ppm	4.507440175	4.318665211	125
Sr_ppm	153.2277536	117.4748412	125
Zn_ppm	24.45657044	24.22540330	125
Ti_ppm	385.4964978	1162.898276	125

Table B44. Kaiser-Meyer-Olkin and Bartlett's test in multivariate comparison of the lateral variation within Zone 1 (profile 10 and eastward).

KMO and Bartlett's Test		
Kaiser-Meyer-Olkin Measure of Sampling Adequacy.		,720
Bartlett's Test of Sphericity	Approx. Chi-Square	1136,563
	df	78
	Sig.	,000

Table B45. Total variance explained in multivariate comparison of the lateral variation within Zone 1 (profile 10 and eastward).

Component	Initial Eigenvalues			Extraction Sums of Squared Loadings			Rotation Sums of Squared Loadings		
	Total	% of Variance	Cumulative %	Total	% of Variance	Cumulative %	Total	% of Variance	Cumulative %
1	4,114	31,644	31,644	4,114	31,644	31,644	3,717	28,589	28,589
2	2,903	22,327	53,971	2,903	22,327	53,971	3,037	23,363	51,952
3	1,960	15,074	69,045	1,960	15,074	69,045	2,005	15,422	67,374
4	1,229	9,451	78,496	1,229	9,451	78,496	1,446	11,122	78,496
5	,648	4,988	83,484						
6	,570	4,382	87,866						
7	,463	3,563	91,429						
8	,347	2,672	94,101						
9	,258	1,986	96,088						
10	,219	1,686	97,774						
11	,145	1,118	98,891						
12	,086	,662	99,554						
13	,058	,446	100,000						

Extraction Method: Principal Component Analysis.

Table B46. Rotated component matrix in the multivariate comparison of the lateral variation within Zone 1 (profile 10 and eastward).

	Component ^a			
	1	2	3	4
Ag_ppm	-,140	-,148	,821	,011
Au_ppm	,008	-,055	,238	,822
Al_prosent	,948	,035	-,091	,121
Ba_ppm	,276	-,090	-,256	,791
Cr_ppm	,043	,878	,067	,028
K_prosent	,913	,019	-,032	,231
Ni_ppm	,304	,837	-,080	-,035
P_ppm	,944	-,115	-,065	,066
S_prosent	-,161	-,078	,875	,100
Sc_ppm	,819	,344	-,045	-,090
Sr_ppm	-,396	-,367	-,639	,180
Zn_ppm	,092	,838	-,022	-,126
Ti_ppm	-,205	,745	-,088	-,056

Extraction Method: Principal Component Analysis.

Rotation Method: Varimax with Kaiser Normalization. ^a

a. Rotation converged in 5 iterations.

Table B47. Wilks' Lambda test in multivariate comparison of the lateral variation within Zone 1 (profile 10 and eastward).

Test of Function(s)	Wilks' Lambda	Chi-square	df	Sig.
1 through 4	,020	385,086	124	,000
2 through 4	,148	189,036	90	,000
3 through 4	,476	73,503	58	,082
4	,896	10,819	28	,999

Multivariate analysis – comparison of new samples and old samples in Zone 1 (Profile 10 and westward)

Table B48. Eigenvalues in multivariate comparison of new samples and old samples in Zone 1 (profile 10 and eastward).

Function	Eigenvalue	% of Variance	Cumulative %	Canonical Correlation
1	3,251 ^a	100,0	100,0	,875

a. First 1 canonical discriminant functions were used in the analysis.

Table B49. Wilks' Lambda in multivariate comparison of new samples and old samples in Zone 1 (profile 10 and eastward).

Test of Function(s)	Wilks' Lambda	Chi-square	df	Sig.
1	,235	164,978	4	,000

Multivariate analysis – comparison of new and old samples in Zone 1, Zone 2 and Zone 3

Table B50. Descriptive statistics in multivariate comparison of new and old samples in zone 1, 2 and 3.

Descriptive Statistics			
	Mean	Std. Deviation	Analysis N
Al_prosent	2.795690199	2.345586679	248
Ca_prosent	9.950160508	7.298330686	248
Cr_ppm	126.8883241	161.7368137	248
K_prosent	1.514607198	1.303651164	248
Na_prosent	,7786718	,86510653	248
Ni_ppm	40.33770888	81.25977332	248
P_ppm	207,19887	251,562081	248
Sr_ppm	141.7187604	113.2686133	248

Table B51. Kaiser-Meyer-Olkin (KMO) and Bartlett's test in multivariate comparison of new and old samples in zone 1, 2 and 3.

KMO and Bartlett's Test		
Kaiser-Meyer-Olkin Measure of Sampling Adequacy.		,708
Bartlett's Test of Sphericity	Approx. Chi-Square	2005,933
	df	28
	Sig.	,000

Table B52. Total variance explained in multivariate comparison of new and old samples in zone 1, 2 and 3.

Component	Initial Eigenvalues			Extraction Sums of Squared Loadings			Rotation Sums of Squared Loadings		
	Total	% of Variance	Cumulative %	Total	% of Variance	Cumulative %	Total	% of Variance	Cumulative %
1	3,776	47,205	47,205	3,776	47,205	47,205	3,456	43,196	43,196
2	2,318	28,976	76,181	2,318	28,976	76,181	1,980	24,749	67,945
3	1,137	14,215	90,396	1,137	14,215	90,396	1,796	22,451	90,396
4	,327	4,086	94,482						
5	,211	2,634	97,116						
6	,105	1,309	98,425						
7	,080	,999	99,424						
8	,046	,576	100,000						

Extraction Method: Principal Component Analysis.

Table B53. Rotated component matrix in multivariate comparison of new and old samples in zone 1, 2 and 3.

Rotated Component Matrix^a

	Component		
	1	2	3
Al_prosent	,968	-,116	,118
Ca_prosent	-,182	,942	-,194
Cr_ppm	-,105	-,262	,893
K_prosent	,898	-,233	,171
Na_prosent	,864	,080	-,172
Ni_ppm	,179	-,097	,928
P_ppm	,942	-,104	,046
Sr_ppm	-,044	,964	-,160

Extraction Method: Principal Component Analysis.

Rotation Method: Varimax with Kaiser ...

a. Rotation converged in 4 iterations.

Table B54. Wilks' Lambda in multivariate comparison of new and old samples in zone 1, 2 and 3.

Wilks' Lambda

Test of Function(s)	Wilks' Lambda	Chi-square	df	Sig.
1	,159	432,759	3	,000

Multivariate analysis – comparison of new samples from Zone 1, Zone 2 and Zone 3

Table B55. Eigenvalues in multivariate comparison of new samples from Zone 1, 2 and 3.

Eigenvalues

Function	Eigenvalue	% of Variance	Cumulative %	Canonical Correlation
1	,028 ^a	65,4	65,4	,165
2	,015 ^a	34,6	100,0	,121

a. First 2 canonical discriminant functions were used in the analysis.

Table B56. Wilks' Lambda in multivariate comparison of new samples from Zone 1, 2 and 3.

Wilks' Lambda

Test of Function(s)	Wilks' Lambda	Chi-square	df	Sig.
1 through 2	,959	5,166	6	,523
2	,985	1,794	2	,408

Multivariate analysis – comparison of new samples within Zone 2

Table B57. Selected elements and descriptive statistics in the PCA model in the multivariate comparison of new samples within Zone 2.

Descriptive Statistics			
	Mean	Std. Deviation	Analysis N
Cu_prosent	1,19222671	,879673096	71
Ag_ppm	20,0786667	18,39065523	71
Cr_ppm	84.24772232	76.75807553	71
Na_prosent	,6887867	,86208005	71
Ti_prosent	.0920492139	.1036691139	71
V_ppm	32.27386769	33.36664325	71
Al_prosent	2.688655048	2.510757632	71
Ba_ppm	414.2523942	662.4641859	71
Ca_prosent	9.651280380	6.923690426	71
K_prosent	1.439753627	1.369188422	71
Mo_ppm	20.15891628	26.30342812	71
Sc_ppm	3.986015428	3.928403645	71
Sr_ppm	131.1540219	109.2521084	71
P_ppm	202,27320	240,103381	71

Table B58. Kaiser-Meyer-Olkin (KMO) and Bartlett's test in the multivariate comparison of new samples within Zone 2.

KMO and Bartlett's Test		
Kaiser-Meyer-Olkin Measure of Sampling Adequacy.		,792
Bartlett's Test of Sphericity	Approx. Chi-Square	1522,917
	df	91
	Sig.	,000

Table B59. Rotated component matrix in the multivariate comparison of new samples within Zone 2.

	Component		
	1	2	3
Cu percent	,177	-,310	,816
Ag ppm	-,065	-,010	,891
Cr ppm	-,118	-,794	,104
Na present	,750	,144	,042
Ti_ present	,967	-,109	,097
V ppm	,936	-,172	,122
Al present	,980	,006	,053
Ba ppm	,794	-,069	-,108
Ca percent	-,334	,891	-,071
K present	,967	-,157	,009
Mo ppm	,084	,022	,777
Sc ppm	,928	-,169	,135
Sr ppm	-,054	,914	-,037
P ppm	,980	,033	,086

Table B60. Wilks' Lambda in the multivariate comparison of new samples within Zone 2.

Test of Function(s)	Wilks' Lambda	Chi-square	df	Sig.
1 through 3	,265	41,121	18	,001
2 through 3	,644	13,639	10	,190
3	,879	4,010	4	,405

Multivariate analysis – comparison of new and old samples within Zone 3

Table B61. Descriptive statistics in multivariate comparison of new and old samples within Zone 3 (Lower horizon)

	Mean	Std. Deviation	Analysis N
Ca_prosent	13.45420625	5.388066065	20
Co_ppm	19.44217439	10.10914163	20
Cr_ppm	46.05232464	26.28426796	20
K_prosent	1.565592874	.9995612114	20
Mg_prosent	2.357897090	1.914609479	20
Zn_ppm	56.20198257	35.48272727	20
Sc_ppm	4.947803325	2.487896777	20
Sr_ppm	220.4489945	82.47056397	20

Table B62. Kaiser-Meyer-Olkin and Bartlett's test in multivariate comparison of new and old samples within Zone 3 (Lower horizon).

Kaiser-Meyer-Olkin Measure of Sampling Adequacy.		,768
Bartlett's Test of Sphericity	Approx. Chi-Square	228,387
	df	28
	Sig.	,000

Table B63. Rotated component matrix in multivariate comparison of new and old samples within Zone 3 (Lower horizon).

	Component	
	1	2
Ca_prosent	-,952	,053
Co_ppm	,067	,958
Cr_ppm	,949	-,210
K_prosent	,940	,007
Mg_prosent	-,173	,969
Zn_ppm	-,200	,963
Sc_ppm	,967	,013
Sr_ppm	-,874	,338

Extraction Method: Principal Component Analysis.
Rotation Method: Varimax with ...

a. Rotation converged in 3 iterations.

Table B64. Wilks' Lambda in multivariate comparison of new and old samples within Zone 3 (Lower horizon).

Test of Function(s)	Wilks' Lambda	Chi-square	df	Sig.
1 through 2	,083	38,576	8	,000
2	,845	2,609	3	,456

Multivariate analysis –comparison between new samples in Zone 1 and Zone 2

Table B65. Descriptive statistics in multivariate comparison between new samples in Zone 1 and Zone 2.

Descriptive Statistics			
	Mean	Std. Deviation	Analysis N
Co_ppm	18.47572816	14.93767750	103
Cr_ppm	78.72815534	90.39740086	103
Cu_prosent	,99036893	,974718531	103
Ag_ppm	12,3718447	16,24408440	103
Ba_ppm	1022.038835	928.7703860	103
Fe_prosent	2.000679612	2.274929545	103
La_ppm	16.01941748	9.324204831	103
Mg_prosent	2.384563107	2.235880217	103
Ni_ppm	37.66019417	73.93088365	103
S_prosent	.3654368932	.3300854812	103
Ti_prosent	.1840776699	.2011117965	103
V_ppm	60.27184466	59.40591411	103

Table B66. Kaiser-Meyer-Olkin and Bartlett's test in multivariate comparison between new samples in Zone 1 and Zone 2.

KMO and Bartlett's Test		
Kaiser-Meyer-Olkin Measure of Sampling Adequacy.		,717
Bartlett's Test of Sphericity	Approx. Chi-Square	1188,132
	df	66
	Sig.	,000

Table B67. Rotated component matrix in multivariate comparison between new samples in Zone 1 and Zone 2

	Rotated Component Matrix ^a			
	Component 1	Component 2	Component 3	Component 4
Co_ppm	,822	,092	,292	-,099
Cr_ppm	,910	,012	-,027	-,143
Cu_prosent	-,018	,977	-,039	,008
Ag_ppm	-,065	,902	,104	,009
Ba_ppm	,019	-,009	-,851	-,065
Fe_prosent	,875	-,159	,066	,230
La_ppm	,058	,067	,064	,961
Mg_prosent	,097	-,069	,846	-,001
Ni_ppm	,882	-,071	,129	-,112
S_prosent	-,010	,905	-,139	,062
Ti_prosent	,944	-,029	-,094	,116
V_ppm	,924	-,007	-,123	,198

Extraction Method: Principal Component Analysis.
Rotation Method: Varimax with Kaiser Normalization.

a. Rotation converged in 4 iterations.

Table B68. Wilks' Lambda in multivariate comparison between new samples in Zone 1 and Zone 2.

Wilks' Lambda				
Test of Function(s)	Wilks' Lambda	Chi-square	df	Sig.
1	,737	27,465	4	,000

Multivariate analysis – comparison between new samples in Zone 1 and Zone 3

Table B69. Descriptive statistics in multivariate comparison between new samples in Zone 1 (Profile 10 and westward) and Zone 3 (Lower horizon).

Descriptive Statistics			
	Mean	Std. Deviation	Analysis N
Al_prosent	4.421772152	1.655666850	79
Ca_prosent	11.63037975	7.599589132	79
K_prosent	2.197341772	1.204248578	79
P_ppm	373,54430	205,532691	79
Sr_ppm	178.4683544	119.0506071	79
Zn_ppm	28.12658228	28.39165961	79
Cu_prosent	1,00753797	1,038454812	79
Ag_ppm	13,6050633	20,35816411	79
Cr_ppm	84.26582278	100.0923559	79
Mg_prosent	2.054810127	1.840832351	79
S_prosent	.3483544304	.3053851304	79
Sc_ppm	6.354430380	4.811945538	79
Ti_prosent	.1916455696	.2187460205	79

Table B70. Kaiser-Meyer-Olkin and Bartlett's test in multivariate comparison between new samples in Zone 1 (Profile 10 and westward) and Zone 3 (Lower horizon).

KMO and Bartlett's Test		
Kaiser-Meyer-Olkin Measure of Sampling Adequacy.		,780
Bartlett's Test of Sphericity	Approx. Chi-Square	1181,947
	df	78
	Sig.	,000

Table B71. Rotated component matrix in multivariate comparison between new samples in Zone 1 (Profile 10 and westward) and Zone 3 (Lower horizon).

Rotated Component Matrix^a

	Component		
	1	2	3
Al_prosent	,935	,152	-,109
Ca_prosent	-,935	-,175	,009
K_prosent	,884	,051	-,128
P_ppm	,865	,100	,120
Sr_ppm	-,898	-,098	,092
Zn_ppm	,043	,105	,906
Cu_prosent	,087	,967	-,029
Ag_ppm	,002	,925	,118
Cr_ppm	,771	-,167	,249
Mg_prosent	,071	-,057	,870
S_prosent	,003	,953	-,056
Sc_ppm	,875	-,089	,181
Ti_prosent	,801	-,211	,272

Extraction Method: Principal Component Analysis.

Rotation Method: Varimax with Kaiser ...

a. Rotation converged in 4 iterations.

Table B72. Wilks' Lambda in multivariate comparison between new samples in Zone 1 (Profile 10 and westward) and Zone 3 (Lower horizon).

Wilks' Lambda

Test of Function(s)	Wilks' Lambda	Chi-square	df	Sig.
1	,569	40,289	3	,000

12. Appendix C

Thin section observations – drill core NUS-DD-13-004

Eleven thin sections from core samples in drill core NUS-DD-13-004 were studied (Figure C102). The host rock of copper minerals in drill core NUS-DD-13-004, consisted of a stratigraphic sequence of metasedimentary rocks. It was divided into an overburden hang wall slate, Upper mineralized horizon, mid wall slate, Lower mineralized horizon and footwall slate. The hang wall slate and the footwall slate was composed by a fine-grained quartz-rich arkoses, rich in chlorite, quartz, biotite and a matrix rich in muscovite with veins and aggregates of calcite. The matrix contained dissemination of fine-grained and subhedral shaped quartz and feldspar in the Upper mineralized horizon (Figure C111), while the Lower mineralized horizon contained a carbonate-rich matrix upon the Lower mineralized horizon, and a biotite-rich matrix below the Lower mineralized horizon (Figure C112). The biotite formed tabular grains with the grain size 0.02-0.2 mm. Green and brown biotite was observed along margins of veins, and with the sign of chloritization. Plagioclase and microcline contained the grain size 0.02-2 mm, with a subhedral grain shape. Grains of feldspar showed seritization. The grain size of quartz varied (0.02-0.5 mm) and contained an anhedral shape. Grains of quartz situated in veins, contained a larger grain size than the quartz situated in the bedrock. Grain boundary migration and sub grain rotation was observed in the quartz grains. The hang wall slate, mid wall slate and the footwall slate showed differences, the mid wall slate and the footwall slate showed coarser grain size and a lower content of matrix and chlorite. The hang wall slate contained a denser schistose texture, and showed sigma-clasts of quartz and feldspar. An example of the hang wall slate in drill core NUS-DD-13-004, is shown in a picture of thin section NUS_002 (Figure C103). The Upper- and Lower mineralized horizon was composed by fine-grained dolomite with chlorite and biotite-rich matrix. Calcite occurred in veinlet's and as aggregates in the mineralized horizon, and in hang wall, mid wall- and footwall slate. The grain size of calcite varied (0.002-0.2 mm). The grain shape was mainly subhedral in veins and in aggregates. In thin section NUS_005, NUS_008 and NUS_011 from drill core NUS-DD-13-004, grains of calcite situated in veins, contained an elongated shape with bended texture. Quartz and calcite-rich veins occurred, and also single quartz veins. Cross cutting veins was not observed in the thin sections.

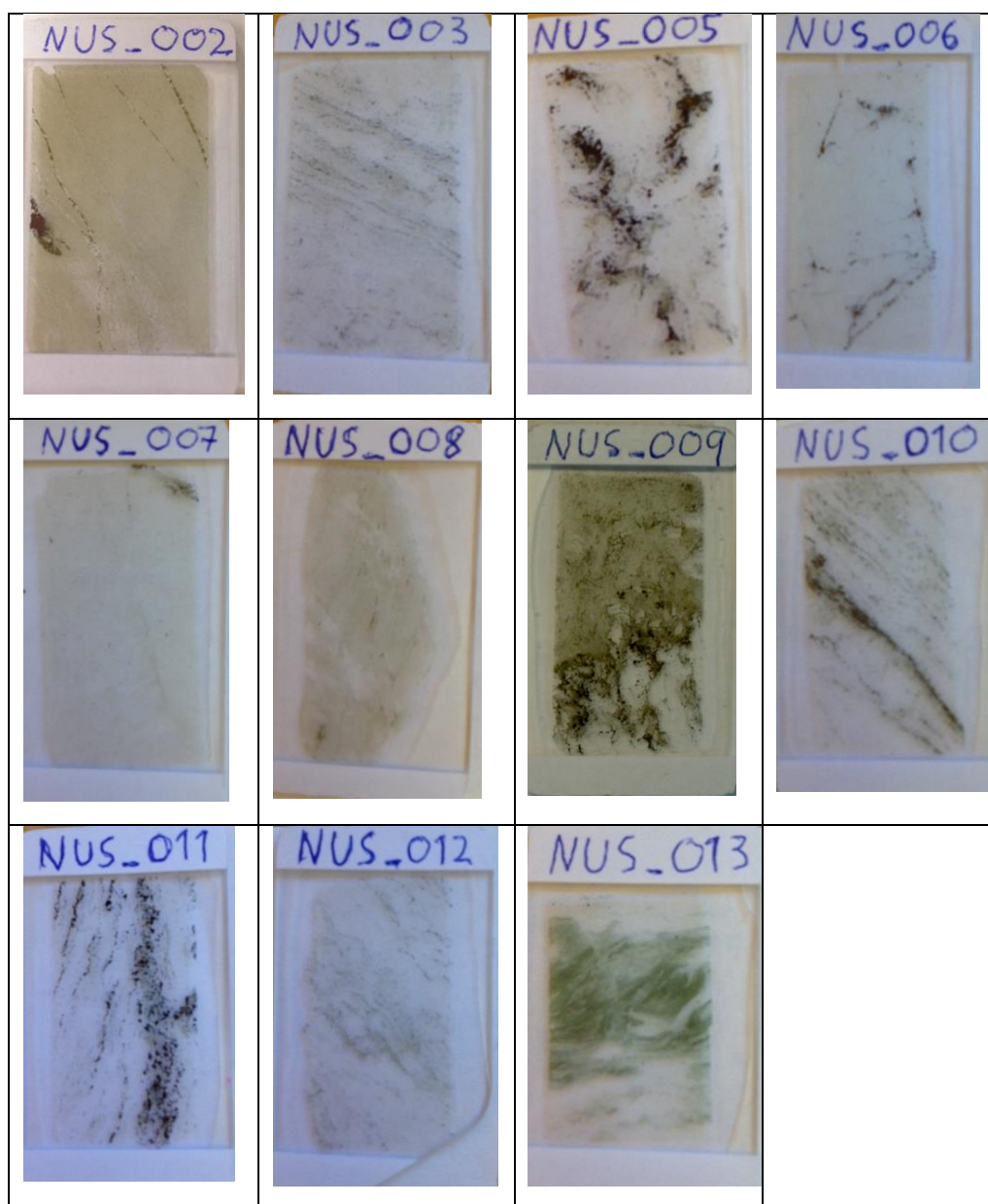


Figure C102. Thin sections from core samples in drill core NUS-DD-13-004.



Figure C103. Picture of hang wall slate in thin section NUS_002. Mica-rich matrix form a schistose texture. Layer of green biotite and chlorite with quartz grain.

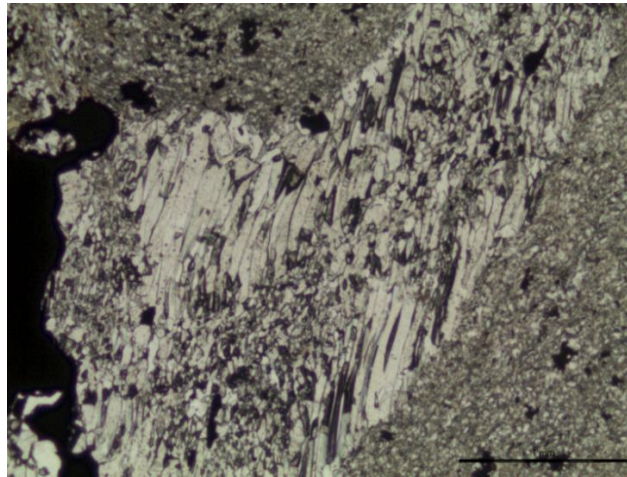


Figure C104. Picture of calcite vein in the Upper mineralized horizon. The calcite have elongated grain shape. Picture taken from thin section NUS_005 in drill core NUS-DD-13-004.

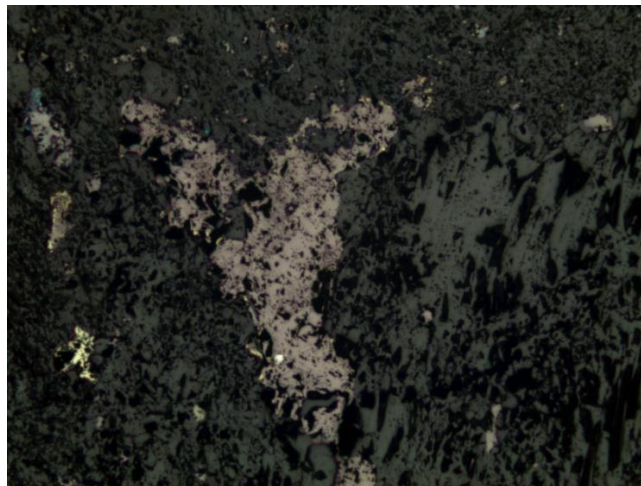


Figure C105. Mineralization of bornite and chalcopyrite in the Upper mineralized horizon. Picture taken by reflection light in thin section NUS_005 in drill core NUS-DD-13-004. The picture represents the opaque part in the left part of Figure C104.

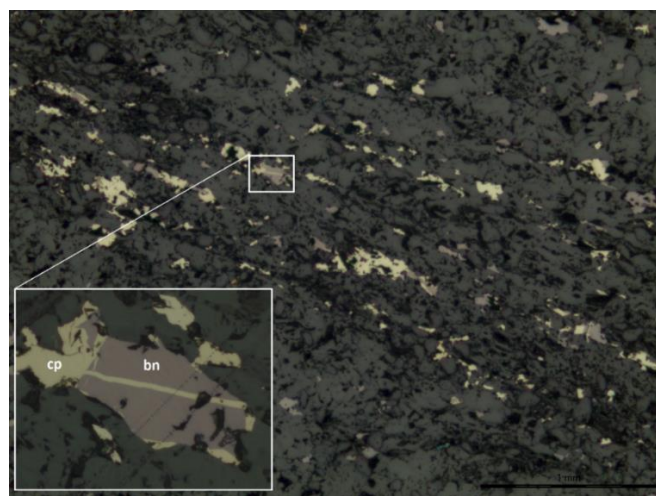


Figure C106. Picture of the Upper mineralized horizon in thin section NUS_003 in drill core NUS-DD-13-004. Bornite and chalcopyrite occurs as disseminated grains and in veins. The square zoom in on a grain of bornite and chalcopyrite, and show how chalcopyrite and bornite occurs together.

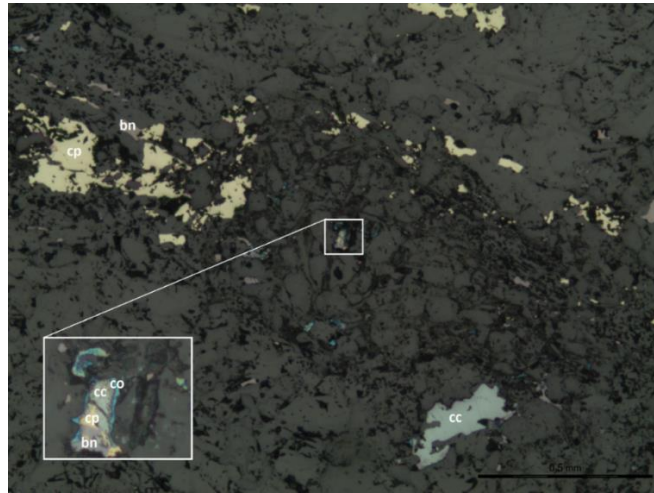


Figure C107. Picture of the Upper mineralized horizon in thin section NUS_003 in drill core NUS-DD-13-004. Chalcopyrite and bornite occurs as disseminated grains and in veins. Chalcocite and covellite form rims in grains of bornite and chalcopyrite.

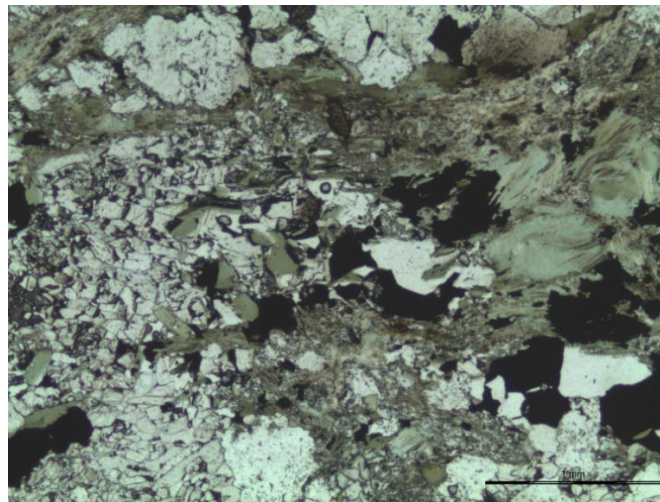


Figure C108. Part of a calcite vein with green biotite and chlorite. The picture was taken in the Lower mineralized horizon in thin section NUS_009 in drill core NUS-DD-13-004.

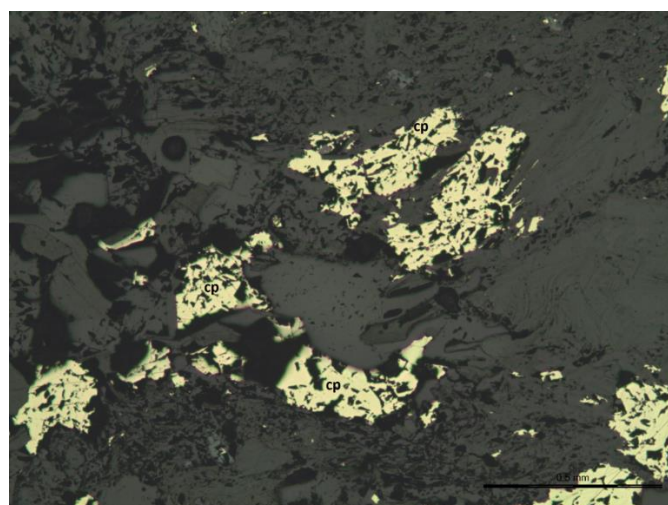


Figure C109. Mineralization of chalcopyrite in calcite vein. Picture taken in reflection light from the Lower mineralized horizon in thin section NUS_009 in drill core NUS-DD-13-004.

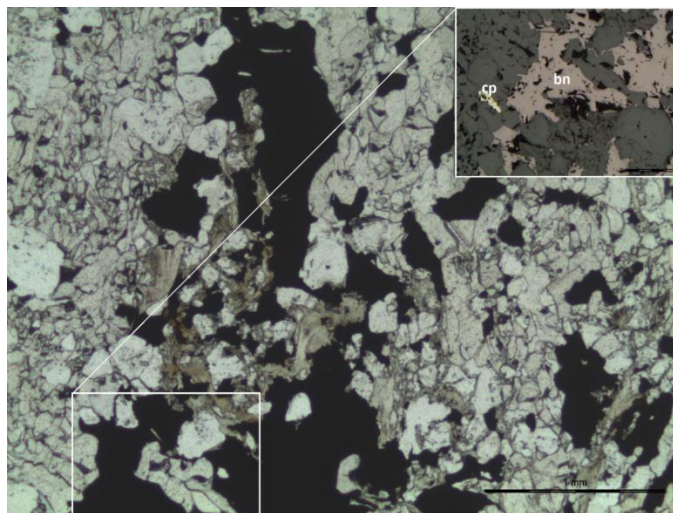


Figure C110. Picture shows the Lower mineralized horizon in plane polarised light in thin section NUS_011 in drill core NUS-DD-13-004. Veins were dominated by calcite, with mineralization of biotite and chlorite. The area marked by a frame, shows the mineralization of bornite and chalcopyrite in reflected light.

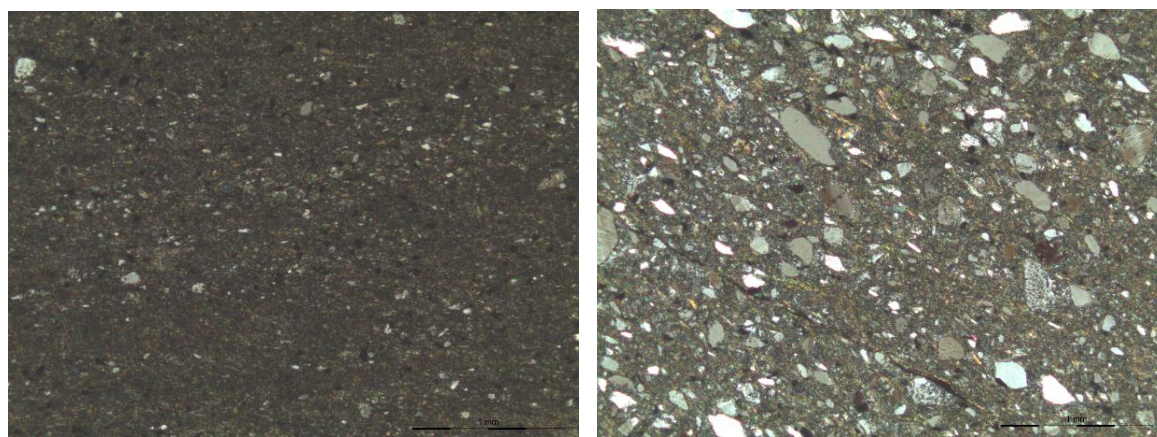


Figure C111. Photomicrographs of the matrix above the Upper mineralized horizon (left) and beneath the Upper mineralized horizon (right) in drill core NUS-DD-13-004.

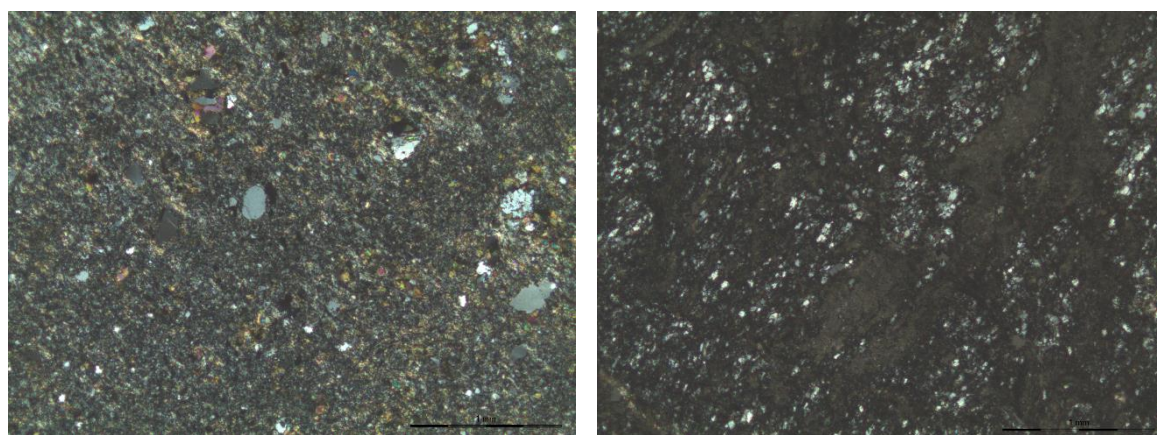


Figure C112. Photomicrograph of the matrix above (left) and beneath (right) the Lower mineralized horizon in drill core NUS-DD-13-004.

Thin section observations – drill core NUS-DD-13-002

Six thin sections from core samples in drill core NUS-DD-13-002 were studied (Figure C113). The thin sections constitute samples from the mid wall slate, Lower mineralized horizon, and the footwall slate. The hang wall- and footwall slate was dominated by fine-grained quartz, feldspar and mica-rich matrix. The matrix formed a schistose texture (Figure C114). Carbonate and quartz-rich veins cut through the bedrock. The grains of carbonate contained an elongated and bended shape. The quartz crystals in veins contained subgrain rotation.

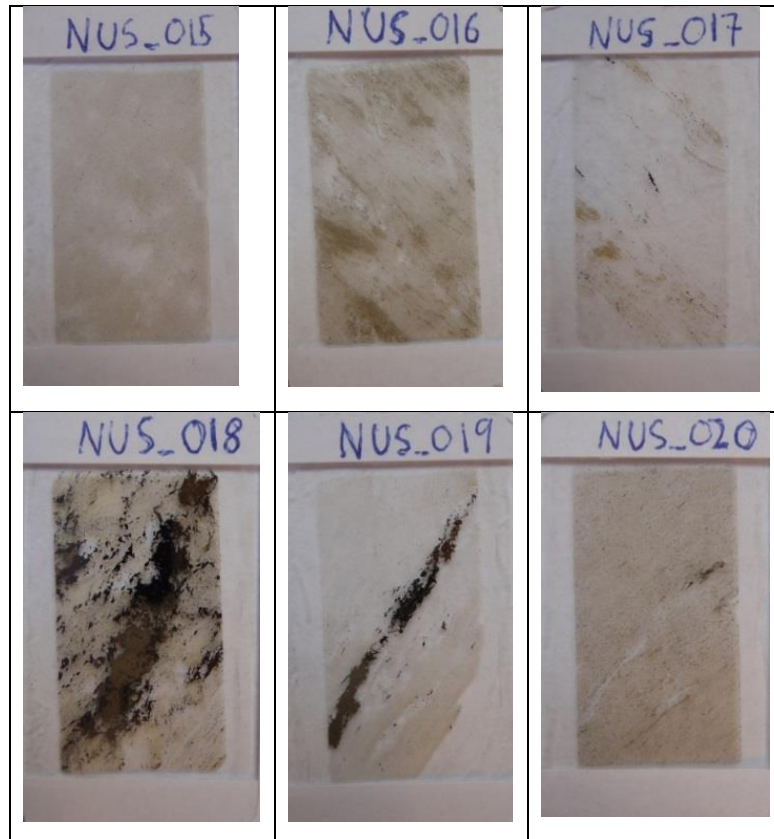


Figure C113. Thin sections from core samples in drill core NUS-DD-13-002.

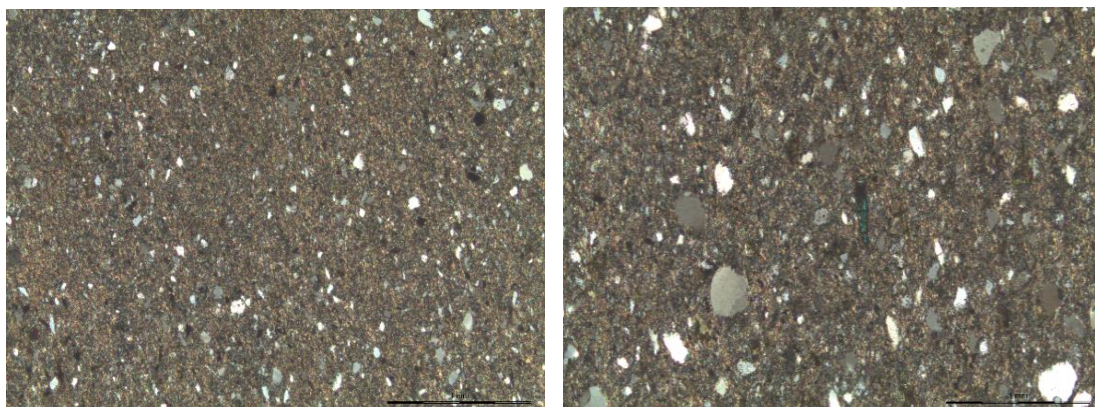


Figure C114. Photomicrograph of the matrix above (left) and beneath (right) the Lower mineralized horizon in drill core NUS-DD-13-002.

Thin section observations – drill core NUS-DD-13-012

Six thin section from core samples were studied in drill core NUS-DD-13-012 (Figure C115) in polarization microscope. Fine-grained quartz and feldspars, with mica-rich matrix and green biotite (Figure C116), dominated the hang wall- and footwall slate. Sericitization was observed in grains of quartz. Titanite occurred in association to sulphide mineralization. Carbonate-rich veins with elongated and bended grain shape dominated the mineralized horizon.

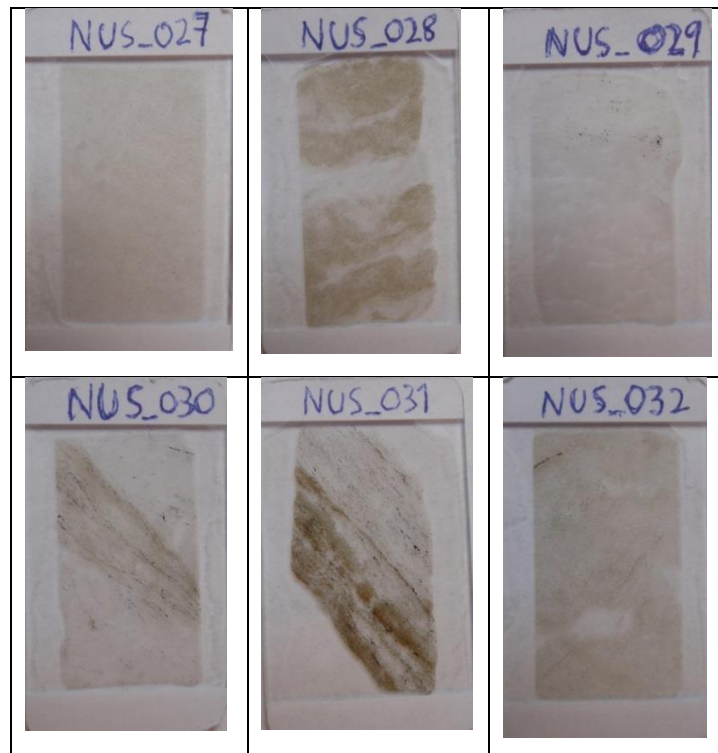


Figure C115. Thin sections from core samples in drill core NUS-DD-13-012.

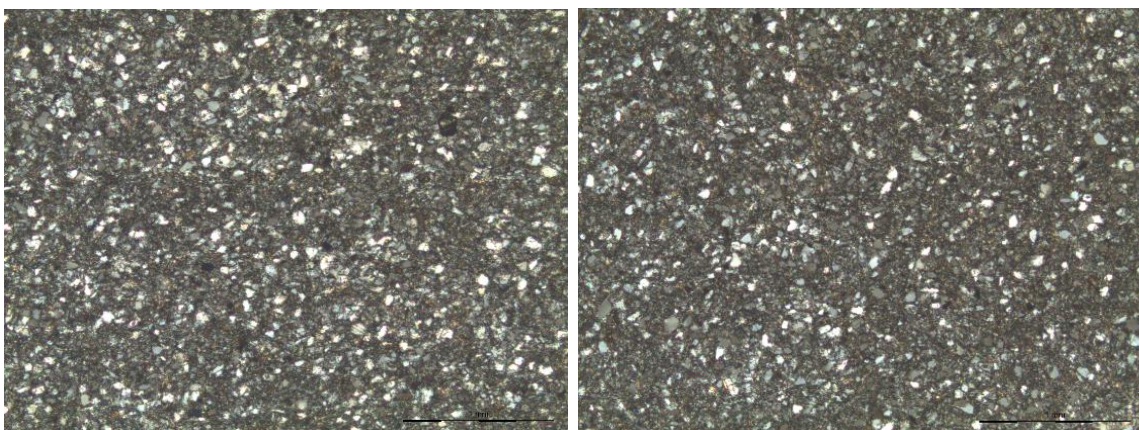


Figure C116. Photomicrograph of the matrix above (left) and beneath (right) the Upper mineralized horizon in drill core NUS-DD-13-012.

Thin section observations – drill core NUS-DD-13-003

Six thin section from core samples were studied in drill core NUS-DD-13-003 (Figure C117) in polarization microscope. These thin sections was sampled above (NUS_021), in the Lower mineralized horizon (NUS_022-NUS-025) and below the Lower mineralized horizon (NUS_026) in drill core NUS-DD-13-003. Fine-grained quartz and feldspar, with a mica-rich matrix, dominated the hang wall slate (Figure C118). Carbonate- and quartz-rich veins cut through the rock. Grains of carbonate showed an elongated and bended shape. Disseminated titanite occurred in the matrix as subhedral grains.

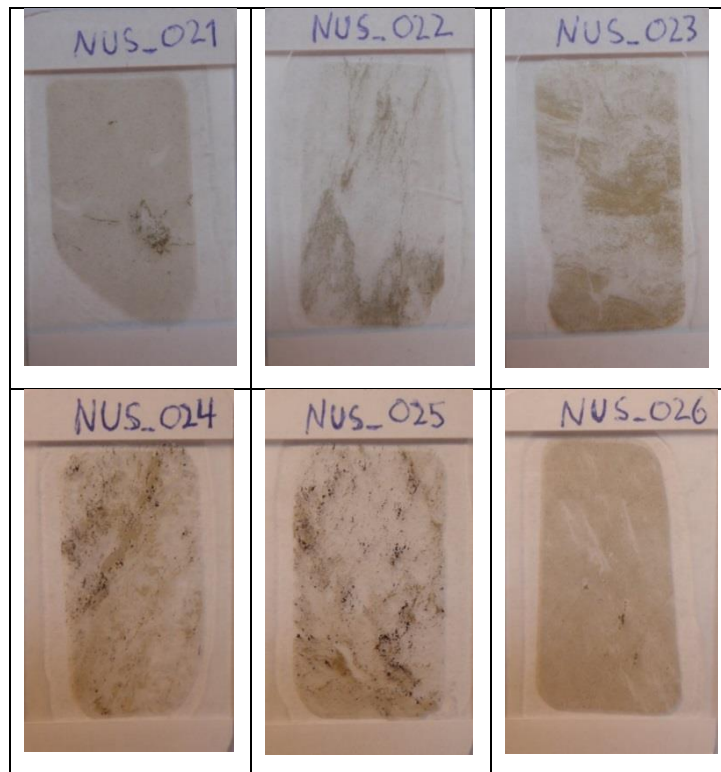


Figure C117. Thin sections from core samples in drill core NUS-DD-13-003.

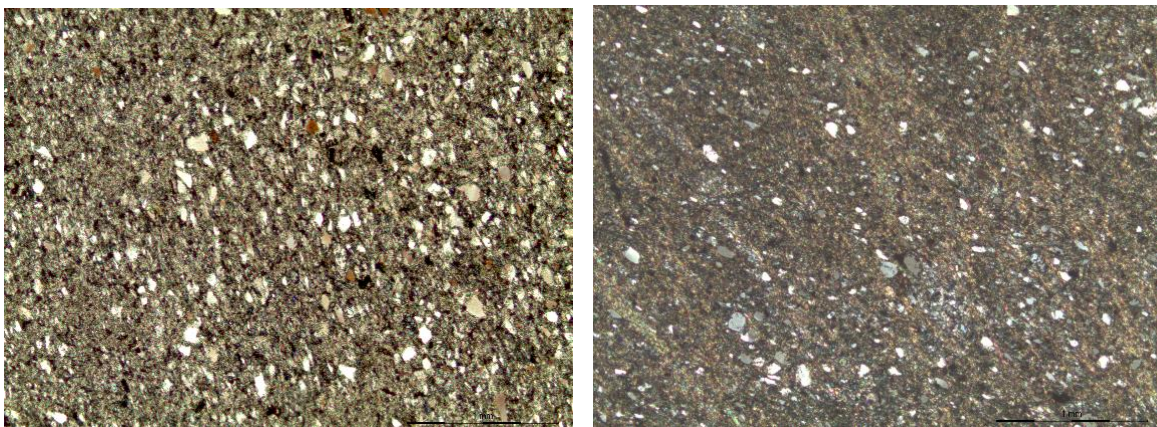


Figure C118. Photomicrograph of the matrix above (left) and beneath (right) the Lower mineralized horizon in drill core NUS-DD-13-003.

13. Appendix D

Micro probe analysis

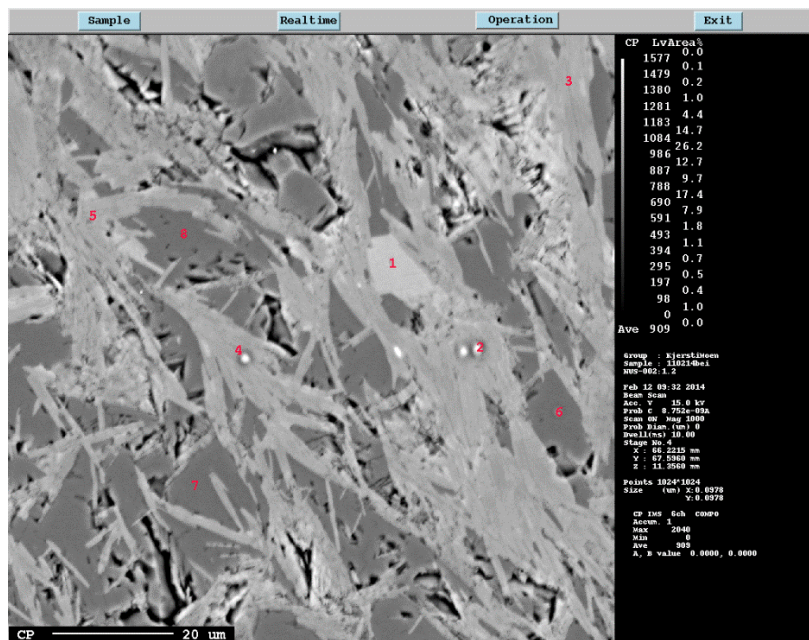


Figure D119. Scatter map of point analysis of matrix in hang wall slate (thin section NUS_002, spot NUS_002:1.1 in area NUS_002:1). Point 1-8 in the scatter map represents number 5-12 in table 5.

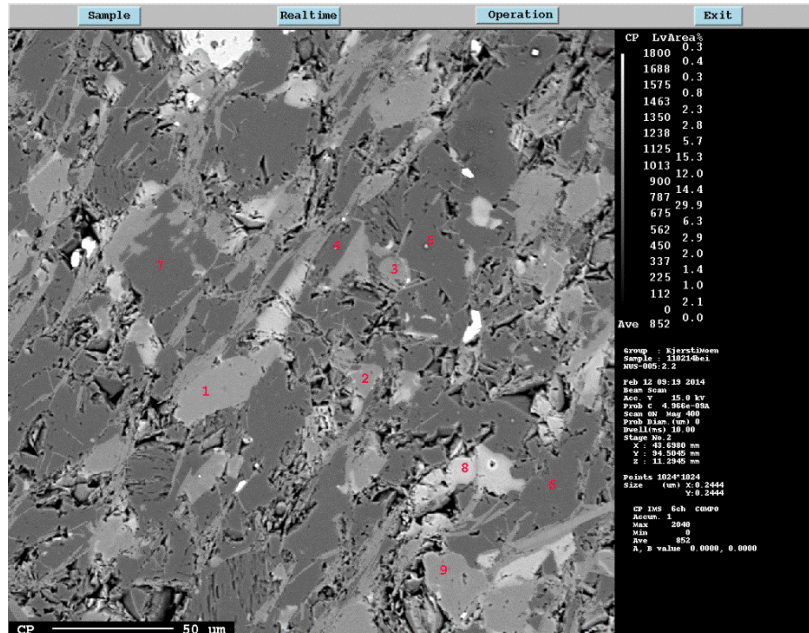


Figure D120. Scatter map of point analysis of matrix in thin section NUS_005 (figure 10), area NUS_005:2 (figure 10), and spot NUS_005:2.2 (figure 11). The marked number (1-9) represents analyse number 43-51.

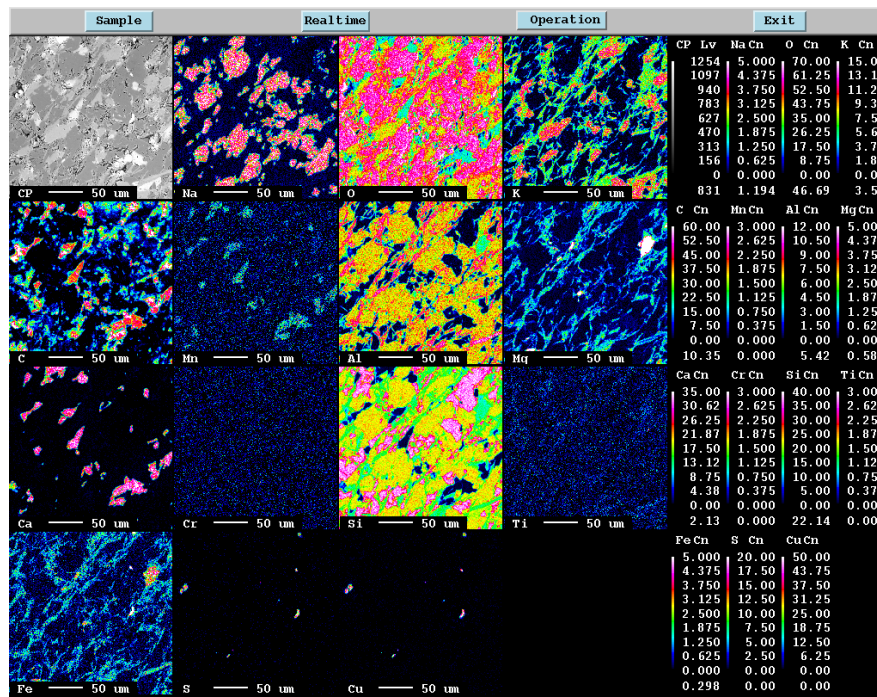


Figure D121. Scanning map of thin section NUS_005, area NUS_005:2 and spot NUS_005:2.2.

Table D73. Overview of thin section, area of thin section, spot, point and number of WDS analysis performed in micro probe analysis, Table 1:2.

Thin section	Area of thin section	Selected spot	Mineral /Matrix	Points	No.	Comment
NUS_002	NUS_002:1	NUS_002:1.2	Mineral	NUS_002:1. 2.1	2	Biotite
				NUS_002:1. 2.2	3	Biotite
				NUS_002:1. 2.3	4	Biotite
NUS_002	NUS_002:1	NUS_002:1.1	Matrix	NUS_002:1. 1.2	5	Hang wall slate
				NUS_002:1. 1.3	6	Hang wall slate
				NUS_002:1. 1.4	7	Hang wall slate
				NUS_002:1. 1.5	8	Hang wall slate
				NUS_002:1. 1.6	9	Hang wall slate
				NUS_002:1. 1.7	10	Hang wall slate
				NUS_002:1. 1.8	11	Hang wall slate
NUS_002	NUS_002:2	NUS_002:2.1	Mineral	NUS_002:2. 1.1	13	Chlorite
				NUS_002:2. 1.2	14	Chlorite
				NUS_002:2. 1.3	15	Chlorite
NUS_002	NUS_002:2	NUS_002:2.2	Mineral	NUS_002:2. 2.1	16	Biotite
				NUS_002:2. 2.2	17	Biotite
				NUS_002:2. 2.3	18	Biotite
NUS_002	NUS_002:2	NUS_002:2.3	Sulphide	NUS_002:2. 3.1	19	Chalcopyrite
				NUS_002:2. 3.2	20	Chalcopyrite
				NUS_002:2. 3.3	21	Chalcopyrite
NUS_002	NUS_002:2	NUS_002:2.4	Sulphide	NUS_002:2. 4.1	22	Bornite
				NUS_002:2. 4.2	23	Bornite
				NUS_002:2. 4.3	24	Bornite
NUS_005	NUS_005:1	NUS_005:1.1	Mineral	NUS_005:1. 1.1	25	Unknown
				NUS_005:1. 1.2	26	Unknown
				NUS_005:1. 1.3	27	Unknown
NUS_005	NUS_005:1	NUS_005:1.2	Sulphide	NUS_005:1. 2.1	28	Chalcocite
				NUS_005:1. 2.2	29	Chalcocite
				NUS_005:1. 2.3	30	Chalcocite

Table D74. Overview of thin section, area of thin section, spot, point and number of WDS analysis performed in micro probe analysis, Table 2:2.

NUS_005	NUS_005:1	NUS_005:1. 3	Sulphide	NUS_005:1. 3.1	31	Bornite
				NUS_005:1. 3.2	32	Bornite
				NUS_005:1. 3.3	33	Bornite
NUS_005	NUS_005:1	NUS_005:1. 4	Mineral	NUS_005:1. 4.1	34	Biotite
				NUS_005:1. 4.2	35	Biotite
				NUS_005:1. 4.3	36	Biotite
NUS_005	NUS_005:1	NUS_005:1. 5	Mineral	NUS_005:1. 5.1	37	Calcite/dolomite
				NUS_005:1. 5.2	38	Calcite/dolomite
				NUS_005:1. 5.3	39	Calcite/dolomite
NUS_005	NUS_005:2	NUS_005:2. 1	Mineral	NUS_005:2. 1.1	40	Calcite
				NUS_005:2. 1.2	41	Calcite
				NUS_005:2. 1.3	42	Calcite
NUS_005	NUS_005:2	NUS_005:2. 2	Matrix	NUS_005:2. 2.1	43	Ore (upper)
				NUS_005:2. 2.2	44	Ore (upper)
				NUS_005:2. 2.3	45	Ore (upper)
				NUS_005:2. 2.4	46	Ore (upper)
				NUS_005:2. 2.5	47	Ore (upper)
				NUS_005:2. 2.6	48	Ore (upper)
				NUS_005:2. 2.7	49	Ore (upper)
				NUS_005:2. 2.8	50	Ore (upper)
				NUS_005:2. 2.9	51	Ore (upper)
NUS_005	NUS_005:3	NUS_005:3.1	Mineral	NUS_005:3. 1.1	52	Calcite/dolomite
				NUS_005:3. 1.2	53	Calcite/dolomite
				NUS_005:3. 1.3	54	Calcite/dolomite
NUS_013	NUS_013:1	NUS_013:1. 1	Mineral	NUS_013:1. 1.1	55	Calcite/dolomite
				NUS_013:1. 1.2	56	Calcite/dolomite
				NUS_013:1. 1.3	57	Calcite/dolomite
NUS_013	NUS_013:1	NUS_013:1. 2	Mineral	NUS_013:1. 2.1	58	Chlorite?
				NUS_013:1. 2.2	59	Chlorite?
				NUS_013:1. 2.3	60	Chlorite?

Table D75. Results of WDS analysis in electron probe micro-analyzer: Massoxide, Table 1:2.

No.	Al2O3	F	K2O	Cr2O3	SiO2	Na2O	CaO	MnO	MgO	TiO2	FeO	SrO	Total	Comment
2	14.401	0.058	9.726	0.04	41.361	0.054	0.01	0.276	17.21	1.045	11.789	0	95.946	NUS-002:1. 2.1
3	14.605	0.072	9.763	0.033	40.987	0.056	0	0.281	17.32	1.04	12.252	0	96.379	NUS-002:1. 2.2
4	14.246	0.105	9.179	0	40.72	0.023	0.001	0.254	17.573	0.993	12.249	0	95.299	NUS-002:1. 2.3
5	14.32	0.188	9.133	0.063	42.003	0.168	0.025	0.224	17.392	0.99	11.001	0	95.428	NUS-002:1. 1.1
6	25.574	0	9.367	0.1	51.931	0.217	0	0.022	3.66	0.384	4.171	0	95.426	NUS-002:1. 1.2
7	26.475	0	9.56	0.069	51.23	0.2	0.004	0.081	3.551	0.346	4.261	0	95.777	NUS-002:1. 1.3
8	25.958	0	9.449	0.063	52.063	0.259	0.024	0.007	3.406	0.34	4.009	0.073	95.651	NUS-002:1. 1.4
9	27.075	0	9.589	0.026	51.428	0.205	0.019	0.003	3.009	0.328	3.944	0.037	95.663	NUS-002:1. 1.5
10	18.727	0	0.333	0.019	70.164	9.228	0.005	0	0.09	0.008	0.202	0.035	98.811	NUS-002:1. 1.6
11	18.871	0	0.3	0.041	70.263	9.039	0.014	0.012	0.085	0.011	0.236	0	98.872	NUS-002:1. 1.7
12	18.855	0.004	0.222	0.003	70.464	7.978	0.18	0.035	0.066	0	0.198	0	98.003	NUS-002:1. 1.8
13	18.892	0.06	0	0.052	29.698	0.001	0	0.43	24.675	0	12.767	0	86.55	NUS-002:2. 1.1
14	18.771	0	0.021	0.032	30.031	0.039	0	0.462	24.554	0	12.804	0	86.714	NUS-002:2. 1.2
15	19.067	0	0.003	0	29.807	0.035	0.012	0.443	24.467	0	12.967	0	86.801	NUS-002:2. 1.3
16	14.266	0.167	9.631	0.01	40.84	0.033	0	0.21	17.235	0.989	11.601	0	94.912	NUS-002:2. 2.1
17	14.367	0.082	9.723	0	40.625	0.015	0.021	0.28	17.279	0.901	11.423	0	94.681	NUS-002:2. 2.2

Table D76. Results of WDS analysis in electron probe micro-analyzer: Massoxide, Table 2:2.

No.	Al2O3	F	K2O	Cr2O3	SiO2	Na2O	CaO	MnO	MgO	TiO2	FeO	SrO	Total	Comment
18	14.303	0.287	9.645	0.022	41.607	0.026	0.029	0.283	17.315	0.793	11.097	0	95.286	NUS-002:2. 2.3
25	1.007	0.069	0.054	0.011	31.745	0.033	27.443	0.065	0.019	38.082	0.055	0	98.554	NUS-005:1. 1.1
26	1.396	0.054	0.159	0	31.656	0.057	27.416	0.081	0.138	36.835	0.074	0	97.843	NUS-005:1. 1.2
27	1.483	0	0.197	0.005	31.892	0.075	26.967	0.027	0.049	37.336	0.06	0	98.091	NUS-005:1. 1.3
34	13.566	0.593	9.417	0.035	43.785	0.058	0.093	0.287	21.451	0.3	5.721	0	95.056	NUS-005:1. 4.1
35	13.598	0.492	9.285	0.037	42.684	0.044	0.053	0.305	20.984	0.571	5.975	0.019	93.84	NUS-005:1. 4.2
36	13.42	0.511	9.432	0	43.157	0.047	0.078	0.287	21.393	0.573	6.362	0	95.045	NUS-005:1. 4.3
37	0.006	0	0.009	0.012	0	0.016	56.326	1.785	0.525	0	0.224	0	58.903	NUS-005:1. 5.1
38	0.036	0.025	0.001	0	0	0	56.362	1.739	0.588	0.004	0.242	0	58.986	NUS-005:1. 5.2
39	0.022	0	0	0	0	0.002	57.784	1.707	0.528	0.006	0.242	0	60.291	NUS-005:1. 5.3
58	18.521	0.012	0	0.042	30.637	0	0.007	0.335	19.377	0.019	18.201	0.02	87.166	NUS-013:1. 2.1
59	16.342	0	0.042	0.029	30.695	0.031	0.214	0.292	21.541	0.063	16.573	0	85.822	NUS-013:1. 2.2
60	19.252	0	0.012	0.064	29.653	0	0.053	0.4	19.235	0.027	18.971	0	87.667	NUS-013:1. 2.3
Minimum	0	0	0	0	0	0	0	0	0.003	0	0.022	0	54.292	
Maximum	28.468	0.593	15.556	0.103	98.881	9.228	57.828	2.401	24.675	38.082	18.971	0.176	100.604	
Average	12.841	0.057	4.52	0.024	40.75	1.132	14.42	0.48	6.344	2.183	4.038	0.008	86.772	
Sigma	9.683	0.126	5.629	0.028	27.813	2.611	23.562	0.681	8.853	8.387	5.535	0.026	16.139	

Table D77. Results of electron probe micro-analyzer: Massulphide

No.	Mg	S	Cr	As	Pd	Fe	Ag	Co	Te	Ni	Sb	Cu	Zn	Pt	Au	Total	Comment
19	0.003	32.772	0	0	0	33.016	0.002	0.008	0	0	0	34.227	0.058	0	0.133	100.22	NUS-002:2. 3.1
20	0.011	34.379	0.022	0.008	0.027	33.114	0.047	0.039	0	0	0	34.285	0.006	0	0	101.94	NUS-002:2. 3.2
21	0.004	34.798	0	0	0.016	33.435	0.042	0.051	0	0	0	34.398	0.088	0	0	102.83	NUS-002:2. 3.3
22	0	25.818	0.013	0.058	0	12.556	0.196	0.031	0	0	0.097	62.806	0.121	0	0	101.7	NUS-002:2. 4.1
23	0.071	25.845	0.004	0.031	0.008	12.577	0.239	0.045	0	0	0	63.318	0	0	0	102.14	NUS-002:2. 4.2
24	0.068	25.793	0	0.005	0.084	12.512	0.133	0	0	0.001	0.012	62.894	0.089	0	0	101.59	NUS-002:2. 4.3
28	0.022	20.672	0	0	0	0.073	0.246	0.009	0	0	0	78.308	0.073	0	0.113	99.516	NUS-005:1. 2.1
29	0.055	20.604	0	0	0	0.07	0.355	0	0	0.014	0	78.199	0	0	0.239	99.536	NUS-005:1. 2.2
30	0.054	25.225	0	0	0.032	11.281	0.304	0	0	0	0.136	62.299	0.072	0	0	99.403	NUS-005:1. 2.3
31	0	25.784	0	0.021	0	12.44	0.186	0	0	0	0.128	63.453	0.158	0	0.049	102.22	NUS-005:1. 3.1
32	0.015	26.258	0	0.074	0	12.614	0.181	0.047	0	0	0.137	62.493	0.198	0	0	102.02	NUS-005:1. 3.2
33	0	26.117	0	0	0	12.497	0.211	0.032	0	0	0.066	62.752	0.119	0	0.562	102.36	NUS-005:1. 3.3
Minimum	0	20.244	0	0	0	0.006	0.002	0	0	0	0	34.227	0	0	0	97.428	
Maximum	0.071	34.798	0.024	0.074	0.084	33.435	0.544	0.051	0	0.014	0.137	80.348	0.198	0	0.562	102.83	
Average	0.021	25.77	0.005	0.012	0.014	12.454	0.226	0.02	0	0.001	0.042	62.556	0.08	0	0.079	101.28	
Sigma	0.026	4.46	0.008	0.022	0.023	10.991	0.131	0.02	0	0.004	0.051	14.781	0.053	0	0.142	1.451	

Table D78. Table show the standards used in the analysis of minerals (massoxides).

Element	Stand.name	Mass (%)	ZAF Fac.	Z	A	F
Al ₂ O ₃	Chlori.As15	18.0830	3.4233	5.8248	0.5848	1.0050
Na ₂ O	Plagl. Ast35	4.3540	5.2197	10.7618	0.4830	1.0043
K ₂ O	Sanidi.Ast41	12.1063	1.0720	1.2031	0.8908	1.0003
Cr ₂ O ₃	Cr ₂ O ₃ . Ast17	100.0131	0.3636	0.3706	0.9811	1.0000
SiO ₂	Chlori.As15	30.0343	2.8001	4.3851	0.6386	1.0000
F	Apatit.Ast4	3.7700	3.3213	21.5122	0.1543	1.0000
CaO	Plagl.Ast35	11.5973	0.8593	0.9353	0.9187	1.0001
MnO	Wille.Ast46	4.8163	0.2888	0.2842	0.9738	1.0437
MgO	Olivi.Ast34	50.4414	4.8510	7.8678	0.6146	1.0032
TiO ₂	Rutile.Ast40	99.9834	0.5904	0.6060	0.9742	1.0000
FeO	Olivi.Ast34	7.5516	0.1954	0.1981	0.9851	1.0012
SrO	SrSo.Ast13	56.1975	3.4081	4.3528	0.7792	1.0048

Table D79. Table show the standards used in analysis of sulphide minerals (massulphides).

Element	Stand. name	Mass (%)	ZAF Fac.	Z	A	F
Ag	Ag.AST26	100.0000	1.5455	1.7832	0.8667	1.0000
As	CoNiAs.As19	79.1000	4.9375	9.3209	0.5297	1.0000
Au	Au.AST.39	100.0000	0.0223	0.0226	0.9875	1.0000
Co	CoNiAs.As19	15.5000	0.1818	0.1860	0.9771	1.0000
Cr	Cr2O3.Ast17	68.4300	0.3636	0.3706	0.9811	1.0000
Cu	Cu2O.Ast14	88.8200	0.0926	0.0935	0.9908	1.0000
Fe	Olivi.Ast34	5.8700	0.1954	0.1981	0.9851	1.0012
Mg	Olivi.Ast34	30.4200	4.8510	7.8678	0.6146	1.0032
Ni	CoNiAs.As19	4.4000	0.1354	0.1379	0.9820	1.0000
Pd	Pd.AST25	100.0000	1.7223	2.0070	0.8582	1.0000
Pt	Pt.AST38	100.0000	0.0288	0.0292	0.9858	1.0000
S	FeS2.Ast30	53.4500	2.2814	2.7738	0.8220	1.0006
Sb	SbTe.Ast53	38.8800	1.0788	1.2098	0.8917	1.0000
Te	SbTeAst53	61.1200	0.9706	1.0742	0.9036	1.0000
Zn	Wille.Ast46	53.7400	0.0604	0.0609	0.9922	1.0000

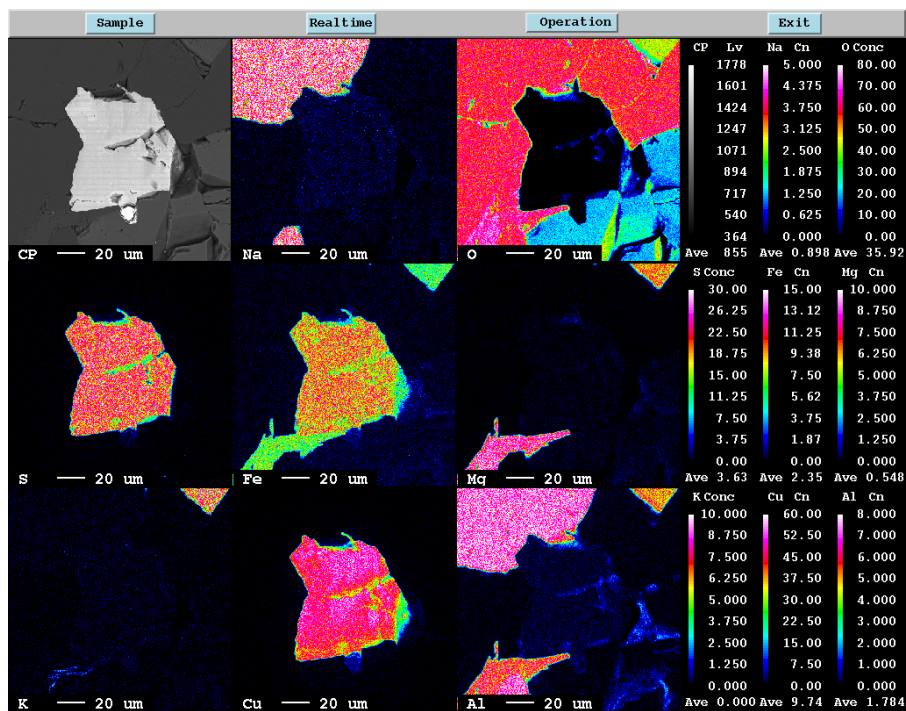


Figure D122. Scanning map from drill core NUS-DD-13-004 in thin section NUS_011 at spot NUS_011:3.1, No. 94-96. Scanning map show the element concentration in colour scale at the right side of the map. Map show that the analysed mineral have high content of copper with minor amount of sulphur and iron. Analysis of more elements is given in Figure D123.

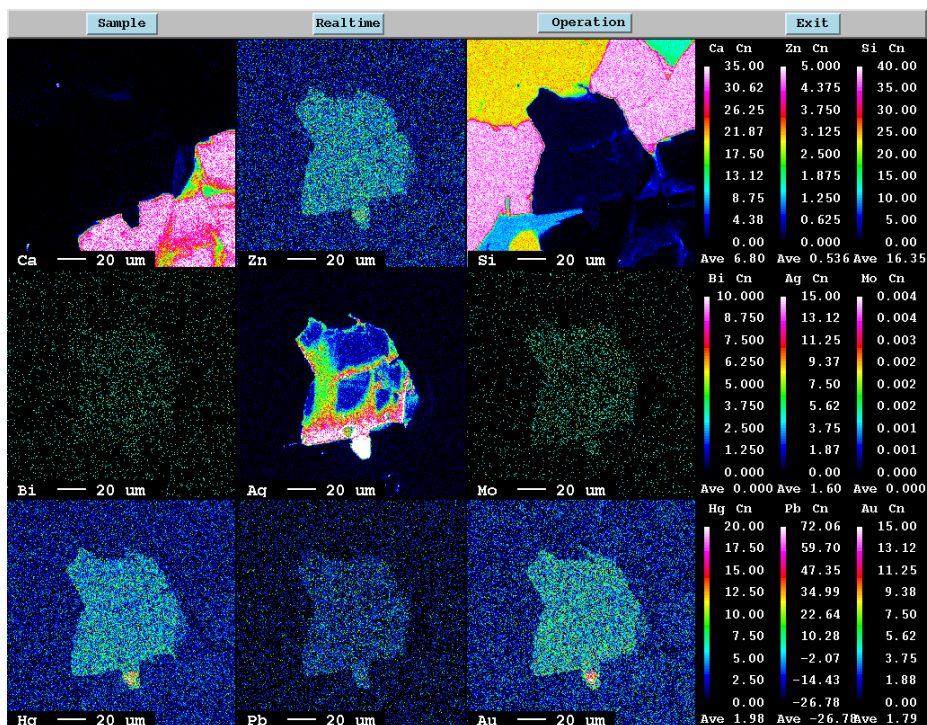


Figure D123. Scanning map from drill core NUS-DD-13-004 in thin section NUS_011 at spot NUS_011:3.1, No.94-96. Scanning map show the element concentration in colour scale at the right side of the map. Map show that the analysed mineral have high content of silver and minor content of gold and mercury. Analysis of more elements is given in Figure D122.

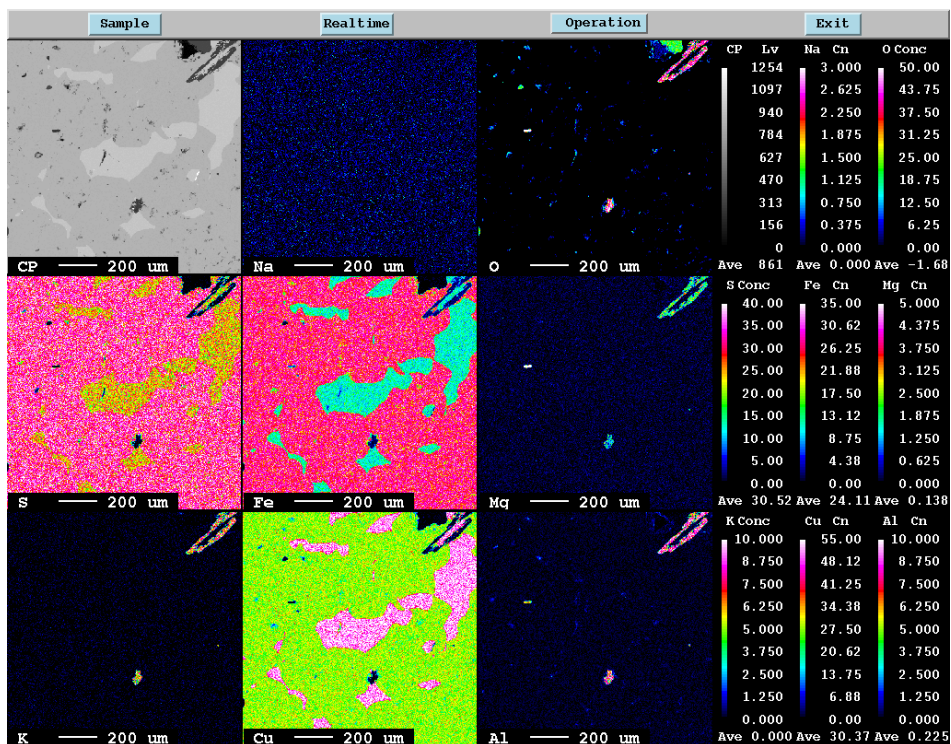


Figure D124. Scanning map from drill core NUS-DD-13-002 in thin section NUS_018 in area NUS_018: 3. Scanning map show the element concentration in colour scale at the right side of the map. Map show that the analysed mineral have high content of sulphur, iron and copper. More element analysed is given in Figure D125.

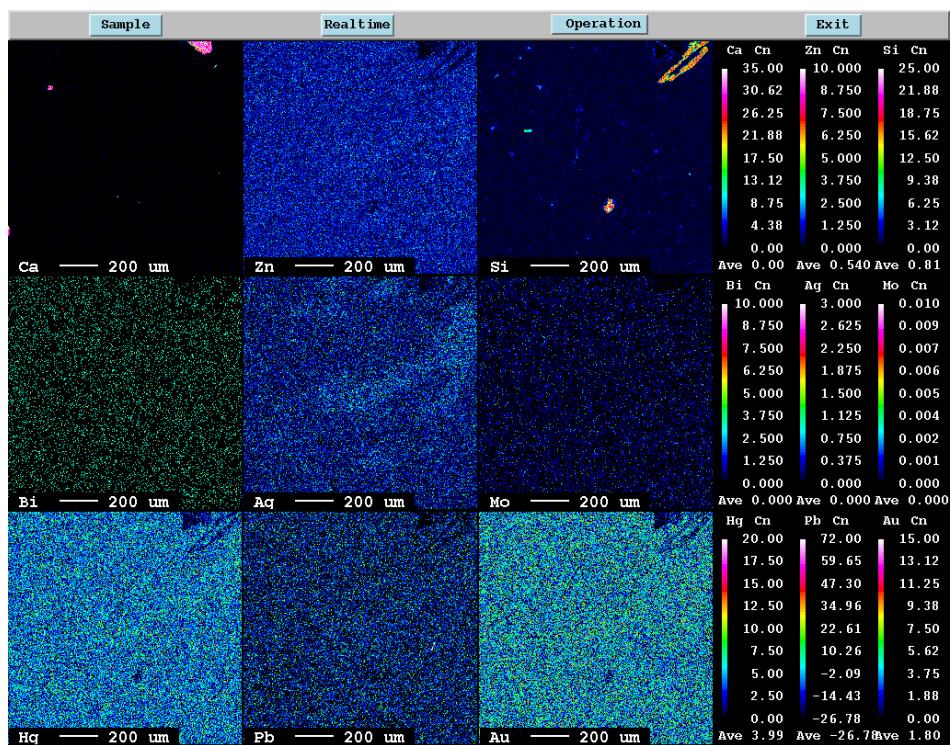


Figure D125. Scanning map from drill core NUS-DD-13-002 in thin section NUS_018 in area NUS_018: 3. Map show the element concentration in colour scale at the right side of the map and show that the analysed minerals have some concentration of gold, mercury and negligible amount of lead, silver and zinc. Analysis of more elements is given in Figure D124.

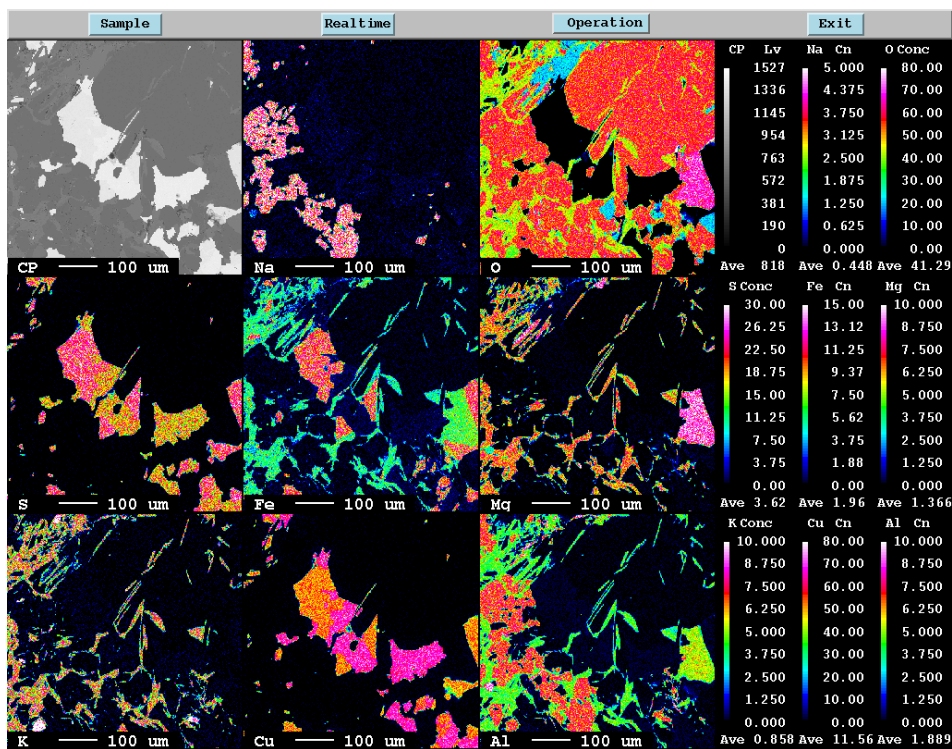


Figure D126. Scanning map from drill core NUS-DD-13-012 in thin section NUS_025 of the point NUS_025:1.3 and NUS_025:1.3. Map show the element concentration in colour scale at the right side of the map and show that the analysed sulphide minerals have high concentration of sulphur, iron and copper. Analysis of more elements is given in Figure D127.

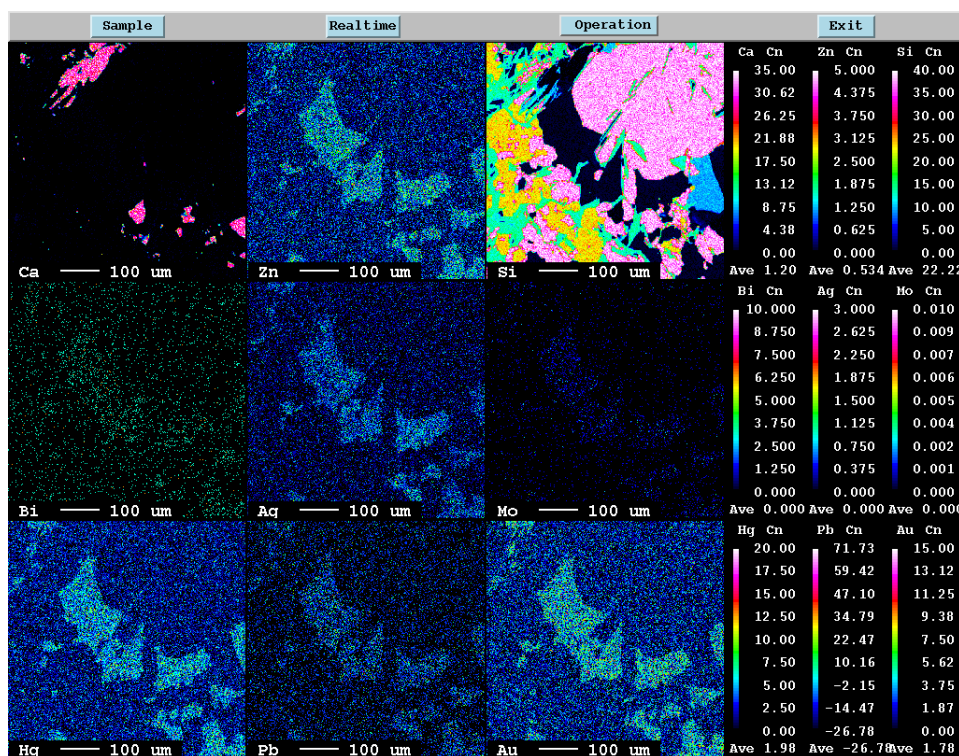


Figure D127. Scanning map from drill core NUS-DD-13-012 in thin section NUS_025 of the point NUS_025:1.3 and NUS_025:1.3. Map show the element concentration in colour scale at the right side of the map and show that the analysed sulphide minerals have very small concentration of gold, silver, zinc, mercury and lead. Analysis of more elements is given in Figure D126.

Table D80. Overview of the analysed thin sections with given area, selected spot, point and interpreted sulphides in polarized microscope, Table 1:3.

Drill core	T.section	Area	Selected spot	Points	Sulphide	No.		
NUS-DD-13-004	NUS_011	NUS_011:1	NUS_011:1.1	NUS_011:1.1.1	Bornite	76		
				NUS_011:1.1.2		77		
				NUS_011:1.1.3		78		
			NUS_011:1.2	NUS_011:1.2.1	Bornite	79		
				NUS_011:1.2.2		80		
				NUS_011:1.2.3		81		
			NUS_011:1.3	NUS_011:1.3.1	Chalcocite	82		
				NUS_011:1.3.2		83		
				NUS_011:1.3.3		84		
		NUS_011:2	NUS_011:2.1	Chalcopyrite	NUS_011:2.1.1	85		
					NUS_011:2.1.2	86		
					NUS_011:2.1.3	87		
			NUS_011:2.2	Bornite	NUS_011:2.2.1	88		
					NUS_011:2.2.2	89		
					NUS_011:2.2.3	90		
			NUS_011:2.3	Bornite	NUS_011:2.3.1	91		
					NUS_011:2.3.2	92		
					NUS_011:2.3.3	93		
		NUS_011:3	NUS_011:3.1	Chalcocite	NUS_011:3.1.1	94		
					NUS_011:3.1.2	95		
					NUS_011:3.1.3	96		
			NUS_011:3.2	Bornite	NUS_011:3.2.1	97		
					NUS_011:3.2.2	98		
					NUS_011:3.2.3	99		
		NUS-DD-13-002	NUS_018	NUS_018:1	NUS_018:1.1	NUS_018:1.1.1	Chalcocite	100
						NUS_018:1.1.2		101
						NUS_018:1.1.3		102
NUS_018:1.2	Chalcopyrite				NUS_018:1.2.1	103		
					NUS_018:1.2.2	104		
					NUS_018:1.2.3	105		
NUS_018:1.3	Bornite				NUS_018:1.3.1	106		
					NUS_018:1.3.2	107		
					NUS_018:1.3.3	108		
NUS_018:1.4	Bornite				NUS_018:1.4.1	109		
					NUS_018:1.4.2	110		
					NUS_018:1.4.3	111		

Table D81. Overview of the analysed thin sections with given area, selected spot, point and interpreted sulphides in polarized microscope, Table 2:3.

NUS-DD-13-002	NUS_018	NUS_018:1	NUS_018:1.5	NUS_018:1.5.1	Chalcopyrite	112		
				NUS_018:1.5.2		113		
				NUS_018:1.5.3		114		
			NUS_018:1.6	NUS_018:1.6.1	Chalcopyrite	115		
				NUS_018:1.6.2		116		
				NUS_018:1.6.3		117		
		NUS_018:2.1	NUS_018:2.1.1	Chalcocite	118			
			NUS_018:2.1.2		119			
			NUS_018:2.1.3		120			
		NUS_018:2.2	NUS_018:2.2.1	Bornite	121			
			NUS_018:2.2.2		122			
			NUS_018:2.2.3		123			
		NUS_018:2.3	NUS_018:2.3.1	Chalcopyrite	124			
			NUS_018:2.3.2		125			
			NUS_018:2.3.3		126			
		NUS_018:3.1	NUS_018:3.1.1	Bornite	127			
			NUS_018:3.1.2		128			
			NUS_018:3.1.3		129			
		NUS_018:3.2	NUS_018:3.2.1	Chalcopyrite	130			
			NUS_018:3.2.2		131			
			NUS_018:3.2.3		132			
		NUS-DD-13-003	NUS_025	NUS_025:1	NUS_025:1.1	NUS_025:1.1.1	Chalcocite	133
						NUS_025:1.1.2		134
						NUS_025:1.1.3		135
					NUS_025:1.2	NUS_025:1.2.1	Bornite	136
						NUS_025:1.2.2		137
						NUS_025:1.2.3		138
NUS_025:1.3	NUS_025:1.3.1				Chalcocite	139		
	NUS_025:1.3.2					140		
	NUS_025:1.3.3					141		
NUS_025:1.4	NUS_025:1.4.1			Bornite	142			
	NUS_025:1.4.2				143			
	NUS_025:1.4.3				144			
NUS_025:2	NUS_025:2.1			NUS_025:2.1.1	Bornite	145		
				NUS_025:2.1.2		146		
				NUS_025:2.1.3		147		

Table D82. Overview of the analysed thin sections with given area, selected spot, point and interpreted sulphides in polarized microscope, Table 3:3.

NUS-DD-13-003	NUS_025	NUS_025:2	NUS_025:2.2	NUS_025:2.2.1	Chalcocite	148
				NUS_025:2.2.2		149
				NUS_025:2.2.3		150
			NUS_025:2.3	NUS_025:2.3.1	Chalcocite	151
				NUS_025:2.3.2		152
				NUS_025:2.3.3		153
NUS-DD-13-012	NUS_031	NUS_031:1	NUS_031:1.1	NUS_031:1.1.1	Bornite	154
				NUS_031:1.1.2		155
				NUS_031:1.1.3		156
			NUS_031:1.2	NUS_031:1.2.1	Chalcocite	157
				NUS_031:1.2.2		158
				NUS_031:1.2.3		159
			NUS_031:1.3	NUS_031:1.3.1	Covellite	160
			NUS_031:1.4	NUS_031:1.4.1	?	161
				NUS_031:1.4.2		162
		NUS_031:1.4.3		163		
		NUS_031:2	NUS_031:2.1	Chalcopyrite	NUS_031:2.1.1	164
					NUS_031:2.1.2	165
					NUS_031:2.1.3	166
			NUS_031:2.2	NUS_031:2.2.1	Chalcopyrite	167
				NUS_031:2.2.2		168
NUS_031:2.2.3	169					

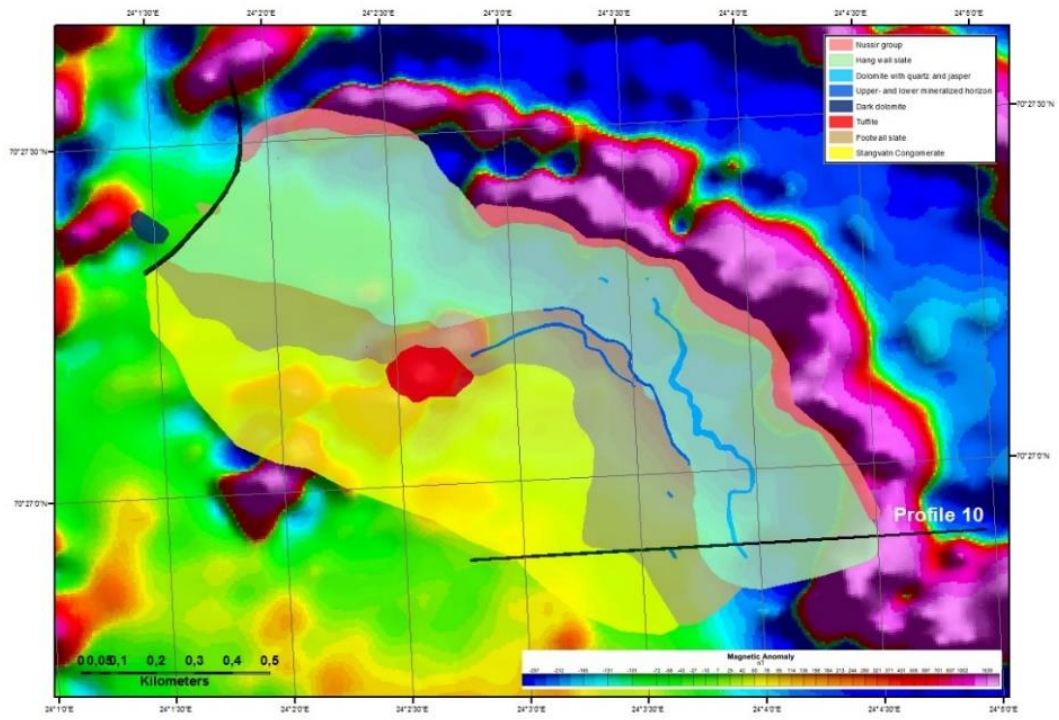


Figure E129. Geological map on geophysical map with magnetic survey (NGU).